

الجمهورية الجزائرية الديمقراطية الشعبية
République Algérienne Démocratique et Populaire
وزارة التعليم العالي و البحث العلمي
Ministère de l'enseignement supérieur et de la recherche scientifique

Université Mohamed Khider – Biskra
Faculté des Sciences et de la technologie
Département de chimie industrielle
Ref :



جامعة محمد خيضر بسكرة
كلية العلوم و التكنولوجيا
قسم: الكيمياء الصناعية.
المرجع: 2016/

Thèse présentée en vue de l'obtention
Du diplôme de
Doctorat en sciences
Spécialité : Génie chimique

**ETUDE MICROSTRUCTURALE DE LA ZONE
AFFECTÉE THERMIQUEMENT DANS UN
ACIER SOUDÉ**

Présentée par : Kelthoum DIGHECHE

Soutenue publiquement le

Devant le jury composé de :

Pr. Abdelouahad Chala	Professeur	Président	Université de Biskra
Pr. Zakaria Boumerzoug	Professeur	Rapporteur	Université de Biskra
Pr. Djamal Bradai	Professeur	Examineur	Université de STHB
Pr. Aissa Belkacem Bouzida	Professeur	Examineur	Université de Batna1
Pr. Belkacem Nessararak	Professeur	Examineur	Université de Sétif 1

الجمهورية الجزائرية الديمقراطية الشعبية
People's Democratic Republic Of Algeria
وزارة التعليم العالي و البحث العلمي
Ministry of Higher Education And Scientific Research

University of Mohamed Khider – Biskra

Faculty of Sciences and technology

Department of chemical industry

Ref :



جامعة محمد خيضر بسكرة
كلية العلوم و التكنولوجيا
قسم: الكيمياء الصناعية.
المرجع: 2016/

Thesis submitted in candidacy for the degree of
Doctorate in sciences
Specialty: **Chemical engineering**

MICROSTRUCTURAL STUDY OF THE HEAT AFFECTED ZONE IN WELDED STEEL

Presented by : Kelthoum DIGHECHE

In front of the jury composed of:

Pr. Abdelouahad Chala	Professor	Chairman	University of Biskra
Pr. Zakaria Boumerzoug	Professor	Supervisor	University of Biskra
Pr. Djamal Bradai	Professor	Member	University of STHB
Pr. Aissa Belkacem Bouzida	Professor	Member	University of Batna 1
Pr. Belkacem Nessararak	Professor	Member	University of Setif 1

ACKNOWLEDGEMENTS

I would like to express my sincere gratefulness to my supervisor professor **Zakaria Boumerzoug**, Mechanical Engineering, for giving me the opportunity to work under him and also providing excellent guidance, their many and useful comments and continuous assistance throughout this research work.

I Would like to thank Mrs **Abdlouahed CHALA**, professor at Biskra university, Who has accepted to be te president of this jury. I would also like to express my sincere gratitude to the members of the jury : Mrs **Djamal Bradai**, professor at USTHB university, Mrs **Nessark Belkacem**, Professor at setif university and Mrs **Bouzida Aissa Belgacem**, professor at Batna university for their patience in the examination of this manuscript.

I would like to thank Mrs **Ji Vincent**. professor at Paris –Sud11 university for the residual stress measurments.

I would like to thank Mrs **Lahcene Fellah**, doctor at Ouargla university for the fruitful technical discussions on related matters. I wish also to thank him for the use of the PM2K softwar.

I also wish to express my deep sense of gratitude to Dr.**Yasmina Bellaroussi**, the responsible of SEM laboratory in Advanced Technologies Developpement Center in algiers for the facilitation and his patience for complement this work .

DEDICATION

TO MY PARENTS

TO MY MOTHER-IN-LAW

TO MY HUSBAND

TO MY CHILDREN

TO MY SISTER AND BROTHERS

TO THE BROTHER AND SISTERS OF MY HUSBAND

TO MY FAMILY

TO MY FRIENDS

CONTENT

GENERAL INTRODUCTION.....	2
----------------------------------	----------

CHAPTER I

I.2 Classification of Steels	5
I.3 Carbon and low alloy steels	7
I.3.1 Carbon Steels.....	7
I.3.1.1 Low Carbon Steel	8
I.3.1.2. Medium Carbon Steel	8
I.3.1.3. High Carbon Steel.....	9
I.3.2 low alloy steel.....	9
I.3.2.1 High Strength Low Alloy (HSLA) Steels.....	9
I.3.2.2 Quenched and tempered low alloy steels.....	11
I.3.2.3 Heat treatable low alloy steels	11
I.4 Phases in steels.....	11
I.5 Crystal Imperfections and Slip	14
I.6 Purposes and effects of alloying additions	17
I.6.1 Common elements of steel	17
I.6.2 Austenite, ferrite and carbide forming elements	18
I.6.3 Ability of alloying elements to impart special characteristics.....	19
I.7 Heat treatments of steel	20
I.7.1 Annealing	21
I.7 .1.1 Full annealing.....	21
I.7 .1.2 Process annealing.....	22
I.7 .1.3 Normalizing	22
I.7 .1.4 Stress-relief annealing.....	22
I.7 .1.5 Spheroidizing	23
I.7 .1.6 Tempering (also called drawing)	24
I.7 .2 Hardening	24
I.7 .3 Tempering.....	24
I.7 .4 Surface hardening.....	25
I.8 The Fe-C phase diagram	25

CONTENT

I.9 Elements of microstructure in steels	27
I.9.1 Cementite Formation	27
I.9.2 Ferrite Formation	28
I.9.4 Pearlite Formation	31
I.9.5 Martensite Transformation	33
I.9.6 Bainite Formation	35
I.10 Transformation Diagrams	38

CHAPTER II

II. 1 Introduction.....	45
II.2 Welding Definition	45
II.3 Welding of piping and pipelines.....	46
II.4 Welding Processes	46
II.4.1 Shielded Metal Arc Welding.....	47
II.4.2 Submerged Arc.....	48
II.4.3 Gas Metal Arc Welding	49
II.4.4 Flux Core Arc Welding.....	50
II.4.5 Gas Tungsten Arc Welding.....	50
II.5 Basic metallurgy of welding	51
II.5.1 Temperature and time in welding.....	51
II.5.2 Heat input	52
II.5.2 Heating Rate.....	53
II.5.3 Peak Temperature.....	53
II.5.4 Cooling Rate.....	54
II.6. Metallurgical effect of the weld thermal cycle.....	55
II.6.1 Weld Metal Solidification	55
II.6.2 Heat affected zone	57
II.6.3 Phases Transformations and microstructures of weld metal	57
II.6.3.1 The as-deposit microstructure	58
II.6.4 Transformation and microstructure in the heat-affected zone	62
II.7 Mechanical properties and residual stress of the welded joint.....	64
II.7.1 Mechanical properties of weld metal	64

CONTENT

II.7.2 Mechanical properties of the heat-affected zone	66
II.7.2.1 Hardness of the heat-affected zone.....	66
II.7.2.2 <i>Fracture toughness of the heat-affected zone</i>	68
II.7.3 Residual stress in weld joint.....	68
II.7.3.1 Definition.....	69
II.7.3.2 Role of residual stresses	69
II.7.3.3 Origin of Stresses.....	72

CHAPTER III

III.1 Introduction	75
III.2 Samples preparation	77
III.3 Heat treatments.....	79
III.4 Microstructural observations.....	79
III.4.1 Metallography	79
III.4.2 Scanning electron microscopy	80
III.5 X-ray diffraction.....	80
III.5 Mechanical tests	82
III.5.1 Microhardness.....	82
III.5.2 Residual stress tests	84

CHAPTER IV

IV.1 Introduction	88
IV.2 Structural characterization by the optical microscope (OM) and the scanning electron microscope (SEM).....	88
IV.2.1 Effect of heat treatment temperature(time =10 min , 30 min and 1 h)	89
IV.2.1.1 Optical micrograph of the base metal	89
IV.2.1.2 Optical micrograph of the heat affected zone (HAZ)	93
IV.2.1.3 Optical micrograph of the fusion zone (FZ)	104
IV.3 Phases characterization	119
IV.3.1 Peaks displacements	128

CONTENT

IV.3.2 Peak characterization	135
IV.4 Basic theory of the profile analysis of XRD spectrums	141
IV.4.1 Diffracted intensity from a defected material	143
IV.4.2 Crystallite size	144
IV.4.3 Planar faults and planes	145
IV.5 Analysis of diffraction profiles	147
IV.5.1 Untreated sample	147
IV.5.1.1 Base metal	147
IV.5.1.2 Heat affected zone.....	149
IV.5.1.3 Fusion zone	150
IV.6 Study of the residual stress	172
IV.7 Hardness examination	175
General coclusion..	182
References.....	186
ANNEXE	

FIGURES LIST

CHAPTER I

Figure I.1: Classification of steels.

Figure I.2: Body-centered cubic (b.c.c.) crystal structure. Ferrite in Steel is b.c.c.

Figure I.3: Face-centered cubic (f.c.c.) crystal structure. Austenite in Steel is f.c.c.

Figure I.4: Schematic of slip bands and associated slip steps on the surface of a single crystal.

Figure I.5: Edge dislocation produced by slip in a simple cubic lattice.

Figure I.6: Slip that produces a screw dislocation in a simple cubic lattice.

Figure I.7: Effects of alloying elements on the eutectoid temperature.

Figure I.8: Effect of substitutional alloying elements on the eutectoid carbon content in steel.

Figure I.9 : Solid solution hardening effects of various alloying elements dissolved in α -iron.

Figure I.10: Iron-iron carbide phase diagram.

Figure I.11: Thin cementite allotriomorphs formed on austenite grain boundaries in a 1.0 wt.% C, 1.5 wt.% Cr steel.

Figure I.12: Polycrystalline, single-phase ferrite microstructure in a steel containing 0.004 wt.% C.

Figure I.13: Ferrite-pearlite microstructure in (a) 0.2 wt. %C steel, (b) 0.4 wt.%C steel.

Figure I.14: Widmanstätten ferrite in a low C steel weld metal.

Figure I.15: SEM micrograph of microalloyed steel contains Pearlite inside the mixture of phase islands.

Figure I.16: Transition from coarse (C) to fine (F) pearlite due to a decrease in the transformation temperature.

Figure I.17: Austenite (fcc) to martensite (bcc) transformation

Figure I.18: Tetragonal martensite in some steels.

Figure I.19: Schematic representation of the formation of upper and lower bainite along with coalesced bainite.

Figure I.20: Microstructure in the as-deposited last bead of weld metals of two low carbon steels imaged using FEGSEM.

FIGURES LIST

Figure I.21: Isothermal transformation diagram for eutectoid steel.

Figure I.22: TTT diagram for hypoeutectoid steel.

Figure I.23: Continuous cooling diagram for hypoeutectoid steel.

CHAPTER II

Figure II.1: Shielded metal arc welding (SMAW) or manual metal arc welding (MMA).

Figure II.2: Illustration of Submerged Arc Welding.

Figure II.4: Gas tungsten arc welding.

Figure II.6: Thermal cycles in weld zones.

Figure II.7: Solidification modes (a) planar; (b) cellular dendritic and (d) columnar dendritic.

Figure II.8: Schematic diagrams showing competitive growth with a teardrop shaped weldpool and an elliptical weldpool.

Figure II.9: (a) Replica transmission electron micrograph of acicular ferrite plates in steel weld deposit, (b) An illustration of the essential constituents of the primary microstructure of a steel weld deposit.

Figure II.10: Morphologies of grain boundary ferrite and degenerate pearlite of the steel without Nb at a cooling rate of 1 k/s/.

Figure II.11: Optical microscopy of weld metals associated with carbon-manganese steel in the as welded condition.

Figure II.12: Lamellar structure in submerged arc weld metal.

Figure II.13: Change from a bainitic (a) microstructure to one which is predominantly acicular ferrite.

Figure II.14: Schematic illustration of the microstructural variation to be expected in the HAZ of steel welds.

Figure II.15: Coupling of temperature, stress, and microstructure.

Figure II.16: Definition of different types of stresses at various spatial scales of a polycrystalline material.

Figure II.17: First and second order stresses induced by external loads or long-scale forces for single phase (a) and two phase (b). Also, the third order stresses III.

Figure II.18: Residual stress distribution in case of welding without phase change.

FIGURES LIST

CHAPTER III

Figure.III.1: X70 pipeline steel after industrial arc welding.

Figure III.2: Microstructure of X70 pipeline steel.

Figure III.3: Steps of the weld joint preparation.

Figure III.4: Sample (30x20 cm) of the welded pipe line.

Figure III.5: Different samples of X70 steel after welding.

Figure III.6: Optical microscope HUND T100-WETZLAR.

Figure III.7: Spectrum of EDAX analysis of X70 pipeline steel.

Figure III.8: Diffractometre BRUKER D8 ADVANCE AXS (XRD).

Figure III.9: Digital Micro Vickers Hardness Tester (HVS-1000Z)

Figure III.10: Diffraction on a stress free lattice (a) and on a deformed lattice (b).

Figure III.11: General view of the X-ray apparatus.

CHAPTER IV

Figure IV.1: SEM micrograph of the welded joint.

Figure IV.2: Optical and SEM micrographs of the untreated base metal.

Figure IV.3: Optical and SEM micrographs of the heat treated base metal for 10 min.

Figure IV.4: Optical and SEM micrographs of the heat treated base metal for 30 min.

Figure IV.5: Optical and SEM micrographs of the heat treated base metal for 1h.

Figure IV.6: SEM micrograph of junction zone between heat affected zone(HAZ) and fusion zone of the untreated sample.

FigureIV.7: SEM micrograph of junction zone between heat affected zone(HAZ) and fusion zone for the heat treated sample at 200°C for 10 min.

FigureIV.8: SEM micrograph of junction zone between heat affected zone(HAZ) and fusion zone for the heat treated sample at 400°C for 10 min.

FigureIV.9: SEM micrograph of junction zone between heat affected zone(HAZ) and fusion zone for the heat treated sample at 600°C for 10 min.

FIGURES LIST

FigureIV.10: SEM micrograph of junction zone between heat affected zone (HAZ) and fusion zone after heat treatment at 200°C for 30 min.

FigureIV.11: SEM micrograph of junction zone between the sub-zones of the heat affected zone (HAZ) after heat treatment at 400°C for 30 min.

FigureIV.12: SEM micrograph of junction zone between heat affected zone (HAZ) and fusion zone after heat treatment at 600°C for 30 min.

FigureIV.13: SEM micrograph of junction zone between heat affected zone (HAZ) and fusion zone after heat treatment at t 200°C for 1h.

FigureIV.14: SEM micrograph of junction zone between heat affected zone (HAZ) and fusion zone after heat treatment at 400°C for 1h.

FigureIV.15: SEM micrograph of junction zone between heat affected zone (HAZ) and fusion zone after heat treatment at 600°C for 1h.

Figure IV.16: Optical and SEM micrographs of the untreated fusion zone (first pass).

Figure IV.17: Optical micrographs and SEM micrographs of the fusion zone (first pass) for 10 min.

Figure IV.18: Optical micrographs and SEM micrographs of fusion zone (first pass) for 30 min.

Figure IV.19: Optical micrographs and SEM micrographs of fusion zone (first pass) for 1 h.

Figure IV.20: Microstructure obtained after a thermal cycle with a peak temperature of 600°C (Spheroidization of lamellar cementite) in microalloyed steel.

Figure IV.21: Spheroidized carbide region: pearlite (black) and ferrite (white) in medium steel.

Figure IV.22: Optical and SEM micrographs of the untreated fusion zone (second pass).

Figure IV.23: Optical and SEM micrographs of fusion zone (second pass) for10 min.

Figure IV.24: Optical and SEM micrographs of fusion zone (second pass) for30 min.

Figure IV.25: Optical and SEM micrographs of fusion zone (second pass) for 1h.

Figure IV.26: Optical and SEM micrographs of untreated fusion zone (third pass).

Figure IV.27: Optical and SEM micrographs of fusion zone (third pass) for10 min.

Figure IV.28: Optical and SEM micrographs of fusion zone (third pass) for30 min.

Figure IV.29: Optical and SEM micrographs of fusion zone (third pass) for1h

Figure IV.30: X-ray diffraction profiles of base metal for 10 min.

Figure IV.31: X-ray diffraction profiles of base metal for 30 min.

FIGURES LIST

Figure IV.32: X-ray diffraction profiles of the base metal for 1h.

Figure IV.33: X-ray diffraction profiles of the heat affected zone for 10.

Figure IV.34: X-ray diffraction profiles of the heat affected zone for 30 min.

Figure IV.35: X-ray diffraction profiles of the heat affected zone for 1h.

Figure IV.36: X-ray diffraction profiles of the fusion zone for 10 min.

Figure IV.37: X-ray diffraction profiles of the fusion zone for 30 min.

Figure IV.38: X-ray diffraction profiles of the fusion zone for 1h.

FigureVI.39: (a) X-ray diffraction profile of the untreated sample (BM), (b) Fifth peak, (c) The mean domain size.

FigureVI.40: (a) X-ray diffraction profile of the untreated sample (HAZ), (b) Fourth peak, (c) The mean domain size.

FigureVI.41: (a)X-ray diffraction profile of the untreated sample(FZ), fitting by PM2K, (b)Fifth peak, (c)The mean domain size

FigureVI.42:X -ray diffraction profile of the base metal before and after heat treatments for 10 min at 200°C, 400°C and 600°C respectively, fittings by PM2K.

FigureVI.43: X-ray diffraction profiles of the base metal before and after heat treatments for 30 min at 200°C, 400°C and 600°C respectively, fittings by PM2K.

Figure VI.44: X-ray diffraction profiles of the base metal before and after heat treatments for 1h at 200°C , 400°C and 600°C respectively, fittings by PM2K.

Figure VI.45: X-ray diffraction profiles of the heat affected zone before and after heat treatments for 10 min at 200°C, 400°C and 600°C respectively, fittings by PM2K.

Figure VI.46: X-ray diffraction profiles of the heat affected zone before and after heat treatments for 10 min at 200°C , 400°C and 600°C respectively, fittings by PM2K.

Figure VI.47: X-ray diffraction profiles of the heat affected zone before and after heat treatments for 30 min at 200°C, 400°C and 600°C respectively, fittings by PM2K.

Figure VI.48: X-ray diffraction profiles of the fusion zone before and after heat treatments for 10 min at 200°C, 400°C and 600°C respectively, fittings by PM2K.

Figure VI.49: X-ray diffraction profiles of the fusion zone before and after heat treatments for 30 min at 200°C and 600°C respectively, fittings by PM2K.

Figure VI.50: X-ray diffraction profiles of the fusion zone before and after heat treatments for 1h at 200°C, 400°C and 600°C respectively, fittings by PM2K.

Figure IV.51: (a) The stress distributions and (b) width peak evolution in the weld region of X70 pipeline steel

FIGURES LIST

Figure IV.52: (a) Stress distributions and (b) width peak diffraction evolution in the weld region of X70 pipeline steel heat treated 1 h at 200°C.

Figure IV.53: Stress distributions and (b) width peak diffraction evolution in the weld region of X70 pipeline steel heat treat 1 h at 600°C.

Figure VI.57: Hardness graphs in first pass of specimen which is not heat treated and specimens which are heat treated at 200°C, 400°C and 600°C for 10 min after welding.

Figure VI.58: Hardness graphs in first pass of specimen which is not heat treated and specimens which are heat treated at 200°C, 400°C and 600°C for 30 min after welding.

Figure VI.59: Hardness graphs in first pass of specimen which is not heat treated and specimens which are heat treated at 200°C, 400°C and 600°C for 1h after welding.

Figure VI.60: Hardness graphs in last pass of specimen which is not heat treated and specimens which are heat treated at 200°C, 400°C and 600°C for 10 min after welding.

Figure VI.61: Hardness graphs in last pass of specimen which is not heat treated and specimens which are heat treated at 200°C, 400°C and 600°C for 30 min after welding.

Figure VI.62: Hardness graphs in last pass of specimen which is not heat treated and specimens which are heat treated at 200°C, 400°C and 600°C for 1h after welding.

TABLES LIST

CHAPTER II

Table II.1: AWS designation for Arc Welding Processes and friction stir welding(FSW).

CHAPTER III

Table III.1: Chemical composition of pipeline steel (wt %).

Table III.2: Chemical composition of electrode 1 (wt %).

Table III.3: Available hardness charges values.

CHAPTER IV

Table IV.1: Displacements of the five first peaks in the base metal (BM).

Table IV.1 (continued): Displacements of the five first peaks in the base metal (BM).

Table IV.2: Displacements of the five first peaks in the heat affected zone (HAZ).

Table IV.2 (continued): The displacements of the five first peaks in the heat affected zone (HAZ).

Table IV.3: Displacements of the five first peaks in the fusion zone (FZ).

Table IV.3 (continued): Displacements of the five first peaks in the heat affected zone (HAZ).

Table IV.4: Results of the diffraction profiles analysis in the base metal (BM).

Table IV.4 (continued): Results of the diffraction profiles analysis in the base metal (BM).

Table IV.5: Results of the diffraction profiles analysis in the heat affected zone (HAZ).

Table IV.5 (continued): Results of the diffraction profiles analysis in the heat affected zone (HAZ).

Table IV.6: Results of the diffraction profiles analysis in the fusion zone (FZ).

Table IV.6 (continued): Results of the diffraction profiles analysis in the fusion zone (FZ).

Table VI.7: Results of PM2K calculus (Sample1(BM)).

Table VI.8: Results of the PM2K calculus (sample 1 (HAZ)).

Table VI.9: Results of the PM2K calculus (sample 1 (FZ)).

Table VI.10: Results of the PM2K calculus in the base metal before and after heat treatment for 10 min.

Table VI.11: Results of the PM2K calculus in the base metal before and after heat treatment for 30 min.

TABLES LIST

Table VI.12: Results of the PM2K calculus in the base metal before and after heat treatment for 1h.

Table VI.13: Results of the PM2K calculus in the heat affected zone before and after heat treatment for 10 min.

Table VI.14: Results of the PM2K calculus in the heat affected zone before and after heat treatment for 30 min.

Table VI.15: Results of the PM2K calculus in the heat affected zone before and after heat treatment for 1h.

Table VI.16: Results of the PM2K calculus in the fusion zone before and after heat treatment for 10 min.

Table VI.17: Results of the PM2K calculus in the fusion zone before and after heat treatment for 30 min.

Table VI.18: Results of the PM2K calculus in the fusion zone before and after heat treatment for 1h.

Table VI.19: Average hardness values in the first pass.

Table VI.20: Average hardness values in the last pass.

GENERAL INTRODUCTION

GENERAL INTRODUCTION

Welding is a process of joining materials into one piece. Welding is one of the most important technological processes used in many branches of industry such as industrial engineering, shipbuilding, pipeline fabrication among others. Generally, welding is the preferred joining method and most common steels are weldable. However, welding is a complicated process accompanied by shrinkage effects, phase transformations; intensification of corrosion and arising of residual stresses [1].

Heat generated during welding induces an important temperature gradient in and around the welded area. The region outside the welded joint that is thermally affected by the welding treatment is known as the heat-affected zone (HAZ) [2]. Welded joints are heterogeneous by nature and present a gradient of properties in the base metal and the HAZ. The welded joints can be classified on the basis of coherency between the welded zone and the base metal [3]. Mechanical properties of welds are determined by chemical composition, cooling rate (technological parameters such as voltage and current) and microstructure. Microstructure is in fact a function of the other variables. The most important factor determining the weld metal properties is chemical composition [4] and the thermal history (cycles) due to the welding processes [2].

Under thermal effect of welding, evident change of microstructure and property occurs in the base metal adjacent to the weld metal. Sometimes, the change of the microstructure may lead to local brittleness in heat-affected zone (HAZ). In addition defects, stress concentration and higher residual stresses are easy to coexist in the welded joint [5].

The residual stress is internal stress, which is existing for separated system, Not exposed to external forces, and in thermal and mechanical equilibrium [6].

Residual stresses affect the mechanical properties of materials and they are responsible for such processes like fracture, cracks growth, fatigue, creep, recrystallization and many others. However in some cases the residual stresses improve selected properties of materials. For example the presence of the compression stress field can improve endurance for cracking [7] consequently, it is very important to understand and quantify the residual stresses.

The goal of the work initiated in this thesis was to gain a detailed understanding of the microstructure induced after arc welding in weld joint, especially in the HAZ, and their changes after some isothermal heat treatments applied in our laboratory. Systematic

characterization experiments have been undertaken to demonstrate the progress of the isothermal annealing as a function of time and temperature .

One of the aim of this a scientific work is to analyze by X-ray diffraction the residual stress development in the heat affected zone (HAZ) and the fusion zone (FZ) and the measure of the density of dislocations of an X70 pipeline steel obtained from COSIDER company of Biskra. This investigation is a contribution as some scientific works which have been done on welding of low carbon steel [8-11]. Microhardness analysis was also complementary technique during this investigation.

This thesis is divided into four chapters:

-Chapter one presents different characteristics of steels, specially the carbon and the low alloy steels, their heat treatments and equilibrium phases diagrams. We are studied also the phases transformation diagrams.

- Chapter two illustrates the currently welding process which is used for the pipeline welding and their effects on steel. This chapter gives a general knowledge about the basic metallurgy of the welding, metallurgical effect of the weld thermal cycle; the mechanical properties of the welded joint and the residual stress are also presented.

-Chapter three gives all the equipments and characterization methods used in this experimental work like: Optical microscope, scanning electron microscope, X-ray diffraction for the phases analysis, X-ray diffraction of the residual stress determination and microhardness analysis.

-Chapter four shows the different results and their discussions of this study.

CHAPTER I THE STEELS

I.1 Introduction

Steels are alloys of iron and other chemical elements. The chemical components partition themselves into various crystal phases according to the principles of thermodynamics and the requirements of crystal physics. The phases in turn are arranged into microstructures which are characterized by the volume fractions, morphologies, perfection, and arrangements of the various phases which form in a given steel [12].

Steel remains the most successful of all materials, with 1.3 billion tonnes being consumed annually in improving the quality of life. The mechanical properties depend to a reasonable extent on the microstructure, which is influenced in part by precipitation reactions. Phase transformations are therefore important in designing the microstructures for specific applications. Several techniques are used by steel manufacturers to make high performance steels. These include grain refinement, work hardening, precipitation hardening and heat treatment [13].

Steels constitute a very large group of alloys, with the common feature that iron is the major component. Carbon is also a major component in many steels. There is many types of steel, each defined by composition ranges and microstructures which produce properties suitable for certain types of applications. Within a given type or class of steels there may be many grades of steels tailored to produce some-what different microstructures and properties. This chapter describes the microstructures and phase transformations typical of plain carbon and low-alloy carbon steels [12].

I.2 Classification of Steels [14]

Steels can be classified by a variety of different systems depending on:

- The composition, such as carbon, low-alloy, or stainless steels
- The manufacturing methods, such as open hearth, basic oxygen process, or electric furnace methods
- The finishing method, such as hot rolling or cold rolling
- The product form, such as bar, plate, sheet, strip, tubing, or structural shape
- The deoxidation practice, such as killed, semikilled, capped, or rimmed steel
- The microstructure, such as ferritic, pearlitic, and martensitic (Figure I.1)
- The required strength level, as specified in ASTM standards
- The heat treatment, such as annealing, quenching and tempering, and thermomechanical processing

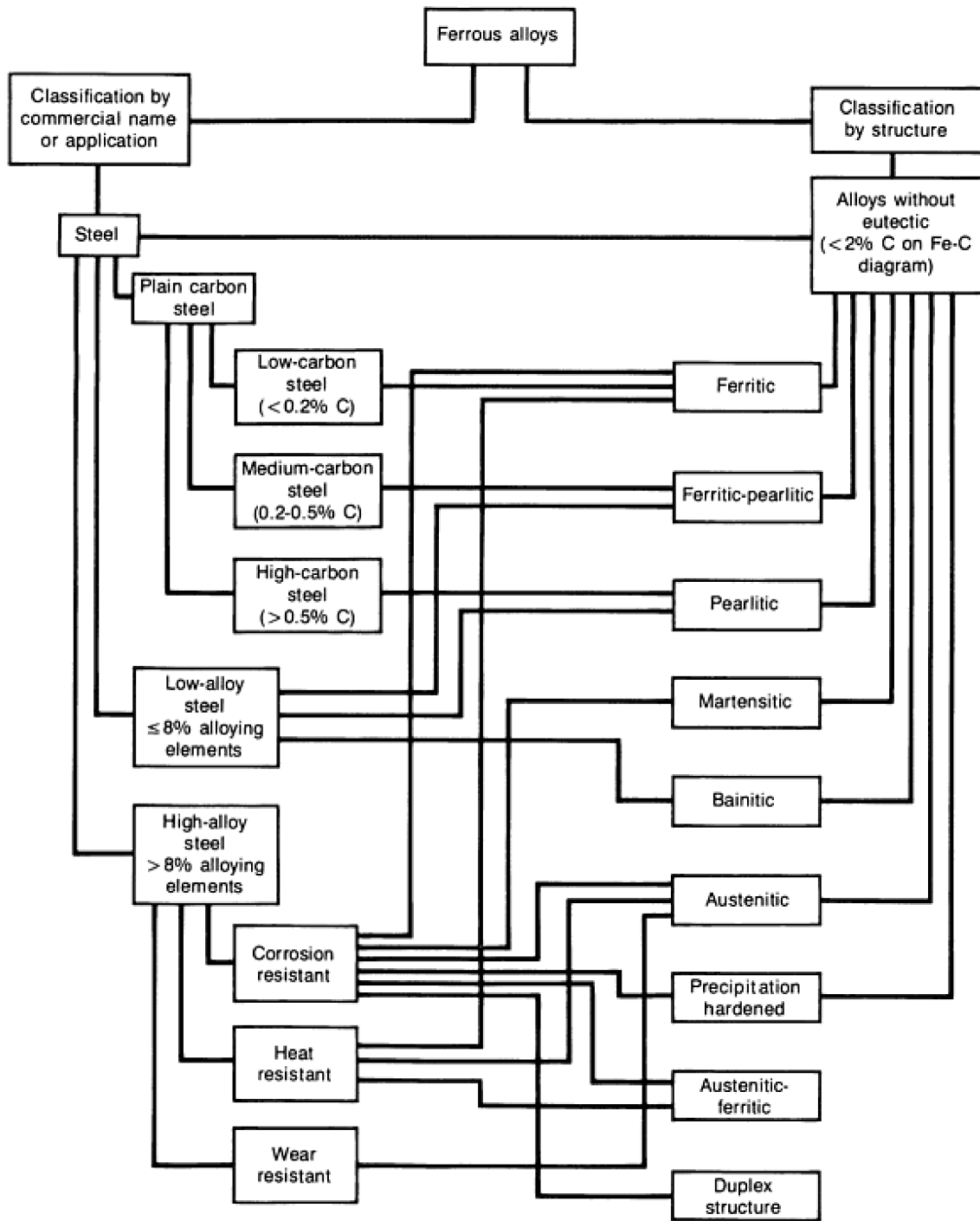


Figure I.1: Classification of steels [14].

From the classification systems, chemical composition is the most widely used internationally and will be emphasized as following:

I.3 Carbon and low alloy steels

Carbon steels are simply alloys of iron and carbon, with carbon as the major strengthening agent. The American Iron and Steel Institute (AISI) defines carbon steels as steels with up to 2% carbon and only residual amounts of other elements except those added for deoxidation (for example, aluminum), with silicon limited to 0.6%, copper to 0.6%, and manganese to 1.65%. Other terms applied to this class of steels are plain carbon steels, mild steels, low-carbon steels, and straight carbon steels. Alloy steel is not a precise term. It could mean any steel other than carbon steels, but accepted application of the term is for a group of steels with varying carbon contents up to about 1% and with total alloy content below 5% [15]. Low alloy steels are those alloy steels with total alloying element contents, including carbon, of less than about 5%. The High Strength Low Alloy (HSLA) steels, can be considered to be intermediate between carbon steels and alloy steels. The HSLA steels are designed to have higher mechanical properties than carbon steels but without the need for the quench and temper heat treatments which are associated with alloy steels.

Carbon and alloy steels are classified in a wide variety of ways. Most common is designation by chemical composition. Steels can be classified on the basis of mechanical properties such as strength, as in ASTM standards, or on the basis of quality descriptors such as forging quality or structural quality. Other bases for classification include the manufacturing method (e.g. basic oxygen furnace or electric furnace), the finishing method (hot rolling, cold rolling, etc.), the product form (bar, sheet, etc.), the deoxidation practice (rimmed, capped, semi-killed, killed), the microstructure (ferritic, pearlitic, martensitic), the heat treatment (annealed, normalized, quenched and tempered) [16].

I.3.1 Carbon Steels

Carbon steel is the most common pipe material in the power, chemical, process, hydrocarbon and pipeline industries. Carbon steel pipe specifications commonly used in steam, water or air service include ASTM A106 and ASTM A53. A common steel for pipelines is API 5L. Carbon steels can in turn be classified as "mild", "medium" and "high" carbon. Mild steel is a carbon steel with less than 0.30% carbon. Medium carbon steel has 0.30% to 0.60% carbon. High carbon steel has over 0.6% carbon [17].

I.3.1.1 Low Carbon Steel

A large amount of steel used today is the variety with low carbon content. The range of carbon from 0.04 to 0.15% is intended as a guide for a group of steels that provide virtually no difficulty with the hardening during welding. Low carbon steel is in auto bodies, sheets and strips used for items stamped and formed, drums, cans, shells and frames of electric motors, and many other applications. Many of these items for mass produced in steel called narrower range of carbon of 0.04 to 0.15%, and various restrictions with manganese and silicon contents [15]. The microstructures of these sheet steels consist predominantly of ferrite, with small amounts of spheroidized carbide. The major microstructural component of low-carbon steels has traditionally been equiaxed or polygonal ferrite, but recent developments have added other major microstructural components. Nevertheless, the performance of low-carbon steels depends essentially on the deformation and fracture mechanisms of ferrite, Deformation, Strengthening, and Fracture of Ferritic Microstructures. Microstructures consisting primarily of ferrite have relatively low strength. Low carbon sheet steel is also available as dual-phase steel which has a desirable combination of strength and formability due to processing which provides a microstructure consisting of islands of martensite in a ferrite matrix[16,18].

Mild steels are mostly used in the as-rolled, forged, or annealed condition and are seldom quenched and tempered. The largest category of mild steels is the low-carbon (<0.08% C, with <0.4% Mn) mild steels used for forming and packaging. Mild steels with higher carbon and manganese contents have also been used for structural products such as plate, sheet, bar, and structural sections [19].

I.3.1.2. Medium Carbon Steel

Medium carbon steels containing 0.30 to 0.60%C and 0.60 to 1.65%Mn are normally used in the quenched and tempered condition. Oil quenching can be used if section size is not too great. These steels, normally produced in the killed condition, are versatile since the balance between strength and ductility can be controlled by adjusting the tempering time and temperature. Quenched and tempered medium carbon steels are used for such applications as automotive engine [16].

I.3.1.3.High Carbon Steel

High carbon steel containing 0.6% to 1.0%C finds applications as springs and as high strength wires. These steels have lower ductility than the medium carbon steels as well as restricted formability and weldability. High carbon steels are normally processed by quenching and tempering, with oil quenching common except in heavy sections and for cutting edges[16].

Medium and high carbon steels with carbon contents over 0.3%C (machine component and rail steels, etc) have a higher hot cracking sensitivity than low-carbon steels (mild steels, etc). This is generally indicated as being due to the fact that, when alloying elements are added to the pure metal, (1) the solidification temperature range increases and (2) the final solidification temperature decreases as their content increases, thereby heightening the hot cracking sensitivity. These features correspond to the case where no special reaction occurs during solidification of carbon steels, ie Fe-C alloys [20].

I.3.2 low alloy steel

Low alloy steels usually contain modest amounts of chromium, nickel, molybdenum and vanadium for hardenability purposes. One of the elements may be present in concentrations of up to about 4 %. In its effect on solidification carbon is still by far the most important element [14, 21].

I.3.2.1 High Strength Low Alloy (HSLA) Steels

High-strength low-alloy (HSLA) steels, or microalloyed steels, are designed to provide better mechanical properties and/or greater resistance to atmospheric corrosion than conventional carbon steels. They are not considered to be alloy steels in the normal sense because they are designed to meet specific mechanical properties rather than a chemical composition. The chemical composition of a specific HSLA steel may vary for different product thickness to meet mechanical property requirements [19].

The HSLA steels are classified as following [14]:

- Weathering steels**, designed to exhibit superior atmospheric corrosion resistance
- Control-rolled steels**, hot rolled according to a predetermined rolling schedule designed to develop a highly deformed austenite structure that will transform to a very fine equiaxed ferrite structure on cooling.

- **Pearlite-reduced steels**, strengthened by very fine-grain ferrite and precipitation hardening but with low carbon content and therefore little or no pearlite in the microstructure.
- **Microalloyed steels**, with very small additions (generally <0.10% each) of such elements as niobium, vanadium, and/or titanium for refinement of grain size and/or precipitation hardening.
- **Acicular ferrite steel**, very low carbon steels with sufficient hardenability to transform on cooling to a very fine high-strength acicular ferrite (low-carbon bainite) structure rather than the usual polygonal ferrite structure
- **Dual-phase steels**, processed to a micro-structure of ferrite containing small uniformly distributed regions of high-carbon martensite, resulting in a product with low yield strength and a high rate of work hardening, thus providing a high-strength steel of superior formability

From these categories of HSLA steels. One of the common ones is the microalloyed steels, so named because they contain alloying elements such as Nb (Cb), V, Ti or Mo in amounts rarely exceeding 0.1%. Manganese levels are generally high, in the vicinity of 1.5%. Another type is the acicular ferrite HSLA steels which contain less than 0.1% carbon, with additions of manganese, along with such elements as molybdenum and boron. This material finds wide application in linepipe for low temperature service [16, 18].

These HSLA steels obtain their high strengths through a combination of mechanisms including extremely fine grain size, with precipitation hardening by carbide, nitride and carbonitride particles. To achieve the desired microstructure and properties it is necessary to carefully control the processing of these steels with emphasis on the temperature and deformation during the final stages of rolling, and the cooling conditions after finish rolling.

There are also dual-phase HSLA steels whose microstructures consist of small, uniformly distributed islands of high-carbon martensite in a ferrite matrix. Martensite typically accounts for about 20% of the volume. These materials have the excellent formability of low strength steel but can yield a high strength in the finished component, because they are greatly strengthened by the plastic deformation during forming [16].

I.3.2.2 Quenched and tempered low alloy steels

The quenched-and-tempered low-alloy (QTLA) steels, usually containing less than 0.25% carbon and less than 5% alloy, are strengthened primarily by quenching and tempering to produce microstructures containing martensite and bainite. The yield strength ranges from approximately 345 to 895 MPa, depending on the composition and heat treatment.

Low carbon content is desired in such alloys for the following two reasons: (i) to minimize the hardness of the martensite and (ii) to raise the M_s (martensite start) temperature so that any martensite formed can be tempered automatically during cooling. Due to the formation of low-carbon auto-tempered martensite, both high strength and good toughness can be obtained. Alloying with Mn, Cr, Ni, and Mo ensures the hardenability of such alloys. The use of Ni also significantly increases the toughness and lowers the ductile-brittle transition temperature in these alloys [22].

I.3.2.3 Heat treatable low alloy steels

The heat-treatable low-alloy (HTLA) steels refer to medium-carbon quenched and tempered low-alloy steels, which typically contain up to 5% of total alloy content and 0.25-0.50% carbon and are strengthened by quenching to form martensite and tempering it to the desired strength level. The higher carbon content promotes higher hardness levels and lower toughness and hence a greater susceptibility to hydrogen cracking than the quenched and tempered low-alloy steels.

The HTLA steels are normally welded in the annealed or over tempered condition except for weld repairs, where it is usually not feasible to anneal or over temper the base metal before welding [22].

I.4 Phases in steels

Phases in metallic systems are characterized by unique crystal structures and chemical compositions and are separated from other phases by well-defined interfaces or boundaries. Pure iron is polymorphic or allotropic, it exists as two quite different phases with different crystal structures. One phase is referred to as alpha (α) iron or ferrite and has a body centered cubic (b.c.c.) crystal structure. The crystal structure of ferrite is characterized by the unit cell shown in Fig. I.2. Ferrite belongs to the cubic crystal system, all three axes of the unit cell are of the same length a and are mutually perpendicular. The space lattice of ferrite is body-centered cubic (bcc). There are a total of two atoms per unit cell: the body-centered atom with coordinates $a/2, a/2, a/2$, and the atom at the origin of the unit cell with coordinates $0, 0, 0$. The latter atom represents all the equivalent corner atoms of the unit cell, each of which is

shared by eight unit cells that come together at a corner. The one-eighth atom per corner times the eight corners of the unit cell therefore accounts for one of the two atoms in a bcc unit cell. The lattice parameter of alpha iron at room temperature is 0.286 nm (2.86 Å). The body diagonals of the unit cell, corresponding to $\langle 111 \rangle$ directions, are the directions in which the iron atoms are in contact in the bcc structure. The other form of iron is referred to as gamma (γ) iron or austenite and has a face centered cubic (f.c.c.) structure. The unit cell of gamma iron or austenite is shown in Figure I.3. Austenite also belongs to the cubic crystal system but has a face-centered cubic (fcc) lattice. There are a total of four atoms per unit cell with coordinates $0, 0, 0; 0, a/2, a/2; a/2, a/2, 0; a/2, 0, a/2$, corresponding to a corner atom and an atom in the center of each face of the unit cell. Each face atom is shared by two adjacent unit cells; the six faces of the cubic cell thus contribute three atoms. As described previously for the bcc cell, the eight corners together contribute only one atom. The lattice parameter of austenite, about 0.356 nm (3.56 Å) is larger than that of ferrite [12, 18].

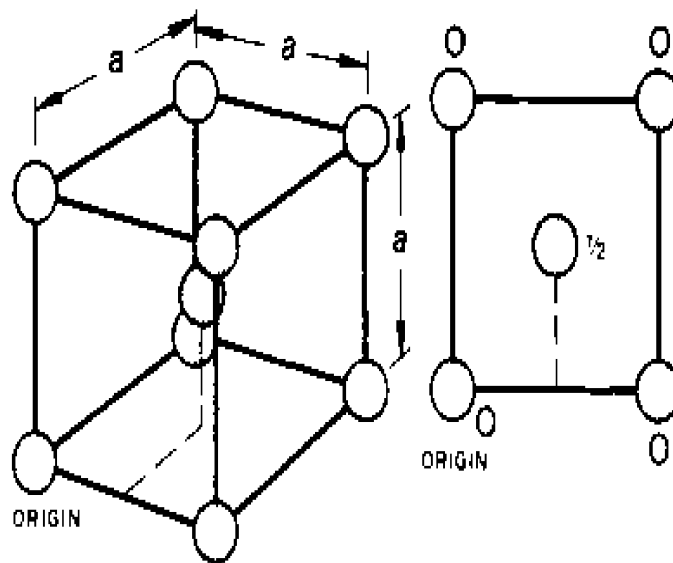


Figure I.2: Body-centered cubic (b.c.c.) crystal structure. Ferrite in Steel is b.c.c [12].

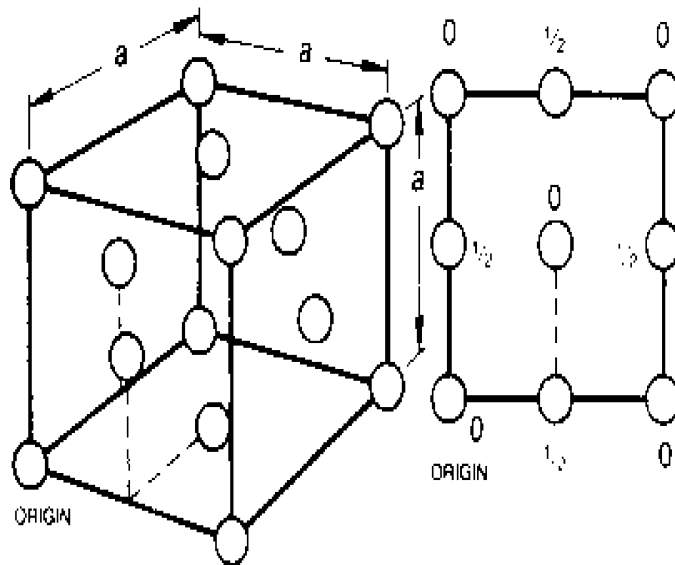


Figure I.3: Face-centered cubic (f.c.c.) crystal structure. Austenite in Steel is f.c.c [12].

Alpha iron is stable from absolute zero to 912 °C, and gamma iron is stable from 912 °C to 1394°C. Between 1394°C and the melting point of pure iron, 1538°C, the body centered cubic form of iron again becomes stable, and to differentiate it from the alpha iron stable at lower temperatures, it is referred to as delta iron or delta ferrite. The various crystal structures of iron are related to crystal atom arrangements of minimum energy as determined by complex temperature dependent electrostatic interactions between the electrons and the lattice of positive iron ions.

The atom arrangements shown in Figures.1.2 and 1.3 show the unit cells or basic repeating unit of b.c.c. and f.c.c. structures. In crystals or grains of iron, the pattern established by the unit cell is repeated or extended over large numbers of atoms, forming parallel sets of atom planes with various atomic densities and various inter-planar spacings.

Certain of these planes play very important rôles in the behavior of iron crystals. For example, dislocations which accomplish plastic deformation or slip of metals tend to glide on crystal planes of maximum atom density and greatest interplanar spacing. Also, certain sets of planes become the habit planes on which new phases precipitate and grow.

As will be shown later, the presence of carbon leads to the formation of the iron Carbide, Fe_3C , referred to as cementite. This has an orthorhombic crystal structure and is a metastable phase, the equilibrium phase being graphite. Nevertheless, cementite is the most common Carbide phase in many steels [12].

I.5 Crystal Imperfections and Slip

All real crystals contain imperfections which may be point, line, surface or volume defects, and which disturb locally the regular arrangement of the atoms. Their presence can significantly modify the properties of crystalline solids.

A very important characteristic of crystals is that they are deformable by a process termed slip: parts of a crystal are displaced or slip relative to other parts of the crystal along well defined crystal planes. Figure I.4 shows schematically how slip can cause permanent changes in the shape of a crystal. Although the results of the slip process make it appear that displacements have occurred across intact planes of atoms, the process is due to atomic scale crystal or line defects identified as dislocations. It will be seen that the behavior and effects of all these imperfections are intimately related [18,23]. Based on ideas of J.M.Burgers [24] that the boundary layers between adjacent coherent lattices domains even in the coldworked could be described in terms of systems of definite "dislocation", built up in such a way that necessary deviation of the atoms from their normal positions in both adjoining blocks are small as possible.

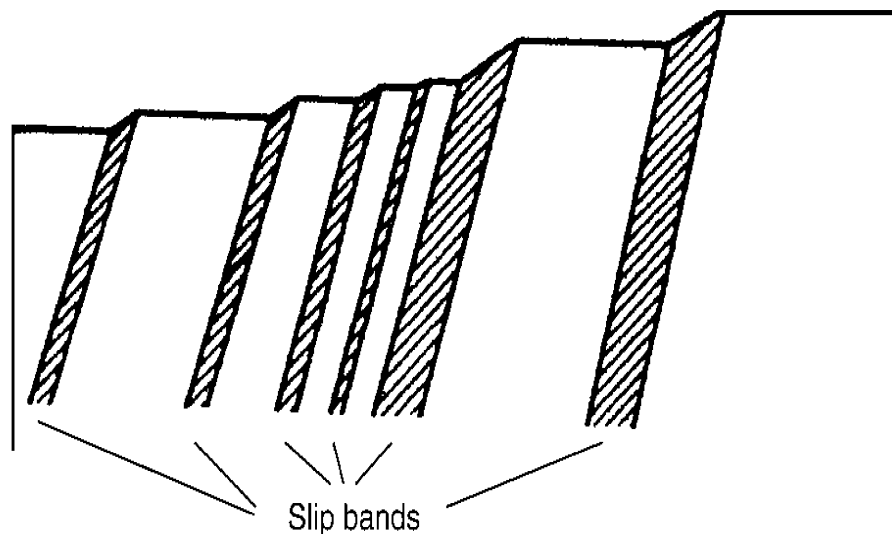


Figure I.4: Schematic of slip bands and associated slip steps on the surface of a single crystal[18].

Dislocations are an important class of defect in crystalline solids, as a result of growth processes or of thermal and mechanical treatments [23, 25]. Dislocations are line defects of the crystal lattice, which border the regions in the crystal interior in which slip has occurred. The measure for the quantity of dislocations in the crystal is given as the dislocation density the total length of all of the dislocation lines per unit volume [24, 26].

The two basic types of dislocations are the edge dislocation and the screw dislocation. Figure I.5 shows the slip that produces an edge dislocation for an element of crystal having a simple cubic lattice. Slip has occurred in the direction of the slip vector over area **ABCD**. The boundary between the right-hand slipped part of the crystal and the left-hand part which has not yet slipped is the line **AD**, the edge dislocation. Note that the parts of the crystal above the slip plane by an amount indicated by the shaded area in Figure I.5. All points in the crystal which were originally coincident across the slip plane have been displaced relative to each other by this same amount. The amount of displacement is equal to Burgers vector **b** of the dislocation. A defining characteristic of an edge dislocation is that its Burgers vector is always perpendicular to the dislocation line.

The second basic type of dislocation is the screw, or Burgers, dislocation. Figure I.6 shows a simple example of a screw dislocation. The upper part of the crystal to the right of **AD** has moved relative to the lower part in the direction of the slip vector. No slip has taken to the left of **AD**, therefore **AD** is a dislocation line. Thus, the dislocation line is parallel to its Burgers vector, or slip vector, and by definition this must be a screw dislocation. Consider the trace of a vector, and by definition this must be a screw dislocation. Consider the trace of circuit around the dislocation, on the front or the crystal. Start at **X** and completing a counterclockwise circuit, we arrive at **X'**, one atomic plane behind that containing **X**. In making this circuit we have traced the path of a right-handed screw [27].

The main characteristic of each dislocation is the Burgers vector, which describes magnitude and direction of slip movement associated with the dislocation. The classification of dislocations is based on the mutual orientation of the dislocation line and the Burgers vector of the dislocation. The direction of an edge dislocation is perpendicular to the Burgers vector. In contrast, the direction of a screw dislocation line is parallel to the Burgers vector.

Most of the dislocations are mixed dislocations. They are a combination of screw and edge segments, as well as a large mixed component; that is, the direction of the Burgers vector of such a dislocation changes along the length of the dislocation. Mixed dislocations usually form dislocation loops [26].

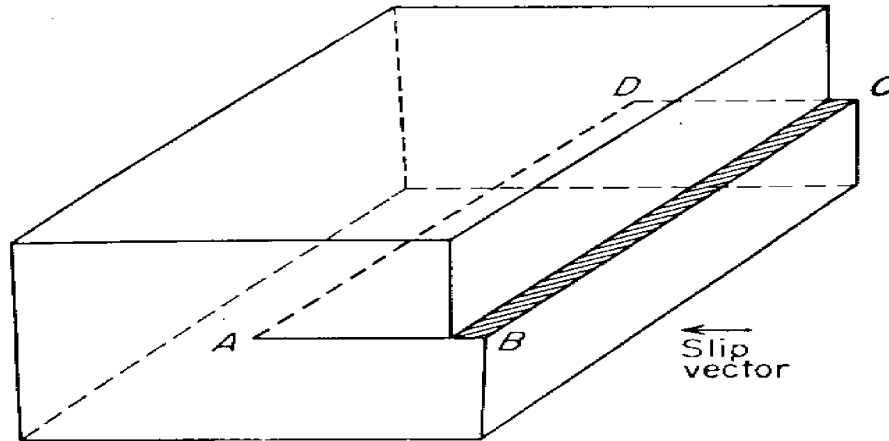


Figure I.5: Edge dislocation produce by slip in a simple cubic lattice. Dislocation lies along AD, perpendicular to slip direction. Slip has occurred over area ABCD [27].

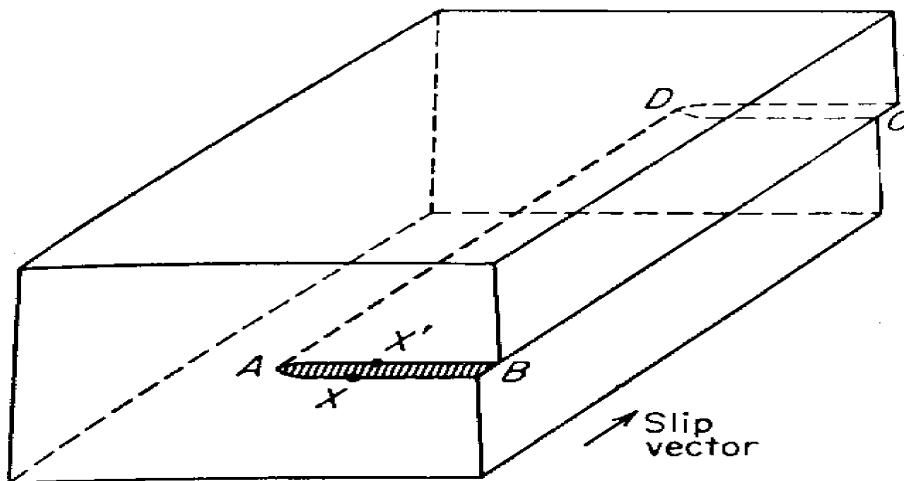


Figure I.6: Slip that produces a screw dislocation in a simple cubic lattice. Dislocation lies along AD, parallel to slip direction. Slip has occurred over area ABCD [27].

Dislocations are one of the most important microstructural features governing the mechanical properties of crystalline materials. They are the main carriers of plasticity; hence most of the related phenomena (e.g. yielding, strain hardening, strain-rate dependence, temperature dependence, etc.) depend on how the dislocation microstructure evolves and how dislocations interact with other material defects. The dislocation microstructure evolution is an immensely complicated phenomenon that is controlled by properties, microstructure and boundary conditions. Several mechanisms, such as dislocation dissociation, recombination, glide, cross-slip and climb, are active during material deformation and they all contribute to the final evolved microstructure. Cross-slip of screw dislocations is recognized as one of the main mechanisms controlling dislocation multiplication in crystals [27].

I.6 Purposes and effects of alloying additions

I.6.1 Common elements of steel [28]

Certain elements are common to all steels, and it may be of help to briefly outline the effects of carbon, manganese, phosphorus, and sulfur on the properties of steel.

✚ **Carbon** is the principal hardening element in steel, and as carbon increases, hardness increases, tensile strength increases, and ductility, notch toughness and weldability generally decrease with increasing carbon content.

✚ **Manganese** contributes to strength and hardness, but to a lesser degree than carbon. Increasing the manganese content generally decreases ductility and weldability, but to a lesser degree than carbon. Because of the more moderate effects of manganese, carbon steels, which attain part of their strength through the addition of manganese, exhibit greater ductility and improved toughness than steels of similar strength achieved through the use of carbon alone.

✚ **Phosphorus.** Phosphorus can result in noticeably higher yield strength and decreases in ductility, toughness, and weldability. In the steels under discussion here, it is generally kept below a limit of 0,04% on heat analysis.

✚ **Sulfur** decreases the ductility, toughness, and weldability, and is generally kept below a limit of 0,05% on heat analysis.

I.6.2 Austenite, ferrite and carbide forming elements

Steels, however, contain alloying elements and impurities that may form new phases or be incorporated into the crystal structures of austenite, ferrite, and cementite. Incorporation is usually by replacement of iron atoms if the alloy or impurity atoms are roughly the same size as iron atoms, but sometimes the atoms go into interstitial sites if they are significantly smaller than iron, as is nitrogen]. In terms of alloying behavior, elements used in tool steels are of two main types. The austenite formers are Mn, Ni, Cu, Co, N and C, whilst the ferrite formers include Si, Al, Cr, W, V, Mo, Nb, Ti, Ta, Zr and S. Effectively, the austenite formers decrease the ferrite/ferrite + austenite phase boundary temperature and the ferrite formers increase it. This phenomenon is related to the crystal structure of the alloying element as no f.c.c. alloying element stabilizes ferrite and similarly no b.c.c. element stabilizes austenite. Another classification of alloying elements, particularly relevant to tool steels, is either as carbide or non carbide forming.

The former are Mn, Cr, Mo, W, V, Nb, Ti, Ta and Zr, whilst the latter are Ni, Mn, Cu, Co, Si and Al. and some are strong carbide formers (titanium, niobium, molybdenum, and chromium, if present in sufficient quantity . Mn does not form separate carbide, but can dissolve in Fe_3C [18].

The eutectoid transformation temperature is raised by most alloying elements, the major exceptions being Mn and Ni (Figure I.7). Figure I.8 shows a related effect of alloying elements on the Fe-C phase diagram: the decrease in carbon content of austenite of eutectoid composition.

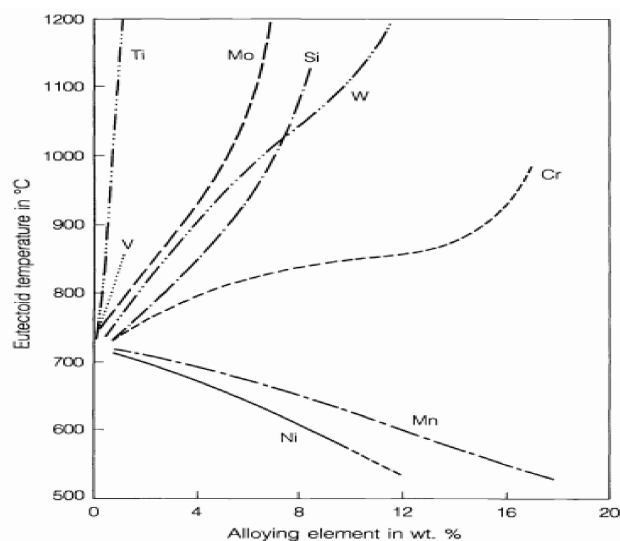


Figure I.7: Effects of alloying elements on the eutectoid temperature [29, 30].

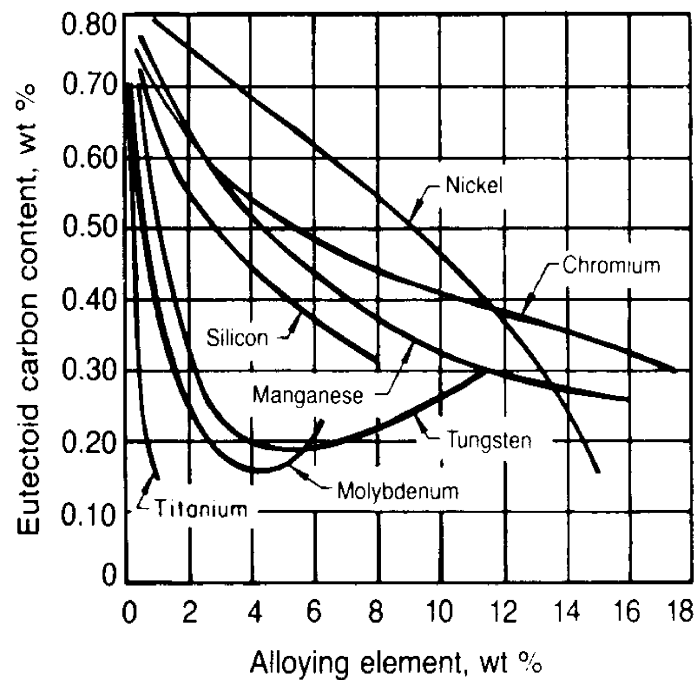


Figure I.8: Effect of substitutional alloying elements on the eutectoid carbon content in steel [18].

I.6.3 Ability of alloying elements to impart special characteristics

Alloying elements are required to fulfill the following functions in tool steels:

- Increase the strength in large sections, i.e. increase the hardenability.
- Reduce distortion resulting from heat treatment.
- Increase the abrasion resistance, at a constant hardness level.
- Give improved toughness at a constant hardness level.
- Increase the hardness and strength at elevated temperatures.

These effects, which lead to improved properties, are achieved by increasing the hardenability, by altering the nature and amount of the carbides present, and by elements dissolved in a iron. The relative strengthening effects of some substitutional solutes in solid solution in α -iron are indicated in Figure I.9. The carbide formers Cr, W, V and Mo are seen to be relatively ineffective [29].

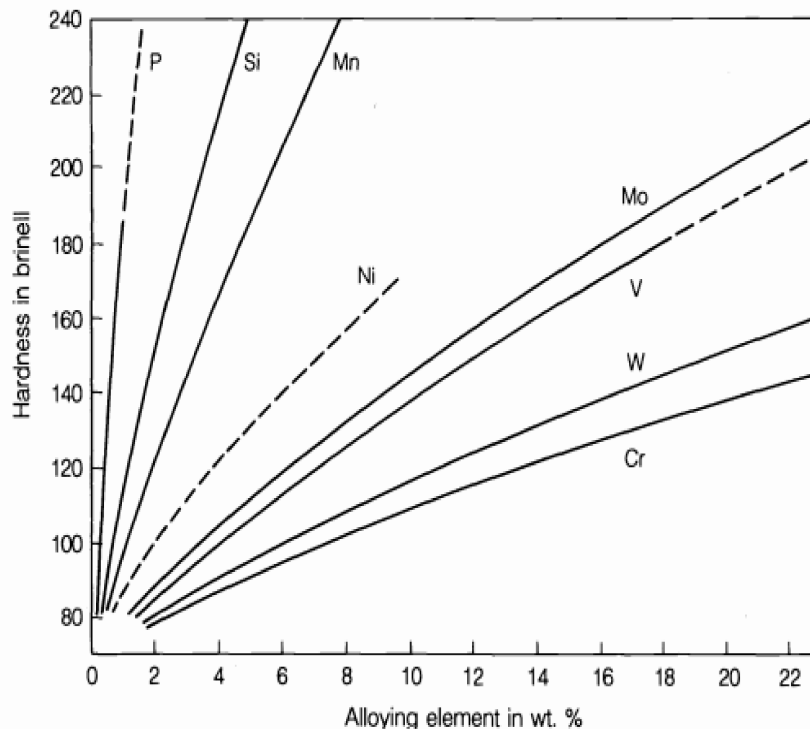


Figure I.9: Solid solution hardening effects of various alloying elements dissolved in α -iron. Alloying element in wt. %; changing the tempering characteristics, particularly by enhancing secondary hardening [29].

Alloying elements obviously affect the heat treatment response, if only by changing the phases present and their compositions. However, they make little contribution to the strength of the matrix ferrite or to the hardness of the martensite produced, the latter being predominantly controlled by its carbon content [29, 30].

I.7 Heat treatments of steel

Most ferrous materials are not subjected to a separate heat treatment. Their microstructure results directly from solidification and/or controlled hot working and cooling. Semi-finished steel products (strip, section, pipe, wire) undergo a combination of hot working and heat treatment during thermomechanical processing, which is also used e.g. for drop forged parts. The desired microstructure of cast iron is often obtained by tailoring the melt composition to the solidification cross section, i.e. the cooling rate in the mould. Another option is to remove the workpiece from the sand mould while it is still hot e.g. to promote growth of pearlite [31].

However, a separate heat treatment is frequently worthwhile because the microstructure produced during shaping (by casting, working, welding, sintering, etc.), may not have optimum manufacturing properties (machinability) or service properties (fatigue strength). The heat treatment process is therefore integrated into the manufacturing process so that it is independent of shaping and so as to allow the microstructure to be adjusted to the operational requirements of the finished component [31].

I.7.1 Annealing

Steel is annealed in order to reduce its hardness for the improvement of machinability and cold workability and also to obtain desirable mechanical, physical and other properties. As far as annealing is concerned, the following terms have been used, full annealing, soaking, isothermal annealing, spheroidizing, dehydrogenization annealing, stress relief annealing, bluing, box annealing, bright annealing, intermediate annealing, process annealing, soft annealing, finish annealing and so forth [32].

Is a process involving the heating of a metal above the critical temperature and subsequent slow cooling? The purpose of such heating may be to remove stresses; induce softness; alter ductility, toughness, electrical, magnetic, or other physical properties; refine crystalline structure; remove gases; or produce a definite microstructure [33].

Annealing is usually required to improve strength homogeneity of the welded joint, to decrease hardness peaks of the underbead zone and to increase the angle of bend before failure in bending tests. Strength properties of the weld metal and the HAZ must not fall below permitted limits.

Annealing is also required for the welded joint parts to have sufficient notch toughness values. The annealing tests at 550-700°C indicated that a 550°C annealing temperature is sufficient for the underbead zone and only temperatures over 650 °C should be used for the weld metal [34]. Some specific heat treatments which fall under the term annealing are :

I.7 .1.1 Full annealing

After austenitizing at temperatures of 20 °C to 30 °C above the A_{c3} temperature, hypoeutectoid steels are cooled slowly to obtain ferrite-pearlite structures.

For hypereutectoid steels, full annealing is not carried out in the austenite region above the A_{cm} temperature because grain boundary films of cementite are formed which can lead to brittleness. Therefore annealing is carried out between the A_1 and A_{cm} temperatures to produce a microstructure comprising spheroidized cementite in a pearlite matrix. The optimum cooling rate to obtain these structures can be estimated from CCT diagrams. When the cooling rate is unacceptably too rapid, hard structures such as martensite or bainite are formed [32].

I.7 .1.2 Process annealing

This is the heating of iron base alloys to a temperature below or close to the lower limit of the critical temperature range, followed by cooling as desired [33].

I.7 .1.3 Normalizing

Except for steels which have been controlled rolled, the microstructures of conventionally rolled or forged steels are coarse grained and inhomogeneous [31]. and normalizing is carried out in order to improve the strength and the toughness. After austenitizing a hypoeutectoid steel or hypereutectoid steel at temperatures of 30 °C to 50 °C above the A_{C3} , or the A_{cm} respectively, not by quenching, but removal from the furnace and cooled at slower rates, such as air cooling, or simply a slow quench, such as perhaps oil quenching. Air cooling is often called normalizing. Since the microstructure changes with cooling rate, accelerated cooling such as mist cooling [32, 35].

Objective: To obtain a uniform and fine grain size in ferritic/pearlitic microstructures. [19, 31, 32] Coarsely grained zones may occur in the heated but not worked regions of partially forged (e.g. headed) parts or in the heat-affected zone (HAZ) of welded joints.

Method: Heating to a temperature slightly above A_{C3} (above A_{C1} in hypereutectoid steels and cast iron) and cooling in static air induces $\alpha \rightarrow \gamma \rightarrow \alpha$ -transformation in which the number of grains is significantly increased due to nucleation and growth of new grains.

Applications: Unalloyed and low-alloy, i.e. readily transformable, that do not have a tendency to harden in air [31, 32].

I.7 .1.4 Stress-relief annealing

Stress relief annealing is carried out on components which have been heat treated, cold or hot formed or welded, in order to remove the induced stress and hence to avoid fatigue or brittle fracture [32]. In addition, the potential for stress corrosion cracking is reduced, and the metallurgical structure can be improved through stress relieving. The steel becomes softer and more ductile through the precipitation of iron carbide at temperatures associated with stress relieving [36].

Objective: To relieve internal stresses and to avoid distortion originating from the dissipation or redistribution of residual stresses during subsequent heat treatment or during machining. Asymmetrically distributed residual stresses caused by previous cold working, straightening or welding operations are particularly unfavourable because they may induce changes in shape when the material is heated.

Method: Lowering of the yield point by heating, but without significant alteration of the microstructure or strength. The residual elastic strain is transformed into plastic deformation, thus forestalling distortion. If the machining allowance is insufficient, the part must be restraightened and subjected to further stress-relief annealing. The treatment temperatures should be as high as possible but below the lower transformation Temperature range and then uniformly cooling it [31, 36]:

-Soft-annealed steels: just below A_{c1b} .

-Ferritic/pearlitic steels: 600 - 650C.

-Quenched and tempered (QT) steels: $\approx 30^\circ\text{C}$ below the tempering temperature.

-Non transforming steels: it is not possible to make any generalisations because the precipitates in these materials make them prone to embrittlement and corrosion. Temperatures of $\approx 580^\circ\text{C}$ are frequently used to avoid 475°C embrittlement, α -phase embrittlement and regions that promote intergranular corrosion [31]. In addition to temper embrittlement during slow cooling through the temperature range 400°C - 600°C , stress relief cracking may occur in a coarse grained weld heat affected zone. Secondary hardening elements such as Mo, Y, Nb and Ti increase stress relief cracking susceptibility, probably due to strengthening of the coarse grained matrix. It is interesting to note that extremely low C steels containing more than 1.5 wt. % chromium are less susceptible to cracking. This might be due to softening of the matrix and the balanced cohesive strengths of the grain boundary and the matrix [32].

I.7 .1.5 Spheroidizing

Spheroidizing treatments to produce a ferrite structure containing a dispersion of globular carbides are comprised of heating, isothermal holding below the A_{c1} temperature and cooling. A spheroidized structure should be used to improve the machinability and to allow severe plastic deformation. The machinability, such as is characterized by tool life in lathe cutting, is generally improved by decreasing the hardness to an optimum value [32].

Methods of spheroidizing generally used are:

- Prolonged heating at a temperature just below the lower critical temperature, usually followed by relatively slow cooling.
- In the case of small objects of high carbon steels, the spheroidizing result is achieved more rapidly by prolonged heating to temperatures alternately within and slightly below the critical temperature range [33].

I.7 .1.6 Tempering (also called drawing)

This is reheating hardened steel to some temperature below the lower critical temperature, followed by any desired rate of cooling.

I.7 .2 Hardening

Plain carbon steel is hardened by heating it above the critical temperature and cooling it rapidly by plunging it into water, iced brine, or other liquid.

When heating through the critical temperature range, iron undergoes a transformation and changes from a form with low carbon solubility to one with high carbon solubility. Upon cooling, a reverse transformation occurs. Since these changes are progressive and require time for completion, they may be stopped if the cooling period is shortened.

- a. If the cooling is very rapid, as in water quenching, the transformation takes place much below the critical temperature range. The carbon is fixed tied in a highly stressed, finely
- b. Divided state, and the steel becomes hard, brittle, and much stronger than steel that is slowly cooled.
- c. The presence of alloying elements alters the rate of transformation on cooling. Each alloy element shows individuality in its effect; therefore, alloy steels are manufactured and heat treated to meet specific performance requirements [33].

I.7 .3 Tempering

After steel is hardened, it is too brittle for ordinary purposes. Some of the badness should be removed and toughness induced. This process of reheating quench hardened steel to a temperature below the transformation range and then, cooling it at any rate desired is called tempering. The metal must be heated uniformly to a predetermined temperature, depending on the toughness desired [33]. A hard martensite produced after quenching is also extremely brittle, virtually all hardenedsteels undergo a subcritical heat treatment referred to as tempering. Tempering improves the toughness of the as-quenched martensite, but also softens the steel, thus causing a decrease in strength and an increase in ductility. This softening is largely due to the rapid coarsening of cementite (Fe_3C) with increasing tempering temperature and a reduction in dislocation density [19]. As the tempering temperature increases, toughness increases and hardness decreases. The tempering range is usually between 188 and 399°C, but sometimes is as high as 593°C [33].

I.7.4 Surface hardening

These treatments, numbering more than a dozen, impart a hard, wear resistant surface to parts, while maintaining softer, tough interior which resistant to breakage due to impacts. Hardness is obtained through quenching, which provides rapid cooling above a steel's transformation temperature. Parts in this condition can crack if dropped. Ductility is obtained via tempering. The hardened surface of the part is referred to as the case, and its softer interior is known as the core.

Gas carburizing is one of the most widely used surface hardening processes. Carbon is added to the surface of low carbon steel at temperature ranging from 850 to 950°C. At these temperatures austenite has high solubility for carbon. In quenching, austenite is replaced by martensite. The result is high-carbon, martensite case. Carburizing steel for case hardening usually have carbon content of approximately 0.2%. Carbon content of carburized case is usually controlled between 0.8 to 1%. Other methods of case hardening low-carbon steels include cyaniding, ferritic nitrocarburizing, and carbonitriding [37].

I.8 Fe-C phase diagram

Phase diagrams define the temperature-composition regions of phase stability in various alloy systems. Pressure also affects phase stability but this variable is generally held constant at one atmosphere. The diagrams assume equilibrium, i.e., that sufficient time at temperature has elapsed for the formation of all phases and complete partitioning of all components into the various phases has occurred in accordance with the principle of minimum free energy. Equilibrium is often not achieved. Nevertheless phase diagrams are useful guides for indicating the phases and microstructures which will be approached in alloys of a given composition in a given temperature range [12].

The phase diagram is basically a map which predicts which phases are stable for any alloy with a given carbon content at a given temperature, i.e. as represented by a point on the phase diagram. Each such point lies either in a single-phase region. The austenite region, or in one of the two-phase regions which exist between the single-phase regions. The single-phase solid solutions are readily apparent on figure I.10, with α -ferrite in the region GQPG and δ -ferrite in region AJKA.

The borders of these regions (e.g. the lines QPG and JKA) represent the limits of solid solubility of carbon. This diagram also illustrates the fact that the carbon solubility is much greater in austenite than in ferrite, the limits of the austenite phase being JIEHGJ with a maximum of 2.1% C at point E. There are other two phases shown on this phase

diagram. One of these is the liquid solution of carbon in iron, which occurs at high temperatures, across the top of the diagram. The lower boundary of this region shows how the freezing temperature (or more accurately the liquidus temperature, the lowest temperature at which the entire material is liquid) of iron-carbon alloys changes with carbon content. The other phase shown on the phase diagram, at the right hand end within the boundary ONMDO, is iron carbide or cementite, a compound with the formula Fe_3C , corresponding to 6.67% C. The crystal structure of cementite is orthorhombic, giving it a very high hardness, strength and brittleness in contrast to the soft ferrite and austenite phases [16].

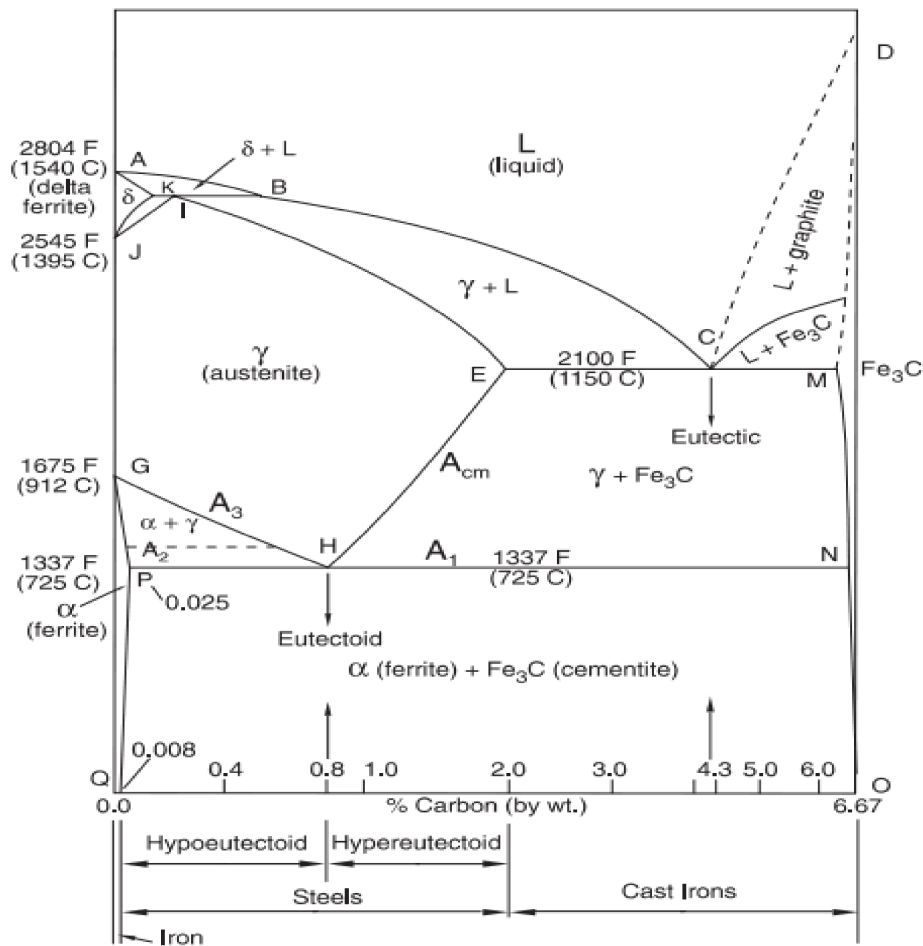


Figure I.10: Iron-iron carbide phase diagram [16].

I.9 Elements of microstructure in steels

I.9.1 Cementite Formation

The cementite phase present in most steels is in the form of the fine plates of pearlite for hypoeutectoid steels and in this form plus thicker plates and globules formed on austenite grain boundaries in hypereutectoid steels. These cementite shapes result because they are the forms that cementite assumes when austenite transforms to pearlite at the A_{r1} temperature and when it nucleates on austenite grain boundaries in hypereutectoid steels at the $A_{r_{cm}}$ temperature. It is possible however to heat treat steels and changes the shape of the cementite into a spherical form, sometimes called spheroidite. Cementite is very hard but very brittle, and by changing its form to isolated spheres in a matrix of, say, ferrite or tempered martensite, the mechanical properties of the steel comes closer to matching that of the matrix phase: soft and machinable with a ferrite matrix or strong and less brittle with a martensite matrix[35].

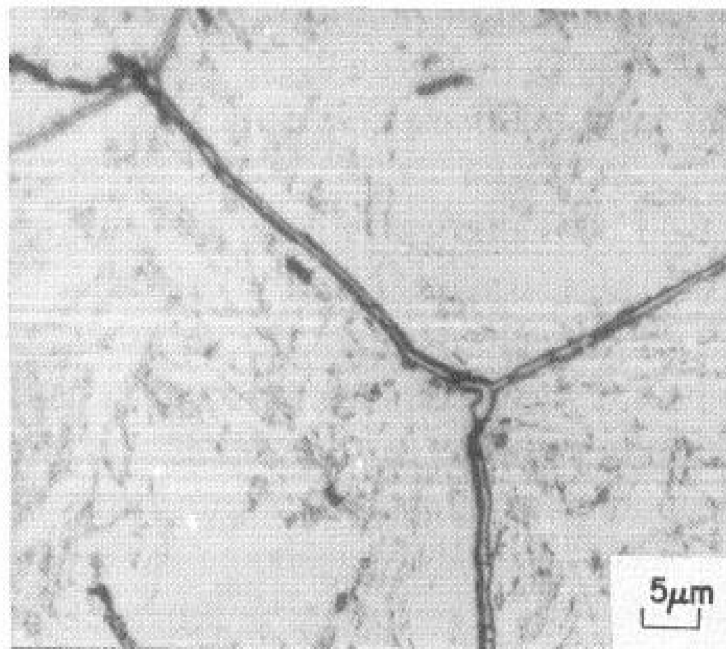


Figure I.11: Thin cementite allotriomorphs formed on austenite grain boundaries in a 1.0 wt. % C, 1.5 wt. % Cr steel. (Optical micrograph)[12].

Figure I.11 shows cementite which has formed on austenite grain boundaries, in a steel which contains nominally 1.00 wt. % carbon and 1.5 wt. % chromium. Crystals which nucleate and grow along grain boundaries, such as shown in Figure I.8, are referred to as grain boundary allotriomorphs. The growth of the cementite requires diffusion of carbon from the

austenite to the cementite and a rearrangement of the iron atoms from the f.c.c. structure to that of the iron atoms in the orthorhombic structure of cementite [12].

Cementite allotriomorph growth is rapid when only carbon diffusion and iron atom rearrangement is required. However, if substantial amounts of carbide forming elements such as chromium must partition from the austenite to the growing cementite crystals, the rate of growth becomes very sluggish. Also, since the carbon content of even high carbon steels is not sufficient to produce large volume fractions of cementite in austenite, the cementite networks are always relatively thin [12] as shown in Figure I.11.

I.9.2 Ferrite Formation

The heat treating of steel normally begins with heating into the austenite temperature range and allowing the preexisting microstructure to transform fully to austenite as required by the phase diagram. This austenitizing process may be carried out in any one of a number of atmospheres including air, inert gas, vacuum or molten salt. The hot austenitic steel is then cooled at some rate ranging from rapid to slow [38].

In low and medium carbon steels, ferrite allotriomorphs first form when austenite is cooled. However, in contrast to the limited volume fractions of cementite which form in high carbon steels, ferrite may compose up to 100% of the microstructure in pure iron or very low carbon steels. Figure I.12 shows a fully ferritic microstructure in ultra low carbon steel [39]. Polycrystalline ferrite microstructure as shown in Figure I.12. Upon slow cooling from the austenitizing temperature, there is no change until the A_3 temperature is reached, at which time the fcc austenite begins to transform to the bcc ferrite [16]. This can be described based on the effect of cooling rate on the ferrite formation. When the cooling rate is low, austenite can first transform to ferrite and, therefore, become enriched with carbon due to rejection of carbon from ferrite [40]. The ferrite, which forms above the eutectoid temperature, is called proeutectoid ferrite. Since the ferrite has a very low carbon content (maximum of about 0.025% C), the carbon content of the remaining (untransformed) austenite increases continuously as more and more of the austenite is replaced by ferrite. By the time the temperature is just above the A_1 temperature, enough ferrite has formed that the carbon content of the remaining austenite has reached 0.8% C, the eutectoid composition [16].

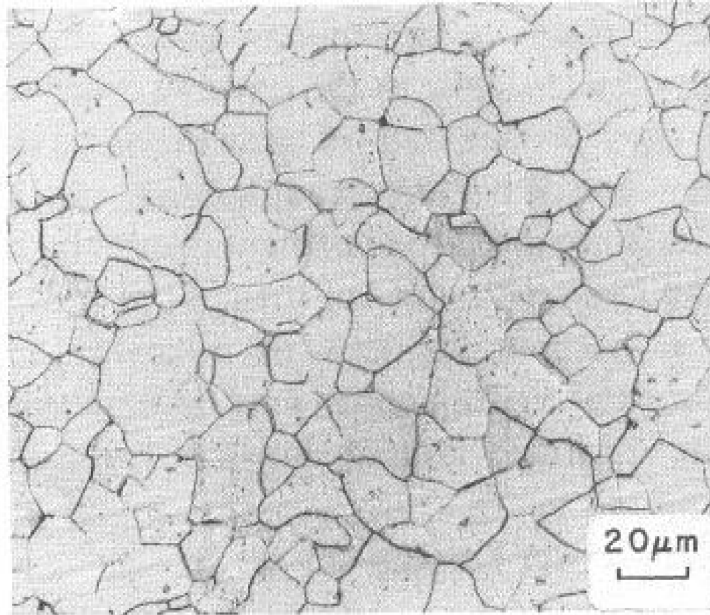


Figure I.12 : Polycrystalline, single-phase ferrite microstructure in a steel containing 0.004 wt.% C. Optical micrograph [39].

As a result, the austenite becomes increasingly enriched in carbon. When the carbon content of the austenite reaches about 0.8 wt.%, the eutectoid transformation of austenite to pearlite, which is a mixture of ferrite and cementite, often of lamellar form. Thus, most low and medium carbon steels have microstructures consisting of mixtures of ferrite, frequently referred to as proeutectoid ferrite because it forms prior to the eutectoid transformation, and pearlite. The ferrite content can range from 100% in ultra low carbon steels (Figure I.12) to zero in eutectoid steels which form microstructures consisting only of pearlite [12].

Under conditions of low undercooling or low supersaturation, substitutional alloying elements attempt to partition between the ferrite and austenite in order to maintain local equilibrium at the interface between the two phases [38]. The austenite growth rate can in those circumstances exceed that of ferrite when the liquid is sufficiently undercooled. Solidification with austenite as the primary phase becomes more feasible as the steel is alloyed with austenite stabilising elements, until the eventually becomes the thermodynamically stable phase [41]. Some micro-alloying elements, such as niobium, titanium or vanadium, have been found to inhibit austenite grain growth by interrupting the migration of the grain boundary.

Thus ferrite-stabilizing substitutional elements diffuse from the austenite to the ferrite, and austenite-stabilizing elements are rejected from the ferrite into the austenite. The growth kinetics of the ferrite then become dependent on the diffusion of substitutional elements and are slowed considerably relative to growth controlled by carbon diffusion. Another mechanism by which substitutional elements may retard the ferrite transformation [38, 42].

The retardation of ferrite growth by substitutional elements is a major reason for the addition of alloying elements such as Cr, Mo, and Ni to medium carbon steels. When ferrite growth rates are retarded sufficiently, rapid cooling or quenching of austenite causes its transformation to martensite [38].

The ferrite grain boundary allotriomorphs which grow uniformly into austenite grain interiors produce the equiaxed ferrite grain morphology shown in figure I.13.

Morphology of ferrite which may form in plain carbon and low alloy carbon steels consists of plate or lath shaped crystals of ferrite. These elongated crystals are referred to as Widmanstätten ferrite or sideplates and tend to form under conditions of cooling which produce substantial undercooling for austenite transformation to ferrite. For example, Widmanstätten ferrite is often formed in low carbon steel weld metal which is rapidly cooled by heat conduction into the surrounding base metal (Figure I.14) [12].

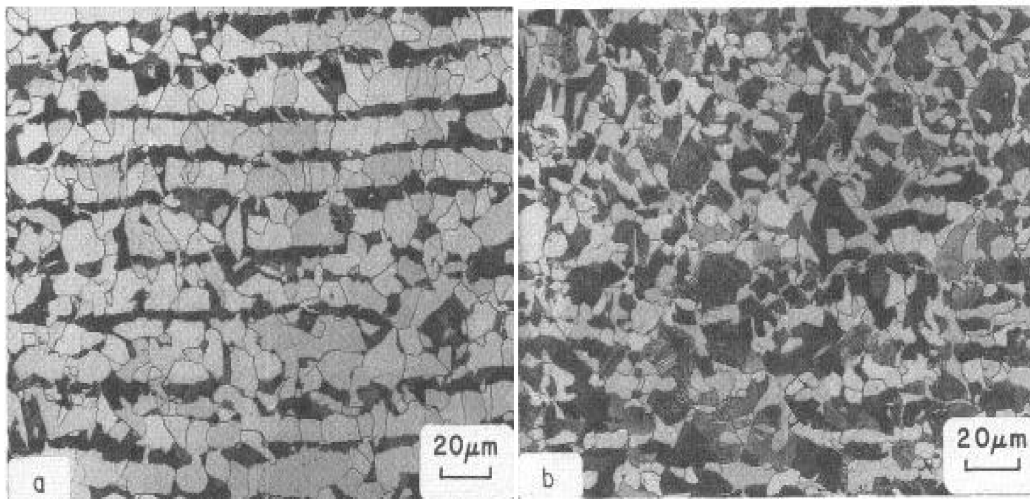


Figure I.13: Ferrite-pearlite microstructure in (a) 0.2 wt. %C steel, (b) 0.4 wt.%C steel. (Optical micrographs)[12].

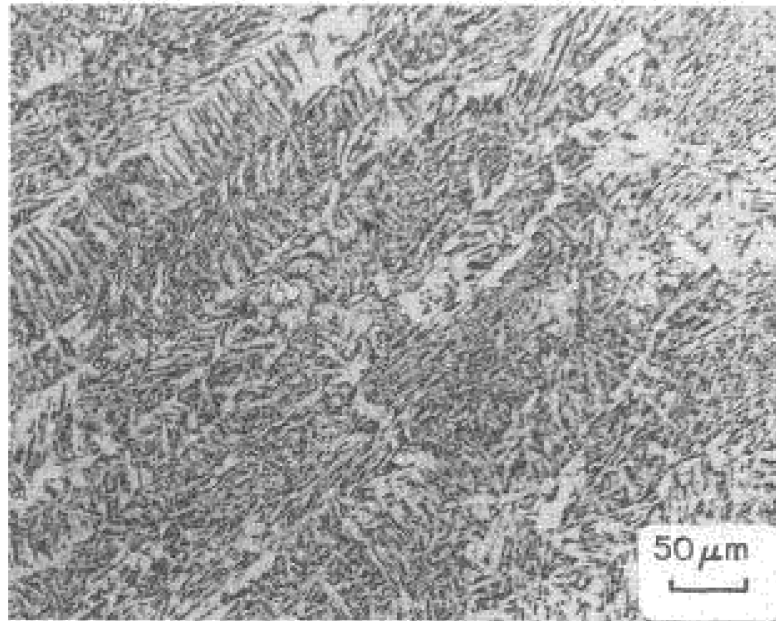


Figure I.14: *Widmanstätten ferrite in a low C steel weld metal. (Optical micrograph)[12].*

I.9.4 Pearlite Formation

Pearlite is the product of the decomposition of austenite by a eutectoid reaction and comprises a lamellar arrangement of ferrite and cementite. The pearlite reaction provides an excellent example of the historical development of physical metallurgy and the importance of the interaction of experimental observations and the development of quantitative models. In reviewing the pearlite reaction, it is appropriate to begin with a simplified description of the reaction in Fe-C alloys and then examine in detail the various complexities which arise from the detailed chemical and microstructural features [38]. SEM micrograph of microalloyed steel contains Pearlite inside the mixture of phases islands as shown in Figure II.15.

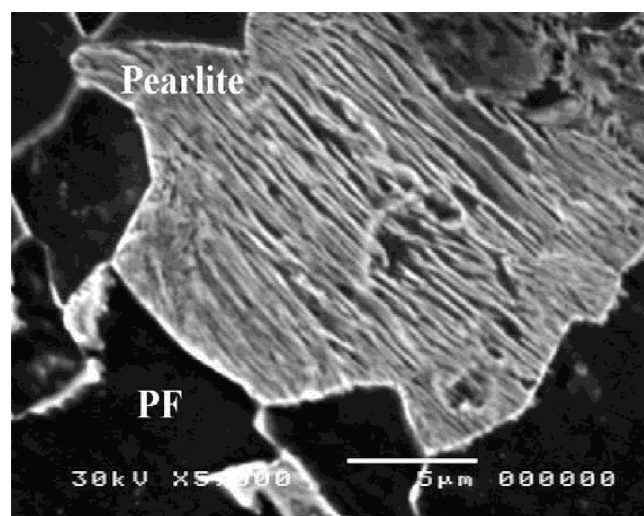
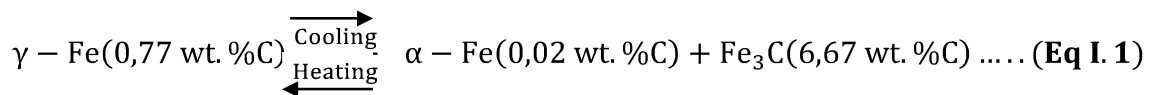


Figure I.15: *SEM micrograph microalloyed contains Pearlite inside the mixture of phases islands [43].*

In Fe-C alloys and steels the eutectoid reaction is written as follows:



At the equilibrium eutectoid temperature, the free energy of austenite is equal to the free energy of ferrite and cementite, and there is no thermodynamic driving force for the transformation. Therefore austenite of the critical composition must be under-cooled to initiate pearlite formation. The greater the undercooling, the greater the free energy decrease available to offset the interfacial energy increase associated the interfaces between the ferrite and cementite lamellae within a colony of pearlite. As a result the interlamellar spacing between ferrite and cementite in pearlite decreases with decreasing transformation temperature. The light microscope the lamellae would not be resolved and the pearlite colonies would appear uniformly dark as is the case in Figure I.16 [38].

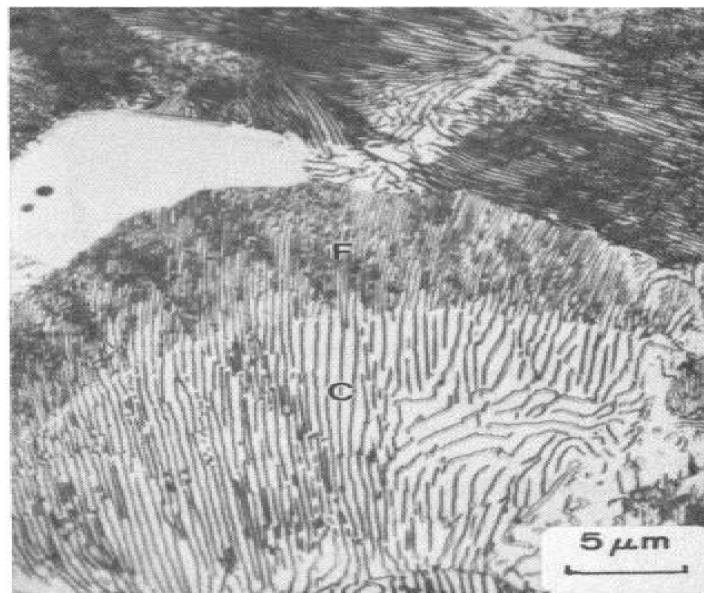


Figure I.16: Transition from coarse (C) to fine (F) pearlite due to a decrease in the transformation temperature. (Optical micrograph) [38].

The nucleation of a pearlite colony requires the nucleation of two phases in order to establish the lamellar morphology of the pearlite. In hypoeutectoid and hypereutectoid steels, steels of lower and higher carbon content than the eutectoid composition respectively, the pearlite colonies are nucleated by the proeutectoid phases. For example, in hypoeutectoid steels the ferrite of the pearlite grows directly from the proeutectoid ferrite and the rejection of carbon from the ferrite causes multiple cementite lamellae to nucleate.

In eutectoid steel, nucleation of pearlite colonies may occur by multiple nucleation of parallel ferrite and cementite lamellae [12].

I.9.5 Martensite Transformation

Carbon partitioning between ferrite and austenite during high temperature diffusional transformations is relatively well understood. These reactions are frequently referred to as reconstructive transformations, because of the short-range diffusional movements of iron (and substitutional) atoms that accomplish a change in crystal structure between bcc and fcc [44].

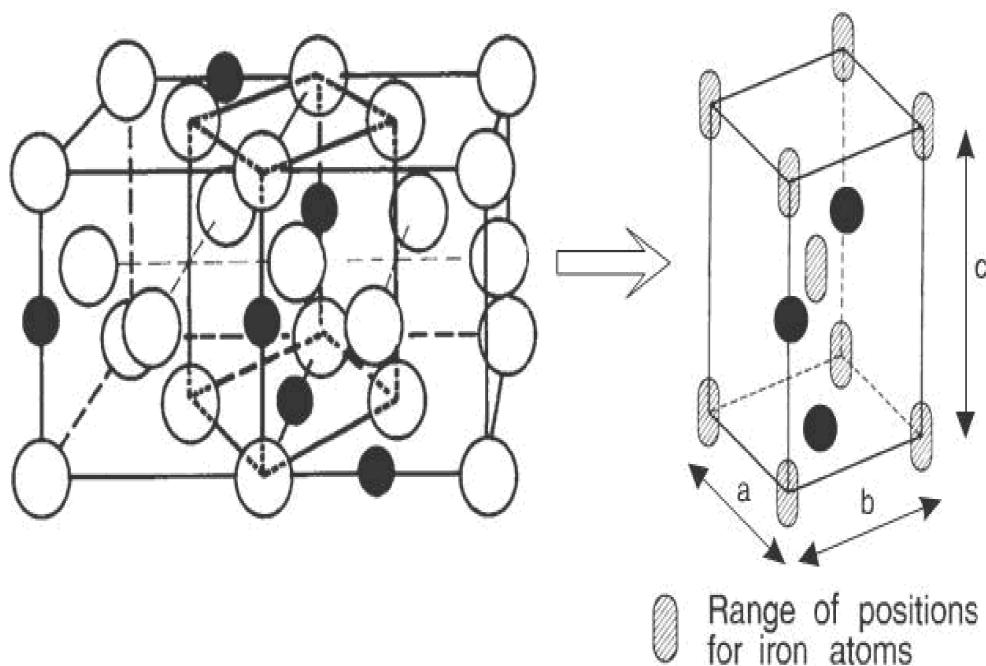


Figure 1.17: Austenite (fcc) to martensite (bct) transformation [16].

If austenite can be cooled to a sufficiently low temperature, for example by cooling very rapidly, its diffusion-controlled transformation to ferrite, pearlite or even bainite will not be possible [16]. The remaining austenite has a higher chance of transforming to martensite as the temperature is lowered. However, at higher cooling rates, from austenite state, carbon free bainitic ferrite is formed, which results in the remaining austenite less enriched with carbon and less prone to transform to martensite compared to the case of initial ferrite formation [40,45]. Instead, the austenite becomes so unstable that it is able to change its crystal structure by a diffusionless shearing transformation which moves blocks of atoms by small distances simultaneously. The transformation product is then martensite, a metastable phase which, like bainite, does not appear on the phase diagram since it does not exist under equilibrium conditions.

The martensite structure is basically the result of the steel's attempt to transform from austenite (fcc) to ferrite (bcc), it is rather a body centered tetragonal (bct) structure as shown in Figure 1.17[16]. Martensite is a phase which forms by a diffusionless, displacive transformation mechanism. Instead of atom by atom transfer across an interface as is typical of diffusion controlled transformations, large numbers of atoms shear cooperatively to form the structure of martensite [12].

The transformation begins at a temperature called the martensite-start temperature or MS. The fraction of martensite increases with the undercooling below MS.

The martensite in steels is supersaturated with carbon. Carbon occupies octahedral interstices in the b.c.c. lattice; these are characterised by three principal axes a $\langle 001 \rangle$, a $\langle 110 \rangle$ and a $\langle 110 \rangle$. There are three sub-lattices of octahedral holes, along directions parallel to the unit cell edges (Figure I.18).

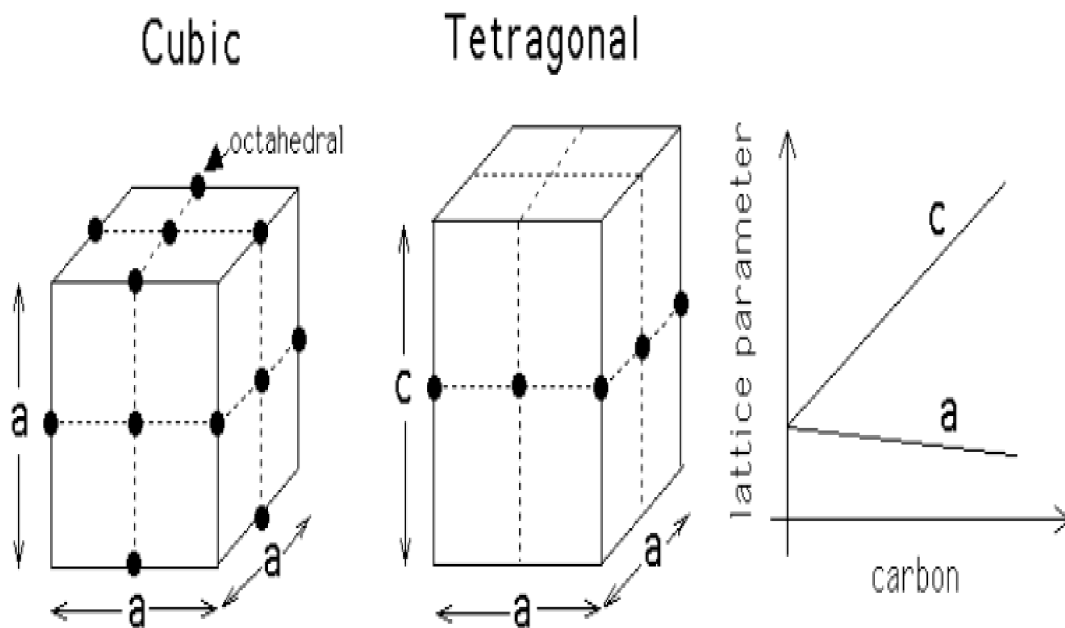


Figure I.18: Tetragonal martensite in some steels [46].

Each carbon atom causes a tetragonal distortion since the principal axis of the octahedral sites is not equivalent. There is an expansion along a $\langle 110 \rangle$ and small contractions along the

other two axes. As a consequence, it is favourable for all the carbon atoms to lie on a single sub-lattice of octahedral interstices, giving rise to a body-centered tetragonal structure for the martensite (Figure I.18) [46].

- Tempering of Martensite

Martensite containing carbon is very strong; this also makes it very brittle. To achieve a compromise between strength and toughness, the martensite is tempered, *i.e.* heat treated at temperatures below that at which austenite can form. The heat treatment causes :

- 200-400 °C. The precipitation of excess carbon at first as transition carbide Fe_{24}C , which then converts to cementite (Fe_3C). This is accompanied by a significant loss of strength but an improvement in toughness.
- 400-500 °C. Recovery with a reduction in dislocation density. Cementite begins to coarsen with further loss in strength.
- 500 °C. Recrystallisation of plates into equiaxed grains of ferrite [46].

I.9.6 Bainite Formation

Is the generic term for fine aggregates of ferrite platelets (or laths) and associated cementite particles that is distinguishable from pearlite [13, 47].

Bainite is classically a product of eutectoid decomposition of austenite in steels [47]. Transformation occurs isothermally or on continuous cooling over a temperature range that is typically below that of the austenite to pearlite reaction and above the M_s temperature for martensite formation, although there is potential overlap at both extremes of the bainite range [13,47]. Among all austenite decomposition reactions, bainite transformation remains the least clearly understood. Bainite plays a key role among solid-solid phase transformations because it exhibits features of both diffusive and displacive transformation [48].

Similarly to pearlite, the classical forms of bainite consist of ferrite and cementite. However the mechanisms of transformation and the morphologies of the resultant ferrite and Carbide structures of pearlite and bainite differ significantly. Pearlite is formed by the diffusion of carbon atoms and the short range diffusional transfer of iron atoms across the austenite-pearlite interfaces which define the pearlite, where even short-range iron atom transfer is suppressed. As a result bainitic ferrite is nucleated by a cooperative iron atom shear mechanism, and the morphology of the ferrite takes on the lath or plate appearance of martensite rather than the spherical or equiaxed morphology of pearlite and proeutectoid ferrite. Carbon, however, is still able to diffuse, and therefore various temperature dependent arrays of cementite particles are associated with bainite. The cementite particles are not

continuous as they are in pearlite, leading to a metallographic definition of bainite as a structure consisting of a non lamellar array of ferrite and cementite [12].

The details of the microstructure vary with composition and temperature of transformation, thus it is common to identify two varieties, namely upper bainite and lower bainite. These form over upper and lower temperature ranges and can be distinguished by less than 0.02 wt% carbon [49]. Temperature of the transition between upper and lower bainite is a function of carbon content. Upper bainite consists of ferrite laths with relatively coarse cementite particles between the laths. The austenite not transformed to bainite at 460 °C transformed to martensite on cooling to room temperature. The bainite forms in groups of laths with a common orientation within the parent austenite grains. Lower bainite forms as ferrite plates containing very fine cementite particles, typically oriented at 60° to the long axis of the plates. The transition from the coarse interlath carbides of upper bainite to the fine intraplate carbides in lower bainite is consistent with decreasing carbon diffusivity with decreasing temperature [38].

In lower carbon steels and certain alloy steels, the formation of the carbide constituent may be suppressed and, since it commonly has a form similar to that of the ferritic constituent of bainite, the ferrite that forms in this temperature range is often identified as bainitic ferrite [31]. Generally the coalesced bainite was found along with upper bainite in dendrite core regions while a lath-like microstructure of martensite was found at interdendritic regions. It was found that cementite precipitates formed within the bainitic ferrite grains [41]. About coalesced bainite the mechanism of how it forms is presented in Figure I.19 along with those of upper and lower bainite. The as-deposited last bead microstructure of weld metals two low carbon steel is shown in figure I.20.

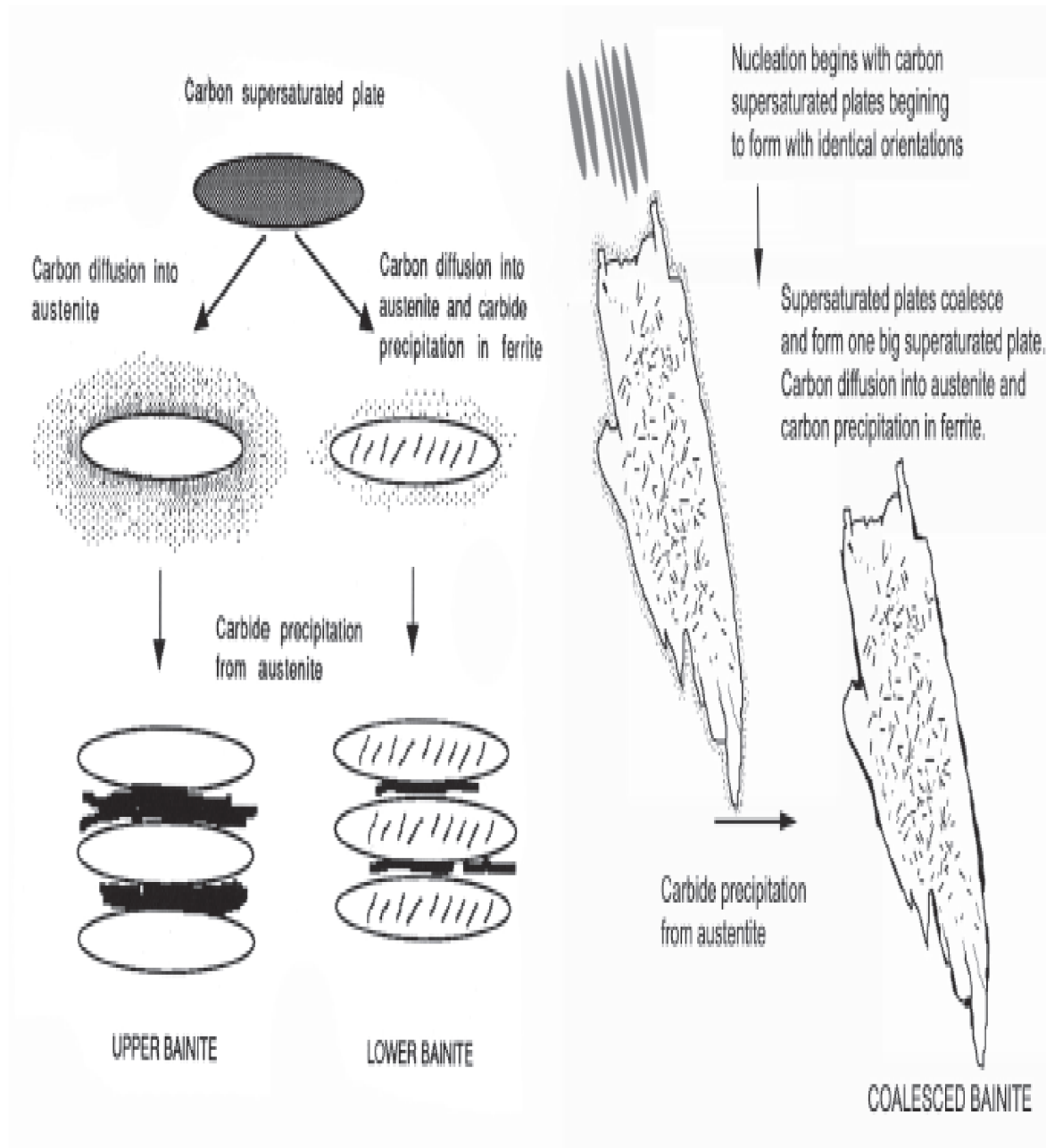


Figure I.19: Schematic representation of the formation of upper and lower bainite along with coalesced bainite [41].

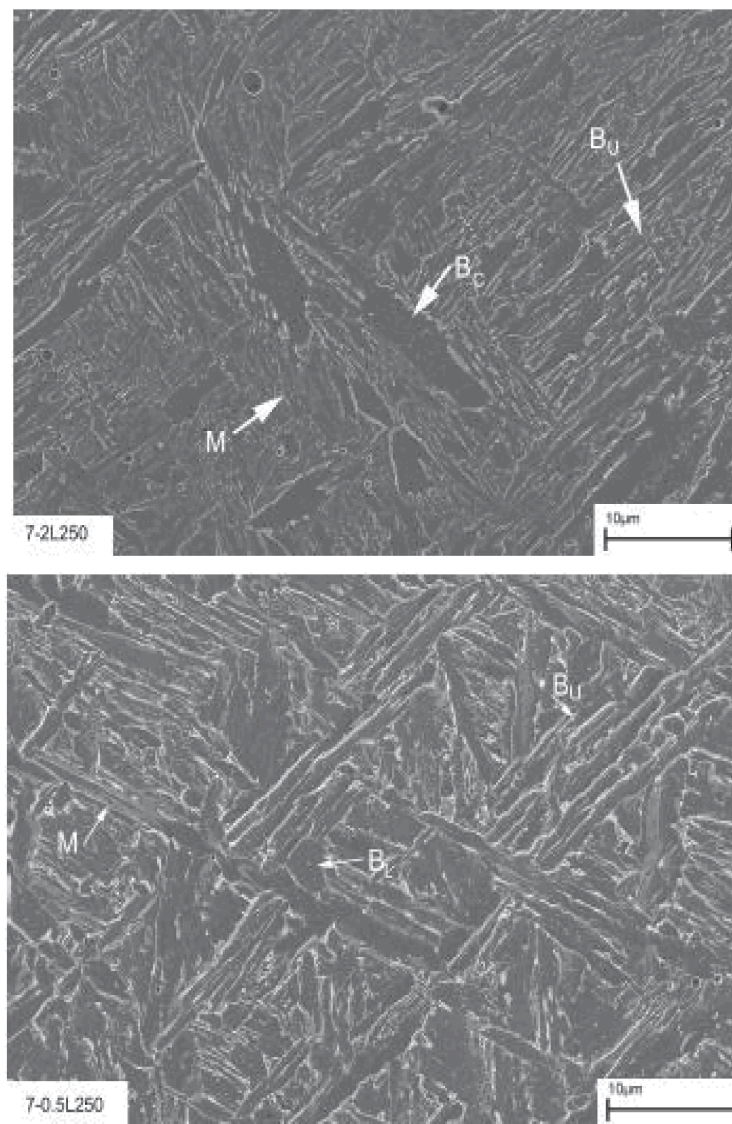


Figure I.20: Microstructure in the as-deposited last bead of weld metals of two low carbon steels imaged using FEGSEM. M is for martensite, BU is upper bainite, BL is lower bainite and BC is coalesced bainite [41].

I.10 Transformation Diagrams

Two types of diagrams are used to display the hardenability characteristics of steels graphically. These are the isothermal transformation (IT) or time-temperature transformation (TTT) diagram, and the continuous cooling transformation (CCT) diagram. The detailed appearance of these diagrams depends on the steel's composition (carbon and alloy content) and its austenite grain size (i.e. austenitization conditions)[16,35] and thus every steel will have its own diagram for a given set of austenitization conditions.

Both types of diagram are designed to predict in detail the transformation characteristics of a particular steel after austenitization, by showing which transformation product microstructures (and in some cases the as-transformed hardnesses) are obtained by various cooling conditions for that steel. The diagrams can also be used in the reverse sense for predicting the cooling conditions necessary to obtain a given microstructure and hardness [16].

Figure I.21 shows a TTT diagram for plain carbon eutectoid steel. They are determined by evaluating the microstructures of austenite which has been quenched from the austenitizing temperature into baths which are at fixed temperatures (hence the name isothermal) below the eutectoid temperature, and held for various amounts of time to allow the austenite to transform. They therefore give a graphical illustration of the time necessary for austenite to transform to its various transformation products at different temperatures. For example the times necessary for the beginning and the end of the formation of pearlite and bainite can thus be determined as can the M_s and M_f temperatures [16]. Curves for the beginning and end of the pearlite and bainite transformations are shown and the horizontal broken line marks the transition between pearlite and bainite formation. There is a temperature above which bainite does not form, called the B_s (bainite start) temperature, and the B_s temperature is lowered by all the common alloying elements in steels. The B_s temperature has been related quantitatively to steel composition by empirical equations. For austenite which does not transform to a microstructure dependent on diffusion, the M_s and estimated temperatures for various amounts of martensite formation are also indicated. In \bar{i} steel, pearlite will not form unless austenite is cooled to below the eutectoid temperature. The pearlite transformation involves diffusion and hence will be slow at low temperatures. It will also be slow close to the eutectoid, this can be represented on the $T - t$ plot [16, 38, 46].

In their simplest form, these transformation curves have a well-defined 'C' shape. Where the nose of the curve represents the temperature at which the reaction proceeds most rapidly, slowing down both at higher and at lower temperatures [50]. The position of the curves on IT diagrams depends on the austenite grain size [35]. TTT diagram reflects a balance between the increasing driving force and decreasing diffusivity with decreasing transformation temperature. A eutectoid steel transformed close to the eutectoid temperature, the degree of undercooling, ΔT , is low so the driving force for the transformation is small.

However, as ΔT increases the driving force also increases, and the reaction occurs more quickly, until the maximum rate at the nose of the curve [38, 46].

Below this temperature, the driving force for the reaction continues to increase, but the reaction is now impeded by the slow diffusivity of the rate-controlling element, which in plain carbon steels may be carbon or iron [38, 46].

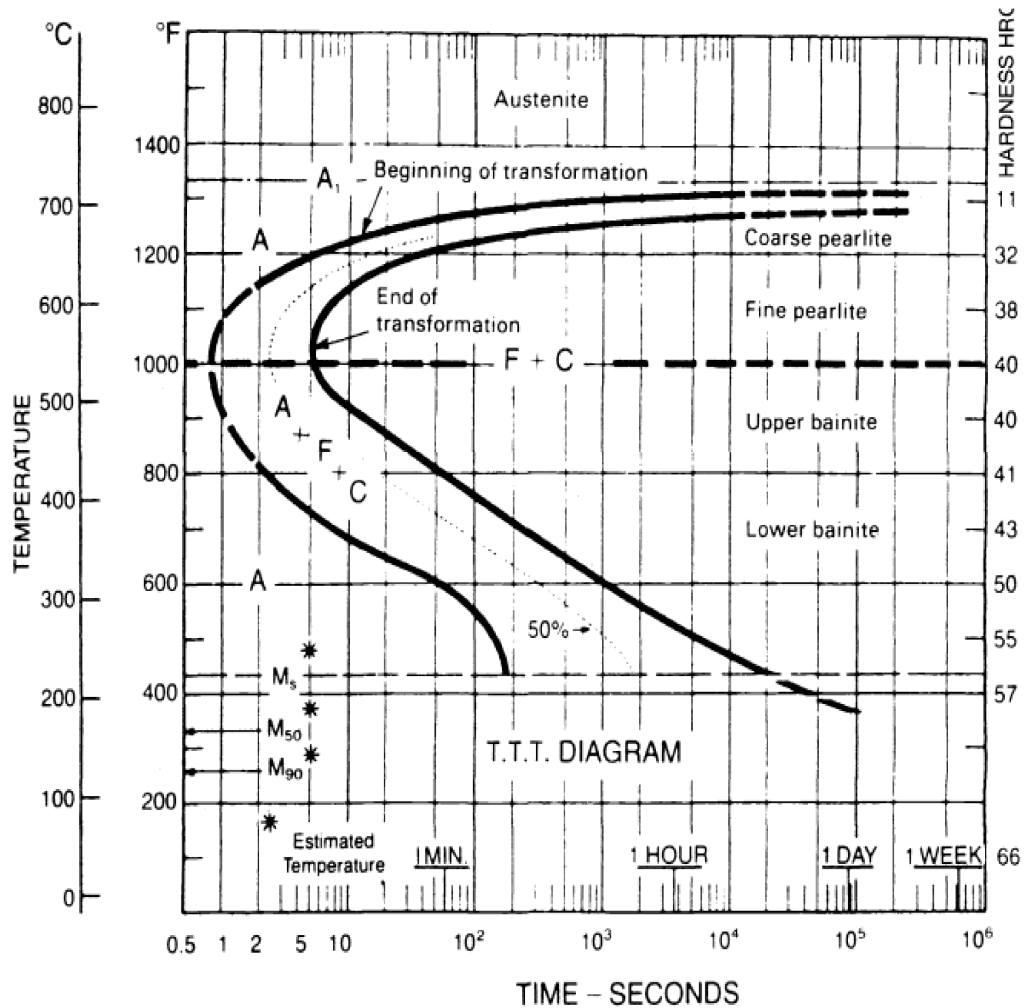


Figure I.21 : Isothermal transformation diagram for eutectoid steel [38].

A real TTT diagram is somewhat more complicated (Figure I.22). Consider for example a hypoeutectoid steel, the first phase to form would be ferrite with transformation becoming possible just below the A_{c3} temperature. Widmanstätten ferrite then begins to grow as a displacive transformation in which the interstitial atoms diffuse.

Pearlite forms below the eutectoid temperature. Pearlite is a mixture of cementite and ferrite, each colony being an interpenetrating bicrystal. At even larger undercoolings we get bainite, which is a displacive transformation like martensite, but unlike martensite does not remain

super-saturated with carbon. The excess carbon rapidly precipitates as fine carbides between the plates of bainite (upper bainite) or within them (lower bainite) [46].

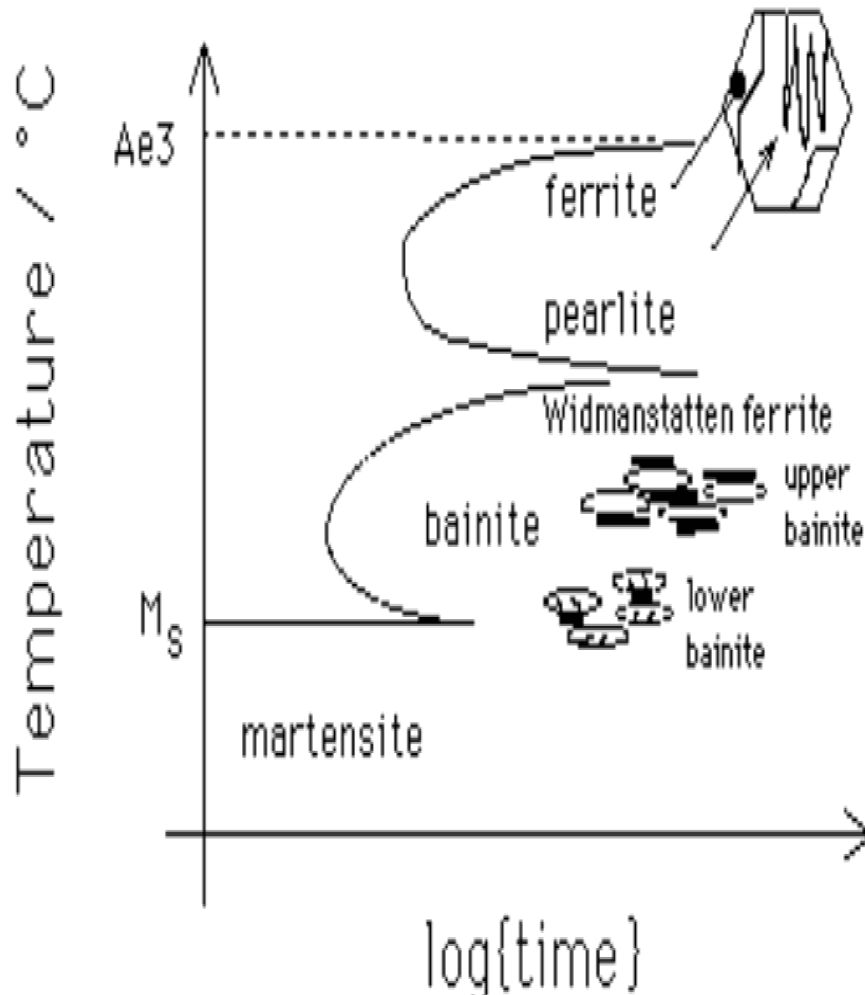


Figure I.22: TTT diagram for hypoeutectoid steel [46].

It is not possible with large components to obtain microstructures by isothermal transformation. However, if the rate of transformation of austenite can be reduced then larger components can be uniformly transformed. Steel in which the austenite transforms relatively slowly is said to possess greater hardenability.

The hardenability of steel depends on the stability of the austenite, Elements like C, Mn, Ni, Mo, and Cr improve the stability and hence retard all transformations, reactive alloying elements such as Cr and Mo will form carbides. Consequently these elements will prefer to go into the cementite (carbide) part of pearlite or bainite when they form. Hence, when pearlite,

for example, forms from austenite these elements have the same problem that C has: They want to rearrange from a uniform distribution in the austenite to a distribution in pearlite where they have higher composition in the cementite plates than in the ferrite plates. Steels containing these elements can be hardened to a greater depth. By contrast, Al and Co can accelerate the transformation of austenite and hence reduce hardenability [35, 46]. The effect of alloying elements is two-fold:

1. A thermodynamic effect as the element alters the stability of the austenite.
2. If the element concerned partitions during transformation then it may further retard the reaction because of the need for diffusion. Thus, transformations involving diffusion are retarded to a much larger extent than for example bainite or martensite [46].

An example of a CCT diagram is shown in figure I.23 for a hypoeutectoid alloy steel. Various cooling curves and the hardness values of the microstructures produced by cooling at the various rates are indicated. The hardest microstructures are those which consist of martensite and the lowest strength microstructures consist of equiaxed ferrite and pearlite. The relatively high alloy content of the steel significantly delays the start of the ferrite and pearlite transformations and produces a prominent range of cooling conditions which produce bainite. Continuous cooling may produce microstructures made up of several different constituents. For example, the cooling rate in Figure I.23 which produces a microstructure with equiaxed ferrite, pearlite, and bainite regions, and would produce microstructures consisting of all three of these structures.

The type of diagram shown in Figure I.23 is typical of hardenable medium carbon steels which can be readily transformed to martensite at moderate rates of cooling such as those produced by oil quenching. Moderate rates of cooling, in contrast to high rates typical of water or brine quenching, reduce distortion, residual stresses, and the possibility of quench cracking in hardened steels [12].

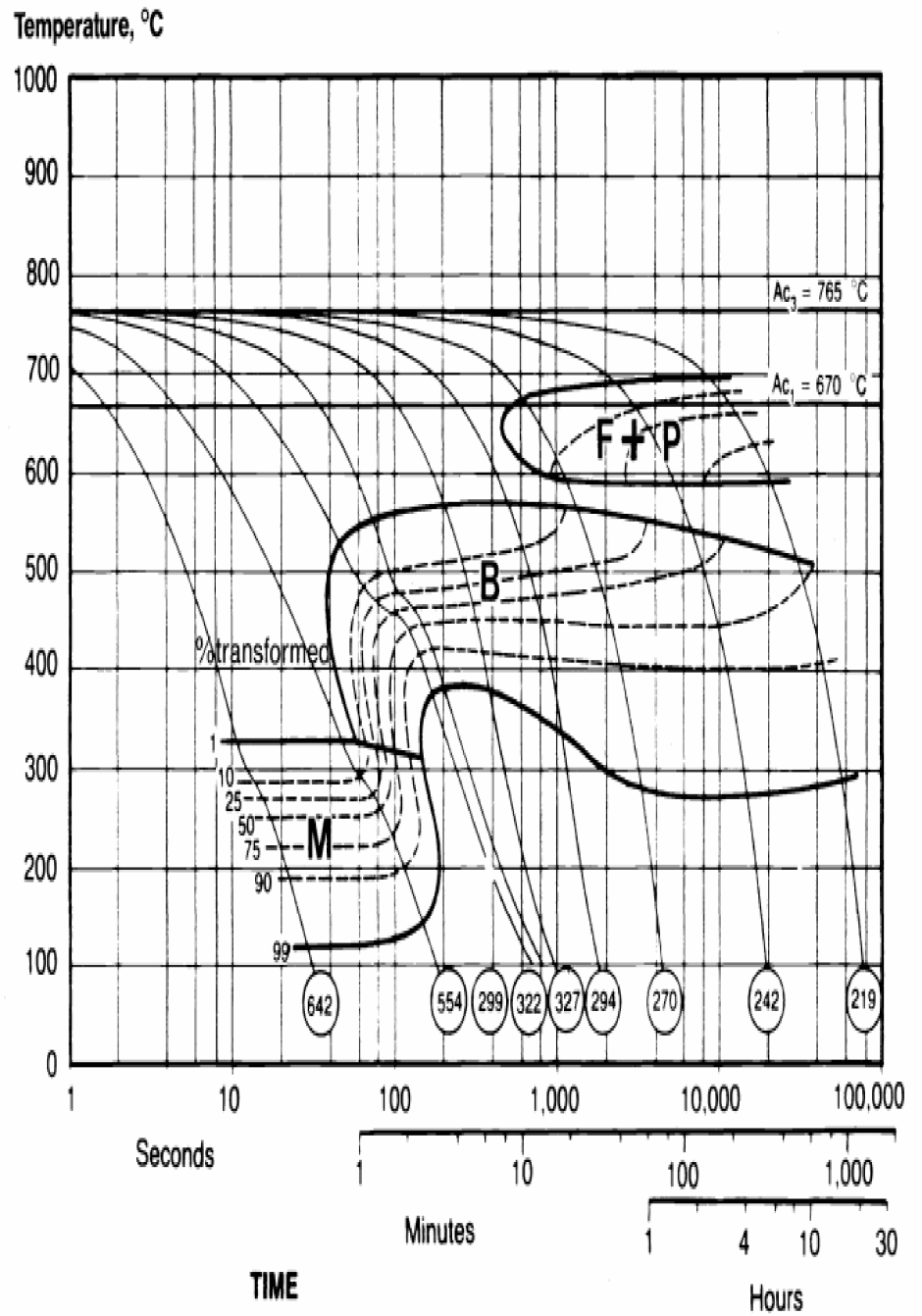


Figure I.23: Continuous cooling diagram for hypoeutectoid steel, the microstructures produced by the various cooling rates are circled, and F, P, B, and M designate ferrite, pearlite, bainite, and martensite, respectively [12].

CHAPTER II

WELDING Of STEELS

II.1 Introduction

Welding procedures have in the past been developed empirically, with some assessment of mechanical properties, and by drawing on accumulated experience. This method has been very successful, as evident in the popularity of the process in virtually all structural engineering applications [41]. But now welding becomes one of the most common processes used in manufacturing and engineering industries. Many materials are joined by welding, non-metals and metals, to create a wide range of structures from domestic consumer goods to highly complex heavy industrial installations. Perhaps the most common perception of the welding process relates to joining of metals, and the most common of all the metals used is steel in its many forms. These range from basic low-carbon ferritic structural steels, increasing in complexity with the addition of alloying elements to produce grades with applications in load bearing and pressure part manufacture [51].

II.2 Welding Definition

Welding is the most important method of joining components made of metallic materials. The technological core of most welding processes is the melting of the surfaces to be joined, either with or without filler metal (surfacing welds included), followed by subsequent cooling. Melting is achieved by local heat input, keeping heat diffusion into the component and heat dissipation into the surroundings as low as possible [27]. The metallurgy of the welded joint can be categorized into two major regions, the fusion zone and the heat-affected zone (HAZ). The fusion zone represents both the deposited metal and the parts of the steel component melted during the process, and is a solidification microstructure. The HAZ, on the other hand, represents those regions in the close proximity of the weld, where the heat input during welding changes the microstructure without melting the steel. This chapter describes the development of microstructure in both zones, beginning with the fused regions. Virtually every aspect of phase transformation in steels is relevant to the subject of welding. There is an opportunity for a whole series of transformations to occur successively as the weld cools from the liquid state [50].

The term arc welding applies to a large and varied group of processes that use an electric arc as the source of heat to melt and join metals. In arc welding processes, the joining of metals, or weld, is produced by the extreme heat of an electric arc drawn between an electrode and the workpiece, or between two electrodes. The formation of a joint between metals being arc welded may or may not require the use of pressure or filler metal.

The arc is struck between the workpiece and an electrode that is mechanically or manually moved along the joint [33].

II.3 Welding of piping and pipelines

Welding of piping and pipelines takes place first in the pipe mill, where skelp (sheets of steel) are rounded and seam welded, longitudinally or spirally. This pipe mill weld is a seam weld. Second, pipes and components (fittings, valves, etc.) are welded together in the shop or in the field. The shop or field weld is generally a girth weld (weld around the circumference) or a fillet weld (for example at socket welded joints, or when welding an external attachment to the pipe). A multi-pass girth weld consists of a root pass (from the inside or outside diameter), a hot pass (root cover), and before the root pass completely cools, one or several fill passes, and a wider cap pass. A common welding technique for shop or field welding metallic piping systems is arc welding. In arc welding, the pipe metal, and the filler metal, if used, are melted by the source of heat provided by a variety of welding methods like an electric arc and then solidify to form the weld joint [17,51]. Melting is achieved by local heat input, keeping heat diffusion into the component and heat dissipation into the surroundings as low as possible. The arc is formed by the flow of current between the parent metal (work-piece) and an electrode, which can be consumable (melts and becomes part of the joint) or non consumable (having a higher melting temperature than the arc, the electrode typically tungsten or carbon does not melt) [17, 27].

II.4 Welding Processes [52].

Table II.1 lists the American Welding Society (AWS) initialisms for some arc welding processes. Electric arcs, using a combination of radiative and resistive heating, are the most commonly used heat sources in commercial welding processes. The most typical example is the shielded metal arc welding (SMAW) process.

The efficacy of a welding arc in putting its energy into the workpieces can be measured. This arc efficiency is calculated as the percent energy transferred to the workpieces compared with the total energy supplied by the power source. Arc efficiency varies considerably among the arc welding processes.

Table II.1: AWS designation for Arc Welding Processes [52].		
AWS Designation	Process Name	Other designation
Arc Welding Processes		
EGW	Electrogas welding	
FCAW	Flux cored arc welding	
GTAW	Gas tungsten Arc welding	TIG
GMAW	Gas metal arc welding	MIG, MAG
GMAW-S	Gmaw -short -circuit	Dip Transfer, Short Arc
GMAW-P	Gmaw-Pulsed	
PAW	Plasma Arc Welding	
SAW	Submerged arc welding	Sub-Arc
SMAW	Shielded Metal Arc Welding	Stick Welding. Manual Metal Arc

II.4.1 Shielded Metal Arc Welding

The shielded metal-arc welding, which is also known as stick welding, is the most widely used process. The arc is struck between the metal to be welded and a flux coated consumable electrode. The fluxes are mostly made from mineral components and cover the hot weld deposit and protect it from the environment [53]. The electrode covering is a source of arc stabilizers, gases to exclude air, metals to alloy the weld, and slags to support and protect the weld. Shielding is obtained from the decomposition of the electrode covering. Pressure is not used and filler metal is obtained from the electrode. Shielded metal arc welding electrodes are available to weld carbon and low alloy steels; stainless steels; cast iron; aluminum, copper, and nickel, and their alloys. Figure II.1 describes the shielded metal arc welding process [33].

Shielded metal arc welding (SMAW) is the most important general purpose welding process and is commonly used for welding steels and for hard-surfacing [54].

The advantages of SMAW are: it welds most metals, thick or thin parts, it is common, it permits the use of a variety of flux covers, it can be used for all welding positions, the equipment is light and easy to transport in the field, the power supply can be direct current (dc) or alternating current (ac), it requires no gas or water supply, and it can utilize an electrode that matches the base metal or a special alloy electrode.

The short comings of SMAW are: the welding process is slowed down since each stick (rod) must be replaced as it is consumed, the slag needs to be cleaned after each pass, and it tends to spatter molten weld metal [17].

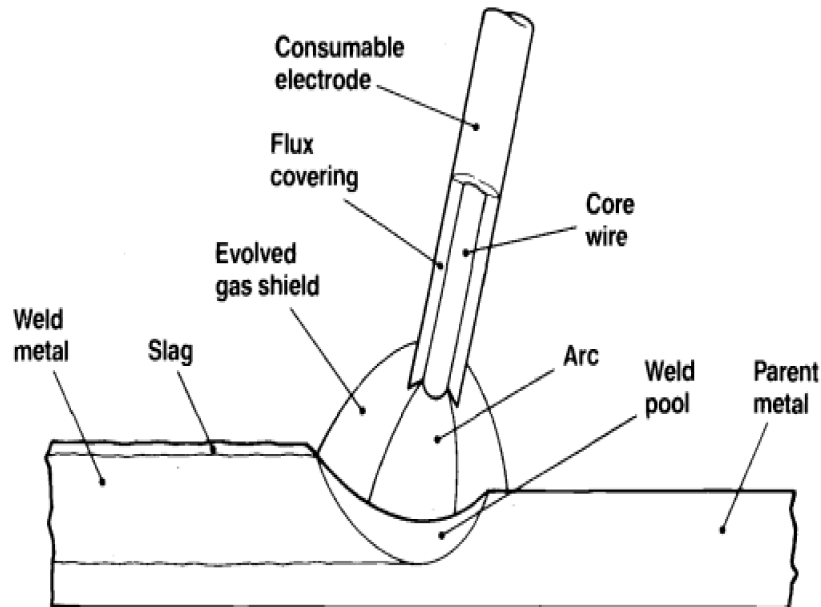


Figure II.1: *Shielded metal arc welding (SMAW) or manual metal arc welding (MMA) [54].*

II.4.2 Submerged Arc

Submerged arc welding (SAW) is a continuous arc welding process employing an electrode in the form of a coil of steel wire. The welding current is introduced to the wire at a point close to the arc and both the arc and molten pool are covered by powdered flux fed down a pipe just in front of the arc. The functions of the flux are the same as in the shielded metal arc welding process. Fluxes are made by fusing the constituents together and crushing the product, or by sintering or agglomerating mixed powders [54]. Figure II.2. shows this process of welding.

Submerged arc welding (SAW) is used extensively in industry to fabricate pressure vessels, pipelines, marine vessels, and wind turbine towers because it offers several advantages such as ease of automation, it can be used to weld large pieces (beams, vessels) because it has a high deposition rate welding speed, high quality welds, excellent surface finish, its deep penetration makes it well suited for thick plates with minimum welding fumes, even with imperfect alignment of weld bevels. Pipe mills commonly employ automated SAW to weld pipe seams.

The normal welding variables of submerged arc welding like current, voltage, travel speed and bead geometry are characterized by bead width, height, penetration, hardness and quality [17,55, 56].

The short comings of SAW are: It is mostly a horizontal (flat) welding technique, the welder can not see the arc that is immediately covered by the flux, the metal stays molten for a longer time (owing to the flux cover) which may require backing, and the welding equipment is large [17].

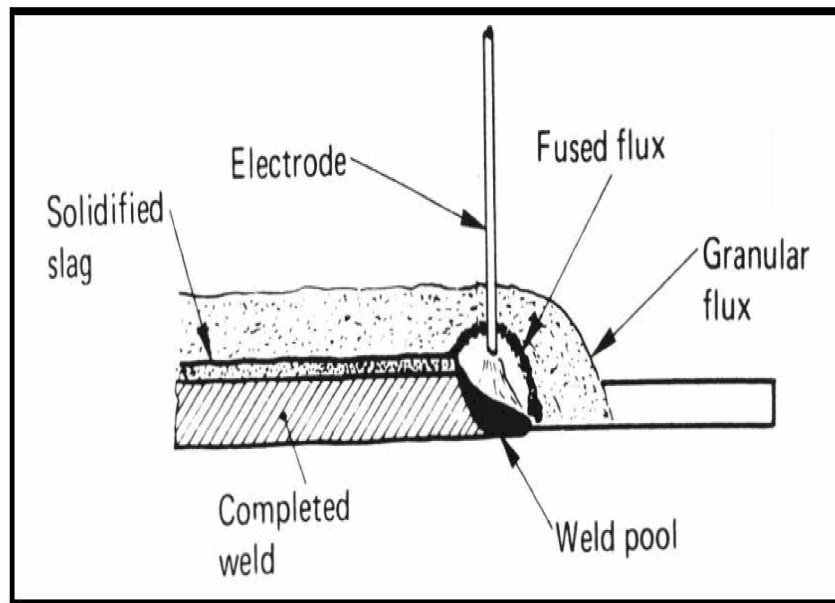


Figure II.2: Illustration of Submerged Arc Welding [57].

II.4.3 Gas Metal Arc Welding

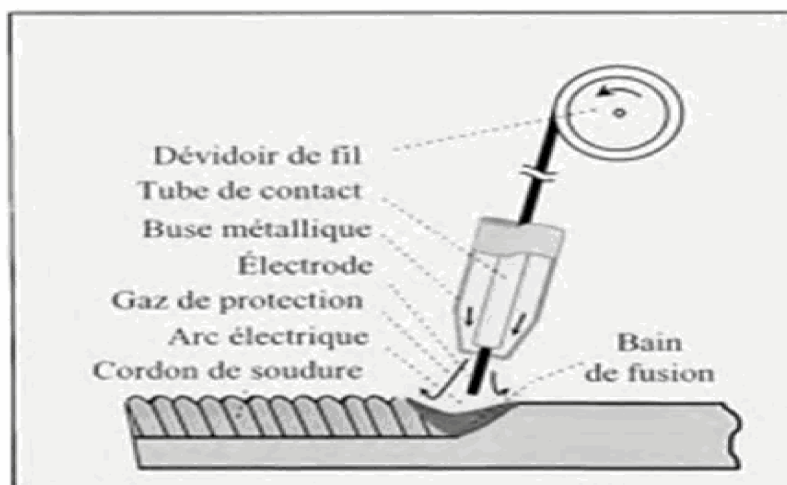


Figure II.3: Illustration of Gas Metal Arc Welding [58].

Gas Metal Arc Welding (GMAW) is also called Metal Inert Gas welding (MIG) when shielded by an inert gas such as helium, and Metal Active Gas welding (MAG) when shielded by a reactive gas such as CO₂. This process welding process uses an uncoated continuous wire. The weld area is shielded from contamination by the gas that is fed through the welding torch. The mode of metal transfer (spray, globular, short-circuiting, pulsed-arc) is varied by adjusting the amperage and the shielding gases used depending on the welding position and the type of joint [53,59]. MIG welding can offer many advantages over conventional gas and arc welding alone. Because a shielding gas is fed around the electric arc, oxidation of the metals, caused by chemical reaction with air, is avoided, leading to high quality welds. In fact, the MIG welding process is widely employed in the automotive industries for joining steels. The use of welded steels has increased with increasing automotive production. However, the mechanical properties of the weld may not always be adequate, as the welding process changes the microstructure (HAZ) and internal stress [59].

The short comings of MIG are: it requires large equipment, shorts can lead to lack of fusion, it requires a gas source (argon, helium, carbon dioxide), when welding outdoors wind can blow the shielding gas away, and it tends to spatter weld metal [17].

II.4.4 Flux Core Arc Welding

In Flux Core Arc Welding (FCAW), the electrode is consumable and contains in its center either a flux that automatically shields the molten pool (self- shielding FCAW), or minerals or alloys, in which case gas shielding is necessary (gas shielded FCAW), The shielding gases and slag are provided by the decomposing flux that is contained within the electrode. Auxiliary shielding is also used in certain instances where deeper penetration is needed.

The advantages of FCAW are: it can be used to weld many metals, it can be used in all positions, it has a high deposition rate, and its slag is relatively thin and readily removed.

The shortcomings of FCAW are: the need to chip-off flux at the end of a weld pass, and welding is accompanied by smoke [54].

II.4.5 Gas Tungsten Arc Welding

This is an arc welding process in which, in contrast to gas metal arc welding with its consumable electrode, the electrode is of non consumable tungsten. The arc provides the heat and filler metal, if needed, is added separately (see Figure. II.4). Both the arc and weld pool are shielded with stream of inert gas, often argon but helium or mixtures of the two gases are also used. Helium gives deeper weld penetration [54].

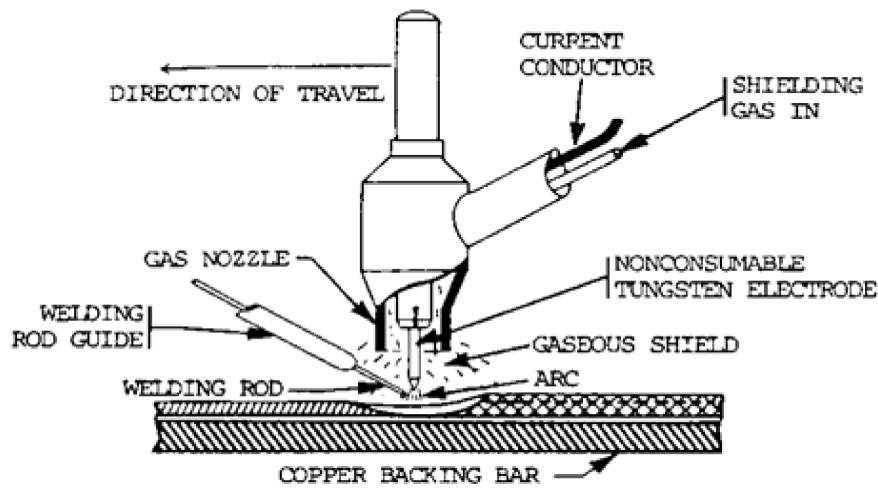


Figure II.4: Gas tungsten arc welding [33].

On carbon steel, TIG is usually limited to thin wall pipe or tubing, and root and hot pass (the first two passes) on standard size pipe. The advantages of TIG are: the electrode and welding rod being separate can be separately controlled leading to good quality welds (smooth, uniform) in most metals, it does not require weld cleanup, it is spatter free. It is particularly well suited for standard wall pipe, or for a first pass on thick wall piping and pipeline. The short comings of TIG are: it is a relatively slow welding process, the tungsten electrode, which remains solid during welding, may chip and form an inclusion; the shielding gas can be affected by wind [17].

II.5 Basic metallurgy of welding

During welding, the interaction of the heat source and the material leads to rapid heating, melting and the formation of the weld pool. In the weld pool, the molten metal undergoes strong recirculation and the flow of liquid metal significantly affects the temperature fields, thermal cycles and the weld pool geometry. When the heat source moves away, the weld pool cools and eventually solidifies. As the temperature drops, various solid state phase transformations take place resulting in the final microstructure of the weldment [60].

II.5.1 Temperature and time in welding

Unusual combinations of temperature and time must be dealt within welding. The temperature changes during welding are wider and more drastic than in any other metallurgical process for several reasons:

- (1) Welding heat sources are hotter than most that are commonly used in industry for heating,
- (2) Welding operations are carried out so rapidly that very steep temperature gradients are established between the weld area and surrounding base metal, and
- (3) Both base metal and any fixturing in intimate contact act as highly efficient heat sinks which promote cooling rates as fast as permitted by the thermal conductivity of the metals involved. The temperature changes in welding, for the most part, are not a favorable treatment for steels. There are exceptions, however, and it can be helpful to know when and where the heat effects of welding can be beneficial [61].

II.5.2 Heat input

The rapid heat input and high energy density involved in welding causes very different thermal effects than do conventional heat treatments. Very rapid heating cycles (fractions of a second to a few seconds), high peak temperatures (in excess of the melting temperature) and relatively rapid cooling rates to ambient temperature (fractions of a second to many minutes) are all involved. A typical thermal cycle for an arc welding process is shown in Figure II.6.

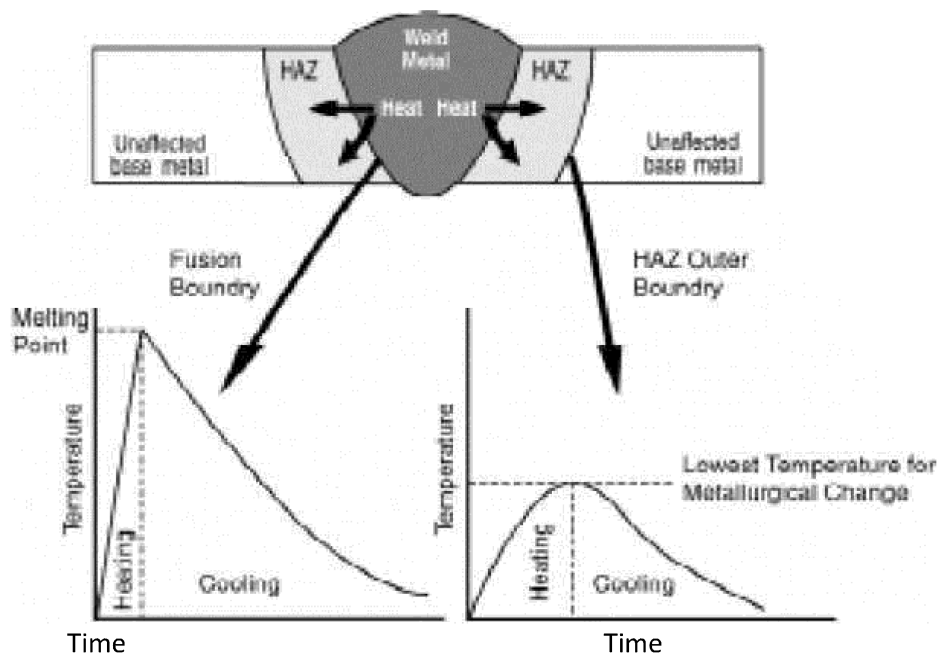


Figure II.6: Thermal cycles in weld zones [52].

The heat input of a given welding process is most easily defined for electric arc processes. It is simply arc voltage times arc current divided by welding speed. Since arcs lose some energy to the surrounding space by radiation, convection and conduction through gas and slag shielding media, less than 100% efficiency of energy transfer to the weld zone occurs [52].

II.5.2 Heating Rate

The rate of heating with a given welding process depends on two basic features are the intensity or temperature level of the heat source, and the efficiency of heat transfer from the source into the workpieces. Of course, the source must be able to supply a sufficient volume of energy [61]. The effects of the rapid temperature rise during the initial heating cycle in welding have not been analyzed extensively, but do have some important implications. The most important is that any existing segregation of alloy elements or impurities in the base metal will not be evened out by diffusion, because the time available is too short. This can lead to a local region in the base metal right next to the fusion line where localized melting can occur. This is most likely where previous segregation in the base metal exists, for example at grain boundaries. These regions may contain higher than average concentrations of alloying elements and/or impurities, which cause a lowering of the melting temperature. The region is therefore called the Partially Melted Zone (PMZ). This localized, restricted area of melting may simply solidify again as the temperature falls after welding, or it may open up under stress to form a small crack, usually known as a liquation crack [52].

II.5.3 Peak Temperature

The maximum or peak temperature reached in workpieces subjected to a heat source is determined by the rate of heat input and the rate of heat loss. As long as the rate of heat input exceeds the rate of heat loss, the temperature will continue to rise. When heat input equals heat loss, the peak temperature is achieved. As the temperature is raised at this location in a workpiece, the temperature also rises at all regions in the vicinity following the physical laws of heat conduction. Therefore, the heat supplied for welding must be sufficient not only to melt the volume of metal required, but also to match the amount of heat removed by conduction. This means that a slow rate of heat input requires more heat to melt a required volume of metal [61].

The high peak temperatures reached in welding (near or above the melting temperature of the base metal) are far in excess of temperatures in conventional heat treating processes. There are two major results [52]:

1. Grain sizes in the heat-affected zone (HAZ) are large and are largest next to the fusion line at the weld metal. This increases hardenability in transformable steels and may concentrate impurities which are segregated to grain boundaries. This may lead to a form of hot cracking.

2. All traces of work hardening and prior heat treatment (e.g. tempering, age hardening) will be removed in at least part of the HAZ and the size of the region affected will be larger as the heat input rises.

II.5.4 Cooling Rate

Understanding cooling rates in the weld zone and heat affected areas is more important than understanding heating rates. Cooling is more complex, however, because many more features of a weldment and welding procedure exert an influence, and because the rate of cooling has a dominating effect on the final microstructure and properties. Three general features have a profound influence on the cooling rates at various locations in a weldment: (1) the weld zone, or nugget, which serves as a heat source during the course of the welding process; (2) the mass of base metal, along with any intimately contacting metal fixtures that can provide a heat sink; and (3) the initial temperature of the base metal and fixtures. Although these three features require individual review, attention also must be given to their interrelationships as factors controlling cooling rate [61].

The rapid cooling cycles for welding after solidification is complete are caused by the quenching effect of the relatively cold parent metal, which conducts heat away from the weld zone. However, the cooling rate must be evaluated, since important weld zone properties such as strength, toughness and cracking susceptibility are affected. As the cooling rate increases, i.e. as the temperature falls more rapidly, several important welding effects occur. In transformable metals, such as ferritic-martensitic steels, the high temperature phase in the weld metal, and particularly in the HAZ is quenched.

If weld zone properties are not as desired, it is possible, in some cases, to improve them by altering the cooling rate in the welding procedure. Two main methods are used. The first is heat input, higher heat input in a given situation slows down the cooling rate. Preheating, by warming the base material before welding, also slows down the cooling rate, with higher preheat leading to slower cooling rates. Combining preheat and heat input variations is called Procedure Control. Further control of cooling rate effects can be included in a welding procedure by defining a value for interpass welding temperature in multipass welding (effectively a preheat value for each succeeding pass) [52].

II.6 Metallurgical effect of the weld thermal cycle

A number of reactions may take place in the liquid weld metal: first in the liquid drop at the electrode tip, secondly during transfer from electrode to weld pool, and thirdly in the weld pool itself. These reactions include:

- 1 Solution of gas, causing gas-metal reactions or reaction with elements dissolved in the liquid metal;
- 2 Evolution of gas;
- 3 Reaction with slag or flux;

Generally, but not invariably, gases other than the inert gases have an unfavourable effect on weld metal properties and it is the object of shielding methods to minimize any metallurgical damage from this cause. Slag-metal reactions occur mainly during the welding of steel.

II.6.1 Weld metal solidification

The evolving microstructure in fusion welding is strongly influenced by the current thermal conditions, and weld metal chemistry. Weld pool conditions give always cellular growth or, in more highly alloyed steels, cellular-dendritic. Under these conditions, the total under cooling is not only a function of the structure of the interface, but is also dependent upon the growth rate and temperature gradient in the liquid before the increment interface [57].

It is often said that weld metal is a casting. While this may be true, and in fact many features observed in castings also occur in welds, the time scale for weld metal solidification is not more than a few seconds compared with minutes or even hours for the solidification of castings. The rapidity of the heating and cooling during welding results in a smaller grain size than in most castings and generally the mechanical properties are substantially higher [54].

The molten pool in fusion welding tends to be pear shaped the tail lengthening as the welding speed is increased. Grains grow from the solid-liquid interface in a columnar epitaxial manner depending on the direction of maximum heat abstraction. The size of the grains depends on the grain size of the solid metal at the interface from which they grow [41, 54, 62].

The type of substructure that appears in weld metal depends on the form of the solidification front (Figure II.7).

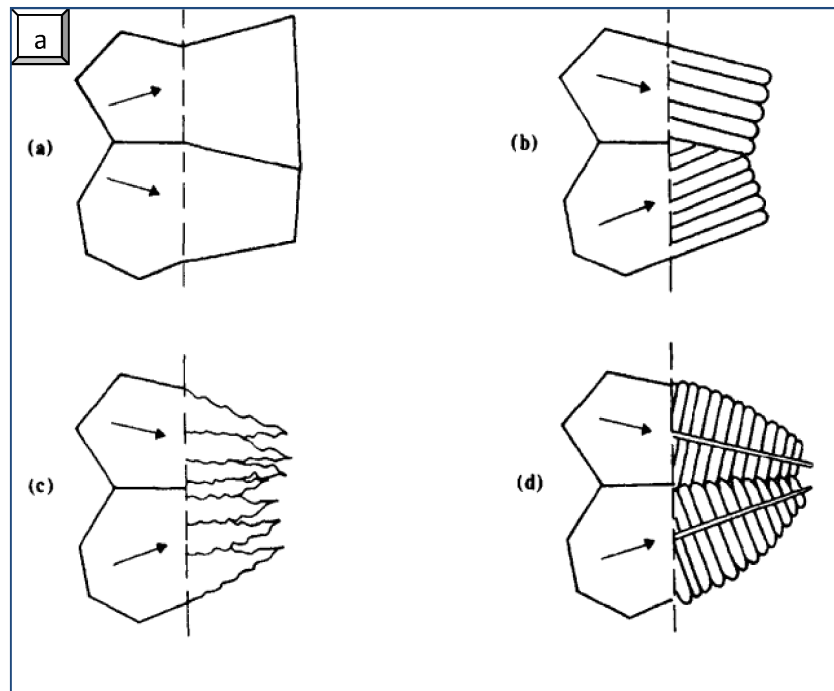


Figure II.7: Solidification modes (a) planar; (b) cellular dendritic and (d) columnar dendritic. The arrows indicate the preferred growth direction ($\langle 100 \rangle$ for steel) [63].

The effect of increasing the welding speed is to change the shape of the weld from an elliptical shape to a narrower tear shape. A tear-shaped weldpool, (Figure. II.8) [57].

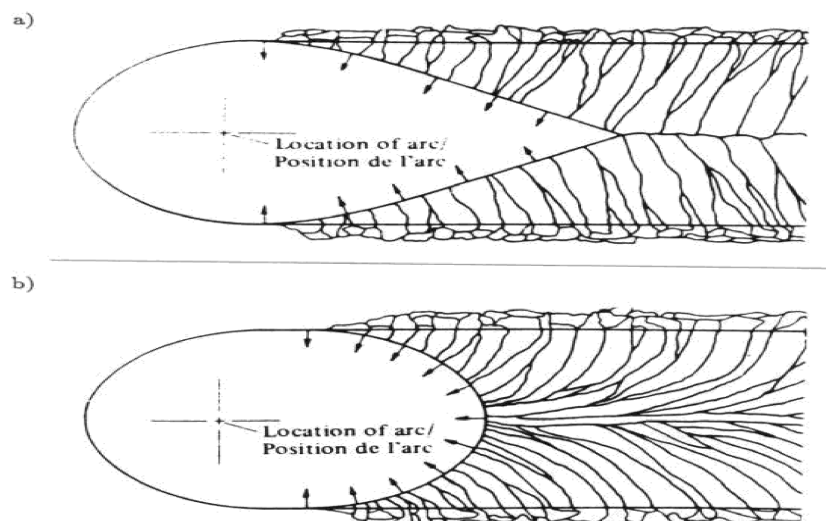


Figure II.8: Schematic diagrams showing competitive growth with a teardrop shaped weldpool and an elliptical weldpool, respectively a and b [57].

II.6.2 Heat affected zone

Welding is very complex process where electrical energy and filler metal are transferred weldment via electric arc. Coupled electromagnetic, thermal, mechanical and metallurgical processes in the heat affected zone. Metallurgical processes: melting, solidification and solid phase transformation, these processes give different sub-zones of the HAZ [64].

Several zones are formed within the HAZ by the combination of heating rate, peak temperature and cooling rate, depending on the alloy system. The subcritical HAZ occurs when the peak temperature is below an important temperature for the metal being welded. This could be, for example, the recrystallization temperature in a work-hardened metal, the solvus temperature for a precipitation-hardened alloy or the allotropic phase change temperature for a transformation hardening alloy. Above the critical temperature, the grain size increases as the temperature increases. Especially in transformation-hardening alloys, two regions exist in this high temperature zone:

1. Fine Grained Heat Affected Zone (FGHAZ) this region exists when an allotropic phase change decreases the average grain size in comparison with the grain size in the subcritical region. This occurs, for example, in the intercritical temperature range in steels.
2. Coarse Grained Heat Affected Zone (CGHAZ) this region occurs at high temperatures when all phase changes are completed. Grain size tends to increase up to the fusion temperature [52, 65].

II.6.3 Phases Transformations and microstructures of weld metal

The character of the weld metal microstructure depends in the first place on alloy content. In carbon, carbon-manganese and microalloyed steel; however, the microstructure and weld metal properties are much affected by details of weld procedure and composition.

Factors that affect the microstructure of this type of weld metal include cooling rate, composition, the presence of non-metallic nuclei and plastic strain [63].

A series of phase transformations take place in both the fusion zone (FZ) and the heat-affected zone (HAZ) during welding of low carbon steels. The microstructural history of the FZ is α -ferrite \rightarrow γ -austenite \rightarrow δ -ferrite \rightarrow liquid \rightarrow δ -ferrite \rightarrow γ -austenite \rightarrow α -ferrite, while the typical microstructure evolution in the HAZ corresponds to α -ferrite

\rightarrow γ -austenite \rightarrow α -ferrite. In the HAZ, $\alpha \rightarrow \gamma$ transformation during heating is of importance because the grain size, phase fraction and concentration homogeneity of transformed γ phase affects the kinetics of subsequent γ grain growth and phase

transformations during cooling. On the other hand, the weld integrity and performance are largely affected by the solidification transformation in the FZ. However, the final microstructure in the weldment is fairly complex because the solid-state $\gamma \rightarrow \alpha$ transformation can significantly alter the solidification microstructure. Therefore, during welding of low carbon steels, the $\alpha \rightarrow \gamma$ transformation in the HAZ during heating and the reverse $\gamma \rightarrow \alpha$ transformation in the FZ and HAZ during cooling are very important [41,60].

II.6.3.1 The as-deposit microstructure

The microstructure in central beads was as expected even more complex which resulted from different thermal histories and tempering depending on the location within the joints [41].

The microstructure obtained as the weld cools from the liquid phase to ambient temperature is called the as-deposited or primary microstructure. Its major components include allotriomorphic ferrite, Widmanstätten ferrite, and acicular ferrite (Figure II.9). There may also be some martensite, retained austenite or degenerate pearlite. These latter phases occur in very small fractions, and are known by the collective term microphases weld [41, 50, 57, 66]. Bainite, consisting of sheaves of parallel platelets, is not generally found in well-designed welding alloys. Instead, acicular ferrite is induced to nucleate heterogeneously on non-metallic inclusions [41, 50, 57].

In practice, the gap between the components to be joined has to be filled by a sequence of several weld deposits. These multirun welds have a complicated microstructure (Figure II. 11). The deposition of each successive layer heat treats the underlying microstructure. Some of the regions of original primary microstructure are reheated to temperatures high enough to cause the reformation of austenite, which during the cooling part of the thermal cycle transforms into a different microstructure. Other regions may simply be tempered by the deposition of subsequent runs. The microstructure of the reheated regions is called the reheated or secondary microstructure [50].

Light micrograph of acicular and widmanstätten ferrite in steel weld deposit is illustrated in Figures II.9.a and b. Grain boundary ferrite and degenerate pearlite are shown in Figure II.10.

Alternative designations for the microstructural constituents shown in figure II.11. Austenite and carbides in Figure II.12.

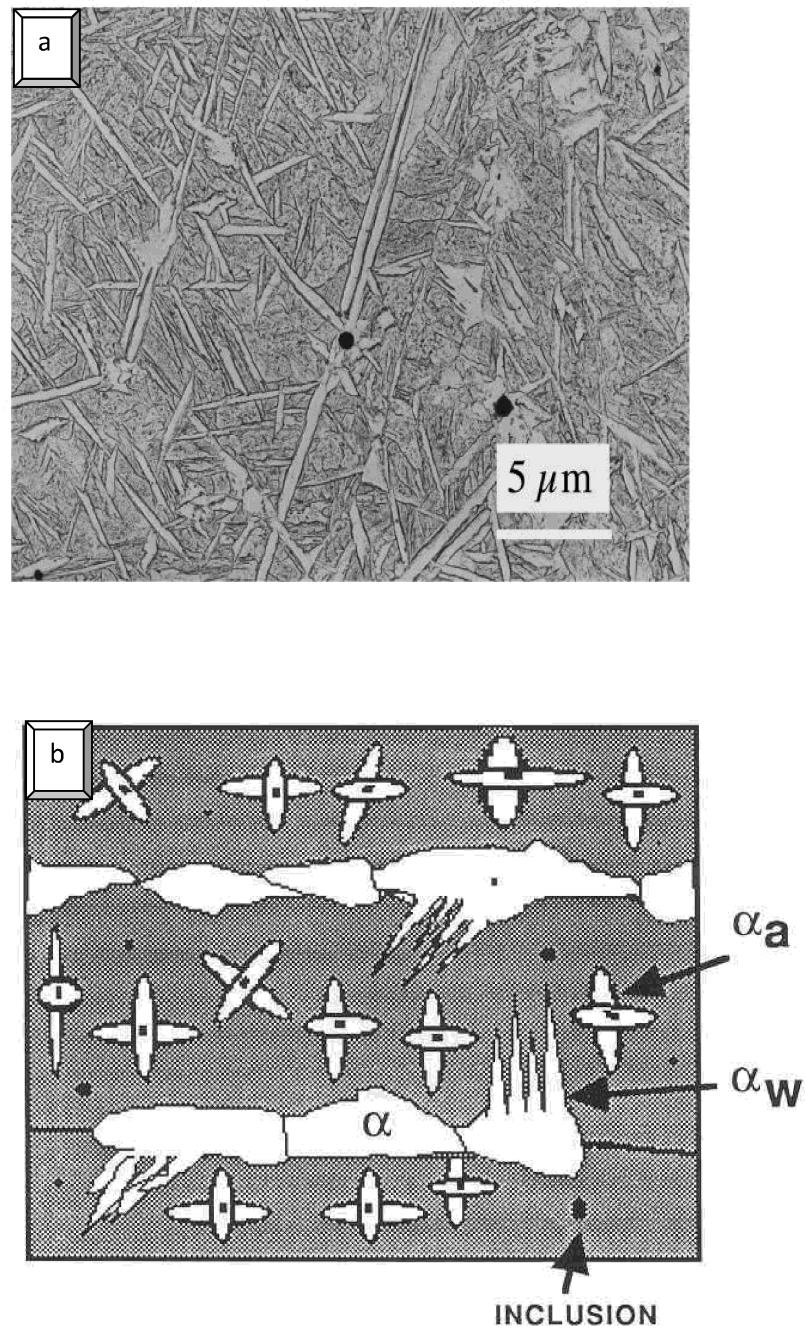


Figure II.9: (a) Replica transmission electron micrograph of acicular ferrite plates in steel weld deposit. (b) An illustration of the essential constituents of the primary microstructure of a steel weld deposit [41].

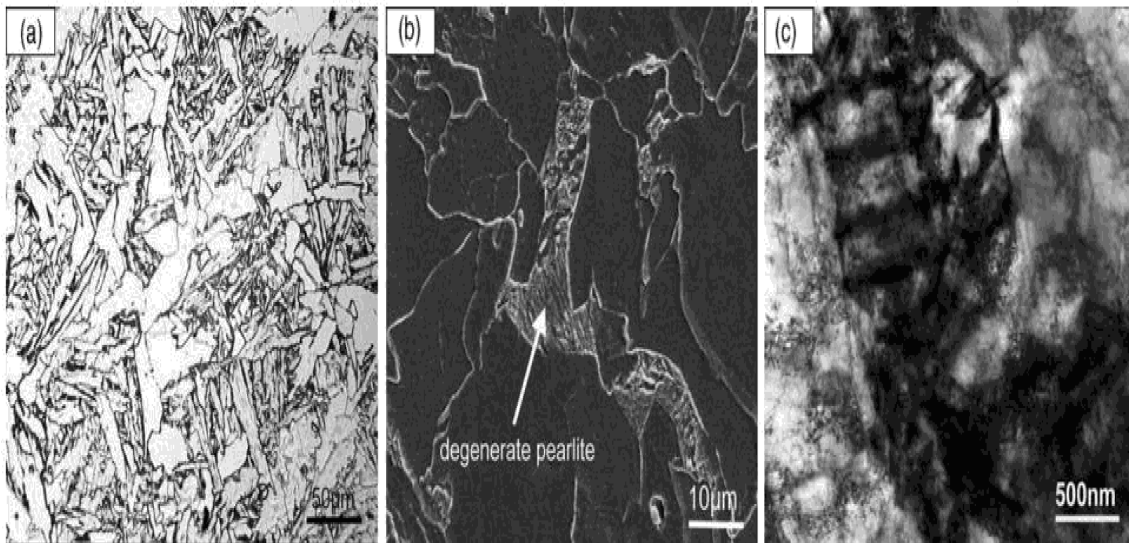


Figure II.10 : Morphologies of grain boundary ferrite and degenerate pearlite of the steel without Nb at a cooling rate of 1 k/s (a) optical micrograph, (b) SEM images indicating grain-boundary and degenerate pearlite, (c) magnified degenerate pearlite imaged by TEM [67].

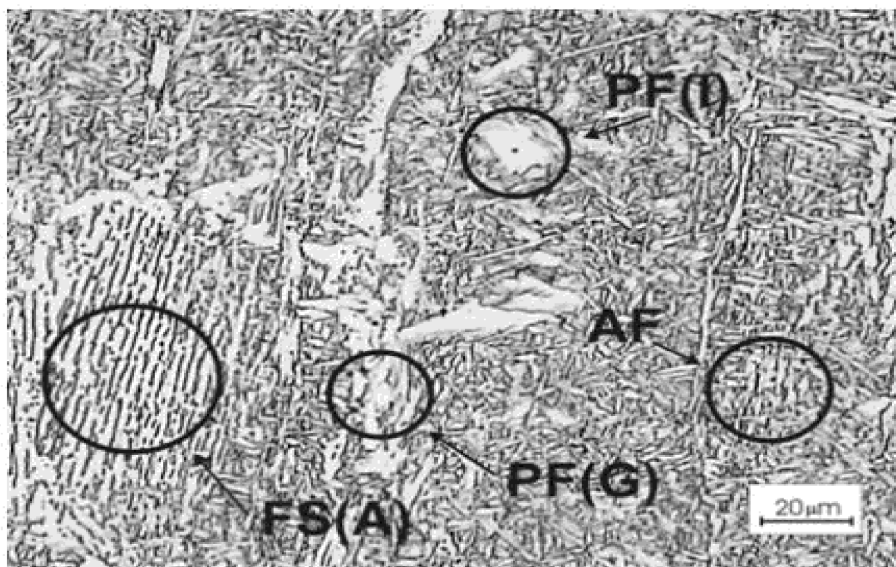


Figure II.11: Optical microscopy of weld metals associated with carbon-manganese steel in the as-welded condition showing acicular ferrite (AF), proeutectoid ferrite (PF(G)), polygonal ferrite (PF(I)) and aligned side plates (FS(A)) [68].

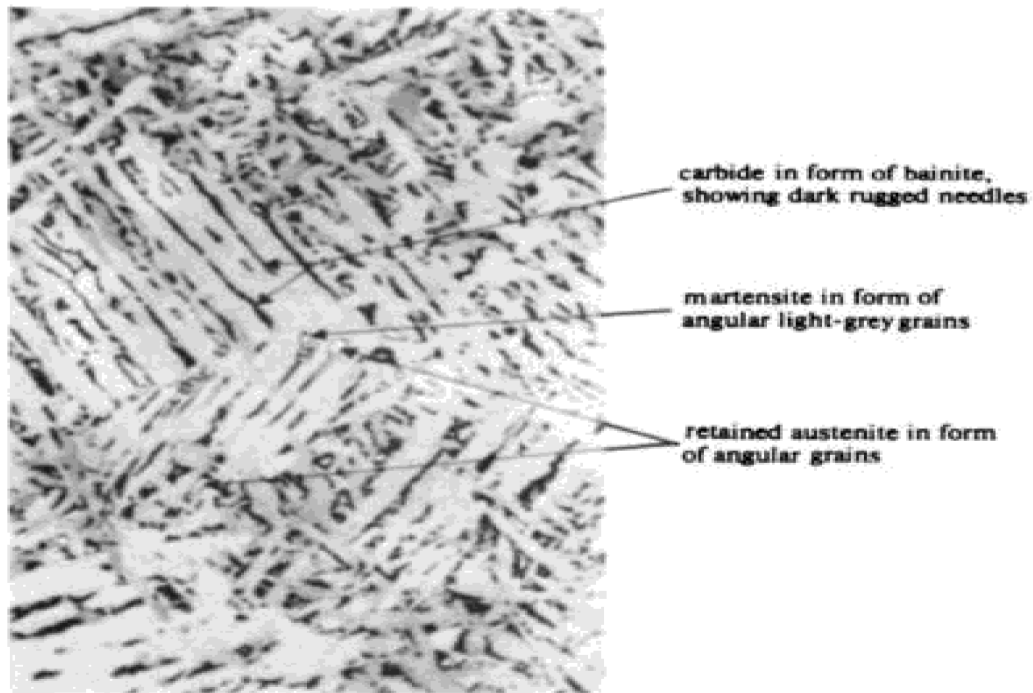


Figure II.12: Lamellar structure in submerged arc weld metal: ferrite with aligned martensite, austenite and carbide(x1000) [63].

Bhadeshia et al [41] confirmed that there is mechanism for the microstructural transition from acicular ferrite to bainite. The removal of allotriomorphs leads to the growth of grain boundary nucleated bainite (Figure. II.13). The ferrite/austenite boundaries, cannot develop into bainite because the adjacent austenite is enriched in carbon, to an extent which drastically reduces its bainite start temperature. A transformation free zone is therefore found ahead of the allotriomorphic ferrite/austenite interfaces.

It is well known that the both the acicular ferrite and bainite were otherwise obtained by isothermal transformation under identical conditions.

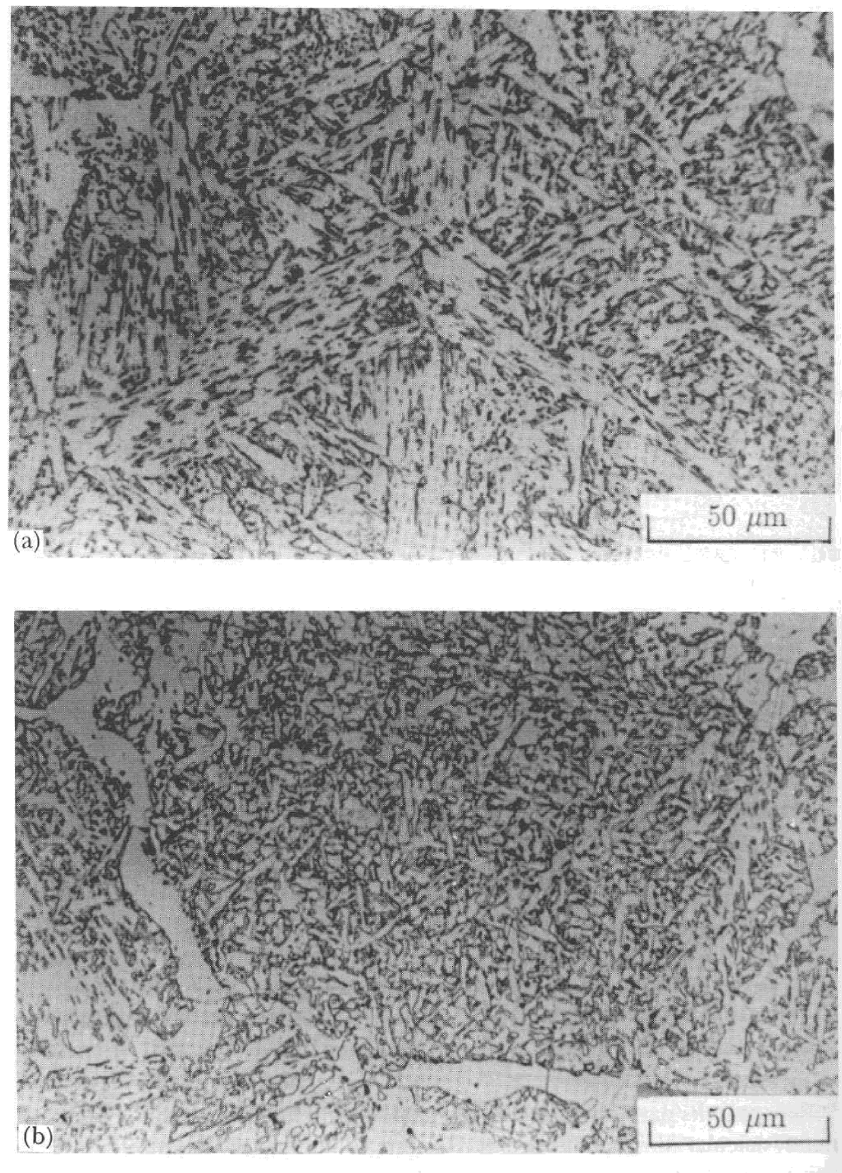


Figure II.13: Change from a bainitic (a) microstructure to one which is predominantly acicular ferrite (b), induced by the introduction of a thin layer of allotriomorphic ferrite at the austenite grain surfaces [41].

II.6.4 Transformation and microstructure in the heat-affected zone

In general, the heat-affected zone may be divided into two regions: the high-temperature region, in which major structural changes such as grain growth take place, and the lower-temperature region. In the grain-growth region the final grain size for any given alloy will depend mainly on the peak temperature to which it is exposed and the time of heating and cooling [63].

There is a well defined gradient of microstructure in the HAZ, as a function of the distance from the fusion boundary (Figure II.14).

1-Those regions immediately adjacent to the fusion boundary are heated to very high temperatures and hence transform completely to austenite. During continuous heating, austenite begins to form at a temperature $Ac_1 \sim 800^\circ \text{C}$, and the samples become fully austenitic at $Ac_3 \sim 950^\circ \text{C}$. These temperatures are different from the corresponding equilibrium temperatures Ac_1 and Ac_3 because they increase with the heating rate. The peak temperatures in the HAZ close to the fusion boundary are well in excess of the Ac_3 temperature of weldable steels. Consequently, the austenite that forms is annealed during heating beyond Ac_3 , giving rise to a very coarse grain structure. This forms the coarse-grained austenite zone [50].

1-Austenite grain growth in the weld HAZ is an important factor to determine the microstructure and mechanical properties of the weld because grain size in the weld metal is controlled by that in the HAZ and austenite grain size influences the kinetics of phase transformation during the cooling cycle [42].

2-The austenite grain size decreases sharply with distance from the fusion boundary. It is necessary to distinguish this as the fine-grained zone because its mechanical properties tend to be superior to those of the coarse zone.

3-As the peak temperature decreases, regions of the HAZ further away from the fusion boundary become only partially austenitic during the heating part of the thermal cycle. The austenite that forms has a rather high carbon concentration, due to the increase in the solubility of carbon in γ with decreasing temperature. The part that does not transform into austenite becomes tempered.

4-When the peak temperature becomes less than the Ac_1 temperature, the only effect of the heat input is to temper the microstructure, the extent of tempering decreasing with distance from the fusion boundary [50].

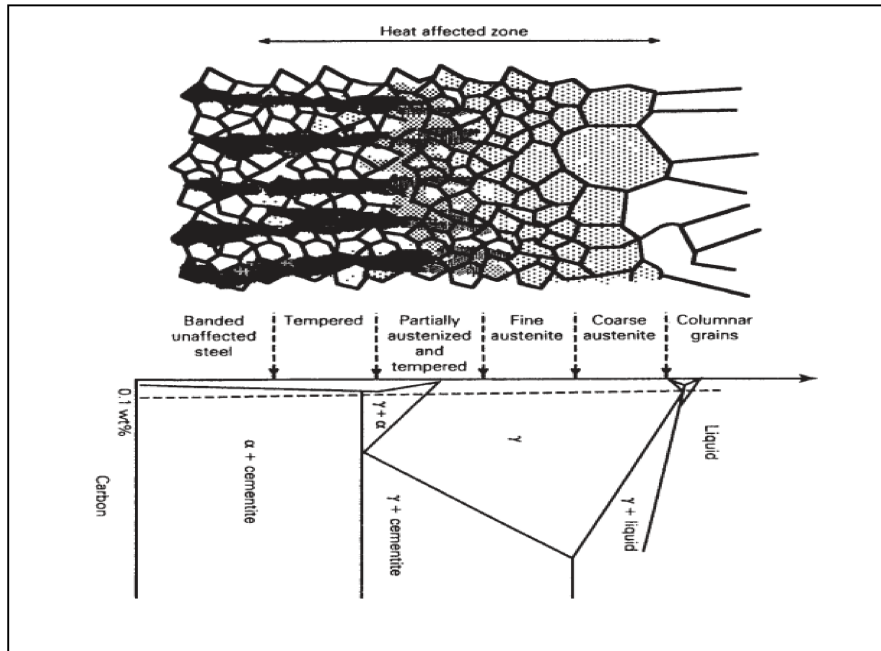


Figure II.14: Schematic illustration of the microstructural variation to be expected in the HAZ of steel welds [50].

II.7 Mechanical properties and residual stress of the welded joint

II.7.1 Mechanical properties of weld metal

The mechanical properties of weld metals such as strength, ductility, toughness, and corrosion resistance are strongly dependent on the microstructure developed during solidification and cooling of the weld pool, and also depend on the weld chemical composition and cooling rate. The chemical composition is determined by base metal and electrode wire composition, dilution, and any pyrometallurgical chemical reactions in the weld arc. The weld metal composition is “matched” to give tensile strength similar to the base metal; however, alloying additions in the majority of weld metals are usually kept to a minimum to avoid the formation of brittle phases and defects, such as cold cracks inside the weld. This is related to the hardenability of the weld metal [60, 69].

The hardness of weld metal correlates with ultimate strength in the same way as for wrought steel, and hardness testing is used as a method of controlling weld metal strength [63].

Tensile strength is usually the first property that receives attention in considering the kind of weld metal needed. For the majority of weldments, the designer’s goal is to just have the weld metal match the base metal in strength. It would appear to be desirable to have the

weld metal in a butt joint equal in strength to the base metal. There are instances, however, where a somewhat lower strength can be tolerated in the weld metal. This is often true of fillet welds where a relatively large cross section of weld metal easily can be deposited to compensate for lower strength, and where the greater toughness and ductility that normally go with lower strength could be an attribute. Fillet welded joints often contain points of stress concentration, and greater demands sometimes are made of the weld metal to exhibit toughness and ductility [15].

The notch ductility of weld metal, as measured for example by impact testing, depends mainly, for any given composition, on microstructure, grain size and inclusion content. Notch ductility is reduced, other things being equal, by the presence of proeutectoid ferrite in the structure, and particularly when it is coarse and block-like in form. Ideally, the weld metal should consist entirely of fine acicular ferrite. The notch ductility is also reduced as the amount of martensite in the structure increases [63].

The impact toughness represents the ability of a material to absorb energy under impact loading in the presence of a notch [17]. The impact toughness of most structural steels can be described in terms of the transition from ductile to brittle behaviour as the test temperature decreases. The most widely used characterisation method for the ductile to brittle transition behaviour is the Charpy V-notch impact test.

The impact toughness of the weld is a complex phenomenon, which is affected by many microstructural parameters. Generally speaking, a uniform and fine microstructure across the weld with the least quantity of inclusions on the junction leads to satisfactory toughness. Particular features in steels, including grain size, various constituents of steel, inclusions, and crystallographic texture all have influence on the ductile to brittle transition temperature (DBTT). These features exist in the weld junction and affect its toughness [70].

A good combination of strength and toughness of low carbon steel welds is achieved by so called acicular ferrite microstructure, consisting of small interweaving ferrite plates formed within austenite grains [71]. The ferrite grain size is largely determined by the size of the prior austenite grains, is a function of the weld thermal cycle.

Weld metal usually contains a relatively high density of dislocations, which also contributes to increased yield strength in carbon and carbon-manganese steels the width of the acicular ferrite grains may be a good measure of grain size, but the properties of the weld metal may also be influenced by the size and morphology of the proeutectoid ferrite.

The effect of increasing carbon and alloy content of weld metal is, in general, to increase strength and hardness. Carbon in particular has a strong effect on these properties. However, for the best combination of fracture toughness and cracking resistance, it is desirable to keep the carbon content within the range 0.05-0.12%. For alloy steel in particular, maintaining about 0.06% C in the deposit helps to avoid excessive hardness values. Carbon and low alloy steels may suffer some degree of embrittlement. When samples are cooled in still air, as is usually the case in laboratory testing, the effect of such treatment is to reduce the level of residual stress, to temper any hard transformation products that may be present, and in most cases to improve the fracture toughness. The yield and ultimate strengths of carbon and carbon-manganese steel weld deposits are not reduced to any significant extent provided that the temperature does not exceed 650 °C [63].

II.7.2 The mechanical properties of the heat-affected zone

The mechanical properties of the heat affected region are different as compared with those of the unaffected weld metal or parent plate. The yield and ultimate strength of the heat affected zone in steel are almost always higher than those of the parent material and the properties of main interest are fracture toughness and hardness [63].

II.7.2.1 The hardness of the heat-affected zone

The heat affected zone (HAZ), has a great influence on the properties of welded joints since it can alter the microstructure and residual stresses [3].

The hardness of the heat-affected zone is a measure of the tensile strength of the steel and, for any given alloy type, gives an indication of the degree of embrittlement. Hardness depends on the hardenability of the steel, on the cooling rate [69]. It is evident that hardness depends strongly on carbon content. There is virtually no influence of the prior austenite condition on the hardness [63, 72].

Hardenability may be described as the property of steel which determines the depth and distribution of the hardened structure produced during quenching from the austenitizing temperature. It is important to note that hardenability is a material property, dependent on the chemical composition and grain size and grain size but independent of the quenchant or quenching system [54].

The hardenability of steel may be generally correlated with the carbon equivalent (CE). In a carbon equivalent formula (EquII.1), the hardening effect of each alloying element is compared with that of carbon, and the relevant alloy content in mass% is divided by a factor that gives the carbon equivalent of that element.

$$CE = C + \frac{Mn}{6} + \frac{(Cu+Ni)}{15} + \frac{(Cr+Mo+V)}{5} \dots\dots\dots (EquII.1)$$

This formula is applicable to plain carbon and carbon-manganese steels, but not to microalloyed high strength low alloy steels or low alloys Cr-Mo types. Carbon equivalents may be used to calculate the hardness of the heat affected zone using a hardness equivalent, which takes account of the cooling rate, and also a weldability equivalent, which determines the maximum permissible cooling rate for the avoidance of hydrogen-induced weld cracking. A maximum carbon equivalent is often specified for structural steel to minimize the risk of excessive hardenability and/or hydrogen cracking [63].

The heat input has an inverse effect on the hardness of welded metal and its HAZ. One of the factors contributing to lower hardness in the HAZ zone is that of high heat input and hence retention of heat in this region.

Generally, grain nucleation and growth of austenite; can lead to reduced dislocations and work hardening compared to its elementary condition. Annealing of the HAZ, can have pronounced effect on phase content and morphology. The net effect is reduced dislocations and hardness.

High hardness in the welded zone may be attributed to fine grain size, needle shaped ferrite or the existence of widmanstatten inside ferrite grains. Hardness and grain size are inversely proportional as given by following equation:

$$H = H_0 + \frac{K}{d^{1/2}} \dots\dots\dots (EquII.2)$$

Where H is hardness, K is proportionality constant and d is grain size. Thus the lower hardness in the HAZ may be related to grain growth and the existence of ferrite phase in this region, which has been reported by previous authors [3].

II.7.2.2 The fracture toughness of the heat-affected zone

The balance of high strength and good toughness in steels can be upset by the thermal cycles experienced during welding, producing poor toughness in the heat affected zone (HAZ). Historically, the lowest toughness has been found in the grain coarsened heat affected zone (CGHAZ), which is the part of the HAZ immediately adjacent to the weld fusion line. During welding, the CGHAZ experiences peak temperatures up to the melting point, followed by rapid cooling. The high temperatures can lead to significant austenite grain coarsening and the combination of coarse austenite grain size and rapid cooling promotes brittle microstructure containing high proportions of ferrite side plates and bainite.

In some cases all the regions of the heat-affected zone (coarse grain, grain refined, intercritical and subcritical) are embrittled to some degree compared with the parent material. However, if the fracture toughness of the parent material is relatively low, the heat-affected zone may have better properties, particularly in the grain refined region. The factors affecting heat-affected zone toughness are the nature of the weld thermal cycle, grain-coarsening temperature, transformation characteristics, alloy content and non-metallic content. As would be expected, low heat input rate processes which give relatively high cooling rates generate a finer-grained heat-affected zone and less embrittlement in low-carbon steel. [63].

The effects of welding parameters on the properties demonstrate that high heat input and low cooling rates widen the HAZ and increase the grain size. The cooling rate is of prime importance. Low cooling rate entails an increase in the size of austenite grains. It is expected that at low welding speeds the grain boundary energy increases leading to grain growth. Excess grain growth can lead to reduced strength and increase crack initiation and growth. Furthermore, it can adversely affect the fracture toughness, which may arise due to heating and cooling cycles [3].

II.7.3 The residual stress in weld joint

During the joining process, as the materials are cooled from the bonding temperature to room temperature, significant residual stresses may develop. Residual stress and distortion result after welding and cause mismatching and cracking. In many cases, residual stress doesn't cause cracking directly but promote fracturing through fatigue, hydrogen cracking, and stress corrosion. A thorough understanding of the magnitude and distribution of the residual stress can be used to increase the reliability of the structure. Therefore, measurement of the residual stress resulting from various welding parameters is important [73-75].

II.7.3.1 Definition

Residual stresses can be defined as those stresses existing within a body in the absence of external loading or thermal gradients. In other words residual stresses in a structural material or component are those stresses which exist in the object without the application of any service or other external loads [76, 77].

It can arise in a two-phase material (e.g, in a composite) due to different plastic flow of grains or due to different thermal expansion coefficients of both phases. A polycrystalline material consists of grains having different lattice orientations. Macroscopic material properties depend on single grain properties, their lattice orientations and interactions between neighboring grains.

According to bhadেশia et al [78] Residual stresses are a consequence of interactions among time, temperature, deformation, and microstructure (Figure. II.15). Material or material related characteristics that influence the development of residual stress include thermal conductivity, heat capacity, thermal expansivity, elastic modulus and Poisson's ratio, plasticity, thermodynamics and kinetics of transformations, mechanisms of transformations, and transformation plasticity.

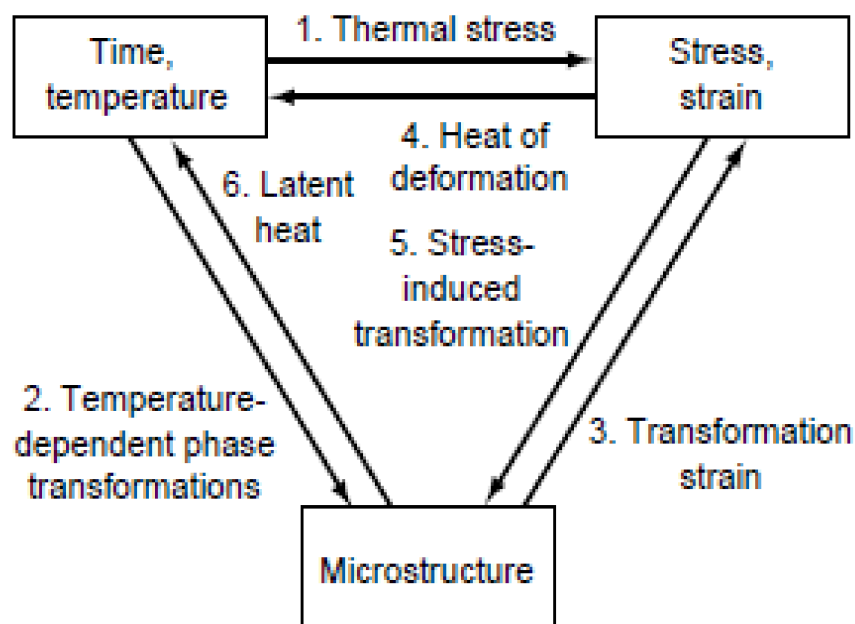


Figure II.15: The coupling of temperature, stress, and microstructure [78].

II.7.3.2 Role of residual stresses

Residual stresses have the same role in a structure's strength as common mechanical stresses. Residual stresses can play a significant role in explaining or preventing failure of a component at times. There are two kinds of residual stress:

-**Tensile residual stresses** may reduce the performance or cause failure of manufactured products.

-**Compressive residual stresses** are beneficial. It must be kept in mind that the internal stresses are balanced in a component.

Tensile residual stresses are counter balanced by compressive residual stresses. Residual stresses are three-dimensional.

There are three orders of residual stress: **Type-I (σ_I)**, **Type-II (σ_{II})** and **Type-III (σ_{III})** [76,79]

- **Macro Residual Stresses (Type-I; σ_I):**

These stresses vary within the body of the component over a range much larger than the grain size. They are homogeneous in very large numbers crystalline fields of the material (several grains). The internal forces related to these stress are in equilibrium in each section and the moments are related to these forces are null around all the axis.

- **Micro Residual stress**

Results from differences within the microstructure of a material. Can change sign and/or magnitude over distances comparable to grain size of the material under analysis

They are of two types, namely Type II or III

- ❖ **Type II (σ_{II}) :**

These stress are homogeneous in the small crystalline fields of the material (a grain or a phase), the internal forces which are related to these stress are in equilibrium in a rather great number of grains.

- This type can vary on the scale on an individual grain, may be expected to exist in single phase materials because of anisotropy in the behavior of each grain and may also develop in multi-phase materials as a result of the different properties of the different phases.

- ❖ **Type III (σ_{III})**

- Exists within a grain, essentially as a result of the presence of dislocations and other crystalline defects.

These stress are homogeneous in more small crystalline fields of the material (some interatomic distances). The internal forces related to these stress are in equilibrium in very small fields. In general it is very difficult to separate the stress of the second and third orders, and the micro stress term can be defined by the sum of the last two orders.

In the case of real materials, the state of the residual stresses results from the superposition of three orders of stress. The residual stresses can be introduced voluntarily in a component to improve its performances, or involuntarily like result of manufacturing processes.

According to. S.Wroński et al [7] the stress field is divided into three types in function of scale: first order stresses, second order stresses and third order stresses. *The first order stresses* are defined as the average stresses over a large volume of the sample. *The second order stress* is the difference between the grain stresses and the first order stresses.

The last type is *the third order stress*; this stress field is a result of the heterogeneity within a single grain.

As it was mentioned, we divide the stresses into three types in function of scale (Figure II.16)

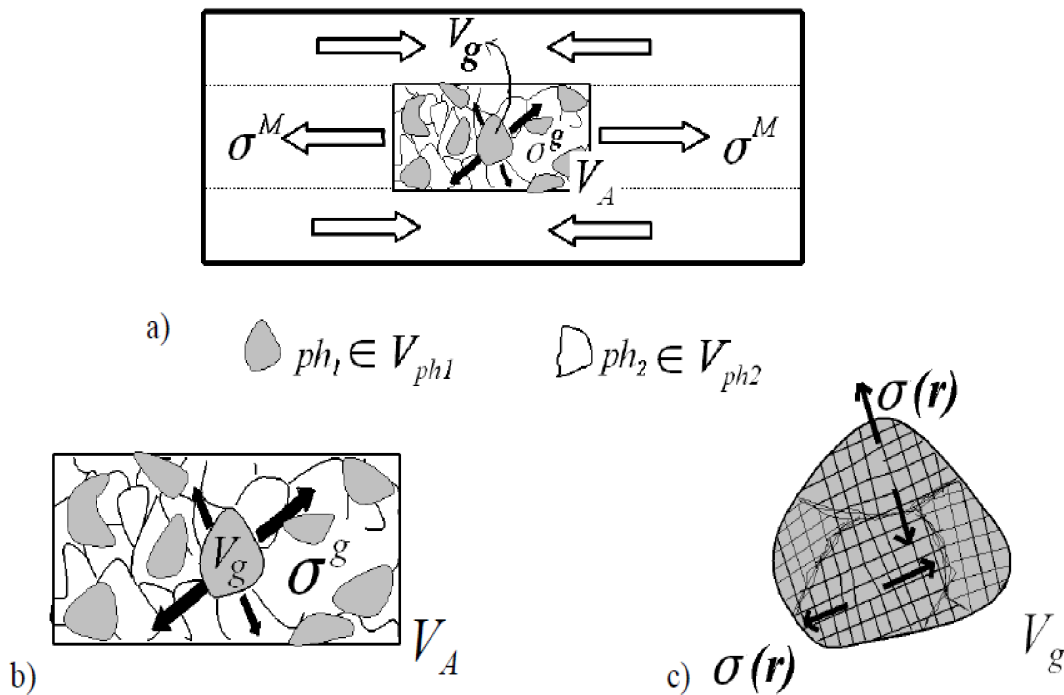


Figure. II. 16: Definition of different types of stresses at various spatial scales of a polycrystalline material. a) First order stresses, b) second order stresses, c) third order stresses [7].

II.7.3.3 The Origin of Stresses

Residual stresses can arise in materials in almost every step of processing. The origins of residual stresses in a component may be classified as: mechanical, thermal, and chemical. Mechanically generated residual stresses are often a result of manufacturing processes that produce non-uniform plastic deformation; these processes produce also high thermal gradients in a solid. They may develop naturally during processing or treatment, or may be introduced deliberately to develop a particular stress profile in a component. The residual stress are primarily of mechanical origin (machining, shot-blasting, cold rolling etc.), thermics (hardening, treatment the laser), thermomechanics (hot rolling, forging, welding etc), thermochemical (cementing, nitriding, carbonitriding etc.) and chemical (deposits in aqueous solution) [7, 78- 82].

Residual stresses arise as a result of welding operations because they involve the deposition of molten filler metal and the localised input of intense heat. when the highly localized transient heat created by a moving heat source and strongly nonlinear temperature fields in both heating and cooling processes cause nonuniform thermal expansion and contraction, high tensile residual stress are generated near the weld metal, when compressive residual stress are formed in the parent metal In the case of steels, the problem can be complicated by the fact that various solid-state phase transformations can occur during cooling of the material. Indeed, the significantly different displacements associated with these phase changes can have dramatically different consequences for the development of residual stress in the system as a whole [83]. The nature and magnitude of residual stresses have significant effect on the integrity and life span of welded structures and could be beneficial or detrimental. The magnitude and distribution of residual stresses are greatly influenced by the welding procedure and parameters and joint geometry [84], the maximum stress values canbe related with the properties like chemical composition and heat treatments of the materials. It is well known that the high tensile residual stresses are to promote fracture and fatigue, while compressive residual stresses may induce undesired [75, 76,79, 84, 86].

Stress relieving (SR) of welded joints at temperature below A_1 is very often required directly by classification societies or by production standars, the principle guiding of relieving is to transform of elastic deformation to plastic deformations. The most practical Procedure based on the metal resistance capacity, which is drop when the temperature rises;the elastic limit decreases [34,86].

The decrease of internal levels can be obtained by several mechanisms: **1.** If at annealing temperature the yield stress of the steel and weld metal are lower than the values of residual stress, then they are balanced by local plastic deformation. **2.** Relaxation of stresses can take place also by the creep mechanism. **3.** Finally the decrease of the residual stresses level can occur also by the mechanism of recovery and recrystallization, mainly in the case of low- carbon steel and weld metals. **4.** Internal stresses of higher order may relax as result of decomposition of oversaturated solutions [34].

Annealing temperature and annealing time play an important roles in all mechanism. Changes of hardness of the underbead zone and decrease of residual first order stresses in this zone in welding of low alloy steel are showed in Figure II.18. We can conclude that not only temperature but also annealing time affect the values of residual stresses [34,76].

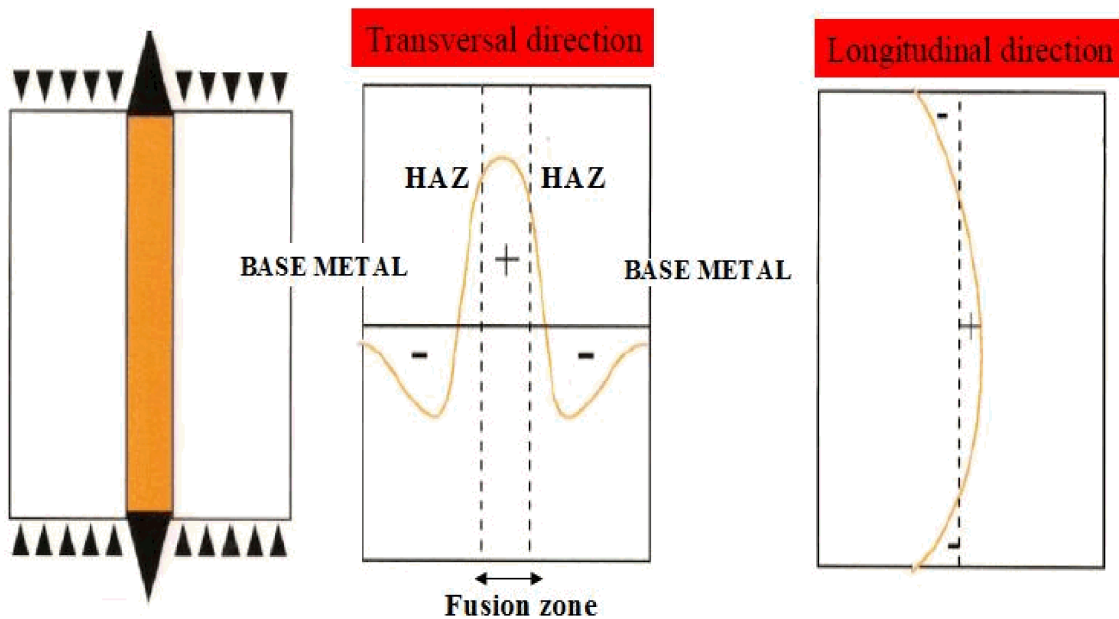


Figure II.18: Residual stress distribution in case of welding without phase change [34,76].

CHAPTER III
EXPERIMENTAL PROCEDURES

III.1 Introduction

The aim of this work is to study the effects of welding on micro-alloyed steel pipe line with a low carbon content used by COSIDER company (Biskra). The different characterization techniques are used like: Optical microscope and scanning electron microscope to discover the different microstructures, X-rays diffraction to study the phases, the size and grain orientations, the density of dislocations and many things. The mechanical behavior are also studied by specific X-rays diffraction for the measurements of the residual stress, the last apparatus is the microhardness tester for the hardness measurements.

The pipe is normal API 5L pipes made from grade X70 strips used by COSIDER company of Biskra. X70 pipeline steel with single-V preparation joint was welded by arc welding (Fig.III.1). The chemical composition of this pipeline steel is given in table III.1:



Figure.III.1: X70 pipeline steel after industrial arc welding.

Table III.1: Chemical composition of pipeline steel (wt %).

C	Si	Mn	P	S	Cr	Ni	Cu	Al	N	Mo
0.064	0.2047	1.573	0.0154	0.0015	0.0553	0.1922	0.0291	0.0319	0.007	0.1353

The microstructure of this base metal is presented in figure III.2. This material is composed of ferrite (85%) with bands of pearlite (15%).

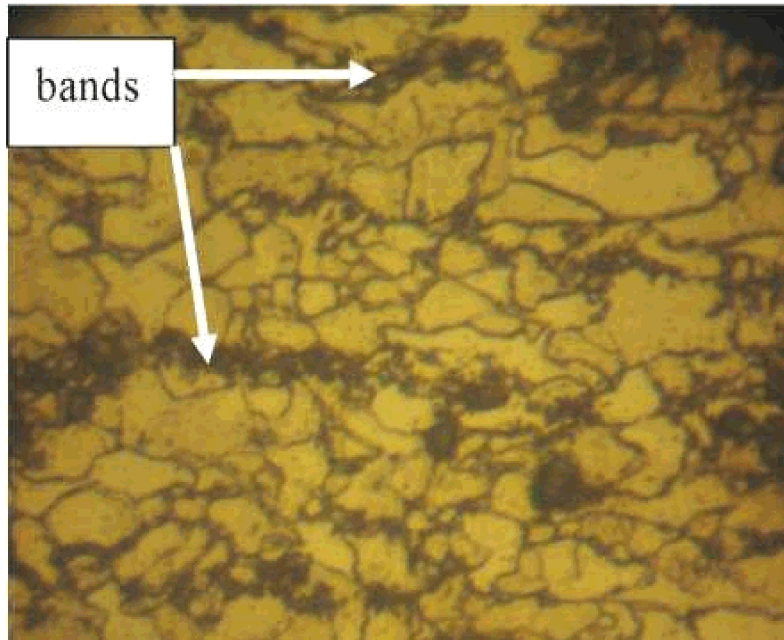


Figure. III.2: Microstructure of X70 pipeline steel.

The welds were deposited using steel electrodes by the shielded metal arc welding process. The chemical composition of the weld metal is presented in table III.2.

Table III.2: Chemical composition of electrode 1 (wt %).

C	Si	Mn	P	S	Cr	Ni	Cu	V	Mo
0.05	0.32	0.87	0.013	0.006	0.03	0.71	0.039	0.01	0.01

III.2 Samples preparation



Figure. III.3 : Steps of the weld joint preparation.

Sample was carried out on the pipe just after welding. All the samples were cut normal to the welding direction. (30*20 cm) (Fig. III.4). This figure presents the weld seam.



Figure III.4: Sample (30x20 cm) of the welded pipe line.

Second step: the first sample was cut into several pieces (2.5cm) long with an electric saw, pouring water to avoid overheating and structural change in the sample (Figure. III.5).



Figure III.5: Different samples of X70 steel after welding.

III.3 Heat treatments

We note that some heat treatments have been applied. The samples were isothermal annealed at 200,400 and 600°C for 10 mn, 30 mn and 1 h and followed by air cooling.

III.4 Microstructural observations

III.4.1 Metallography

Most of the microstructural observations were carried out on the ND-TD surfaces of the pipe segments unless otherwise stated. The surfaces were ground starting with 240-grit silicon carbide grinding paper and finishing with 4000-grit, and then polished with diamond paste of 9 μm ,6 μm and 0,4 μm grade. Some as-polished samples for optical microscopy, scanning electron microscopy and X-ray diffractometry were then etched with 4 % nital (4ml nitric acid with 96ml methanol). The optical microscope used is a Hand Wetzlar T100 optical microscope, each fitted with a digital camera (Figure III.6).



Figure III.6 : Optical microscope HUND T100-WETZLAR.

III.4.2 Scanning electron microscopy

Besides ordinary imaging by scanning electron microscopy, energy dispersive X-ray (EDX) analysis is also used.

Figure III.7 presents the analysis by EDAX of this steel which indicates the high quantity of Mn.

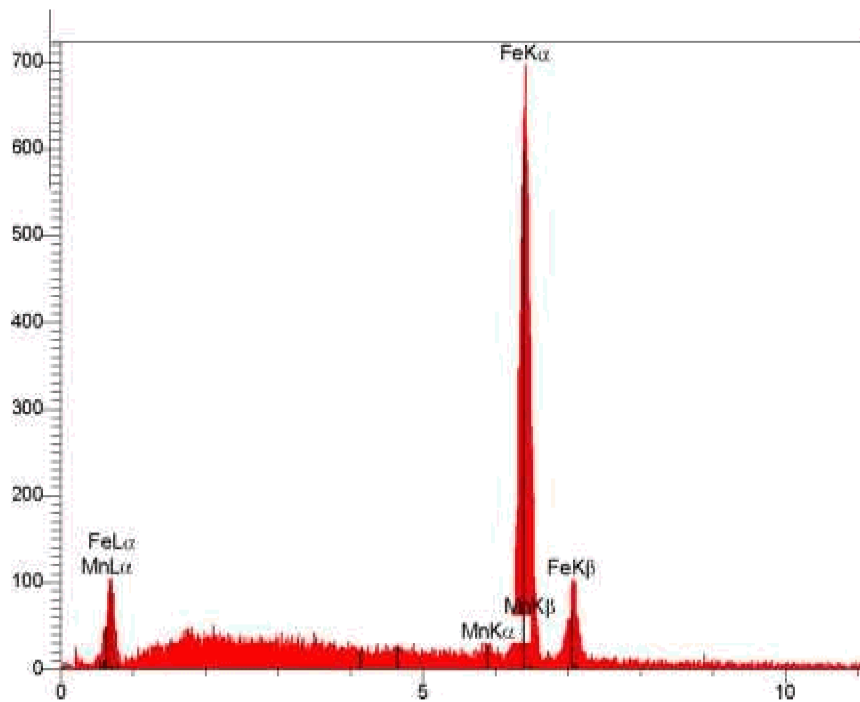


Figure III.7 : Spectrum of EDAX analysis of X70 pipeline steel.

III.5 X-ray diffraction

X-ray diffraction is a tool for the investigation of the structure of matter. This technique had its beginnings in von Laue's discovery in 1912 that crystals diffract X-rays, X-rays are electromagnetic radiation of wave length about 1 Å, which is about the same size as an atom, the manner of the diffraction revealing the structure of the crystal. At first, X-ray diffraction was used only for the determination of crystal structure. Later on, however, other uses were developed, and today the method is applied, not only to structure determination, but to such diverse problems as chemical analysis and stress measurement, to the study of phase equilibria and the measurement of particle size, to the determination of the orientation of one crystal or the ensemble of orientations in a polycrystalline aggregate. Using X-ray diffraction it is also possible to determine the size and shape of the unit cell for any compound [13, 87].

The unit cell is a very useful concept and we use it not only to characterize the symmetry of a crystal, but also to specify crystallographic directions and even interatomic distances. To describe directions and distances, we imagine planes, with various orientations. Since the imaginary planes, characterized by Miller indices, are defined in terms of the lengths of the unit cell edges, then the perpendicular distances between the planes in any family are characteristic of the unit cell size and hence, the crystal structure.

The distances (d_{hkl}) between these planes are on the same order as the distances between atoms. This distance can be measured by the Bragg's Law. It should also be noted that Miller indices defining a plane are usually written in parenthesis, as (h k l), while crystallographic directions which are the normal to any plane, are written in square brackets as [h k l] [87, 88]. The Bragg law may be written in the form:

The diffraction angle 2θ determined from the measured position of the diffraction peak, was used to derive the lattice spacing d , using Bragg's Law:

$$\lambda = 2d \sin\theta \dots \dots \dots \text{(Equ III.1)}$$

Where θ is the Bragg's angle, λ is the wave length of the used radiation and d is the d_{hkl} or distances between planes.

For measured the crystallite size we use the scherrer formula :

$$D_{\text{mean}} = A \cdot \lambda_{\text{Cu}} / \text{FWHM} \cdot \cos\theta_{\text{Bragg}} \dots \dots \dots \text{(Equ III.2)}$$

Where $0,8 \leq A \leq 1,2$ a corrector factor , it depends with the form of the diffracted coherent domains. FWHM is the full width at half maximum.

Figure III.8 illustrates a Bruker D8 advance X-ray diffraction goniometer with Cu Ka = 1.5406 Å radiation was used for continuous scanning with scan step time of 12.5 s at a step size of $2\theta = 0.02^\circ$ on the weld junction. In our study, each zone has been investigated; the base metal adjacent to the weld junction was removed .

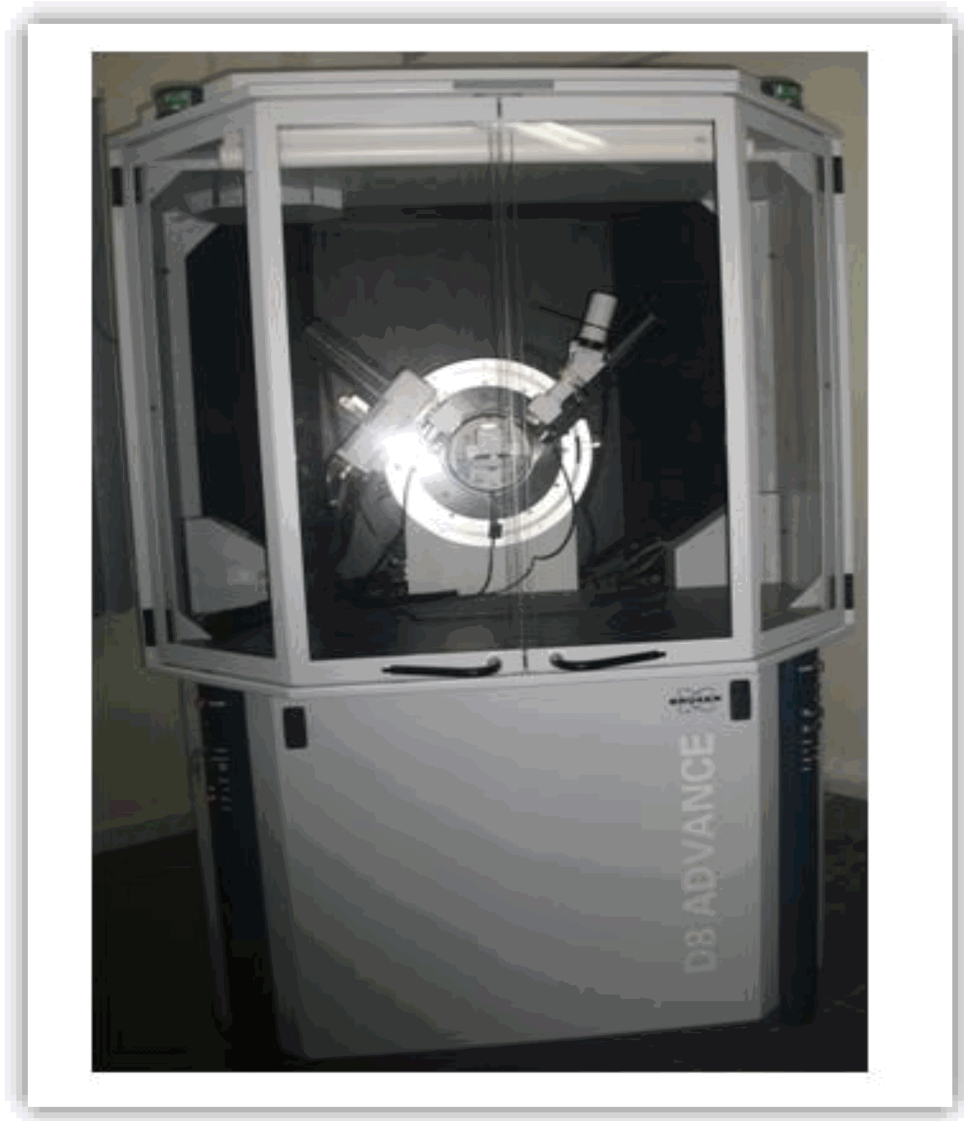


Figure III.8: *Diffractomètre BRUKER D8 ADVANCE AXS (XRD).*

III.5 Mechanical tests

III.5.1 Microhardness

Hardness testing is a quick method of characterizing the overall effect of tempering and provides valuable information of overall changes. The tests were carried out using a Vickers hardness testing machine, using a 2 kg load. The test was developed in 1924 by Smith and Sandland at Vickers Ltd as an alternative to the Brinell method. The Vickers micro-hardness test is convenient since the measurement is independent of the size of the indenter, which can be used for all materials irrespective of hardness [13]. Microhardness measurements were carried out across the welds on the as-etched ND-TD surfaces of the as-welded samples and after post-welding heat treatment, using a Mitutoyo microhardness tester with a load of 200 gf and dwell time of 15 s.

This apparatus is equipped by binoculars (15x) and objectives (10x, 40x) for the positioning of the fingerprint and placement the lines for measuring the diagonals (D_1 and D_2). The hardness values are measured automatically with the formula as following by this apparatus.

$$H_v = F/S \dots\dots\dots \text{(Equ III.3)}$$

Where F is the applied charge by Kg load, S is the area of the fingerprint, obtained by the measuring of the diagonal (D).

$$S = D^2/2 \cdot \cos 22^\circ \dots\dots\dots \text{(Equ III.4)}$$

$$H_v = 1,8544F / D^2 \dots\dots\dots \text{(Equ III.5)}$$

Where $D = (D_1 + D_2)/2$, D_1 and D_2 are the two diagonals.

The table III.3 resumes the available charges.

Table III.3 : The available charges values		
<i>0,01</i>	<i>10 gf</i>	<i>0,098 N</i>
<i>0,025</i>	<i>25 gf</i>	<i>0,245 N</i>
<i>0,05</i>	<i>50 gf</i>	<i>0,490 N</i>
<i>0,1</i>	<i>100 gf</i>	<i>0,980 N</i>
<i>0,2</i>	<i>200 gf</i>	<i>1,960 N</i>
<i>0,3</i>	<i>300 gf</i>	<i>2,940 N</i>
<i>0,5</i>	<i>500 gf</i>	<i>4,900 N</i>
<i>1</i>	<i>1000 gf</i>	<i>9,800 N</i>



Figure III.9: Digital Micro Vickers Hardness Tester(HVS-1000Z)

III.5.2 Residual stress tests

A wide variety of residual stress measurement techniques exist [90-96]. Some are destructive, while others can be used without significantly altering the component; some have excellent spatial resolution, whereas others are restricted to near surface stresses or to specific classes of material [80]. X-ray diffraction is a state of the art measurement method of residual stresses and its use is already well established in the research field but also industrially. XRD is the most widely used non destructive method. Non-destructive micromagnetic methods for the measurement of residual stress have been developed these last three decades. The principal is that when a metal is under stress, the resultant elastic strain cause the spacings of atomic planes in the metallic crystal structure to be changed. XRD can measure the interplanar atomic spacing, and from this quantity the stress can be evaluated [73, 97].

When internal stresses are exist in a material a systematic change of the lattice parameter in each grain is observed. The interplanar spacing is described by Bragg's law

The increase of interplanar spacing $d\{hkl\}$ causes a decrease of θ angle. In typical cases the shift of a peak is: $0,001^{\circ} - 0,1^{\circ}$. It seems to be a small value. The presence of internal stresses causes not only a shift of a diffraction peak ($\Delta(2\theta) = 2\theta - 2\theta^0$) but also a change of its intensity and width (this latter is expressed as FWHM(full width at half maximum)).

Figure III.10 shows the diffraction of free and deformed lattice [6].

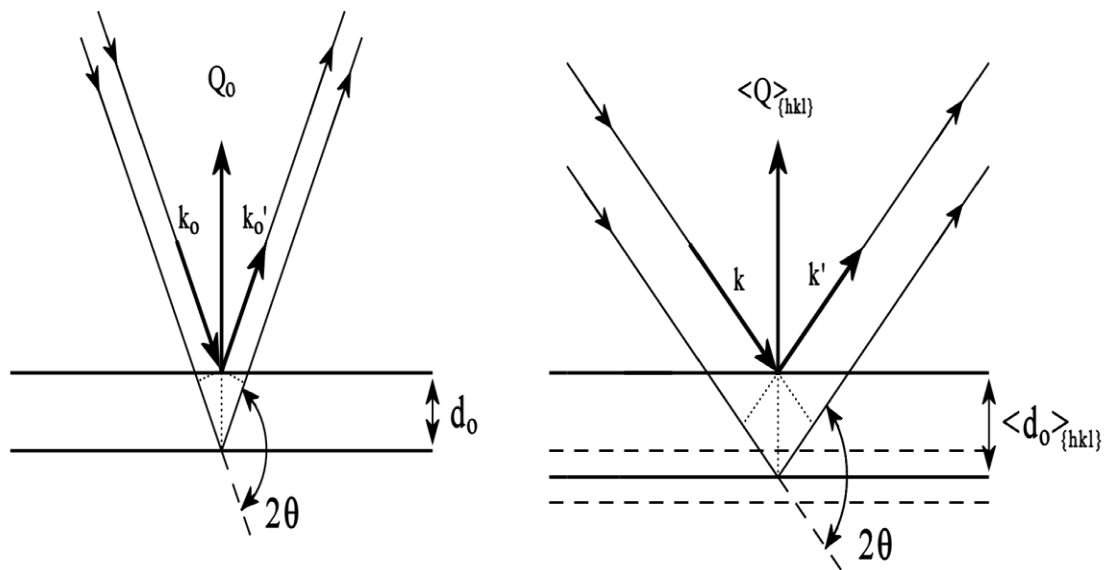


Figure. III.10 : Diffraction on a stress free lattice (a) and on a deformed lattice (b). A range of interplanar spacings in different diffracting crystallites is shown by dashed lines, while the continuous line is used to mark the average distance between reflecting planes [7].

X-ray stress measurements were carried out by SET-X equipment (Figure III.11). A general view of this apparatus is shown on figure III.12. Cr-K α radiation and (211) reflections were used to study residual stress distribution in weld region. Stress measurements were made in the longitudinal and transversal directions (parallel and perpendicular to the weld joint, respectively). In order to remove residual stresses introduced by machining, an electro-polishing technique has been applied.



Figure III.11: General view of the X-ray apparatus.

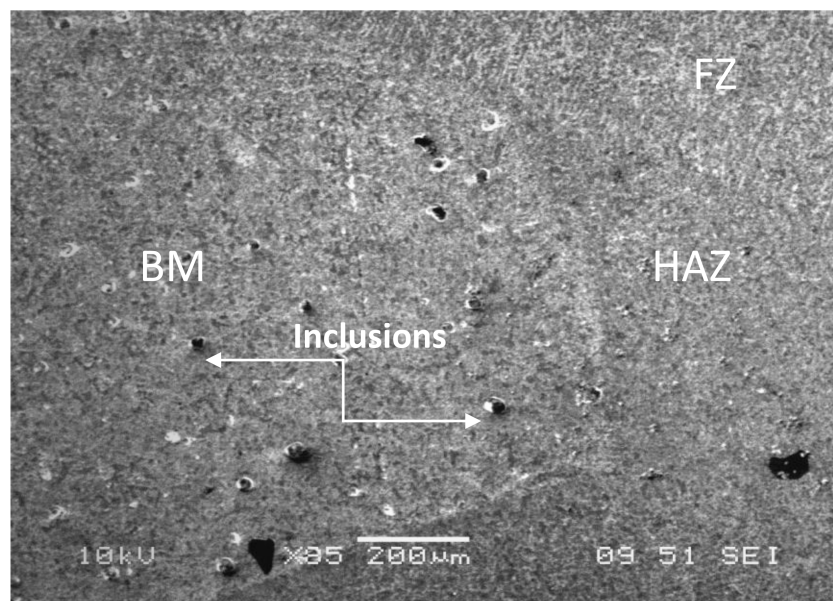
CHAPTER IV
RESULTS AND DISCUSSIONS

IV.1 Introduction

During welding, the interaction of the heat source and the material leads to rapid heating, melting and the formation of the weld pool. In the weld pool, the molten metal undergoes strong recirculation and the flow of liquid metal significantly affects the temperature fields, thermal cycles and the weld pool geometry. When the highly localized transient heat created by a moving heat source and strongly non linear temperature fields in both heating and cooling processes cause nonuniform thermal expansion and contraction. The temperature changes in welding, for the most part, are not a favorable treatment for steels, This change can give different zones in the weld joint which are the base metal(BM), the heat affected zone(HAZ) and the fusion zone(FZ). These zones have different microstructural and mechanical characteristics. The aim of this work is to improve these characteristics, for this reason we have done some heat treatments. Our results are shown in this chapter.

IV.2 Structural characterization by the optical microscope (OM) and the scanning electron microscope (SEM)

The microstructure was observed using light optical microscopy after Nital etching. SEM observations were also carried out to obtain images at higher magnifications. Figure IV.1 shows The SEM micrograph of the obtained zones in welded joint, which are the base metal(BM),the heat affected zone(HAZ) and the fusion zone(FZ) with some inclusions.



FigureIV.1: SEM micrograph of the welded joint.

IV.2.1 The effect of heat treatment temperature (time = 10 min , 30 min and 1 h)

IV.2.1.1 The micrograph of the base metal

The microstructure of the base metal consists of ferrite phase (white by Optical Microscope(OM) and dark by the Scanning Electron Microscope(SEM)) with rare pearlite colonies(contrariwise the ferrite phase, the pearlite is dark by OM and white by SEM) observed at some grain boundaries , Some elongated ferrite entities that are relatively dark in SEM images were found all over the observed region (Figures IV.2.a,b). The base matrix consists of ferritic grains because our steel contains a low amount of carbon. The obtained microstructures after heat treatments at different temperatures (200°C, 400°C and 600°C) for 10 min, 30 min and 1 h, are illustrated in the Figures IV.3-5. Similar result is obtained by Chung et al [98] with a low carbon steel (X65) and they confirmed that the microstructure of the base metal consisted of predominantly polygonal ferrite (white) and pearlite (black). After heat treatment for 10 min the grains are much finer (FG) than those of the untreated sample (Figure IV.3). Concerning this Short heat treatment we can deduce that there is considerable change in the grain size and shape (Figure IV.3.e and f).

The grains became smaller than the untreated sample at 200°C for 30 min (FiguresIV.4.a,b), whereas we obtained coarse ferrite grains (CG) at 400°C and 600°C after the same heat treatment time (FiguresIV.4.e,f), it is clear that this heat treatment induces a high mobility of grain boundaries and new nucleation of small grains. We found a slight growth in of the grain size after the heat treatment for 1h, excepting for the temperature 400°C (FiguresIV.5.c,d) there is a reduction in the grain size .

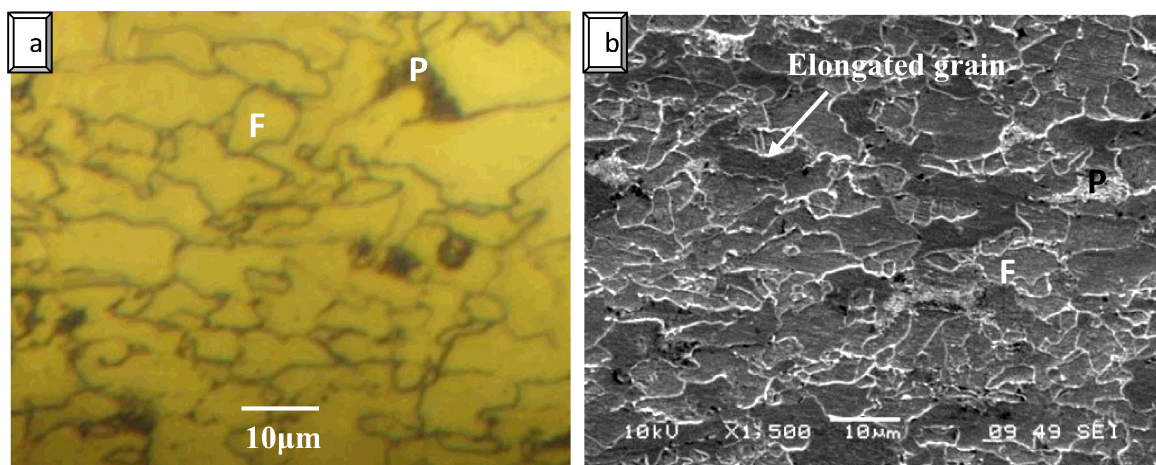


Figure IV.2: Optical and SEM micrographs of the untreated base metal.

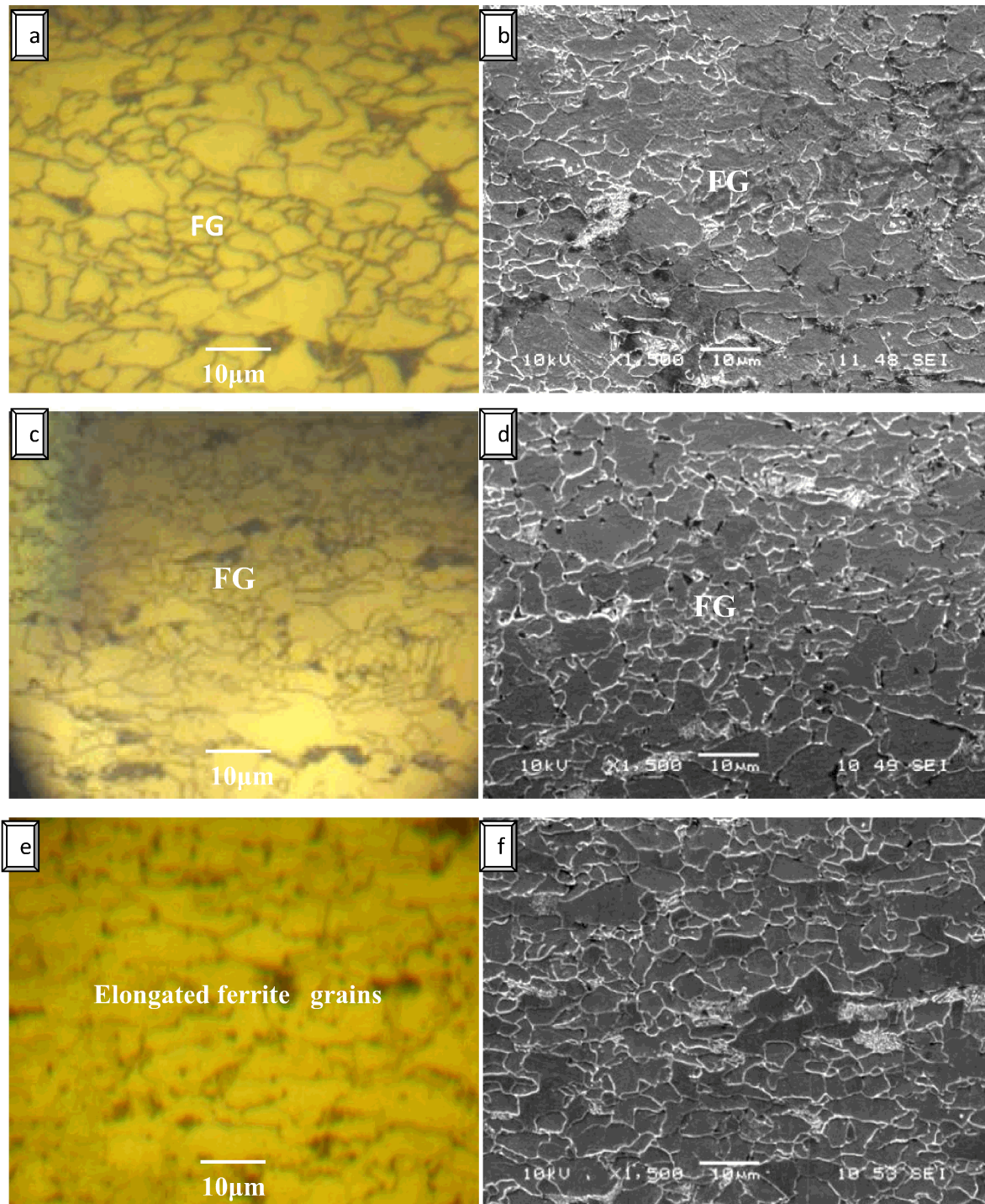


Figure IV.3: Optical and SEM micrographs of the heat treated base metal for 10 min: (a,b) At 200°C, (c,d) At 400°C and (e,f) At 600°C.

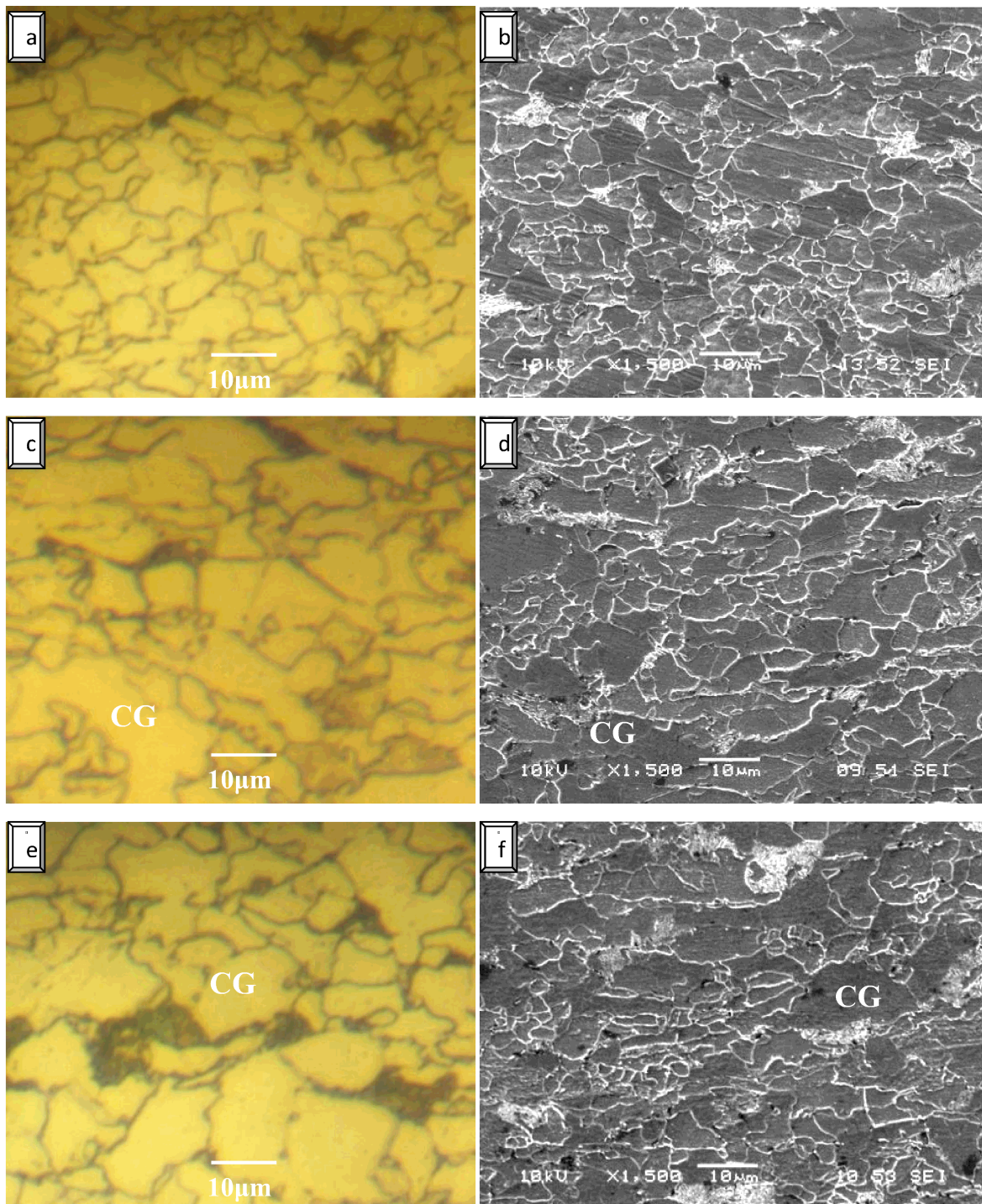


Figure IV.4: Optical and SEM micrographs of the heat treated base metal for 30 min: (a,b) At 200°C, (c,d) At 400°C and (e,f) At 600°C.

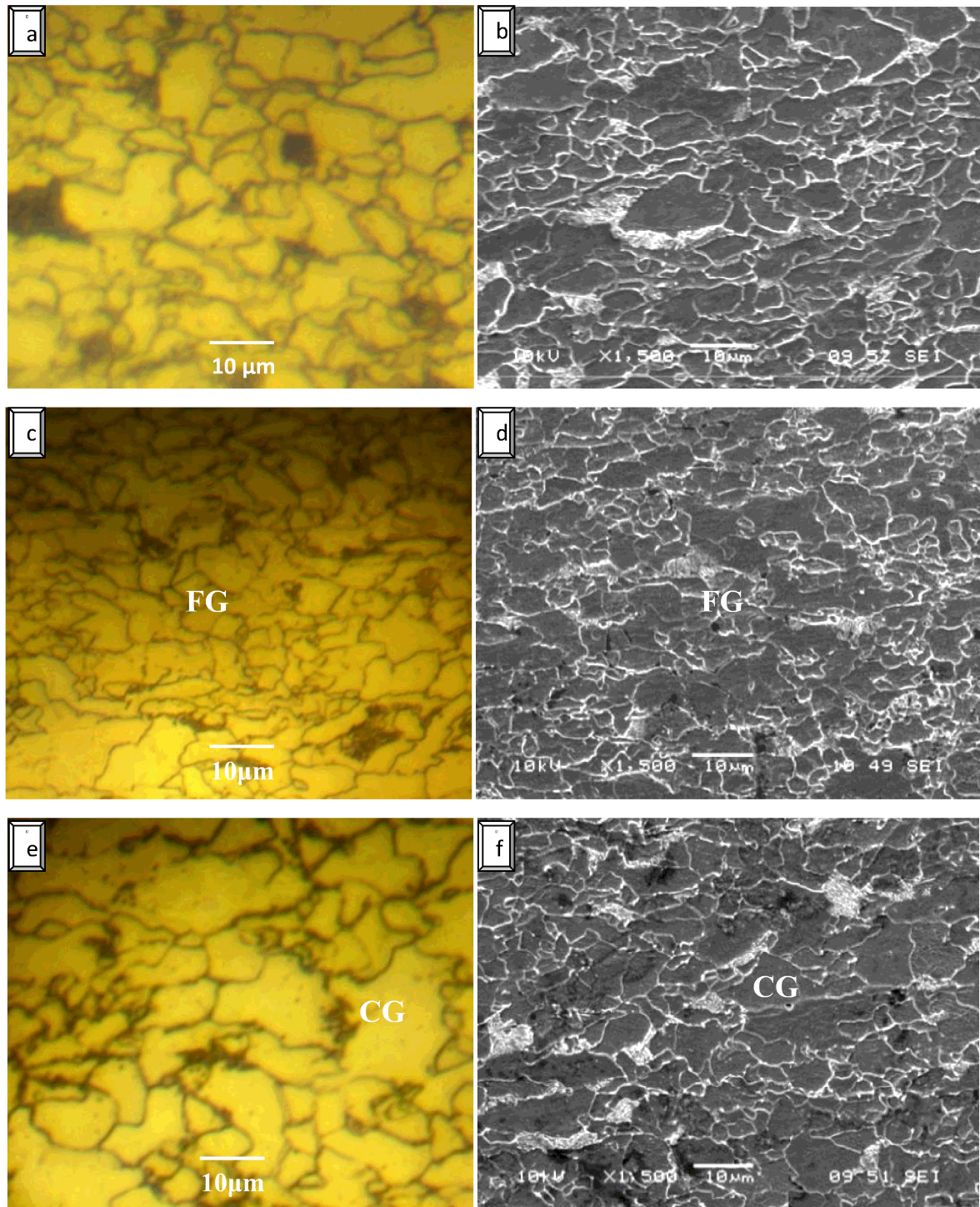


Figure IV.5: Optical and SEM micrographs of the heat treated base metal for 1h : (a,b) At 200°C, (c,d) At 400°C and (e,f) At 600°C.

IV.2.1.2 The micrograph of the heat affected zone (HAZ)

The HAZ has a composition which is essentially the same as the base metal and is identifiable region because of the structural changes induced by the weld thermal cycle, for example the reheat of this region has effect of refining the microstructure [99,100]. The HAZ is important because of its potential to develop structures which adversely affect the properties of the joint [99]. The microstructure of HAZ is determined by the welding condition, prior thermal and mechanical history and more importantly the chemical composition of the material [3, 99].

The HAZ can be divided into number of sub-regions. Each sub-region has its own distinct microstructure, a unique thermal cycle associated with it, and therefore possesses its own mechanical properties [99,101].

Jan.Bog.Jua et al [65] confirmed that HAZ region experiences three or four welding thermal cycles during multi-pass welding process. Among the cycles, the first and second cycles may seriously change the microstructure of the region, whereas the effects of third and fourth cycles on the microstructure are very limited due to their low peak temperature. The HAZ microstructures exposed to the first thermal cycle are typically categorized into four groups based on the peak temperature (TP1): Coarse-grained HAZ (CGHAZ: $TP1 > 1100^{\circ}\text{C}$), fine-grained HAZ (FGHAZ: $1100^{\circ}\text{C} > TP1 > AC3$), inter-critical HAZ (ICHAZ: $AC3 > TP1 > AC1$), and subcritical HAZ (SCHAZ: $AC1 > TP1 > 450^{\circ}\text{C}$).

Grain coarsening in the HAZ can be explained by the operating thermal cycle and diffusion. It can be contributed to grain coarsening is grain boundary mobility and fusion. Grain boundary movement depends on diffusion and atomic migration on both sides of grain boundary. Diffusion itself is a function of retention time at high temperature and leads to the migration of atoms and displacement of grain boundaries [3]. And formation of fine ferrite grains in dynamic transformation can be attributed to the high nucleation rate of ferrite and the other is the random distribution of ferrite grain orientations, as also suggested by other workers in the case of low carbon steels [102].

The microstructure of the junction zone between the fusion zone (FZ) and the heat affected zone (HAZ) is showed in the figure IV.6, it presents a large coarse grained heat affected zone (CGHAZ), which is near of the fusion zone. It consists of equiaxed ferrite grains and the pearlite is distributed unevenly in small quantities among the ferrite grains. However the fusion zone shows a microstructure rich by the pearlite phase than the CGHAZ, it contains predominantly fine-grained ferrite (FG) with some elongated ferrite entities.

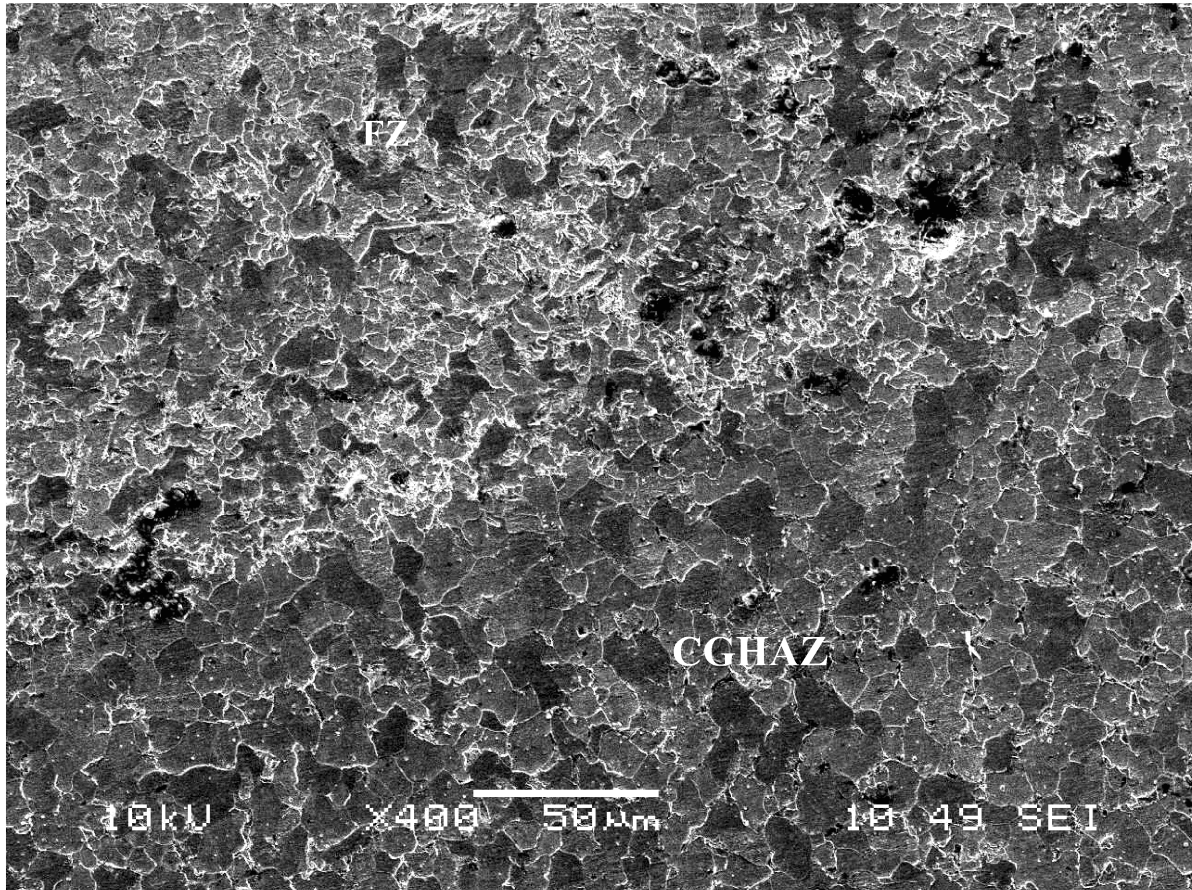


Figure IV.6: SEM micrograph of the junction zone between heat affected zone (HAZ) and fusion zone of the untreated sample.

The figure IV.7 presents the junction zone between the fusion zone and the heat affected zone, it shows two different regions, one from them is rich in pearlite phase, which is the fusion zone, however the second region is poor in that phase, this region is the heat affected zone. The heat treatment at 200°C for 10 min caused the decrease in the grain size in all HAZ and FZ microstructures; we can observe also that these later became more homogenous. Concerning this short heat treatment we can deduce that there is considerable change in the grain size.

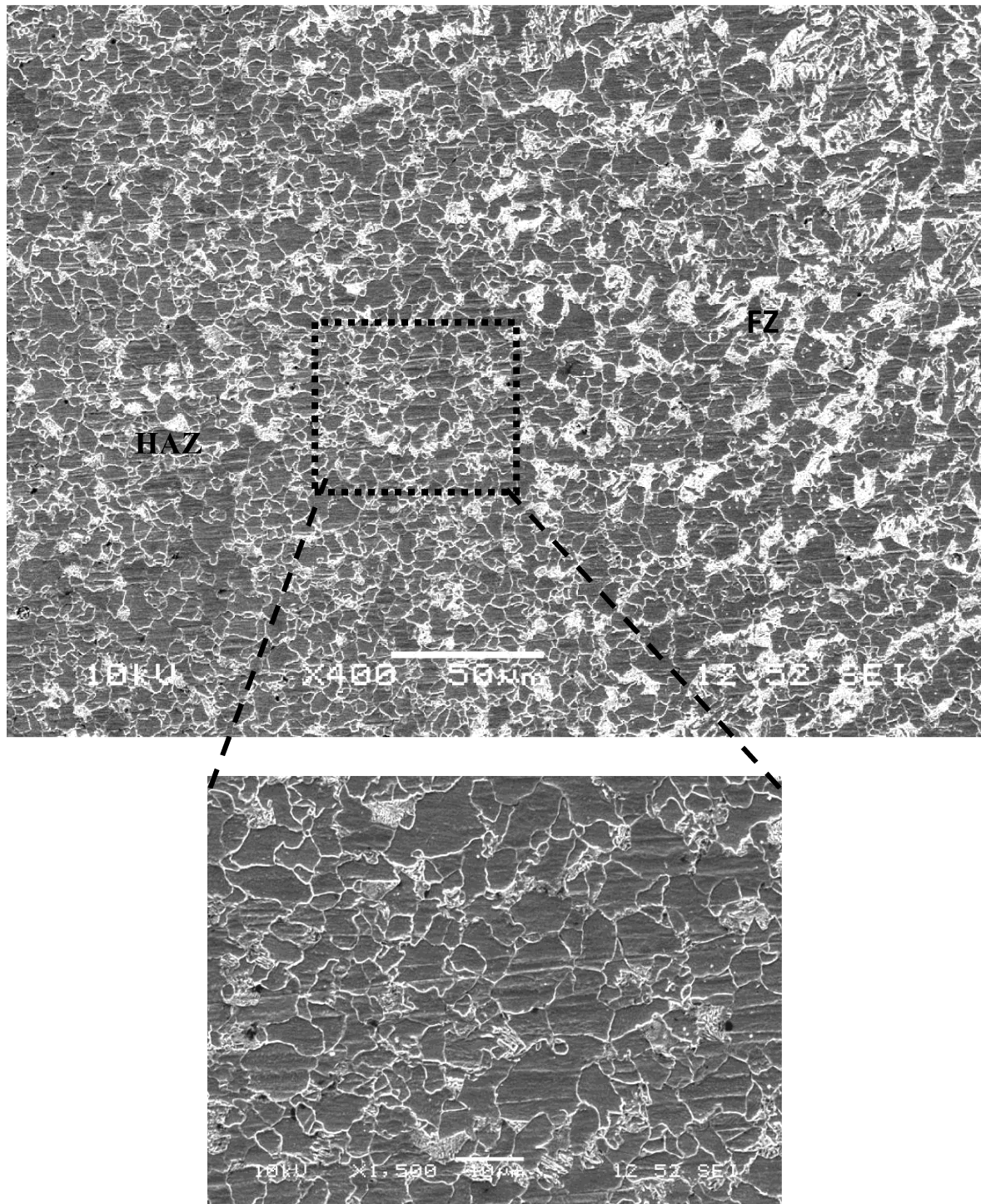
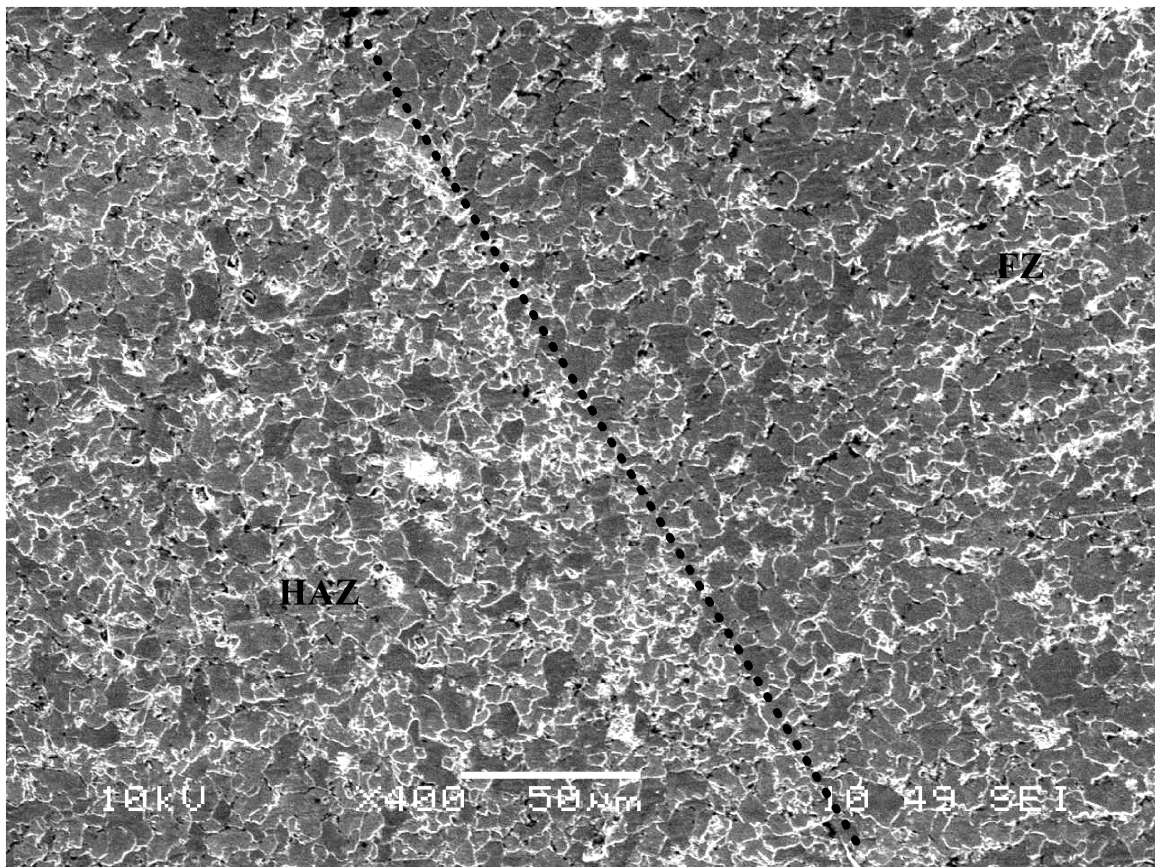


Figure IV.7: SEM micrograph of the junction zone between heat affected zone (HAZ) and fusion zone after heat treatment at 200°C for 10 min.

The junction zone between the fusion zone and the heat affected zone after heat treatment at 400°C for 10 min is presented in the figure IV.8. In general, it contains two different regions which are the fusion zone and the heat affected zone. The fusion zone consists of equi-axed ferrite grains and pearlite, the fusion region became more homogenous after this short heat treatment, however the HAZ presents a microstructure of fine and coarse ferrite grains with few amount of pearlite (P), it can be explained by the dual sized of the HAZ [103].



FigureIV.8: SEM micrograph of the junction zone between heat affected zone(HAZ) and fusion zone after heat treatment at 400°C for 10 min.

The figure IV.9 illustrates two different zones, the fusion zone with fine ferrite grains with lot of pearlite colonies. The second zone is the heat affected zone, it contains coarse with fine ferrite grains. We can said that after the heat treatment at 600°C for 10 min, fusion zone became more homogenous.

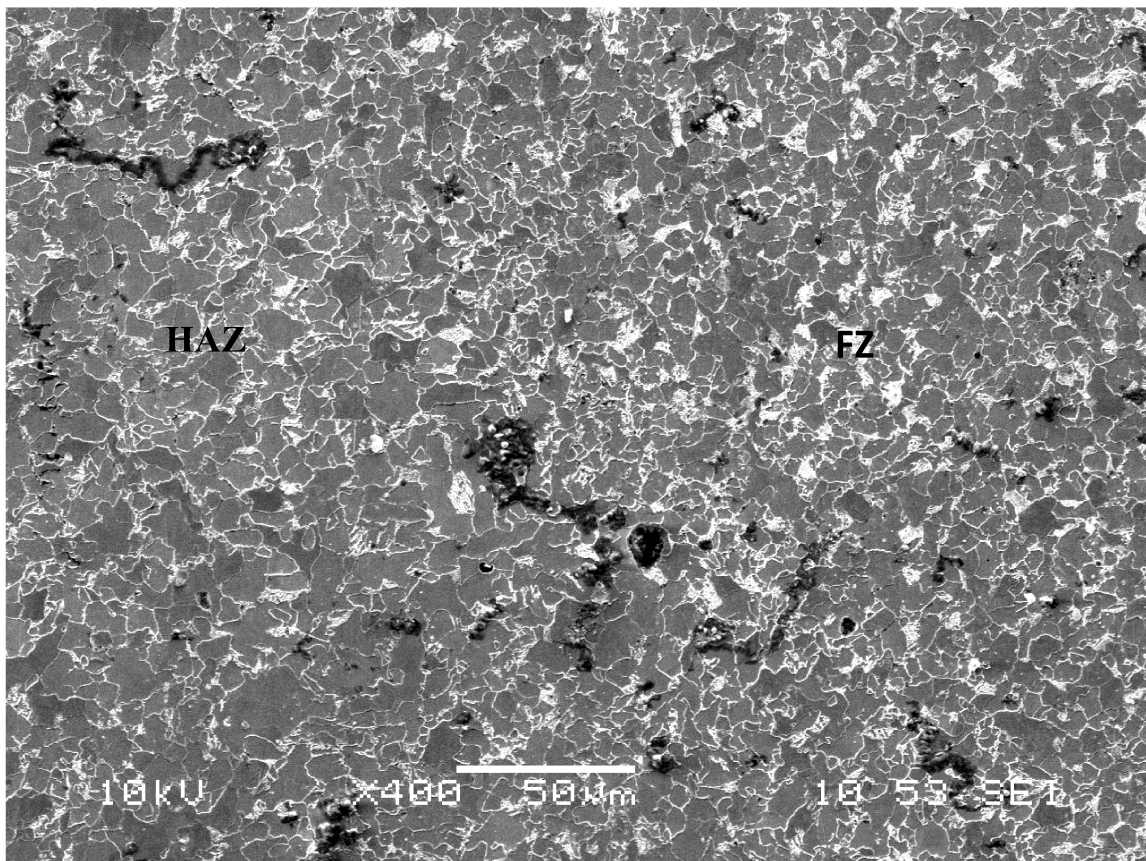


Figure IV.9: SEM micrograph of the junction zone between heat affected zone (HAZ) and fusion zone after heat treatment at 600°C for 10 min.

The figures IV.10, IV.11 and IV.12 present the microstructures of the junction zone between the fusion zone and the heat affected zone after different heat treatments: 200°C, 400°C and 600°C respectively for 30 min. After the first one the grains in all zones became much smaller and the microstructures of the FZ and HAZ were more homogenous. Concerning this heat treatment there is a considerable change in the grain size; we can deduce that there is a recrystallization of the microstructure.

The micrograph after the second heat treatment shows distinct and heterogeneous sub-zones in the heat affected zone, large CGHAZ is composed by equi-axed ferrite grains, narrow FGHAZ, which consists of fine ferrite grains and third sub zone of the HAZ is the ICHAZ, which contains fine, coarse ferrite grains and some elongated entities. M. Eroglu et al [104] confirmed that the intercritical HAZ (ICHAZ) is generally discontinuous. We can conclude that this heat treatment does not affect really the initial grains size.

The third one causes a remarkable diminution in the grains size in the FZ and in the HAZ. The difference between the two regions is the pearlite phase fraction. This heat

treatment affected really the initial microstructures and caused the homogeneity between the HAZ and the FZ.

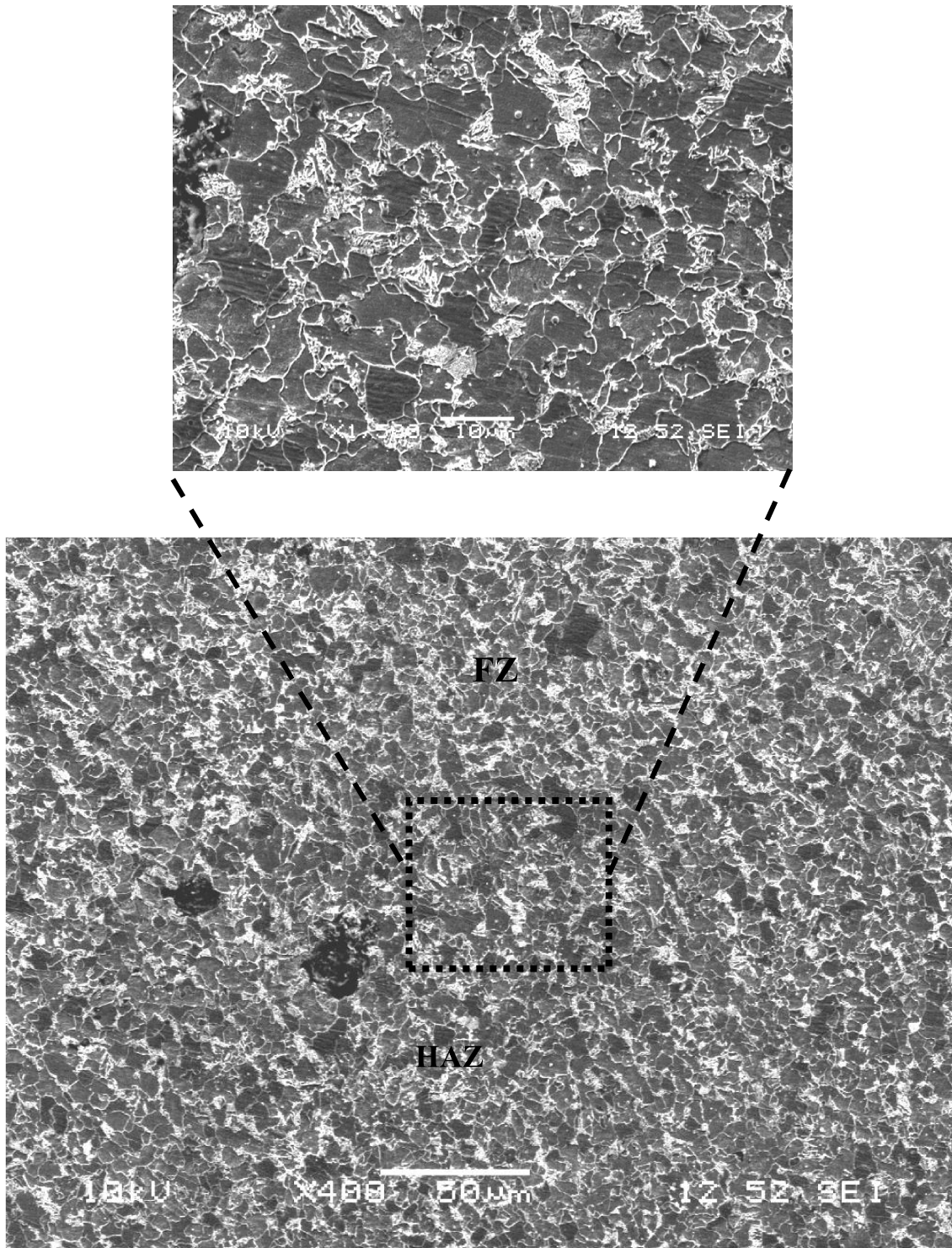


Figure IV.10: SEM micrograph of the junction zone between heat affected zone (HAZ) and fusion zone after heat treatment at 200°C for 30 min.

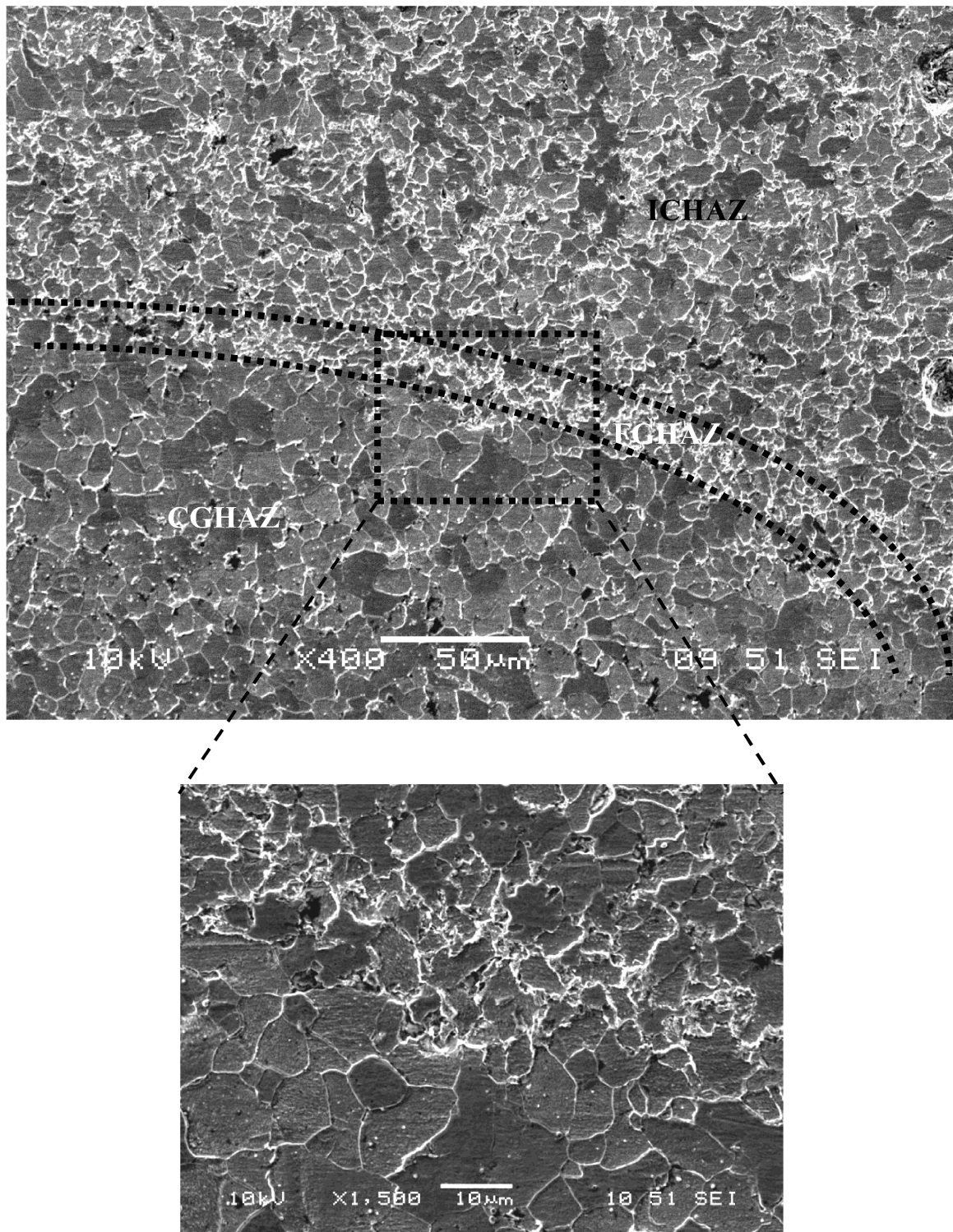


Figure IV.11: SEM micrograph of junction zone between the sub-zones of the heat affected zone (HAZ) after heat treatment at 400°C for 30 min.

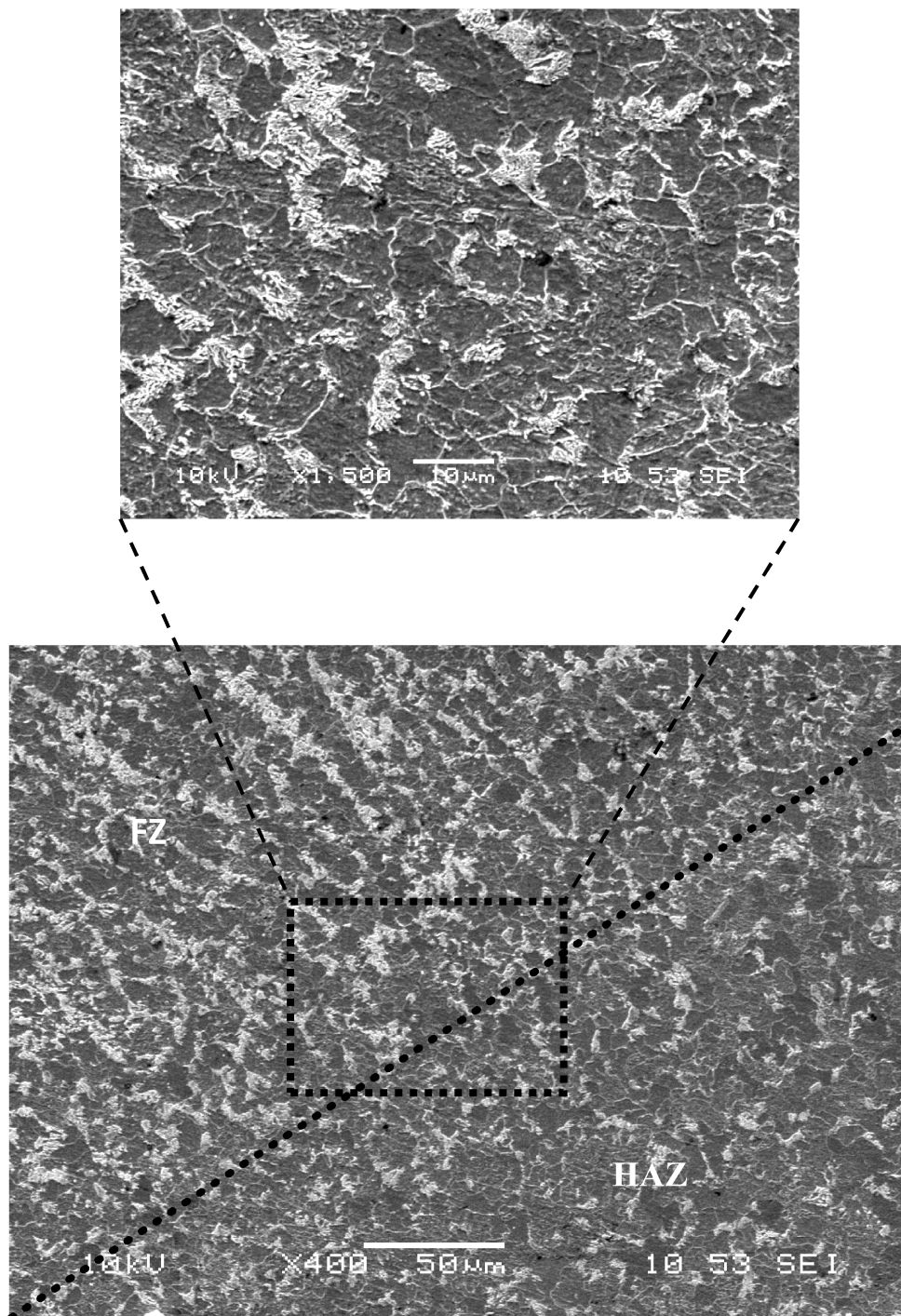


Figure IV.12: SEM micrograph of the junction zone between heat affected zone (HAZ) and fusion zone after heat treatment at 600°C for 30 min.

The microstructures of the junction zone between the fusion zone and the heat affected zone after heat treatments at 200°C, 400°C and 600°C for 1 h are illustrated in the figures IV.13, IV.14 And IV.15 respectively.

The figure IV.13 presents a microstructure of fine ferrite grains and pearlite in the fusion zone and a microstructure of the equi-axed ferrite grains with few amount of pearlite in all sub-zones of the heat affected zone. We observed also that microstructures of the HAZ became more homogenous with convergent grains size.

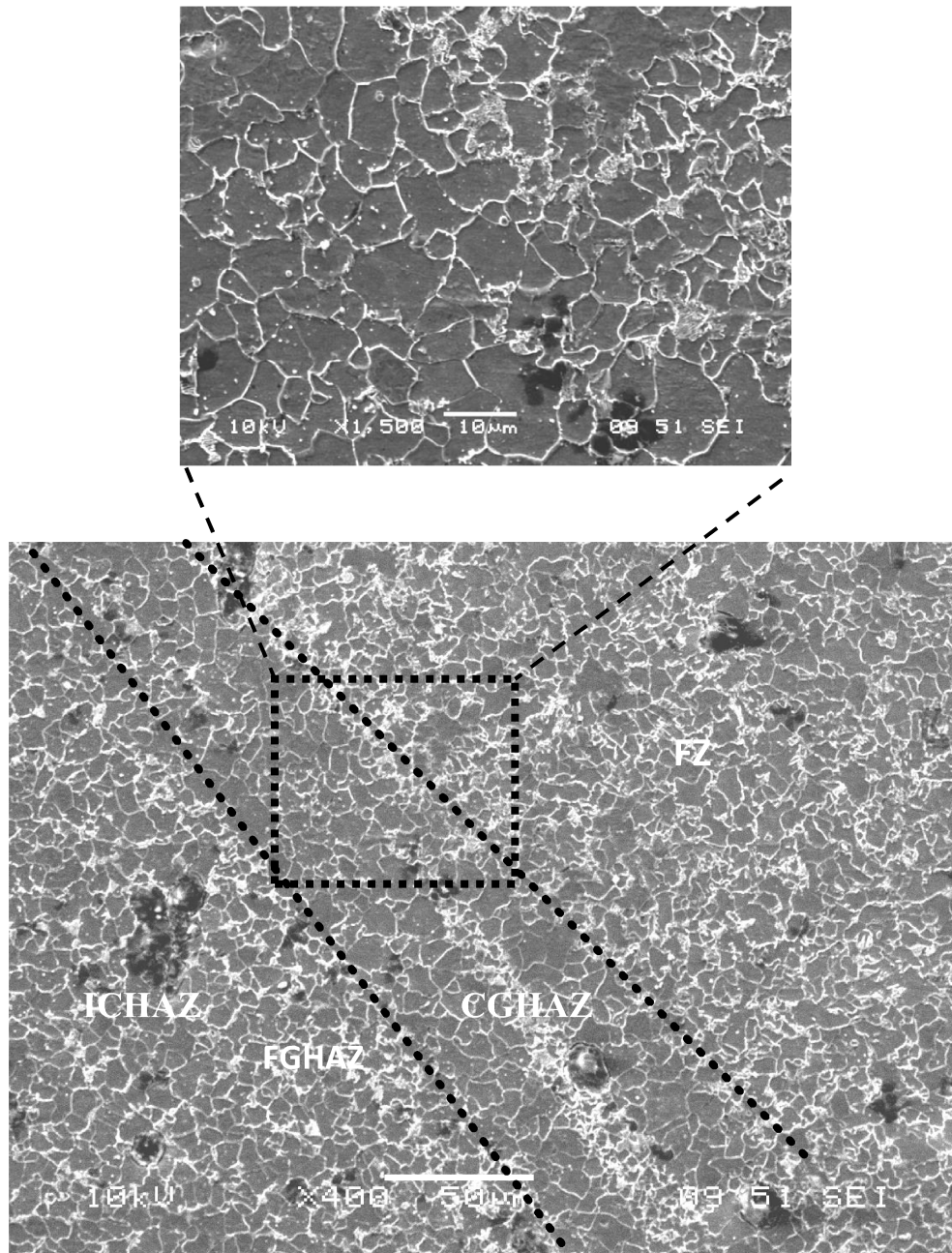


Figure IV.13: SEM micrograph of the junction zone between heat affected zone (HAZ) and fusion zone after heat treatment at 200°C for 1h.

The figure IV.14 shows a microstructure of equi-axed ferrite grains and little amount of pearlite in the CGHAZ, However the FGHAZ and ICHAZ are composed by fine ferrite grains and some coarse grains with convergent grains size. This heat treatment does not affect really the initial microstructures but we can observe a slight growth in of the grain size.

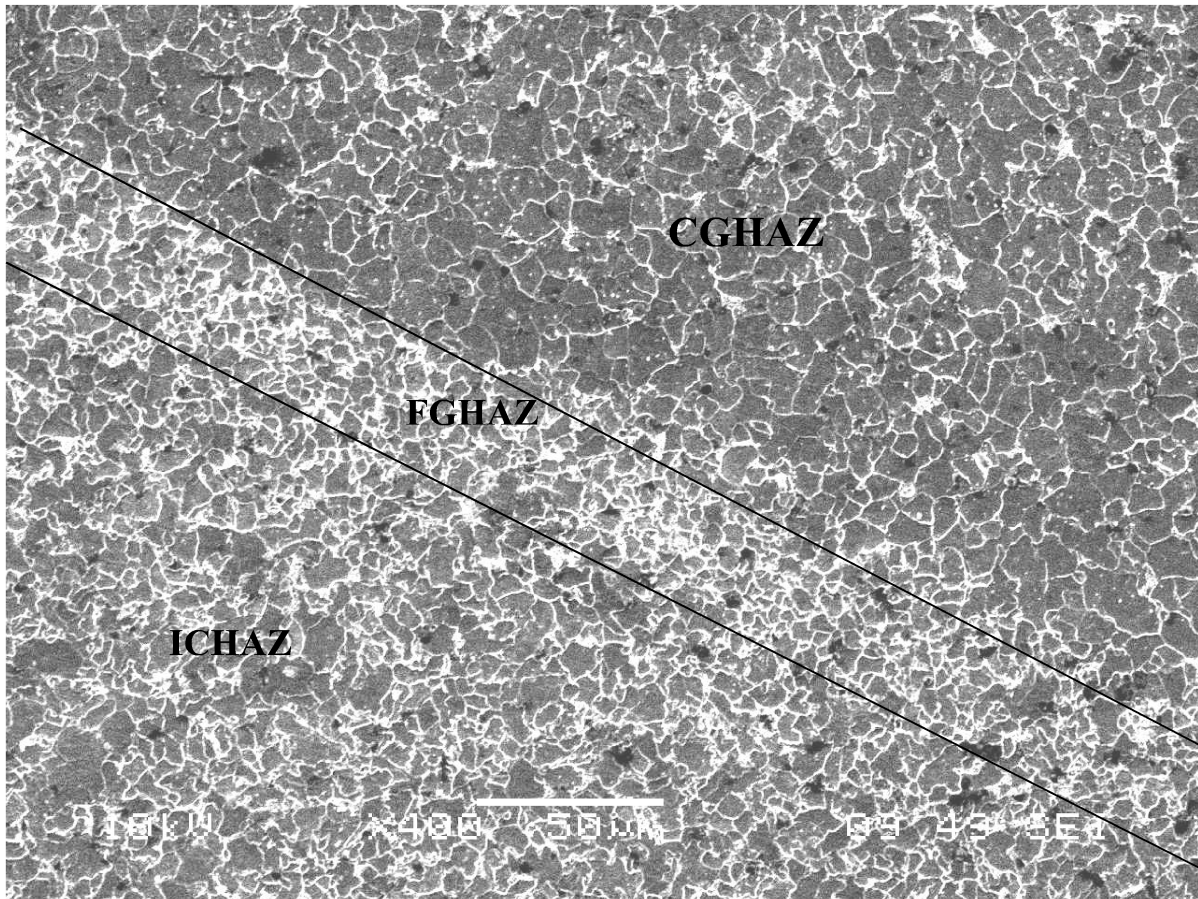
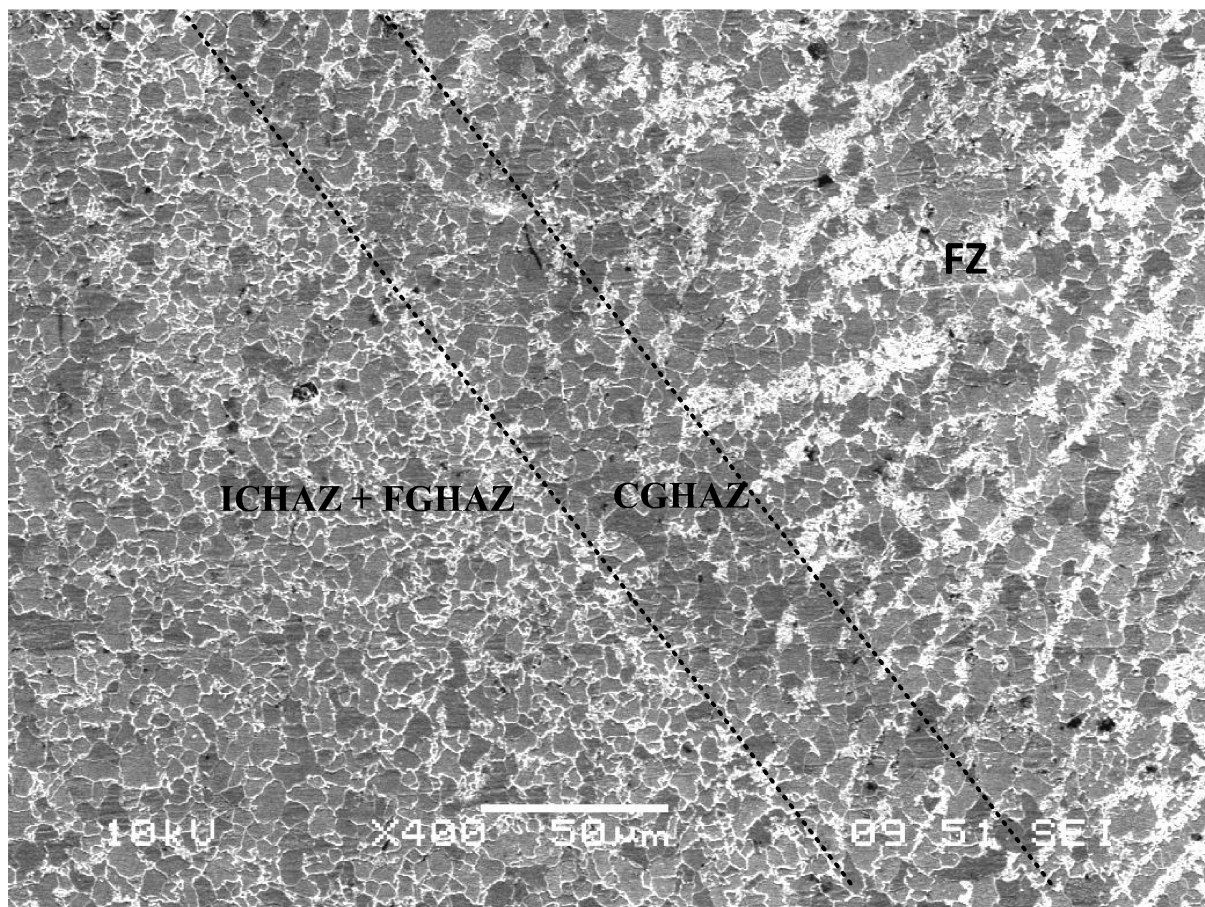


Figure IV.14: SEM micrograph of the junction zone between heat affected zone (HAZ) and fusion zone after heat treatment at 400°C for 1h.



FigureIV.15: SEM micrograph of the junction zone between heat affected zone(HAZ) and fusion zone after heat treatment at 600°C for 1h.

In the figure IV.15 the microstructures of fusion zone and heat affected zone after heat treatment at 600°C for 1 h. The CGHAZ and FZ are composed by fine equiaxed grains with high amount of pearlite in the FZ; we found that microstructures of FZ and CGHAZ are very homogenous. The microstructures of FGHAZ and ICHAZ consist of smaller ferrite grains. In general this heat treatment caused the decrease in grains size of the HAZ.

IV.2.1.3 The micrograph of the fusion zone (FZ)

The microstructures and mechanical properties of these regions determine the weldability of a material. Although the composition of the weld metal can be varied by the choice of filler metal and the extent of dilution [99].

The microstructure obtained as the weld cools from the liquid phase to ambient temperature is called the as-deposited or primary microstructure. It consists of allotriomorphic ferrite (α), Widmanstätten ferrite (WF), acicular ferrite (AF), and the so-called microphases [41,105], (See Figure.II.9,chapter II) . Allotriomorphic ferrite is sometimes called “polygonal” ferrite or “proeutectoid” ferrite, but polygonal simply means many sided (like all ferrite morphologies).

- **First pass**

It is noted that the center of the welded joint is the fusion zone. It has passed to the liquid state after execution of the welding. In the case of multipass welding, we saw several microstructures due to the successive passes. More microstructures appear at a first pass may change significantly by the following passes [3]. During a fusion welding process, the fast cooling rate of the weld pool causes an incomplete equilibrium state of the phase transformation process. The microstructure of the weld metal is an inhomogeneous casting structure, and the chemical composition is uneven as well [106].

The microstructures of the first pass are characterized ferrite phase (F) with rare pearlite colonies (P) observed at some grain boundaries, proeutectoid ferrite Pf(G) with few amount of Acicular ferrite(AF) and pearlite (Figures IV.16,IV.17, IV.18 and IV.19). There is an increase in the grain size after heat treatment at 200°C for 10 min (Figures IV.18.a and b) and at 400°C for 1 h (Figures IV.19.c and d) it is clear that these heat treatments induce a high mobility of grain boundaries. We obtained also a new phenomenon at 600°C heat treatment for 1 h which is the fragmentation of the lamellar cementite (In other term the degradation of Lamellar pearlite to fragment of Fe_3C) (Figures IV.19.e and f).The other heat treatments do not affect really the initial microstructure.

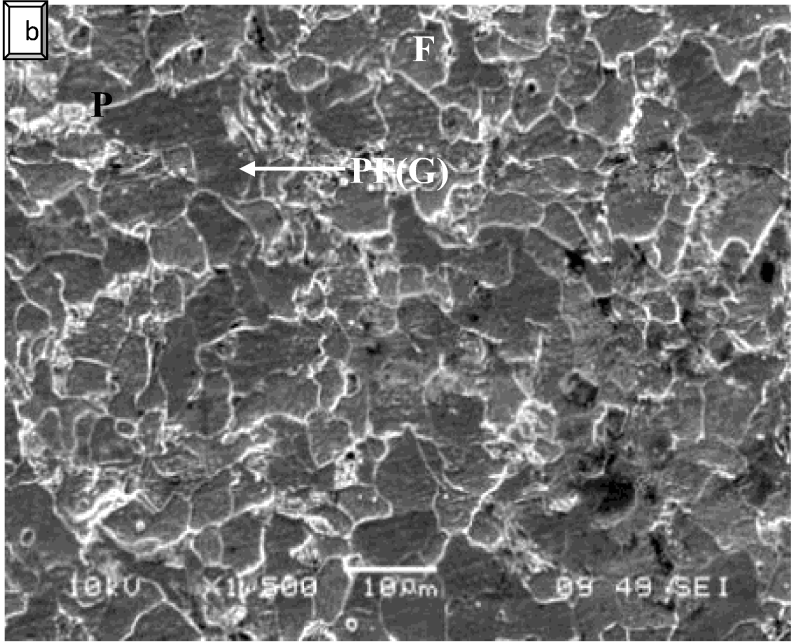
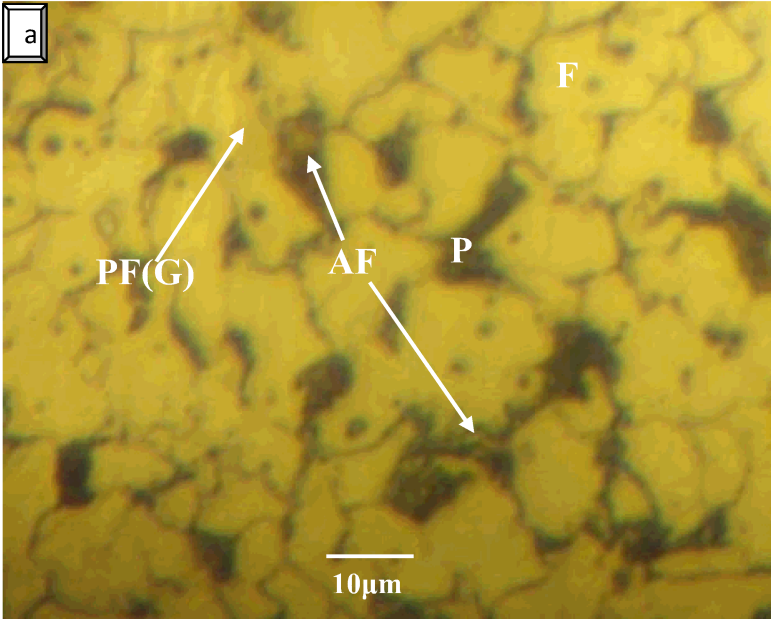


Figure IV.16: Optical and SEM micrographs of the untreated fusion zone (first pass).

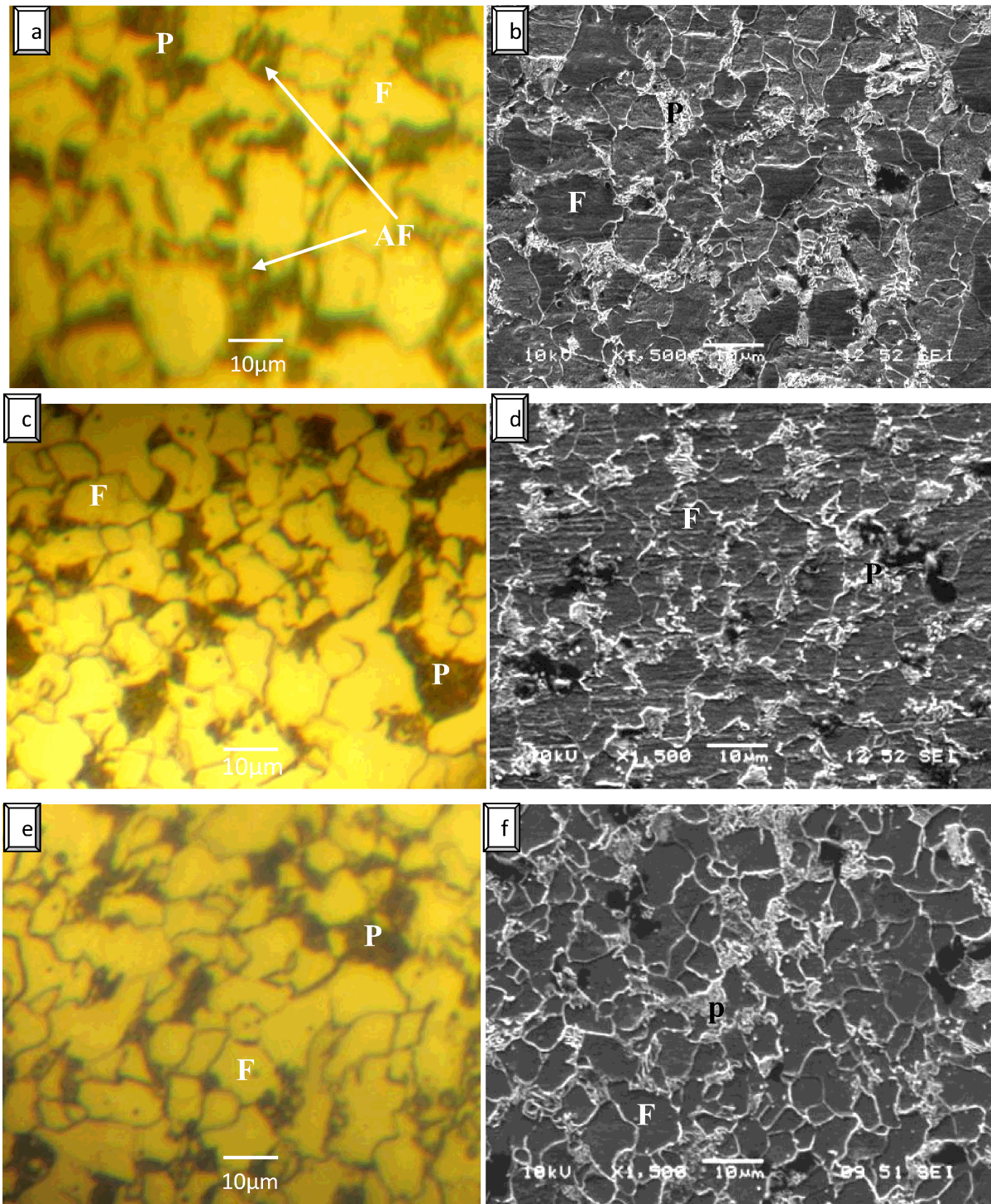


Figure IV.17: Optical and SEM micrographs of fusion zone (first pass) for 10 min: (a, b) heat treated at 200°C, (c, d) heat treated at 400°C and (e, f) heat treated at 600°C,

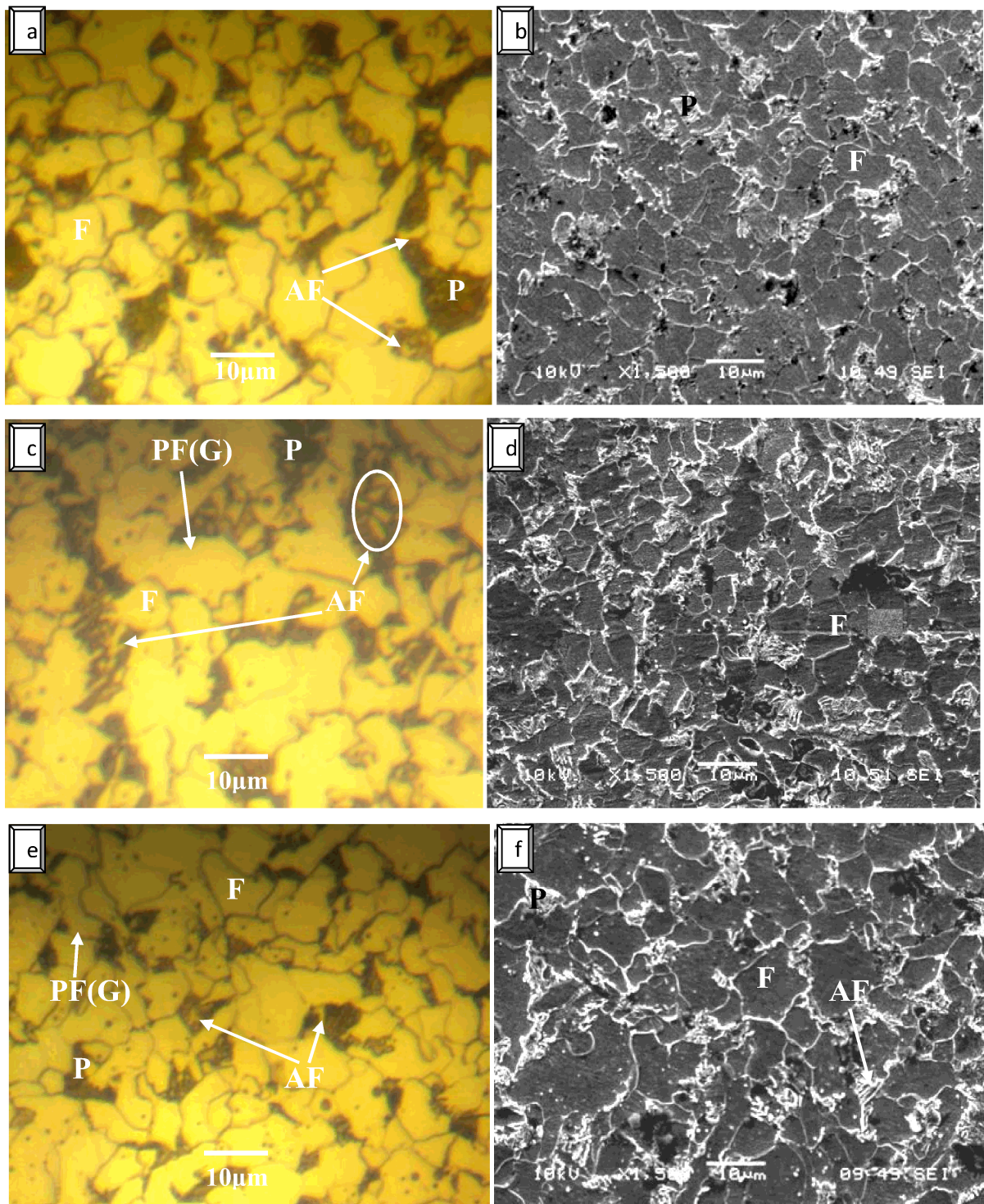
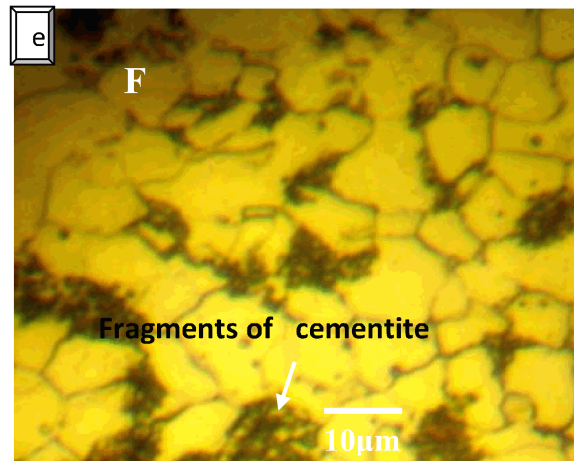
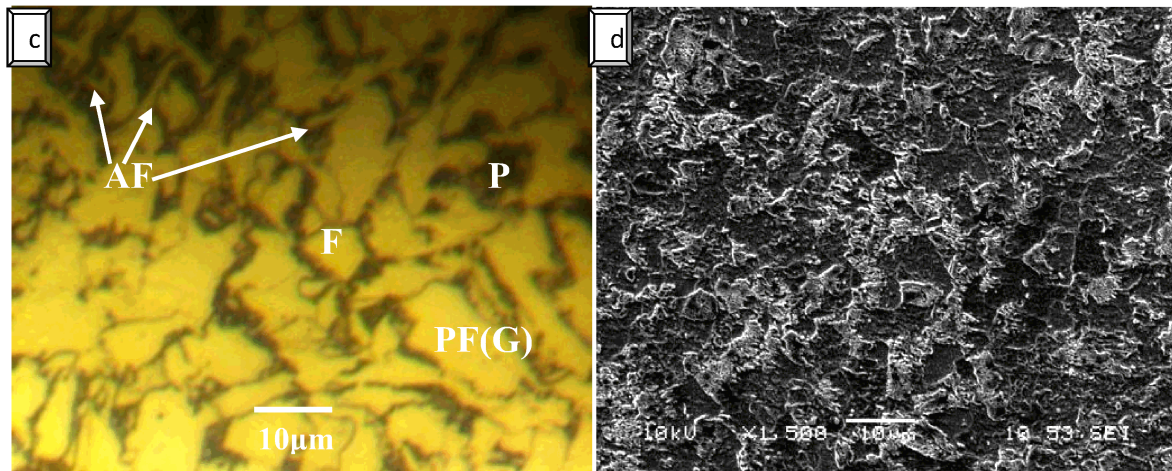
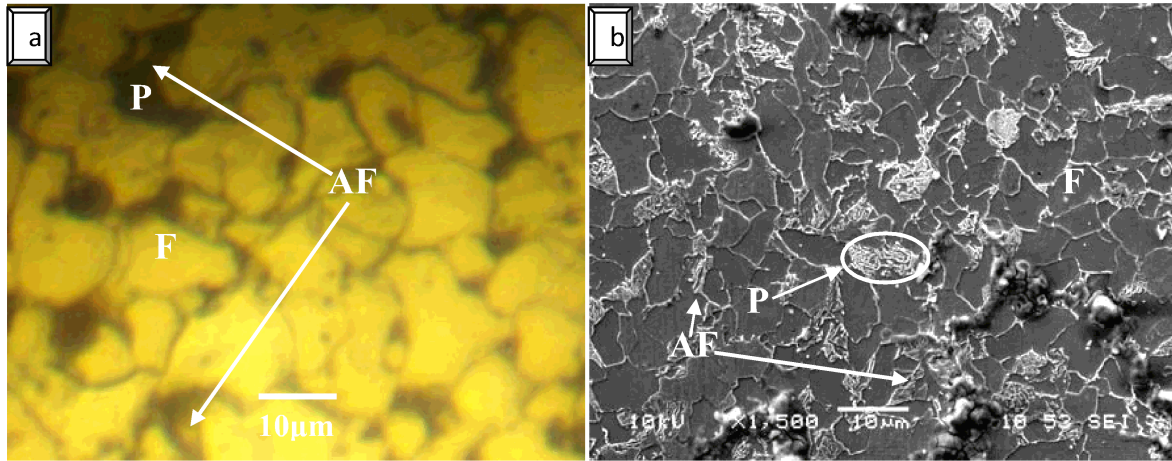


Figure IV.18: Optical and SEM micrographs of fusion zone (first pass) for 30 min: (a,e) heat treated at 200°C, (b,f) heat treated at 400°C and (c,g) heat treated at 600°C.



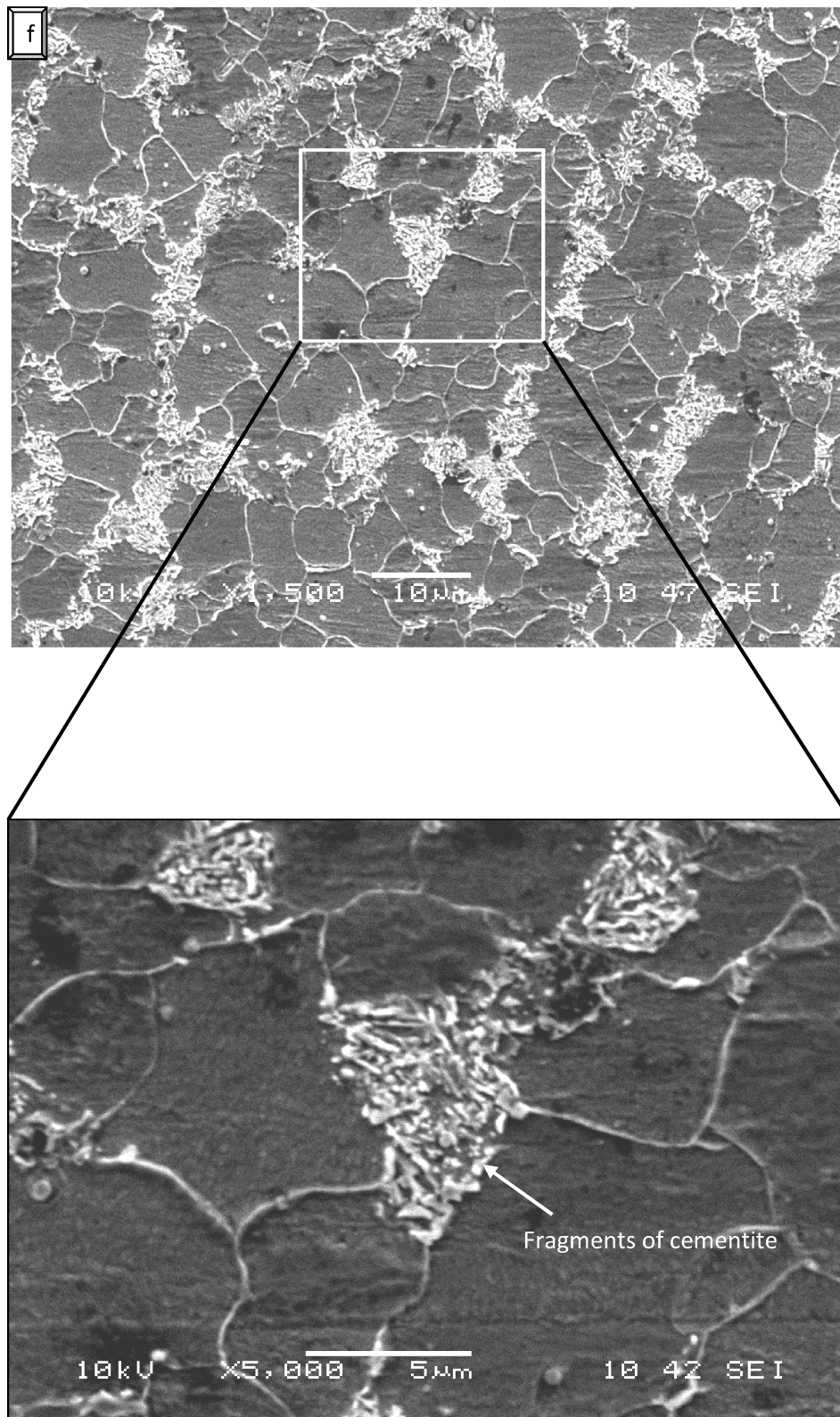


Figure IV.19: Optical and SEM micrographs of fusion zone (first pass) for 1 h: (a,b) heat treated at 200°C, (c,d) heat treated at 400°C and (e,f) heat treated at 600°C.

➤ **Second pass**

In general the second pass of fusion zone (FZ) microstructure was largely composed of fine and coarse ferrite grains (FG and CG), acicular ferrite (AF) with some grain boundaries of ferrite (GBF) (Figures IV.22, IV.23, IV.24 and IV.25). According to Bhadeshia et al., E. Kehan and M. Lord [41,107,108] The term acicular means shaped and pointed like a needle, and sometimes acicular ferrite the shape is stated to be rod-like. However Wan et al [109] Have been seen that the shape of acicular ferrite is a plate or lath, rather than a needle or rod.

“Acicular ferrite” α_a is a phase most commonly observed as austenite transforms during the cooling of low-alloy steel weld deposits. The proportion of the acicular ferrite constituent in the final microstructure is found to be a complex function of cooling rate, alloy composition, inclusion content and austenite grain size of the weld deposit. It provides a relatively strong microstructure, which is known to confer good toughness and strength in the material [41,105].

Kim et al [110] demonstrated that the transformation behaviors of acicular ferrite is according to previous reports, acicular ferrite is considered to be formed in the range of temperatures (approximately 400–600 °C), However Jing-hong et al [111] confirmed that acicular ferrite forms well in the region of 550 - 600°C. Acicular ferrite plates, during the early stages of transformation nucleate on inclusions present in the large columnar austenite grains which are typical of weld deposits. When transformation terminates before this equilibrium fraction is achieved, the reaction is said to be incomplete. This “incomplete reaction phenomenon” can be taken to be a consequence of the non equilibrium character of the transformation product. The acicular ferrite transformation obeys the incomplete reaction phenomenon [41, 112].

The figure (IV.22) shows the typical microstructure of the solidified weld metal from the fusion zone displays acicular ferrite (AF) surrounded by grain boundary proeutectoid ferrite (GBF) and some fine ferrite grains.

The short heat treatment (10 min) at 200°C and 400°C (Figure IV.23.a and b, IV.23.c and d respectively) caused the decrease in the acicular ferrite grains (AF) but after the same time at 600°C we have obtained an increase in the last one, we can deduce that the high temperature affect the grain boundaries mobility and the recrystallization of the grains (Figure IV.24.e and f) The obtained microstructures by the optical microscope after 200°C, 400°C heat treatment for 30 min present slight difference in the grain size, but the

SEM images present zones rich by the acicular ferrite, It is clear that there is decrease in the grains size after heat treatment at 600°C for 30 min and 400°C for 1 h. Shen et al [55] reported the presence of similar weld metal constituents with micro alloyed steel.

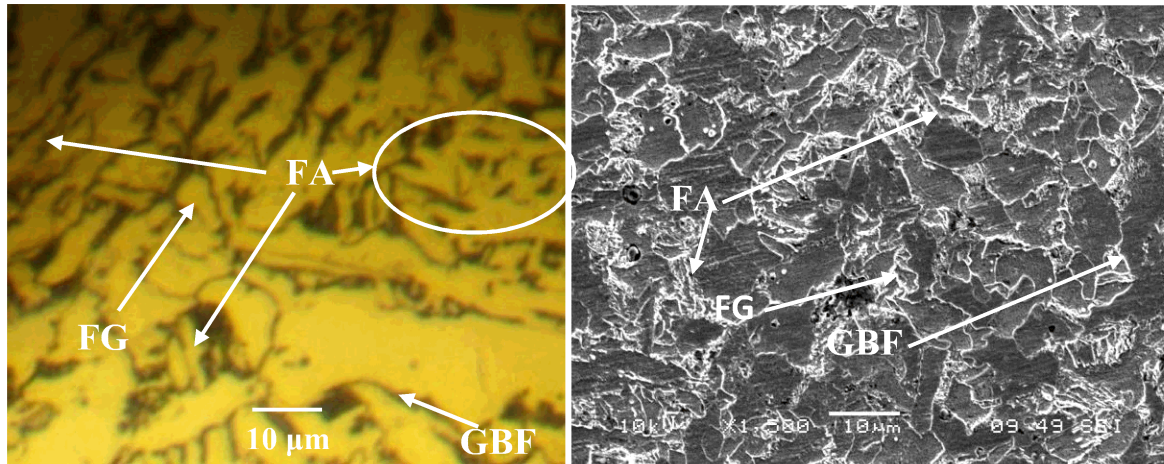
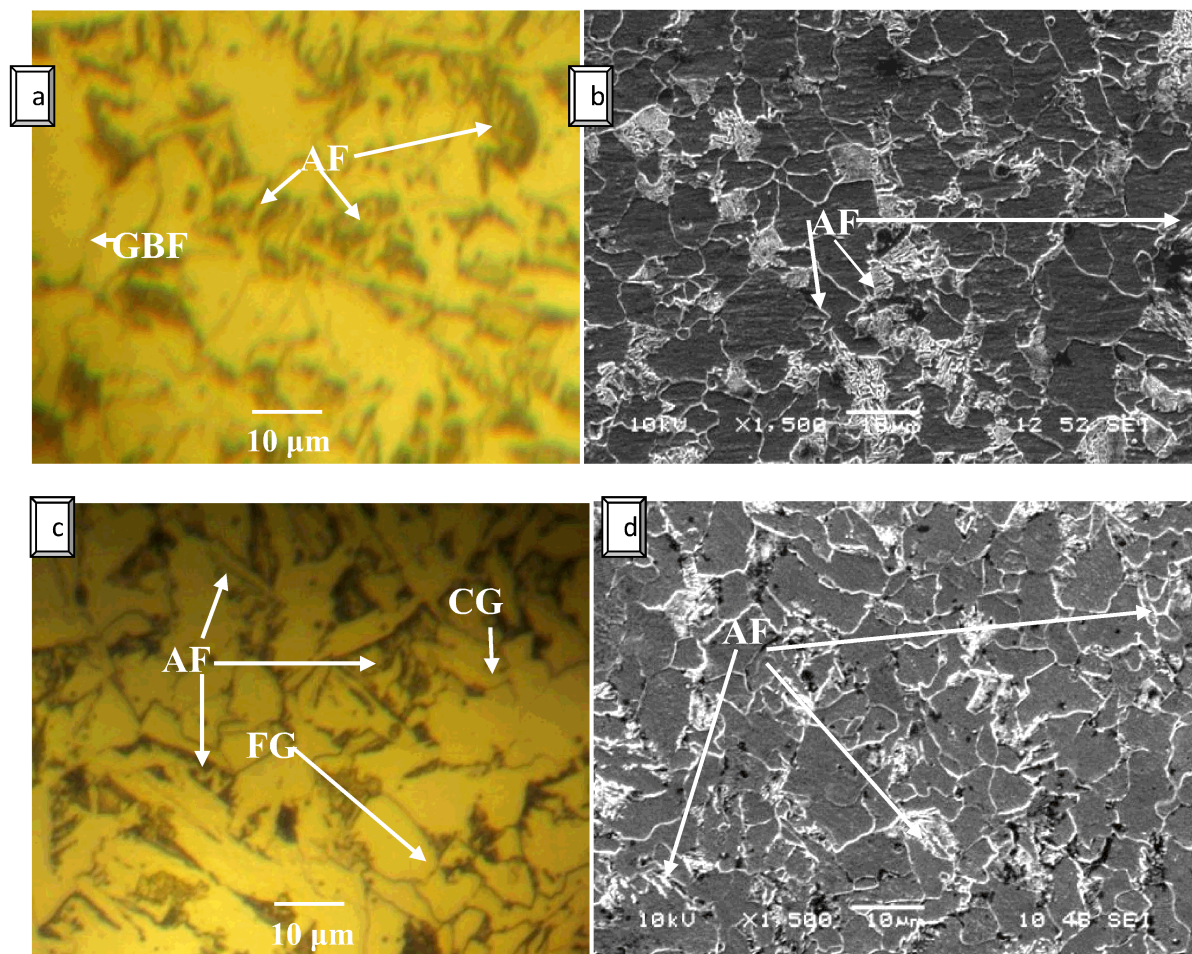


Figure IV.22: Optical and SEM micrographs of untreated fusion zone(second pass) .



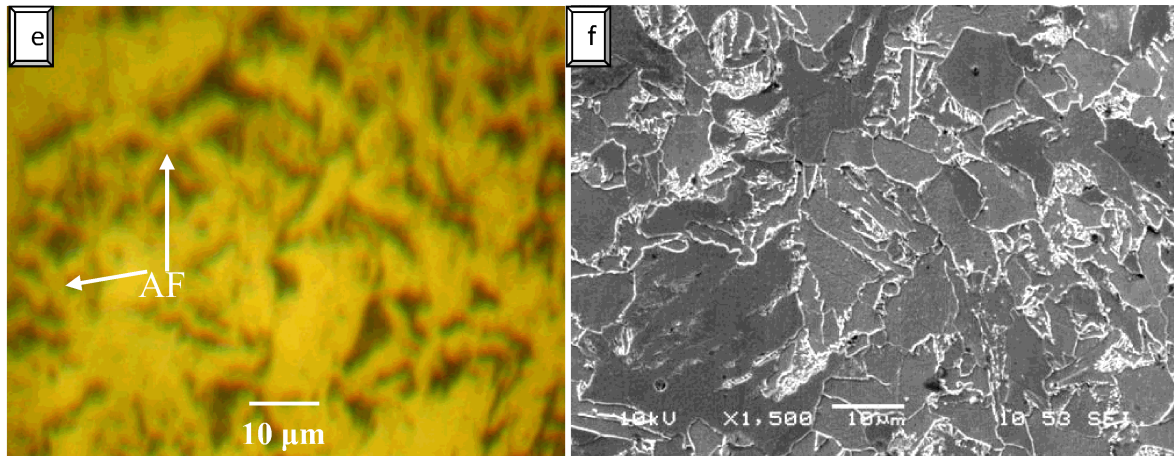
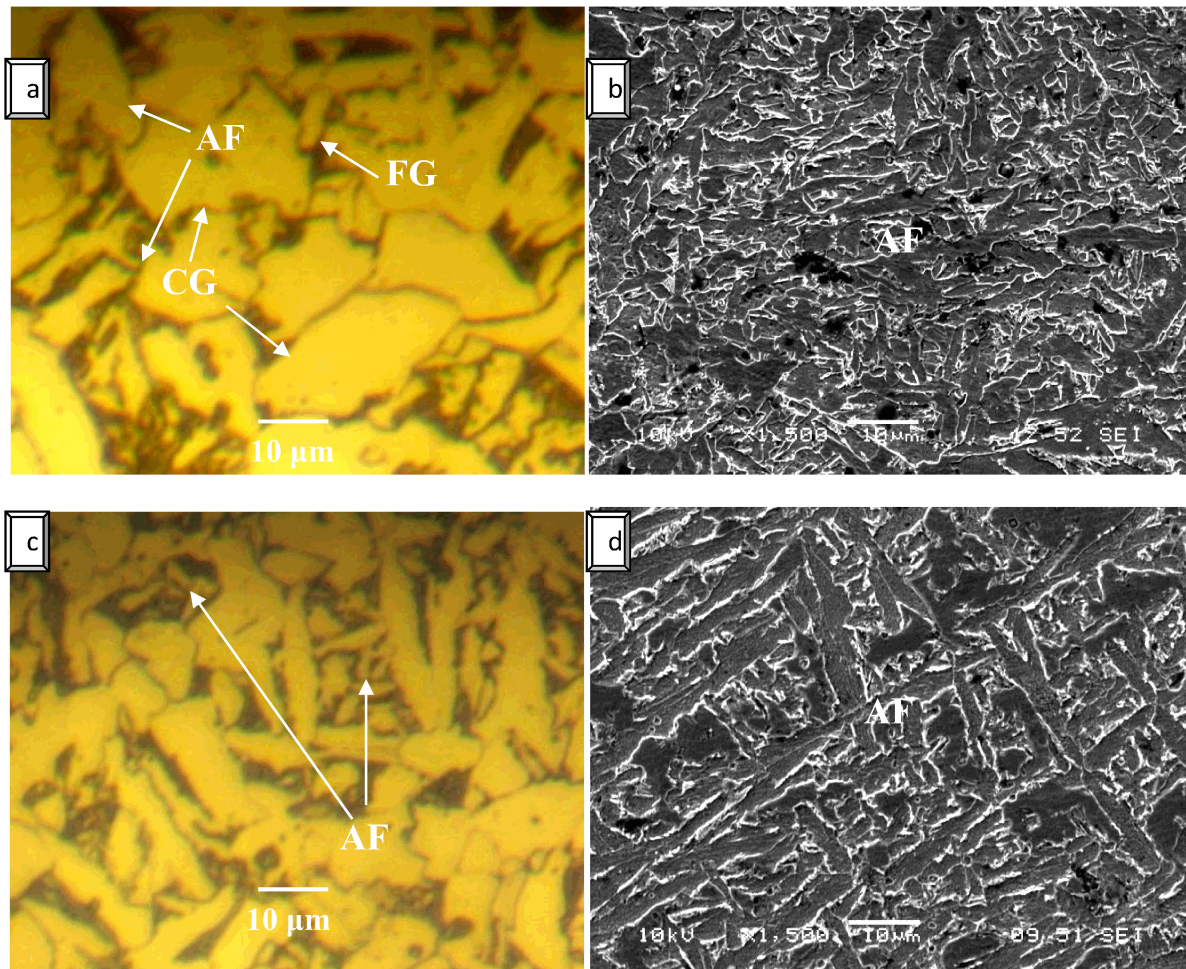


Figure IV.23: Optical and SEM micrographs of fusion zone (second pass) for 10 min: (a,e) heat treated at 200°C, (b, f) heat treated at 400°C and (c, g) heat treated at 600°C.



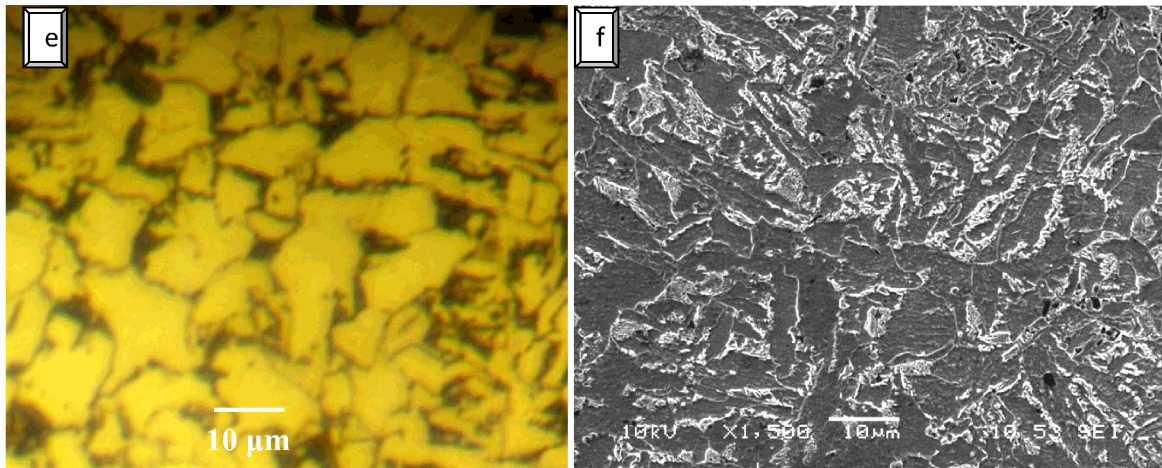
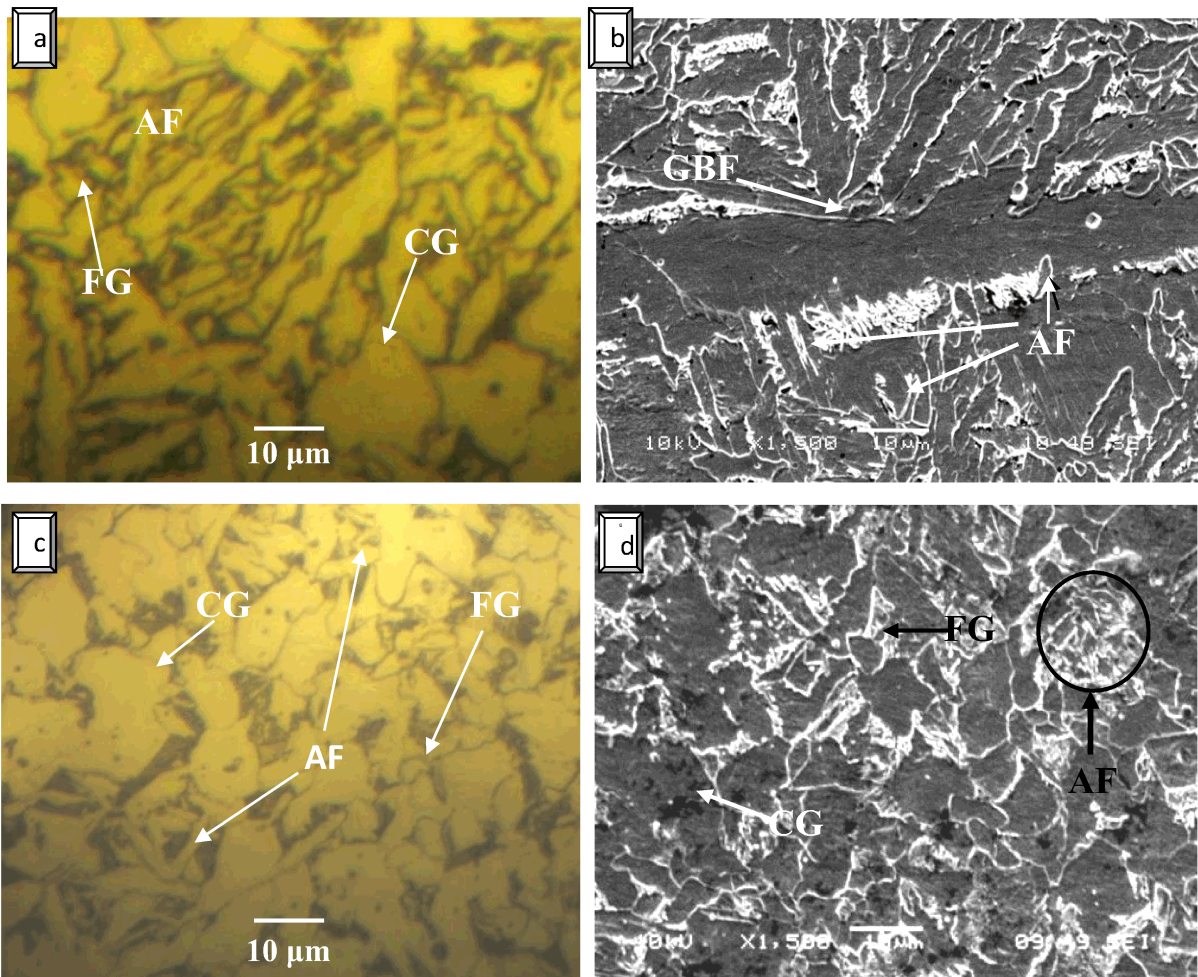


Figure IV.24: Optical and SEM micrographs of fusion zone (second pass) for 30 min: (a,e) heat treated at 200°C, (b,f) heat treated at 400°C and (c,g) heat treated at 600°C.



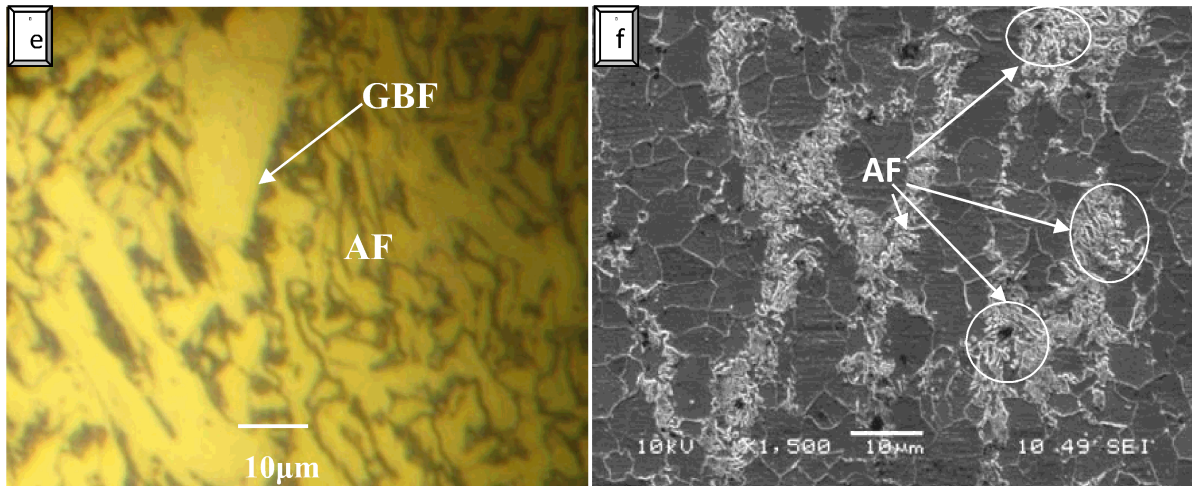


Figure IV.25: Optical and SEM micrographs of fusion zone (second pass) for 1h: (a,e) heat treated at 200°C, (b,f) heat treated at 400°C and (c,g) heat treated at 600°C.

- **Third pass**

The figures IV.26, IV.27 and IV.28 IV.29 Show the interlocking of different ferrite morphologies such as, ferrite side plates (FS) or Widmanstätten ferrite (WF) and acicular ferrite (AF) with some ferrite grain boundaries (GBF). W.Zhang et al [60], Eroglu et al [104], Babu et al [112], and Fattahia et al [113] demonstrated that the parallel side plates have been developed from Grain boundary allotriomorphic ferrite (GBF), because this later is the first phase to form from the γ phase during cooling of the weld metal. It nucleates along the γ grain boundaries and grows by diffusion. As the temperature decreases, the growth rate of allotriomorphic ferrite decreases, and it finally gives way to the growth of Widmanstätten ferrite. In other hand, from a direct consequence of welding is the austenite grains coarsen, because the material was heated up most effectively during the welding process. It is well-known that coarse austenite grains favour the formation of Widmanstätten ferrite [41,70].

Widmanstätten ferrite is sometimes included under the general description “ferrite with aligned MAC”, the abbreviation referring to martensite, austenite and carbide [41].

Widmanstätten ferrite is an undesirable constituent steels and its presence leads to poor toughness in low alloy. The problem of the unwanted it is particularly acute in steel welds deposits, where it is impractical to modify the microstructure which evolves during solidification and during subsequent cooling to ambient temperature [114].

Before heat treatment the microstructure consists of fine acicular ferrite and the ferrite side plates (FS) or Widmanstätten ferrite (WF) (Figure IV.26). After heat treatments at 400°C for 10 min (Figure IV.27.c and d) and 600°C for 1h (Figure IV.29.e and f) we have obtained a coarse acicular ferrite, and fine acicular ferrite (AF) is found after heat treatment at 600°C

for 10 min (FigureIV.27.e and f).There is a remarkable increase in the grains size After 400°C heat treatment for 30 min. The other heat treatments do not affect really the initial microstructures.

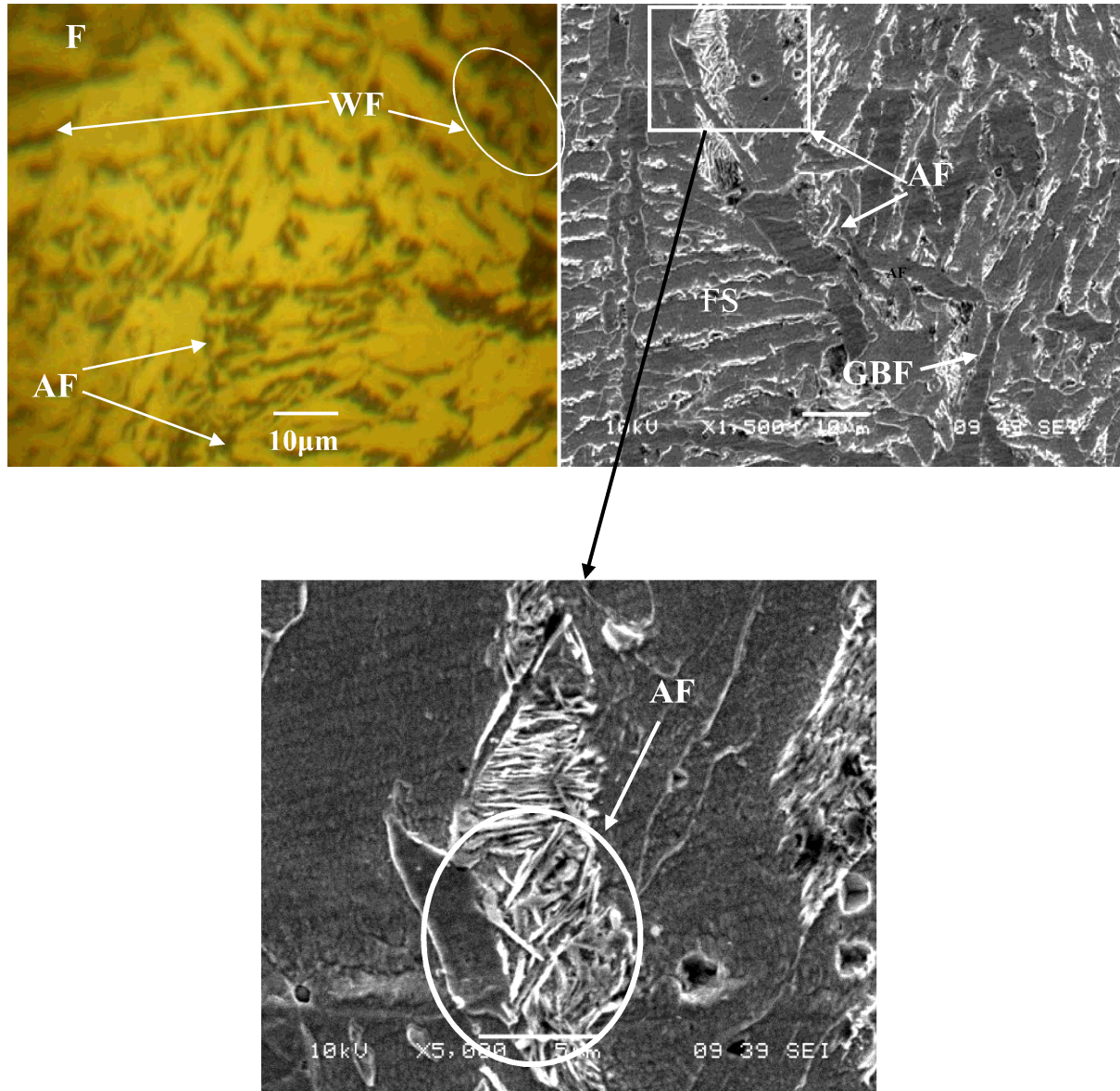


Figure IV.26: Optical and SEM micrographs of untreated fusion zone (third pass).

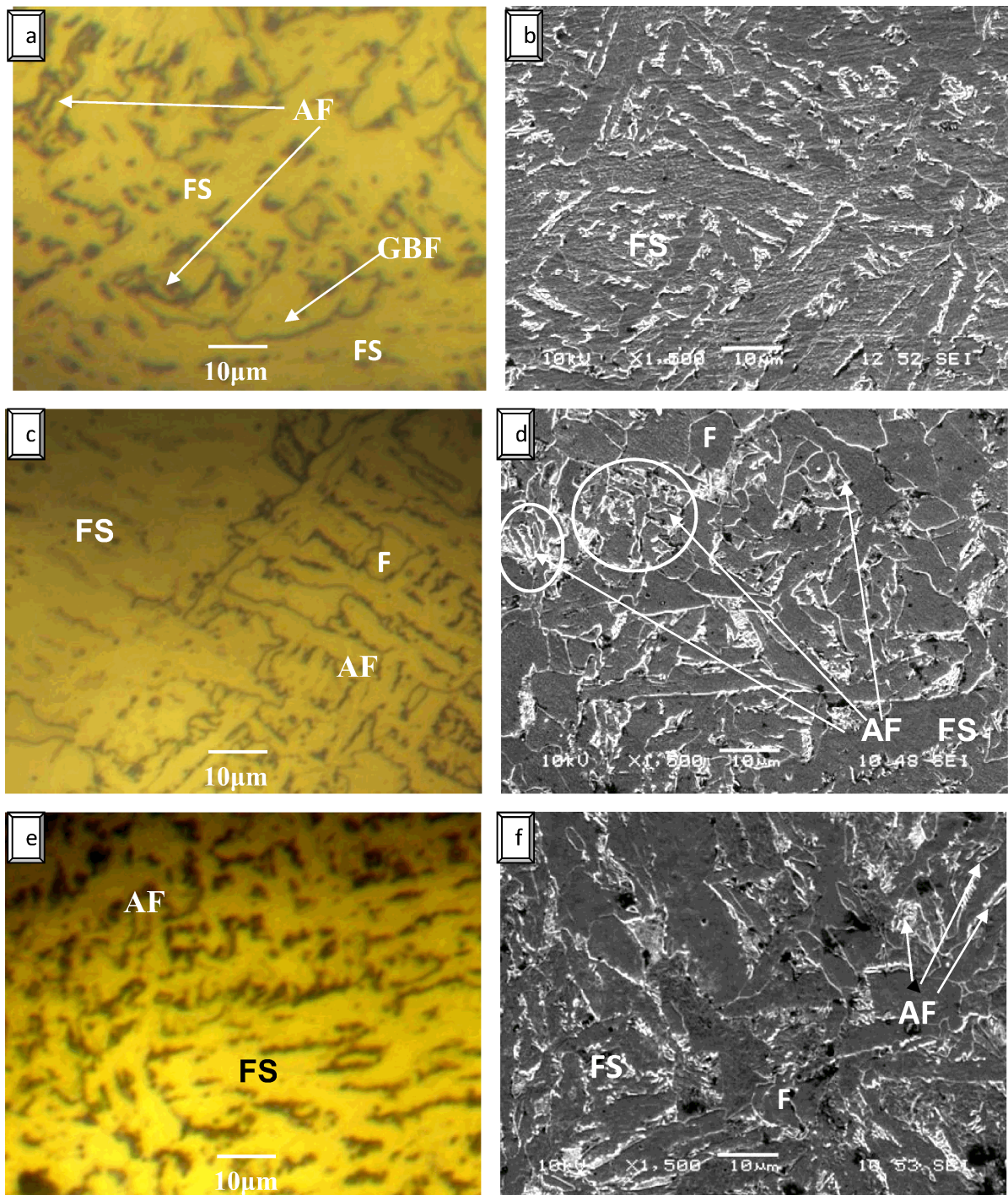


Figure IV.27: Optical and SEM micrographs of fusion zone (third pass) for 10 min: (a,e) heat treated at 200°C, (b,f) heat treated at 400°C and (c,g) heat treated at 600°C.

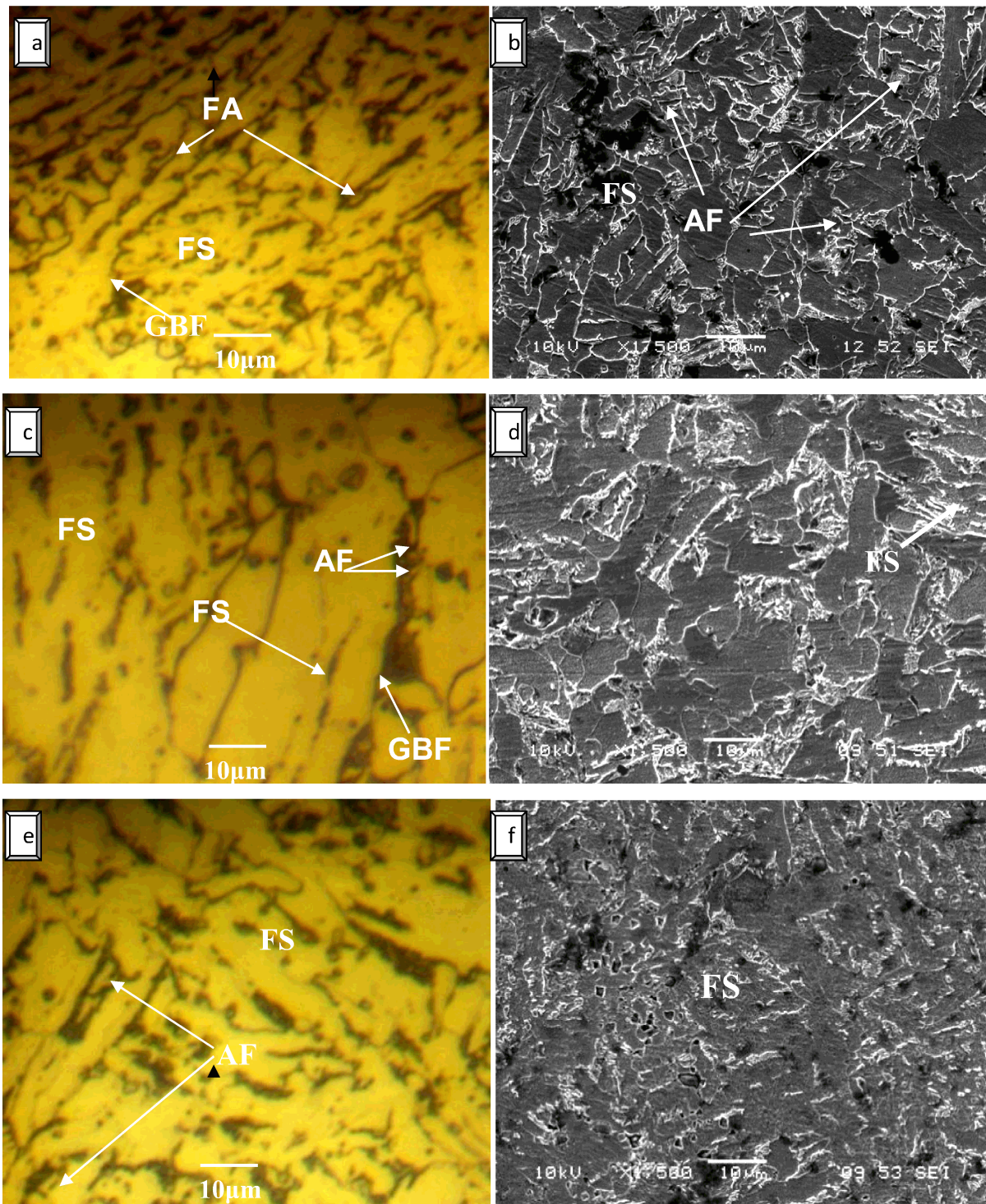


Figure IV.28: Optical and SEM micrographs of fusion zone (third pass) for 30 min: (a,e) heat treated at 200°C, (b,f) heat treated at 400°C and (c,g) heat treated at 600°C.

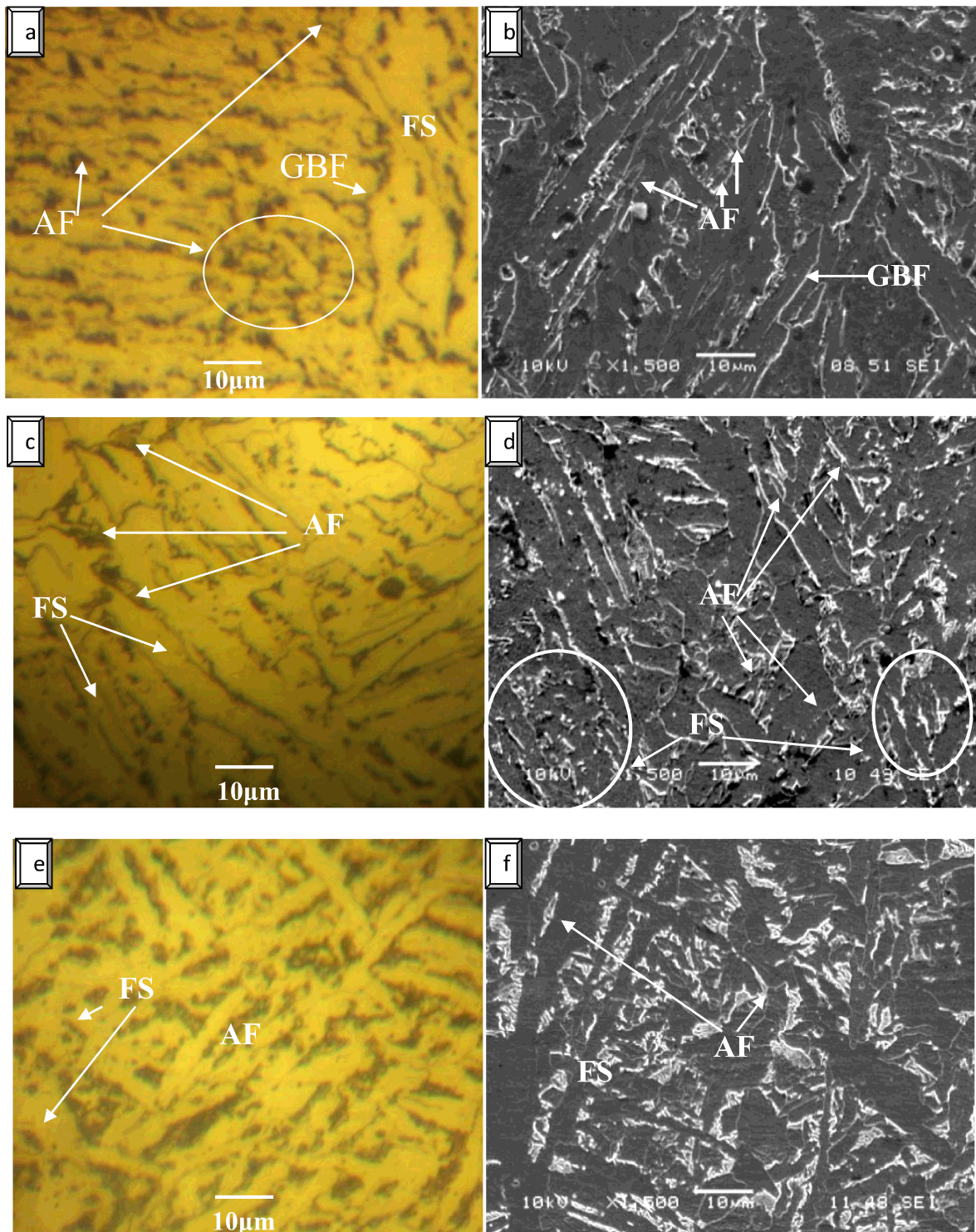


Figure IV.29: Optical and SEM micrographs of fusion zone (third pass) for 1h: (a,e) heat treated at 200°C, (b,f) heat treated at 400°C and (c,g) heat treated at 600°C.

IV.3 Phases characterization

It is well known that X-ray diffraction (XRD) is one of the major techniques which may be successfully used for structure characterization [115]. This case we can also receive the important information on the shape of particles. Data on the crystallite size can be obtained by X-ray diffraction (XRD) technique as the crystallite size is related to the diffraction peak broadening. It is important that XRD method allows not only to measure the crystallite size, but also to identify crystalline phases [116,117].

XRD patterns of low carbon steel before and after heat treatment (Figures IV.30-38) exhibit high-intensity peaks corresponding to the α -Fe phase. As can be seen, the diffraction from three crystalline planes is more intense than that of others; (1 1 0), (2 0 0) and (211).

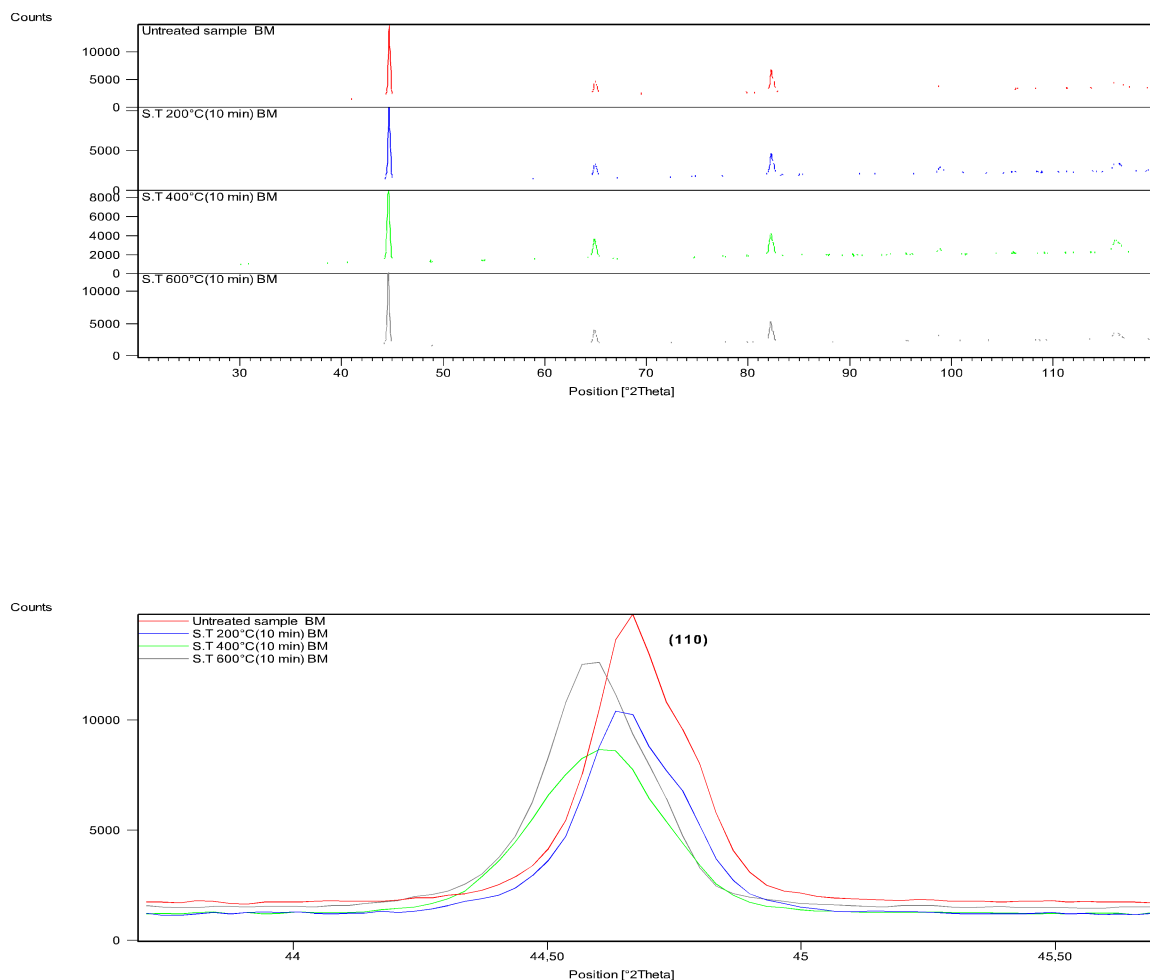


Figure IV.30: X-ray diffraction profiles of base metal after heat treatments for 10 min at 200°C, 400°C and 600°C.

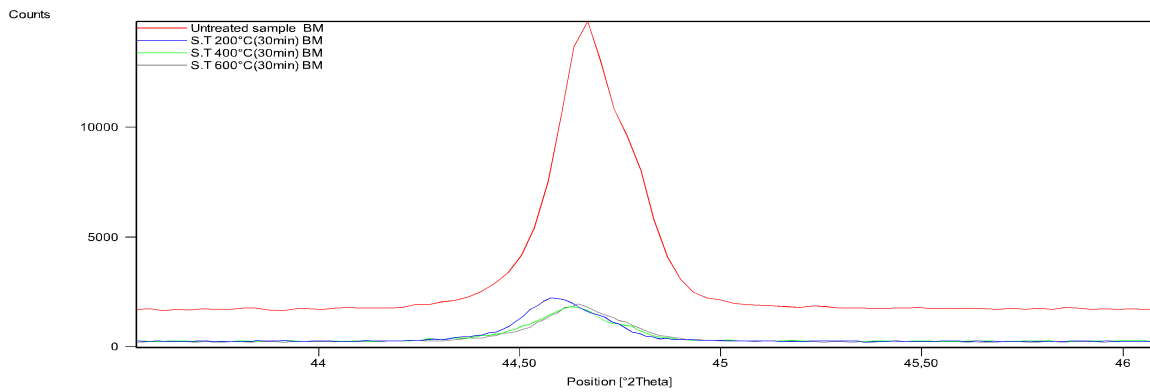
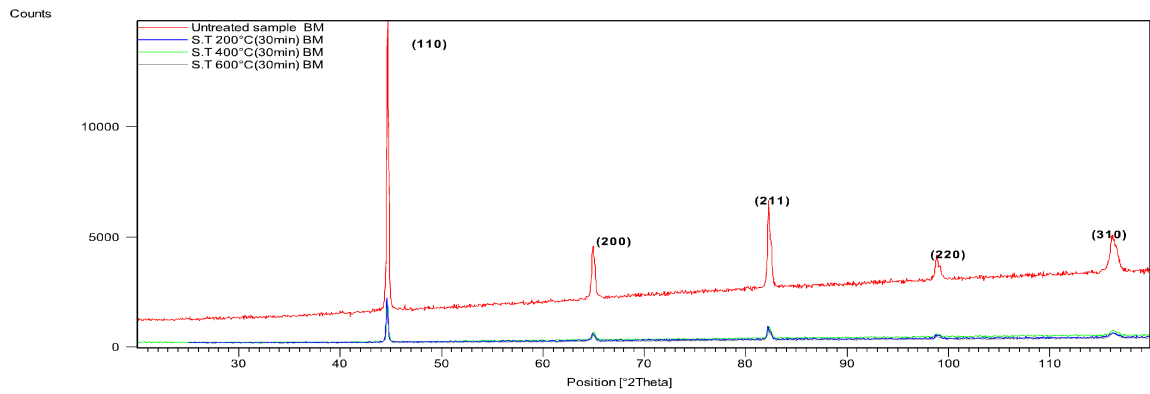
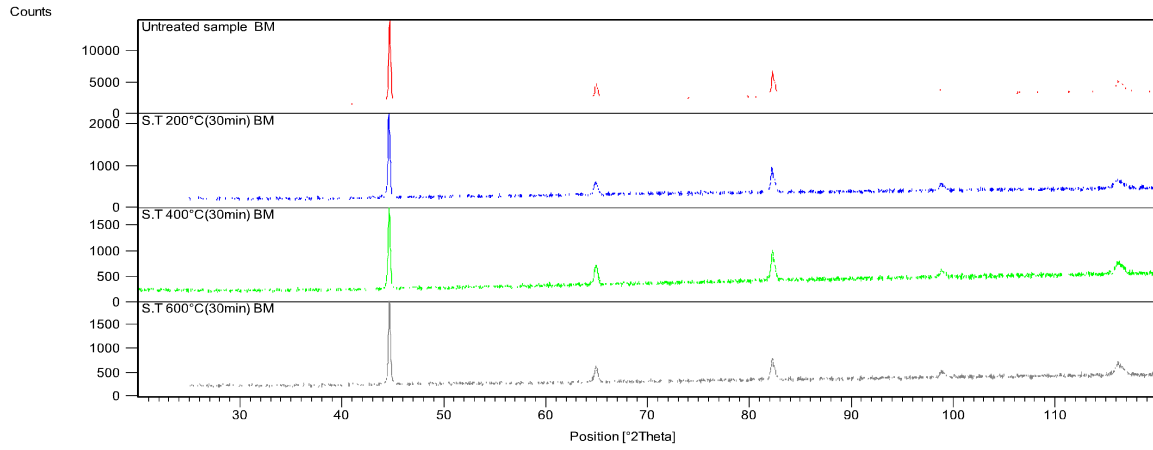


Figure IV.31: X-ray diffraction profiles of base metal after heat treatments for 30 min at 200°C, 400°C and 600°C.

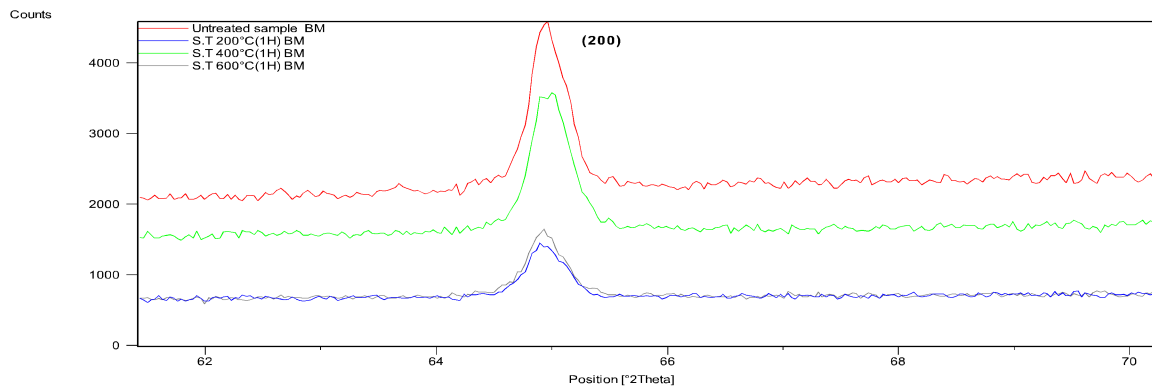
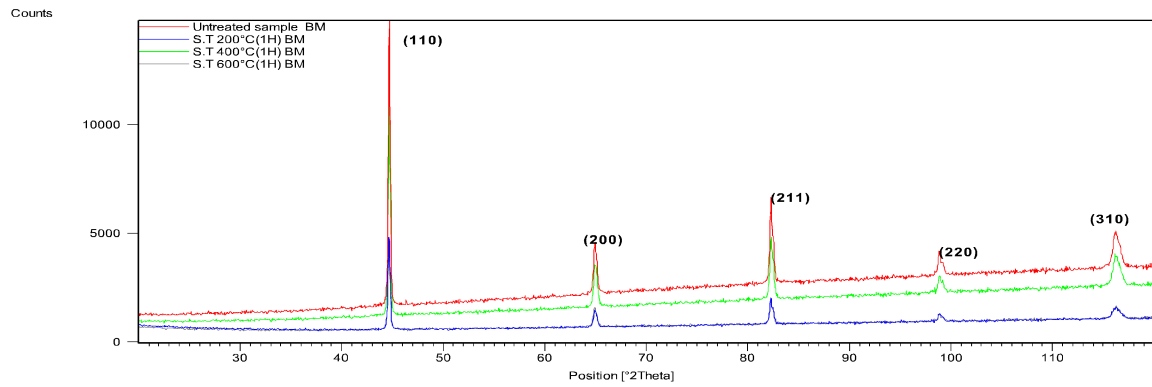
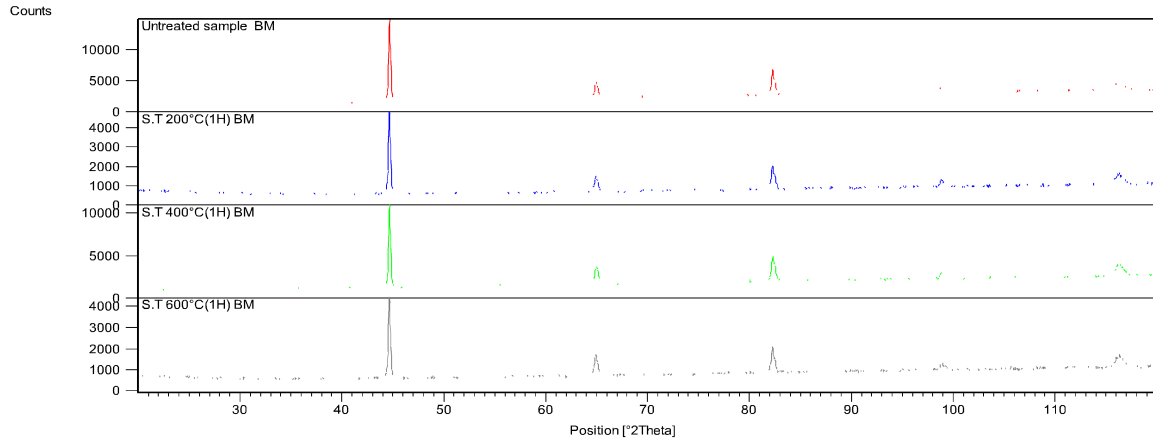


Figure IV.32: X-ray diffraction profiles of base metal after heat treatments for 1hour at 200°C, 400°C and 600°C.

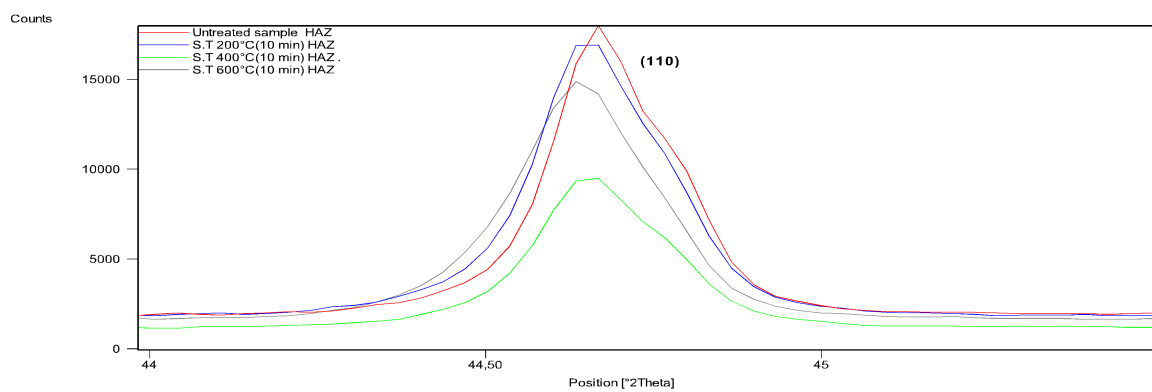
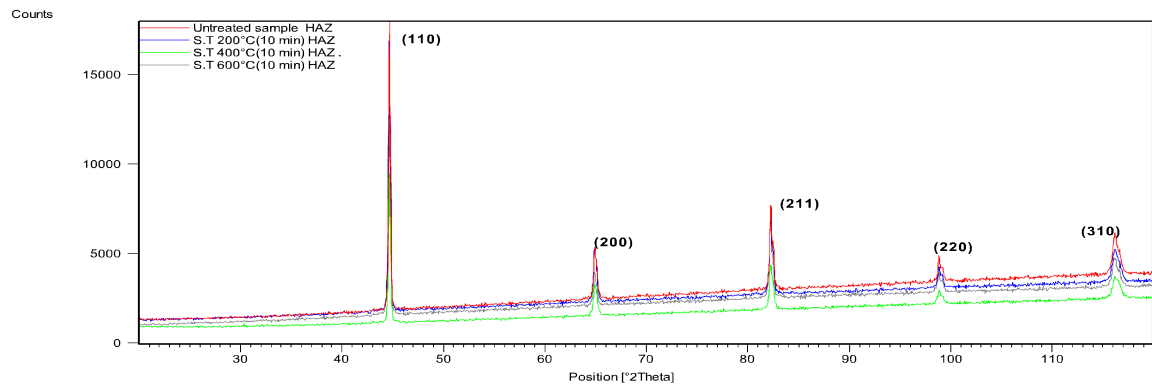
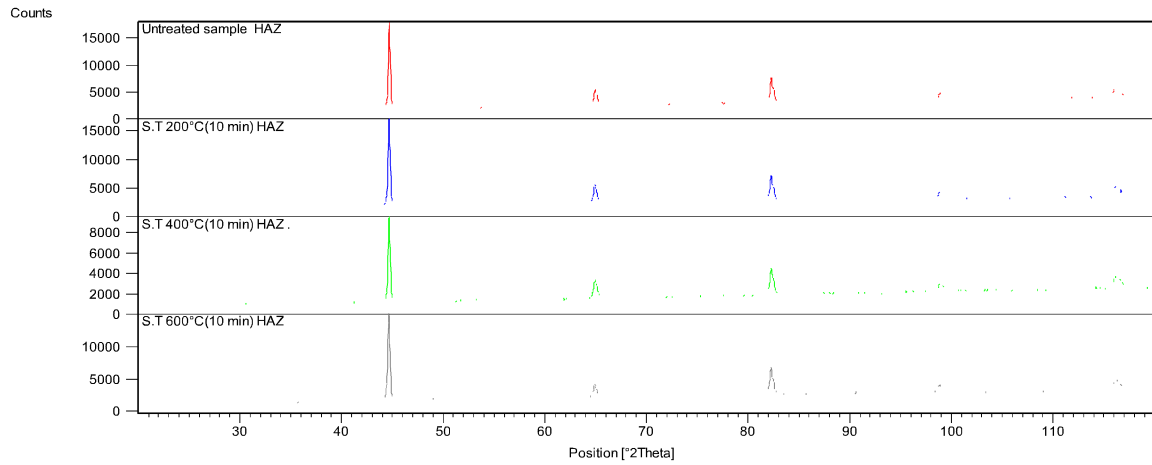


Figure IV.33: X-ray diffraction profiles of heat affected zone after heat treatments for 10 min at 200°C, 400°C and 600°C.

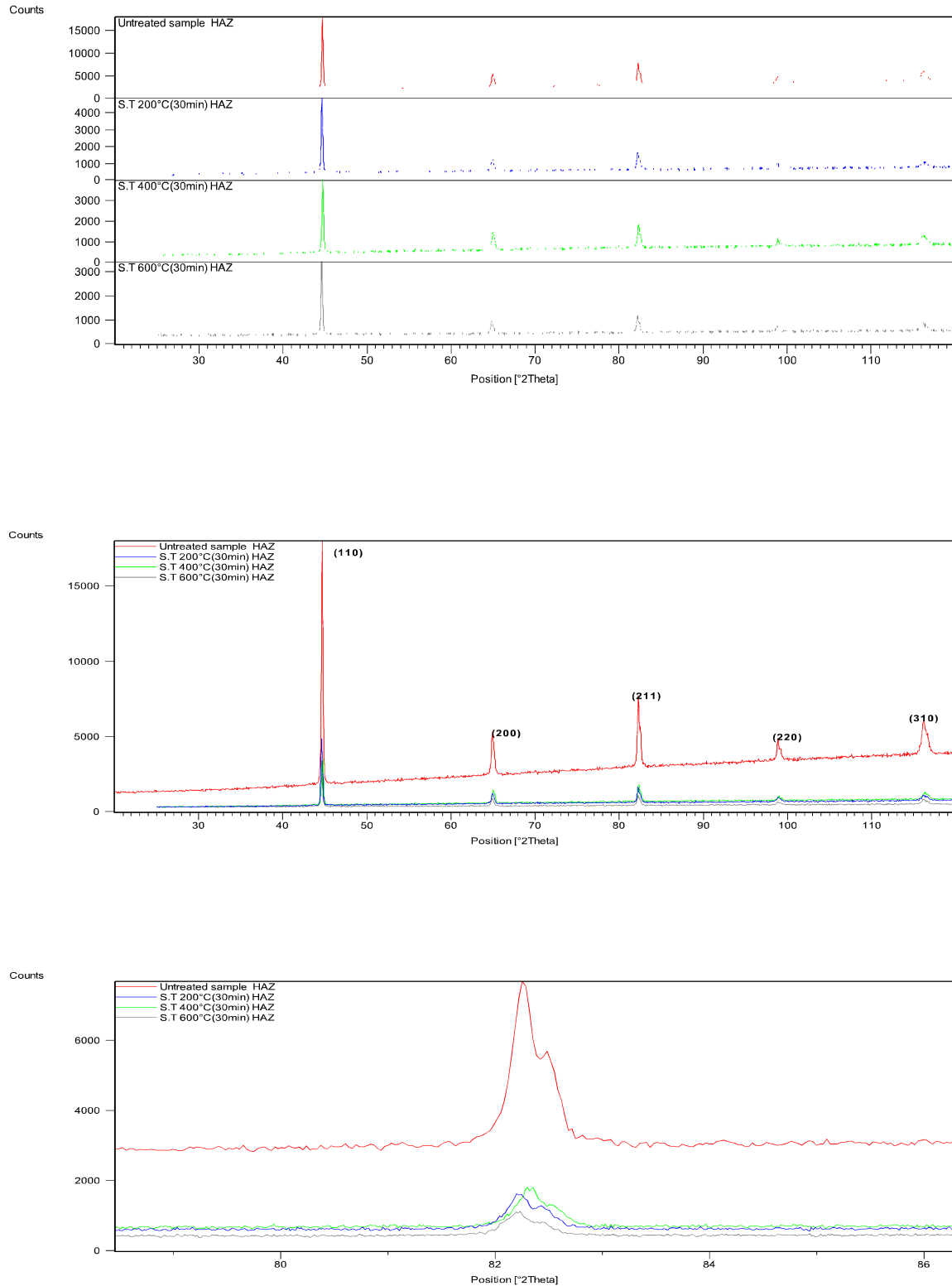


Figure IV.34: X-ray diffraction profiles of heat affected zone after heat treatments for 30 min at 200°C, 400°C and 600°C.

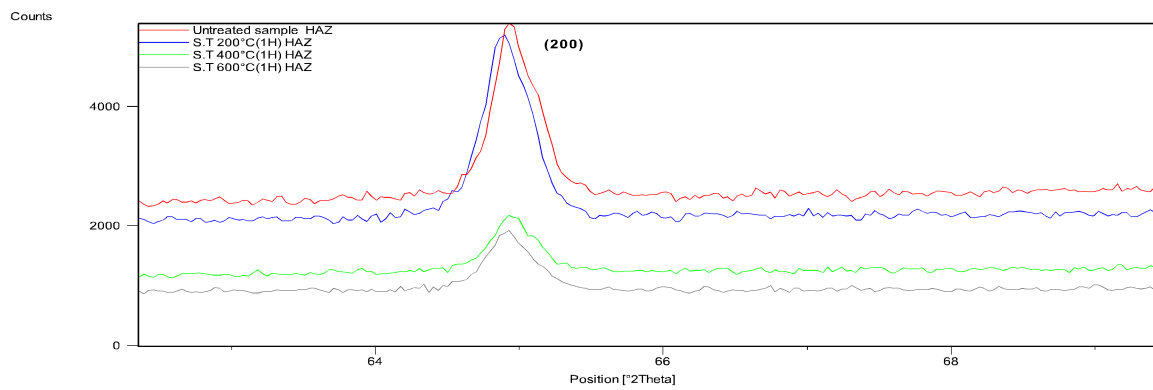
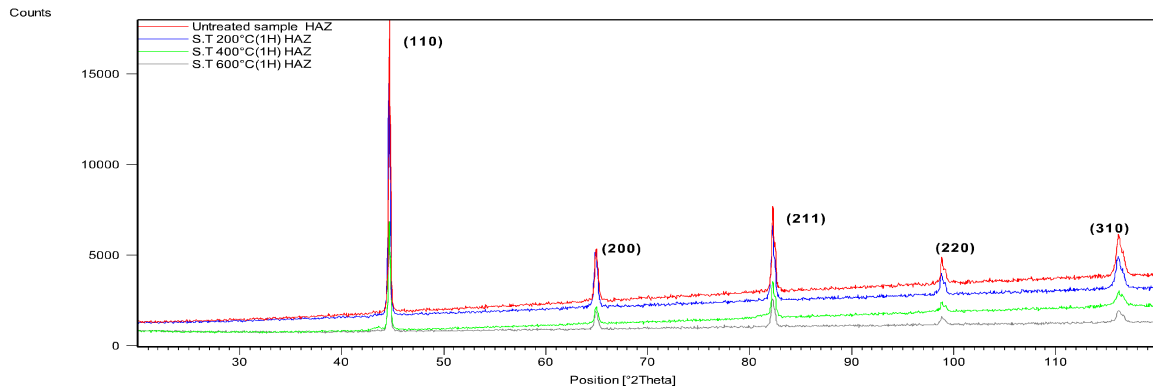
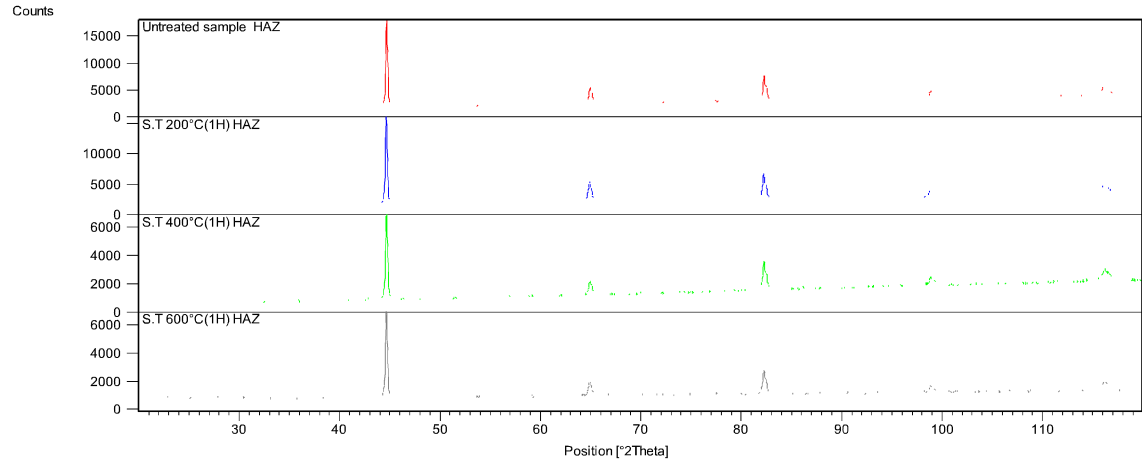


Figure IV.35: X-ray diffraction profiles of heat affected zone after heat treatments for 1h at 200°C, 400°C and 600°C.

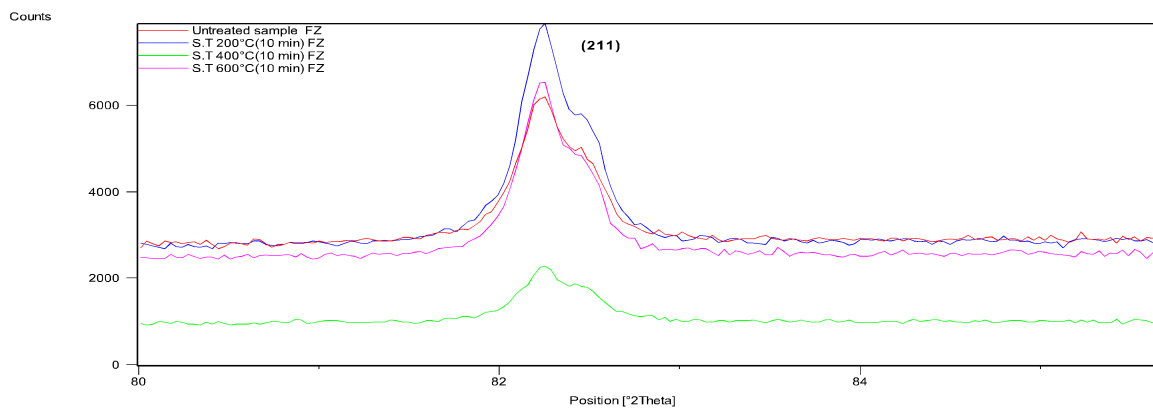
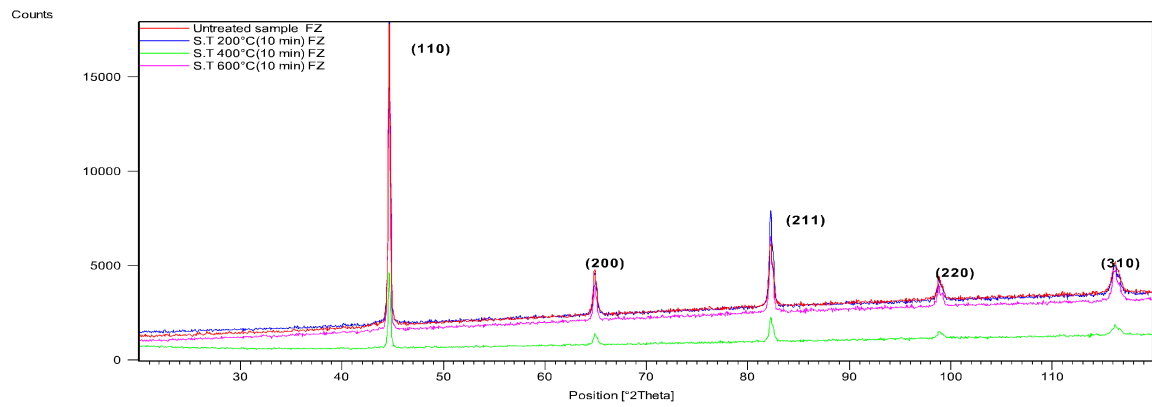
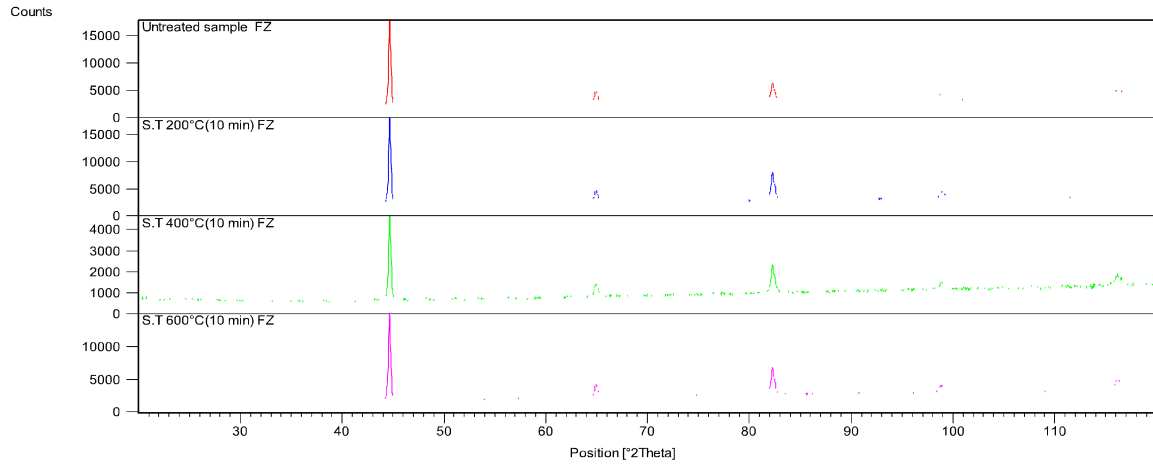


Figure IV.36 : X-ray diffraction profiles of fusion zone after heat treatments for 10 min at 200°C, 400°C and 600°C.

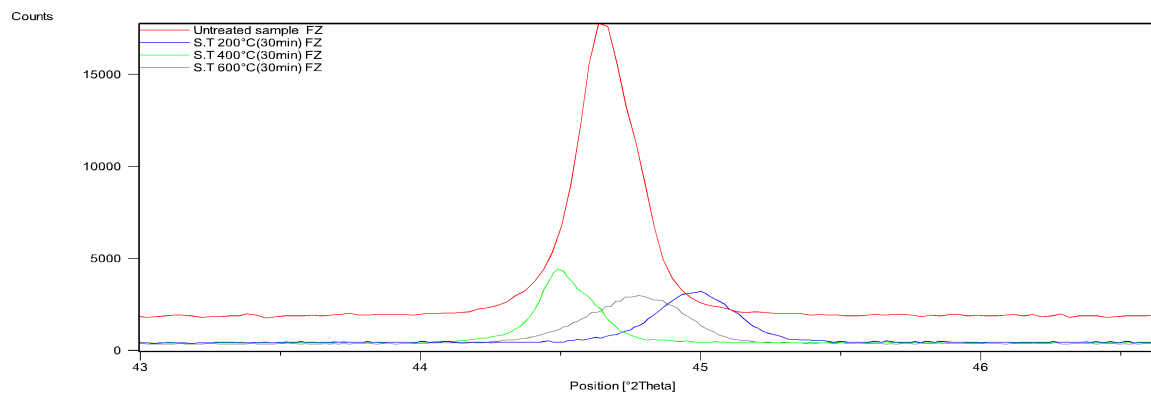
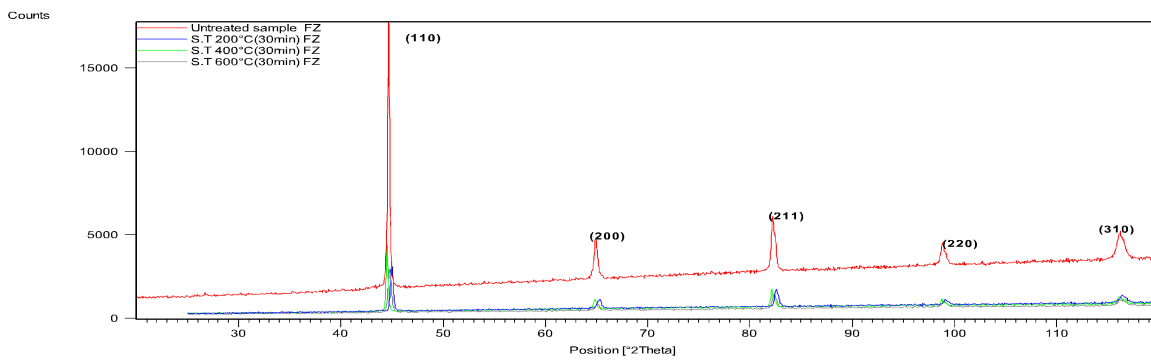
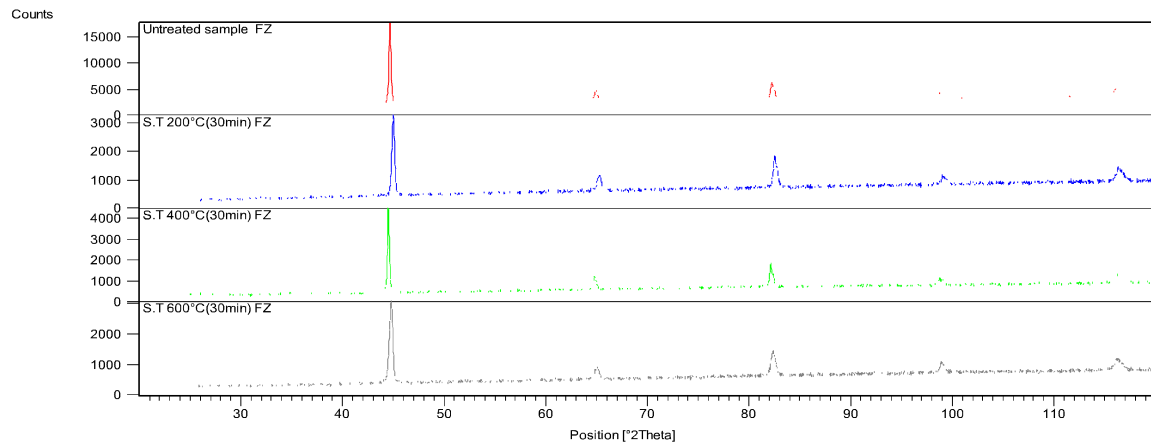


Figure IV.37: X-ray diffraction profiles of fusion zone after heat treatments for 30 min at 200°C, 400°C and 600°C.

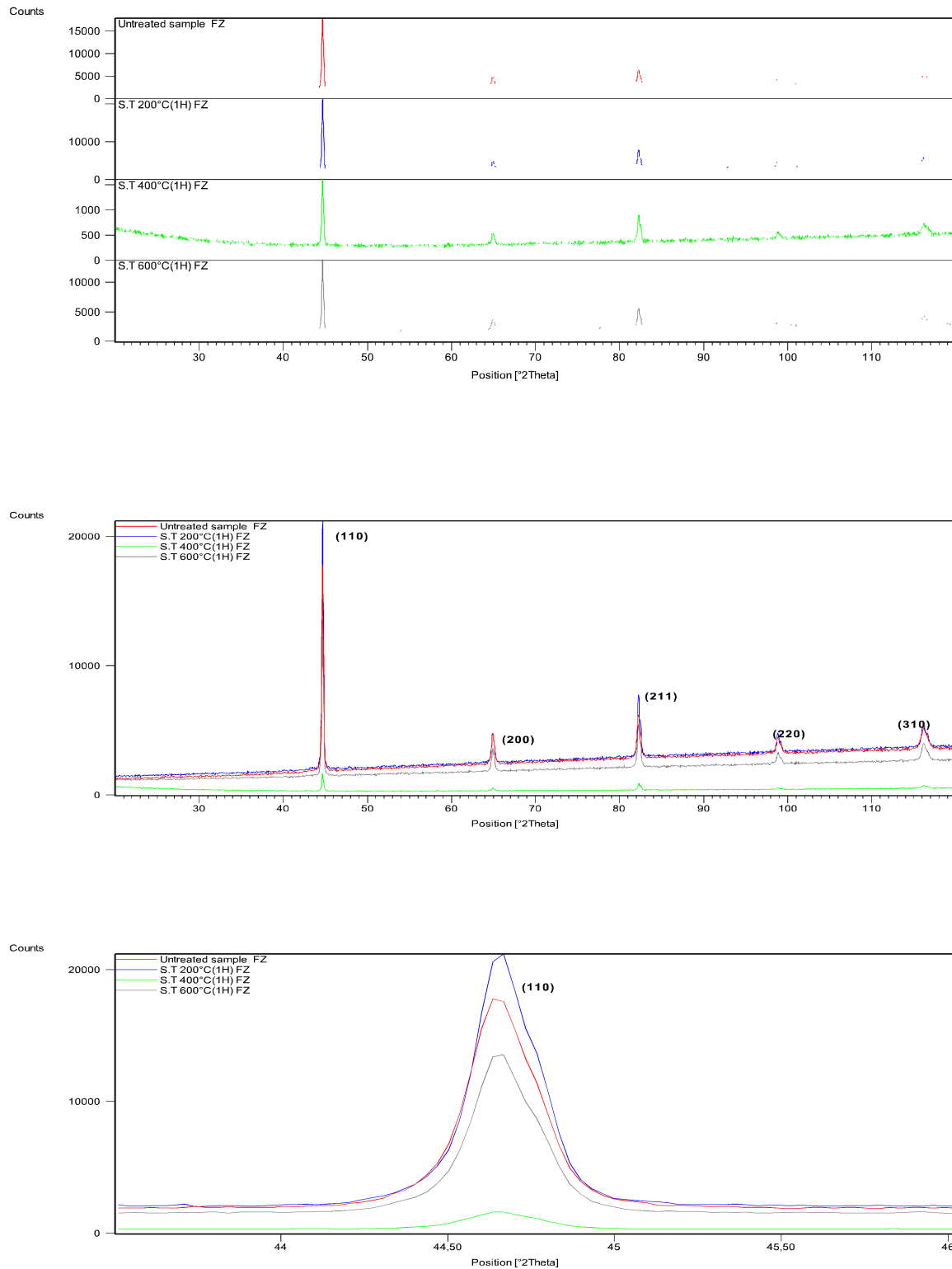


Figure IV.38: X-ray diffraction profiles of fusion zone after heat treatments for 1h at 200°C, 400°C and 600°C.

IV.3.1 The peaks displacements

The tables (IV.1-3) resum the variation of the five first peaks position and the difference between the peak position before and after the heat treatments at 200°C, 400°C and 600°C for 10 min, 30 min and 1 hour in the three studied zones which are the base metal (BM), the heat affected zone (HAZ) and the fusion zone (FZ).

We start by the base metal when the first peak (110), the second peak (200), the third peak (211) and the fourth peak (220) after the heat treatments leaved their first positions to get new positions which are located in the low angles. The remarkable displacements are found after heat treatment at 600°C for 10 min with the $\Delta 2\theta = 0,13^\circ, 0,1^\circ, \text{ and } 0,13^\circ$ corresponding to the displacement of the peaks (110), (200), and (220) respectively and in the fifth peak (310) after 30 min at 200°C, 400°C, 600°C and for 1h at 200°C, 400°C and 600°C which displaced to the high angles with $\Delta 2\theta = -0,12^\circ, -0,12^\circ, -0,0857^\circ, 0,13^\circ, -0,1^\circ$ and $-0,16^\circ$ respectively.

The heat affected zone (HAZ) presents a small variation in the 2θ position of the five peaks excepting for 10 min heat treatments at 400°C there is a remarkable displacement to the low angles where $\Delta 2\theta = 0,34^\circ$ in the second peak (200) and in the fifth peak after heat treatments at 200°C, 400°C and 600°C for 30 min where $\Delta 2\theta = 0,139^\circ, -0,1612^\circ, 0,1261^\circ$ when the displacements were to the high and low angles.

The fusion zone (FZ) shows also a slight difference between the first and the last peak positions after heat treatments at 200°C, 400°C and 600°C for 10 min, however after 30 min we found big displacements, at 200°C the two first peaks have displaced to the low angles, where $\Delta 2\theta = 0,1463^\circ$ and $0,1102^\circ$ corresponding to the peaks (110) and (200) respectively, at 400°C just the first and the second peaks present remarkable displacement because $\Delta 2\theta = +0,1463^\circ, +0,1102^\circ$, at 600°C we find that the displacements were in the first, third and fourth peaks, in this case $\Delta 2\theta = -0,1312^\circ, -0,1074^\circ$ and $0,1244^\circ$ corresponding to the first, third and fourth peaks respectively.

It is well known that when the peak stays in the first position, then there is no stress, when the peak displace to the low angles, we can conclude the presence of uniform stress (dilatation) and when the peak displaces to the high angles we can say that there is a uniform stress (compression). The peak broadening gives information about the presence of the ununiform stress [87].

Table IV.1 : The displacements of the five first peaks in the base metal(BM)				
Sample		(hkl)	2 θ (°)	$\Delta 2\theta$ (°)
1	Untreated sample	(110)	44,6540	0
		(200)	64,9171	0
		(211)	82,2500	0
		(220)	98,8466	0
		(310)	116,079	0
2	S.T.200°C (10min)	(110)	44,6376	0,0164
		(200)	64,9067	0,0104
		(211)	82,2500	0
		(220)	98,8466	0
		(310)	116,1224	-0,0434
3	S.T.400°C (10min)	(110)	44,6447	0,0093
		(200)	64,9140	0,0031
		(211)	82,2402	0,0098
		(220)	98,8317	0,0149
		(310)	116,1229	-0,0439
4	S.T.600°C (10min)	(110)	44,5234	0,1306
		(200)	64,8134	0,1037
		(211)	82,1795	0,0705
		(220)	98,7088	0,1378
		(310)	116,1197	-0,0407
5	S.T.200°C (30min)	(110)	44,5899	0,0641
		(200)	64,8474	0,0697
		(211)	82,2196	0,0304
		(220)	98,7949	0,0517
		(310)	116,1991	-0,1201

Table IV.1 (continued) : Displacements of the five first peaks in the base metal(BM).				
sample		(hkl)	$2\theta(^{\circ})$	$\Delta 2\theta(^{\circ})$
6	S.T.400°C (30min)	(110)	44,6470	0,007
		(200)	64,8842	0,0329
		(211)	82,2674	-0,0174
		(220)	98,839	0,0076
		(310)	116,20	-0,121
7	S.T.600°C (30min)	(110)	44,6379	0,0274
		(200)	64,8897	0,0066
		(211)	82,2434	0,0413
		(220)	98,8053	-0,0857
		(310)	116,1647	0,007
8	S.T.200°C (1h)	(110)	98,8197	0,019
		(200)	116,2100	0,0221
		(211)	98,8197	-0,0114
		(220)	116,2100	0,0269
		(310)	98,8197	-0,131
9	S.T.400°C (1h)	(110)	44,6535	0,0005
		(200)	64,9005	0,0166
		(211)	82,2614	-0,0114
		(220)	98,8567	-0,0101
		(310)	116,1844	-0,1054
10	S.T.600°C (1h)	(110)	44,6284	0,0256
		(200)	64,9289	-0,0118
		(211)	82,2500	-0,0114
		(220)	98,8398	0,0068
		(310)	116,2400	-0,161

Table IV.2: Displacements of the five first peaks in the heat affected zone (HAZ).

sample		(hkl)	$2\theta(^{\circ})$	$\Delta 2\theta(^{\circ})$
1	Untreated sample	(110)	44,6600	0
		(200)	64,9285	0
		(211)	82,2623	0
		(220)	98,8257	0
		(310)	116,2171	0
2	S.T.200°C (10min)	(110)	44,6422	0,0178
		(200)	64,9059	0,0226
		(211)	82,2459	0,0164
		(220)	98,8349	-0,0092
		(310)	116,1300	0,0871
3	S.T.400°C (10min)	(110)	44,6116	0,0484
		(200)	64,5858	0,3427
		(211)	82,1900	0,0723
		(220)	98,8259	-0,0002
		(310)	116,1240	0,0931
4	S.T.600°C (10min)	(110)	44,5762	0,0838
		(200)	64,8880	0,0405
		(211)	82,2030	0,0593
		(220)	98,7633	0,0624
		(310)	116,1367	0,0804
5	S.T.200°C (30min)	(110)	44,6083	0,0517
		(200)	64,8733	0,0552
		(211)	82,2150	0,0473
		(220)	98,8128	0,0129
		(310)	116,0781	0,139

Table IV.2 (continued): Displacements of the five first peaks in the heat affected zone (HAZ).

sample		(hkl)	2 θ (°)	$\Delta 2\theta$ (°)
6	S.T.400°C (30min)	(110)	44,72	-0,06
		(200)	64,9855	-0,057
		(211)	82,36	-0,0977
		(220)	98,944	-0,1183
		(310)	116,3783	-0,1612
7	S.T.600°C (30min)	(110)	44,60	0,06
		(200)	64,8508	0,0777
		(211)	82,2278	0,0345
		(220)	98,8258	-0,0001
		(310)	116,0910	0,1261
8	S.T.200°C (1h)	(110)	44,6125	0,0475
		(200)	64,8767	0,0518
		(211)	82,2030	0,0427
		(220)	98,7865	0,0392
		(310)	116,1500	0,0804
9	S.T.400°C (1h)	(110)	44,6440	0,016
		(200)	64,9448	-0,0163
		(211)	82,2500	0,0123
		(220)	98,8320	-0,0063
		(310)	116,1588	0,0671
10	S.T.600°C (1h)	(110)	44,6432	0,0168
		(200)	64,9079	0,0206
		(211)	82,2247	0,0376
		(220)	98,8072	0,0185
		(310)	116,0877	0

Table IV.3: Displacements of the five first peaks in the fusion zone (FZ).

sample		(hkl)	$2\theta(^{\circ})$	$\Delta 2\theta(^{\circ})$
1	Untreated sample	(110)	44,6363	0
		(200)	64,8870	0
		(211)	82,2328	0
		(220)	98,8194	0
		(310)	116,1892	0
2	S.T.200°C (10min)	(110)	98,8587	-0,0029
		(200)	116,2022	-0,0234
		(211)	98,8587	-0,0172
		(220)	116,2022	0,0553
		(310)	98,8587	-0,0130
3	S.T.400°C (10min)	(110)	44,6396	-0,0033
		(200)	64,8653	0,0217
		(211)	82,2468	-0,014
		(220)	98,8232	0,0908
		(310)	116,1109	0,0783
4	S.T.600°C (10min)	(110)	44,6342	0,0021
		(200)	64,8955	-0,0085
		(211)	82,2388	-0,006
		(220)	98,8480	0,066
		(310)	116,2218	-0,0326
5	S.T.200°C (30min)	(110)	44,9252	0,1463
		(200)	65,1030	0,1102
		(211)	82,5831	0,0772
		(220)	98,0618	0,0656
		(310)	116,3227	0,074

Table IV.3 (continued): Displacements of the five first peaks in the heat affected zone (HAZ).				
sample		(hkl)	2 θ (°)	$\Delta 2\theta$ (°)
6	S.T.400°C (30min)	(110)	44,49	0,1463
		(200)	64,7768	0,1102
		(211)	82,1556	0,0772
		(220)	98,7538	0,0656
		(310)	116,1152	0,074
7	S.T.600°C (30min)	(110)	44,7675	-0,1312
		(200)	64,9438	-0,0568
		(211)	82,3402	-0,1074
		(220)	98,9438	-0,1244
		(310)	116,2729	-0,0837
8	S.T.200°C (1h)	(110)	44,6449	-0,0086
		(200)	64,8036	0,0834
		(211)	82,2466	-0,0138
		(220)	98,8047	0,1093
		(310)	116,1464	0,0428
9	S.T.400°C (1h)	(110)	44,6400	-0,0037
		(200)	64,8962	-0,0092
		(211)	82,2780	-0,0452
		(220)	98,8565	0,0575
		(310)	116,1258	0,0634
10	S.T.600°C (1h)	(110)	44,6284	0,0079
		(200)	64,9074	-0,0204
		(211)	82,2516	-0,0188
		(220)	98,8203	0,0937
		(310)	116,2270	-0,0378

IV.3.2 Peak characterization

The tables (IV.4-6) resume the peaks characterizations (Planes (hkl) , peak position (Pos. $2\theta[^\circ]$), the distance between the planes ($d_m(A^\circ)$), the intensity (Height (cts)), the full width at half maximum (FWHM) and the peak Area) of the five first peaks before and after the heat treatments at 200°C , 400°C and 600°C for 10 min, 30 min and 1 hour in the three studied zones which are the base metal(BM) , the heat affected zone(HAZ) and the fusion zone(FZ). The high intensity of the base metal is always before heat treatment, after all heat treatments the intensities of all peaks have diminished, the highest and the lowest intensities have been obtained after heat treatments for 10 min and 30 min respectively.

In the heat affected zone (HAZ): the high intensity is corresponding to the untreated sample of all peaks, excepting for the second peak after heat treatment at 200°C . The highest intensities have been obtained after heat treatment for 10 min and 1 h at 200°C ; we found the lowest intensities after heat treatment at 200°C , 400°C and 600°C for 30 min of all peaks.

For the fusion zone (FZ): there a decrease in the intensities of the peaks after heat treatment excepting for 1 h at 200°C where we find an increase of the intensities of all the peaks, the lowest intensities are obtained at 400°C for 1 h.

It is well known that the variation of the intensities is corresponding of recrystallization phenomena or reorientation of grains (texture) [79,118].

Table IV.4: Results of the diffraction profiles analysis in the base metal (BM).

Sample		(hkl)	Pos. 2θ [°]	d_m (Å)	Height (cts)	FWHM	Area
1	Untreated sample	(110)	44,6540	2,02767	11281,96	0,1584	2382,75
		(200)	64,9171	1,43528	1930,92	0,1980	509,76
		(211)	82,2500	1,17114	3616,35	0,1980	954,72
		(220)	98,8466	1,01422	1070,64	0,1980	282,65
		(310)	116,0799	0,90771	1339,22	0,1584	636,40
2	S.T.200°C (10min)	(110)	44,6376	2,02838	7935,13	0,1584	0,1584
		(200)	64,9067	1,43548	1930,92	0,2772	0,2772
		(211)	82,2500	1,17125	2408,11	0,2376	0,2376
		(220)	98,8466	1,01417	727,17	0,2376	0,2376
		(310)	116,1224	0,90771	1196,52	0,3168	0,3168
3	S.T.400°C (10min)	(110)	44,6447	2,02951	5373,31	0,1584	1970,02
		(200)	64,9140	1,43649	1685,15	0,2772	533,86
		(211)	82,2402	1,17182	2068,66	0,2376	248,52
		(220)	98,8317	1,01433	588,36	0,3168	442,23
		(310)	116,1229	0,90771	1196,52	0,6336	1970,02
4	S.T.600°C (10min)	(110)	44,5234	2,03104	9327,72	0,2376	1970,02
		(200)	64,8134	1,43585	1682,06	0,2772	532,88
		(211)	82,1795	1,17174	2875,44	0,2772	910,94
		(220)	98,7088	1,01480	627,44	0,2376	247,50
		(310)	116,1197	0,90764	1205,66	0,4752	763,00
5	S.T.200°C (30min)	(110)	44,5899	2,0344	1666,28	0,1632	362,58
		(200)	64,8475	1,43665	233,14	0,2856	88,78
		(211)	82,2196	1,17155	456,44	0,2856	173,81
		(220)	98,7949	1,01456	146,56	0,3264	63,78
		(310)	116,1991	0,90743	163,35	0,5712	124,41

Table IV.4 (continued): Results of the diffraction profiles analysis in the base metal (BM).

Sample		(hkl)	Pos. 2θ [°]	d_m (Å°)	Height (cts)	FWHM	Area
6	S.T.400°C (30min)	(110)	44,6470	2,02798	1187,21	0,1632	258,34
		(200)	64,8842	1,43593	292,12	0,2856	111,24
		(211)	82,2674	1,17099	527,25	0,1632	114,73
		(220)	98,839	1,01423	124,63	0,3264	54,24
		(310)	116,20	0,90729	197,09	0,6528	171,55
7	S.T.600°C (30min)	(110)	44,6379	2,02837	2,02837	0,1836	348,34
		(200)	64,8897	1,43582	1,34582	0,2448	89,13
		(211)	82,2434	1,17127	1,17127	0,2040	103,76
		(220)	98,8053	1,01448	1,01448	0,3264	61,92
		(310)	116,1647	0,90751	0,90751	0,4896	132,17
8	S.T.200°C (1h)	(110)	44,6350	2,02850	3580,29	0,1980	756,16
		(200)	64,8950	1,43572	636,06	0,1980	167,92
		(211)	82,2500	1,17119	1089,06	0,1980	287,92
		(220)	98,8197	1,01437	352,78	0,3168	149,01
		(310)	116,2100	0,90788	391,19	0,4752	247,86
9	S.T.400°C (1h)	(110)	44,6535	2,02770	8239,82	0,1584	2175,2 2
		(200)	64,9005	1,43560	1689,82	0,2772	624,56
		(211)	82,2614	1,17106	2455,92	0,2376	778,03
		(220)	98,8567	1,01409	697,51	778,03	294,63
		(310)	116,1844	0,90741	1233,39	0,3168	775,14
10	S.T.600°C (1h)	(110)	44,6284	2,02878	3154,92	0,1584	666,32
		(200)	64,9289	1,43505	781,27	0,2376	247,50
		(211)	82,2500	1,17087	949,72	0,1980	250,73
		(220)	98,8398	1,01422	280,54	0,2376	247,50
		(310)	116,2400	0,90713	497,54	0,4752	303,83

Table IV.5: Results of the diffraction profiles analysis in the heat affected zone (HAZ).

Sample		(hkl)	Pos. 2 θ [°]	d _m (Å°)	Height (cts)	FWHM	Area
1	Untreated sample	(110)	44,6600	2,02742	14105,84	0,1584	2979,15
		(200)	64,9285	1,43505	2521,17	0,1980	665,59
		(211)	82,2623	1,17105	4363,90	0,3560	921,66
		(220)	98,8257	1,01433	1347,01	0,1584	355,61
		(310)	116,2171	0,90725	1797,54	0,1980	854,19
2	S.T.200°C (10min)	(110)	44,6422	2,02319	13143,10	0,1584	2775,82
		(200)	64,9059	1,43550	2595,60	0,2376	822,29
		(211)	82,2459	1,17124	3848,37	0,1980	1015,97
		(220)	98,8349	1,01426	1066,66	0,2376	337,92
		(310)	116,1300	0,90788	1603,02	0,4752	1015,67
3	S.T.400°C (10min)	(110)	44,6116	2,02880	7176,29	0,3168	1515,63
		(200)	64,5858	1,43340	1411,39	0,2376	521,65
		(211)	82,1900	1,17131	2286,37	0,3168	724,32
		(220)	98,8259	1,01428	613,56	0,3168	259,17
		(310)	116,1240	0,90771	1057,34	0,2772	893,24
4	S.T.600°C (10min)	(110)	44,5762	2,02753	10687,00	0,1584	2821,57
		(200)	64,8880	1,43571	1480,25	0,2376	390,79
		(211)	82,1900	1,17133	3711,92	0,2376	1175,94
		(220)	98,8259	1,01416	1031,86	0,2376	217,93
		(310)	116,1240	0,90722	1355,83	0,4752	429,53
5	S.T.200°C (30min)	(110)	44,6083	2,02965	3776,1	0,1224	616,26
		(200)	64,8733	1,43614	534,04	0,2448	174,31
		(211)	82,2150	1,1716	906,37	0,1224	147,92
		(220)	98,128	1,01443	251,08	0,3264	109,27
		(310)	116,078	0,90793	302,75	0,5712	230,59

Table IV.5 (continued): Results of the diffraction profiles analysis in the heat affected zone (HAZ).

Sample		(hkl)	Pos. 2θ [°]	d_m (Å°)	Height (cts)	FWHM	Area
6	S.T.400°C (30min)	(110)	44,7210	2,02480	2816	0,1428	536,17
		(200)	64,9855	1,43393	669,38	0,1836	163,86
		(211)	82,36	1,169869	919,23	0,1428	175,02
		(220)	98,944	1,01343	224,85	0,2448	73,39
		(310)	116,3783	0,90646	352,41	0,2856	134,20
7	S.T.600°C (30min)	(110)	44,60	2,02994	2324,36	0,1632	505,78
		(200)	64,8508	1,43659	406,46	0,2448	132,67
		(211)	82,2278	1,17145	612,66	0,1428	116,65
		(220)	98,8258	1,01433	198,97	0,3264	86,59
		(310)	116,0910	0,90729	275,25	0,4896	179,68
8	S.T.200°C (1h)	(110)	44,6125	2,02947	12218,63	0,1584	2580,6
		(200)	64,8767	1,43611	2478,97	0,2376	785,34
		(211)	82,2196	1,17155	3704,11	0,1980	977,82
		(220)	98,7865	1,01436	1094,03	0,3168	462,12
		(310)	116,1500	0,90758	1585,33	0,3168	669,64
9	S.T.400°C (1h)	(110)	44,6440	2,02811	5014,65	0,1584	1059,1
		(200)	64,9448	1,43473	780,87	0,1980	206,15
		(211)	82,2500	1,17118	1798,78	0,1980	474,88
		(220)	98,8320	1,01428	533,02	0,2376	168,86
		(310)	116,1588	0,90755	655,12	0,3168	280,94
10	S.T.600°C (1h)	(110)	44,6432	2,02853	5058,60	0,1584	1068,38
		(200)	64,9079	1,43546	796,68	0,2376	252,39
		(211)	82,2247	1,17149	1410,84	0,2376	446,95
		(220)	98,8072	1,01447	448,50	0,3168	189,44
		(310)	116,0877	0,90789	581,02	0,3168	245,42

Table IV.6: Results of the diffraction profiles analysis in the fusion zone (FZ).

Sample		(hkl)	Pos. 2 θ [$^{\circ}$]	d_m (A°)	Height (cts)	FWHM	Area
1	Untreated sample	(110)	44,6363	2,02844	13324,64	0,1584	2814,16
		(200)	64,8870	1,43587	1903,66	0,2376	603,09
		(211)	82,2388	1,17140	2927,68	0,2376	927,49
		(220)	98,8194	1,01438	1145,25	0,2376	362,81
		(310)	116,1892	0,90739	1335,86	0,3544	634,80
2	S.T.200 $^{\circ}$ C (10min)	(110)	44,6392	2,02832	1350,56	0,1584	2852,58
		(200)	64,9104	1,43541	1750,59	0,2376	554,59
		(211)	82,2500	1,17190	4561,92	0,2376	1445,22
		(220)	98,8587	1,01408	1176,67	0,3168	497,02
		(310)	116,2022	0,90732	1213,45	0,4752	768,84
3	S.T.400 $^{\circ}$ C (10min)	(110)	44,6396	2,02830	3319,84	0,1584	701,15
		(200)	64,8653	1,43630	429,98	0,3168	181,63
		(211)	82,2468	1,17121	1177,49	0,1584	248,69
		(220)	98,8232	1,01435	292,88	0,3168	123,71
		(310)	116,1109	0,90777	404,73	0,3960	213,76
4	S.T.600 $^{\circ}$ C (10min)	(110)	44,6342	2,02861	10725,02	0,1980	283,40
		(200)	64,8955	1,43578	1479,38	0,1980	390,56
		(211)	82,2388	1,17140	3645,50	0,2376	1155,21
		(220)	98,8480	1,01419	1021,19	0,1584	215,68
		(310)	116,2218	0,90756	1432,39	0,2376	907,56
5	S.T.200 $^{\circ}$ C (30min)	(110)	44,92523	2,01606	2016 ,3	0,1428	383,9
		(200)	65,1030	1,43163	370 ,74	0,2448	121,01
		(211)	82,5831	1,16731	819 ,96	0,2448	267,64
		(220)	99,0618	1,01254	273 ,52	0,3264	119,03
		(310)	116,3227	0,90668	415,67	0,4080	226,13

Table VI.6 (continued): Results of the diffraction profiles analysis in the fusion zone (FZ).

Sample		(hkl)	Pos. 2 θ [°]	d_m (Å°)	Height (cts)	FWHM	Area
6	S.T.400°C (30min)	(110)	44,49	2,03477	3487,63	0,1428	664,04
		(200)	64,7768	1,43805	489,78	0,2040	133,22
		(211)	82,1556	1,17230	1052,98	0,1224	171,85
		(220)	98,7538	1,01487	330,96	0,2448	108,02
		(310)	116,1152	0,90775	396,99	0,4896	241,53
7	S.T.600°C (30min)	(110)	44,7675	2,02280	1874,15	0,1428	356,84
		(200)	64,9438	1,43475	307,26	0,3264	133,72
		(211)	82,3402	1,17014	659,24	0,4080	358,62
		(220)	98,9438	1,01343	255,41	0,3264	111,15
		(310)	116,0910	0,90697	275,25	0,4080	167,16
8	S.T.200°C (1h)	(110)	44,6449	2,02807	16441,09	0,1584	3472,36
		(200)	64,9036	1,43555	1874,36	0,2376	593,80
		(211)	82,2466	1,17123	4336,39	0,1980	1144,81
		(220)	98,8047	1,01449	1405,87	0,2376	445,38
		(310)	116,1464	0,90760	1708,27	0,1980	450,98
9	S.T.400°C (1h)	(110)	44,6400	2,02870	1054,40	0,2376	278,36
		(200)	64,8962	1,43575	202,22	0,2376	64,06
		(211)	82,2780	1,17092	462,83	0,1980	97,75
		(220)	98,8565	1,01504	75,59	0,4752	95,79
		(310)	116,1258	0,90774	171,33	0,4752	108,56
10	S.T.600°C (1h)	(110)	44,6284	2,02821	10233,86	0,1584	2161,39
		(200)	64,9074	1,43547	1470,64	0,1584	310,60
		(211)	82,2516	1,17118	2877,06	0,1980	759,54
		(220)	98,8203	1,01437	798,03	0,2376	252,81

IV.4 Basic theory of the profile analysis of XRD profiles

XRD is powerful tool to characterize the microstructure of the polycrystalline samples. It gives the microstructures of the sample in statistical manner [119].

X-ray diffraction line profile analysis (XRDLPA) is one of the potential indirect Methods of characterizing the state defect. Basically, XRDLPA provides quantitative as well as qualitative information on several microstructural parameters, small crystallite size, size distribution, microstrain, and density of dislocation stacking faults, energy... from broadening XRD peaks [119-122].

Dislocations are one of the most important microstructural features governing the mechanical properties of crystalline materials. They are the main carriers of plasticity, hence most of the related phenomena (e.g. yielding, strain hardening, strain-rate dependence, temperature dependence, etc.) depend on how the dislocation microstructure evolves and how dislocations interact with other material defects. The dislocation microstructure evolution is an immensely complicated phenomenon on that is controlled by properties, microstructure and boundary conditions. Several mechanisms, such as dislocation dissociation, recombination, glide, cross-slip and climb, are active during material deformation and they all contribute to the final evolved microstructure [123].

Dislocation is frequently occurring lattice defects, as result of growth process or of thermal and mechanical treatments. X-ray diffraction profile analysis applied to the X-ray diffraction pattern from polycrystalline materials is effective for dislocation densities larger than $\approx 10^{14} \text{ m}^{-2}$ [25].

One of the major issues in the study of dislocation by line profile analysis (LPA) is to correctly separate their contribution to line broadening from that given by other lattice defects (like stacking faults), by the size of the coherently scattering domains (crystallites) and by instrument [25,124]. Unfortunately, straight forward extraction of quantitative information on size and strain from shape is normally impossible. The least of the problem met is probably the elimination of instrumental broadening effects, more or less reliable approaches exist which depart either from calculation of the instrumental geometrical details of the diffraction experiment. The profile of the diffraction peak is result of convolution of various effects which contains all contribution with complex manners [121,124,125].

Development of recent years, focusing on distinct anisotropic line-broadening effects, as due to the type, orientation and distribution of dislocation, which is the key for distinguishing the contribution of dislocations of the observed profiles [121,124,126].

Dislocations alter perfect crystalline order and produce anisotropic broadening of the X-ray diffraction profiles, which is described by the dislocation contrast factor. The dislocation contrast factor is the main parameter representing the anisotropic nature of the dislocation strain field and its effects on diffraction phenomena [127]. The average contrast factor (C_{hkl}) which is related directly to the elastic constants and the slip system of dislocation (slip plane and burgers vector Until now, the evaluation of this important parameter has been specific for materials showing cubic and hexagonal symmetry, and carried out through numerical calculations.) [121,127].

The developments in the numerical analysis domain of the elaboration of new complex algorithms and the presence of new calculus machines with big stored capacity and big speed of calculus, this can gives possibly of calculus of presumed parameters number like crystalline symmetry and slip system ... [121].

IV.4.1 Diffracted intensity from a defected material

Peak profiles observed in powder diffraction patterns result from different contributions: an instrumental profile component (g), usually including instrument-related geometrical factors and sample transparency, and a sample profile component (f), due to the microstructure of the studied material. The convolution of the profile components ($h = f \otimes g$) yields the observed experimental peak profile.

The algorithm of WPPM (Whole Powder Pattern Modeling) adopts with Fourier analysis. In this case there is a problem complex of the convolution which is interpreted to the product (L) of the fouriers transformed of peak profile, produced by every component separately [121].

The diffraction profile is conveniently described in terms of the diffraction vector (\vec{d}^*) in the reciprocal lattice, whose modulus is $d^* = 2 \sin \theta / \lambda$, where θ is the diffraction angle and λ the X-ray diffraction wavelength. For cubic materials, in the absence of lattice defects and load or residual strain, the diffraction vector in the Bragg condition is :

$d^*_{\{hkl\}} (d^*_{\{hkl\}} = 2 \sin \theta_{\{hkl\}} / \lambda)$ where the Miller indices are reported in curly brackets, since we refer to the family of planes as a whole. As we will see in the following, it is important to make a distinction between $d^*_{\{hkl\}}$ and d^*_{hkl} the value of the diffraction vector for a specific combination of hkl, which is related to a subcomponent of the observed profile.

The intensity from a set of {hkl} planes can be written as the sum of the contributions from all the hkl profile subcomponents:

$$I_{\{hkl\}}(\mathbf{d}^*, \mathbf{d}^*_{\{hkl\}}) = k(\mathbf{d}^*) \sum_{hkl} w_{hkl} I_{hkl}(\mathbf{d}^* - \mathbf{d}^*_{\{hkl\}} - \delta_{hkl}) \dots \dots \dots (\text{Equ.IV.1})$$

where $k(\mathbf{d}^*)$ includes microstructure-independent terms (e.g Lorentz polarization (Lp).. etc.), which are constant or known functions of \mathbf{d}^* . w_{hkl} is a weight function for the hkl component and δ_{hkl} is a shift from the reciprocal space point corresponding to the Bragg condition in the absence of defects and strain. Both w_{hkl} and δ_{hkl} depend on the specific defects present in the material. The contribution of a given subcomponent can be written as :

$$I_{hkl}(\mathbf{s}_{hkl}) = \int_{-\infty}^{+\infty} T^{TP}(\mathbf{L}) \langle \exp[2\pi i \Psi] \rangle \langle \exp[2\pi i \varphi(L)] \rangle \times \exp[2\pi i \mathbf{L} \cdot \mathbf{s}_{hkl}] d\mathbf{L} \quad (\text{Equ. IV.2})$$

where $T^{TP} \cdot \mathbf{L}$ is the Fourier Transform (FT) of the IP and the two terms in brackets ($\langle \quad \rangle$) are average phase factors due to lattice distortions (Ψ) and crystallite size/faulting (φ), respectively. In this way, we are implicitly assuming that there is no interaction between linear and planar defects (separate averages). The integration variable, L (a length in real space), is inversely proportional to $\mathbf{d}^*_{\{hkl\}}$ and is the conjugate variable of $\mathbf{s}_{hkl} = \mathbf{d}^* - \mathbf{d}^*_{\{hkl\}} - \delta_{hkl}$, the distance from the peak centroid in the reciprocal space [126].

IV.4.2 Crystallite size

The distribution of crystallite size in polycrystalline solid clearly depends on a number of factors, including the nature of the material and the method and condition of preparation. However, by far the commonest distribution reported in the literature is the lognormal distribution, which is asymetric [128]. The effect of diffracted coherent domains size have been modeled by the lognormal distribution of domains size with spherical shape. In the reality, it is a possible to use other kinds of distributions which are adapted for each specific study, but the present choice was proved its efficacy in lot of examples [121].

The lognormal distribution is defined by the following formula:

$$g(D) = \frac{1}{D \cdot \sigma \cdot \sqrt{2\pi}} \cdot e^{-\left[\frac{(\ln D - \mu)^2}{2\sigma^2} \right]} \dots \dots \dots (\text{Eq.IV.3})$$

Where σ and μ are variance and the mean lognormal distribution.

The mean size of distribution is given by this equation:

$$\langle D \rangle = \exp(\mu + \sigma^2/2) \dots \dots \dots (\text{Eq.IV.4})$$

IV.4.3 Planar faults and planes

A stacking fault is a planar defect and, as its name implies, it is a local region in the crystal where the regular stacking sequence is interrupted [23].

The dislocations and stacking faults were the most courant kinds of faults in the crystalline lattice which are can be studied by the WPPM (Whole Powder Pattern Modeling).for the dislocation, the mean density of dislocation (ρ), the cutoff R_E , the factor f_E which characterize the kind of dislocation (edge or screw) and the stacking faults can be described by the probabilities α and β [129].

The dislocations are modeled on the basic theory of Wilkens [131] were the dislocations supposed parallel, linear and with random distribution with regard to all equivalent slip systems. Dislocations alter perfect crystalline order and produce anisotropic broadening of the X-ray diffraction profiles, which is described by the dislocation contrast factor (\bar{C}_{hkl}) [128]. Line broadening anisotropy can be introduced by assuming a linear dependence of the micro-strain on the orientational parameter H. Consequently, the average contrast factor for cubic systems can be written as [126]:

$$\bar{C}_{hkl} = \bar{C}_{h00}(1 + qh) = \bar{C}_{h00} \left[1 + \frac{h^2k^2+h^2l^2+k^2l^2}{(h^2+k^2+l^2)} \right] \dots\dots\dots(\text{Eq.IV.5})$$

$$H = (h^2k^2+h^2l^2+l^2k^2) / (h^2+k^2+l^2)^2 \dots\dots\dots (\text{Eq.IV.6})$$

The expression of the contrast factor for each kind of dislocation is given in the following:

The contrast factor for screw dislocation: $\bar{C}_{hkl, screw} = A_s + B_s \cdot H$

The contrast factor for edge dislocation: $\bar{C}_{hkl, edge} = A_e + B_e \cdot H$

Average dislocation contrast factor (DCF) for mixed straight dislocations do not lie exactly between the limits of the extreme cases of screw and edge dislocations. Differences, however, are limited and not extreme: this means that diffraction can hardly distinguish the presence of a specific mixed dislocation from a mixture of the appropriate fractions of edge and screw dislocations. For this reasons, it is convenient to redefine the average DCF as:

$$C_{\{hkl\}} = f_E C_{\{hkl\},E} + (1 - f_E) C_{\{hkl\},S} \dots\dots\dots(\text{Eq.IV.7})$$

Where f_E is the effective fraction of edge dislocations, whereas $C_{\{hkl\},E}$ and $C_{\{hkl\},S}$ are the average DCF for edge and for screw dislocations, respectively. In this way, if $C_{\{hkl\},E}$ and $C_{\{hkl\},S}$ are known, one can refine f_E from the observed data, as an effective measure of the dislocation character. If extreme values ($f_E = 0$ or $f_E = 1$) are found, this might suggest a more careful evaluation of different slip systems or dislocation types [25].

Where A_e , B_e , A_s and B_s are constant can be calculasated from the elastic constants of studied material single crystal and from its slip system. The values of contrast factors of our material were:

- **Aedge** = 2.64760E-01
- **Bedge** = -3.55950E-01
- **Ascrew** = 3.46780E-01
- **Bscrew** = -8.06017E-01.

and the slip system of α (BCC) micro alloyed steel with low carbon percent was:

A-Fe Primary $1/2 \langle 111 \rangle \{-110\}$.

Owing to the lack of suitable mathematical tools to deal with dislocations in crystals of any symmetry, contrast factors are so far only known for a few slip systems in high-symmetry phases and little detail is given in the literature on the calculation procedure [127].

The graphic results of the Whole Powder Pattern Modeling (WPPM) procedure are illustrated on the Figure IV.42 - IV.53. These figures show the fitting profiles, the agreement between the experimental profiles (the small black circle) and modeled (continued red line) and residual continued gray line, the later presents the difference between the experimental and the modeled data. We can see the form of the residual line which is sufficiency straight. This indicate the good convergence, this later can be explained by the factor named GoF (Goodness of fit).

IV.5 Analysis of diffraction profiles

IV.5.1 Untreated sample

IV.5.1.1 Base metal

The figure IV.39 illustrates the fitting spectrum of the sample untreated base metal and the Table VI.7 gives the results of PM2K calculus (Sample1(BM)). We observe the five first peaks of the iron which are compatible with A.S.T.M fiches. The analysis proves that the coherent domains distribution of the diffraction is the Lognormal, with mean value is equal to **710,1456 nm**, and the standard deviation $Sd=7.585354\text{nm}$. The dimensionless parameter M is the Wilkens factor for characterizing the dislocation arrangement, It gives by this relation $M=Re.\sqrt{\rho}$. This parameter characterizes the distribution and the screening of stress and the strain field of the dislocation, if the value of M is smaller or greater than unity, the screening effect is strong or weak [131]. $M=0,8529995$, this factor is smaller than unity, than there is a strong screening effect, a small value of $M(M<1)$ indicate strong dipole character [132]. Borbvely et al [128] demonstrated that a strong screening indicate a faster decaying of the strain field.

Table VI.7: Results of PM2K calculus(Sample1(BM)).

Unit cell parameter [nm]	0,2871126
Burgers modulus[nm]	0,2486468
Density of dislocations (ρ) $\times 10^{14}[\text{m}^{-2}]$	7.807740
effective outer cut-off radius [nm]	30,52714
Fraction of edge dislocation	0,2996908
Domain size (D)[nm]	710,1456
Standard deviation(Sd)[nm]	7.585354
Wilkens parameter(M)	0,8529995
WSS= 5120.72, Rwp=2.6599%,GoF=1.31174	

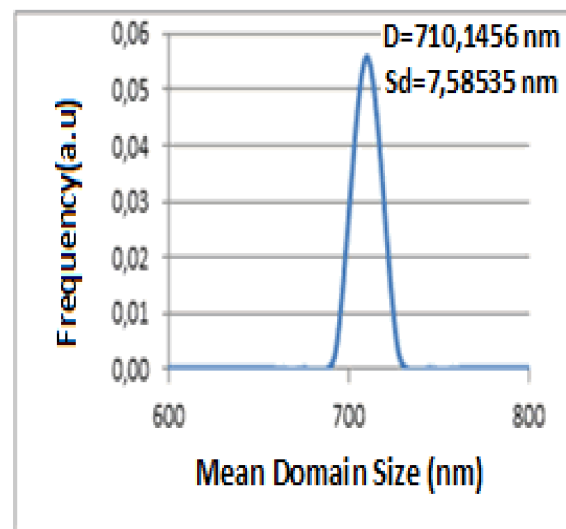
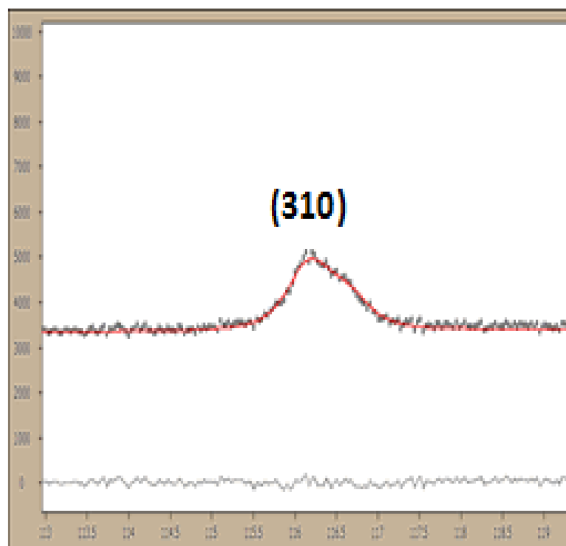
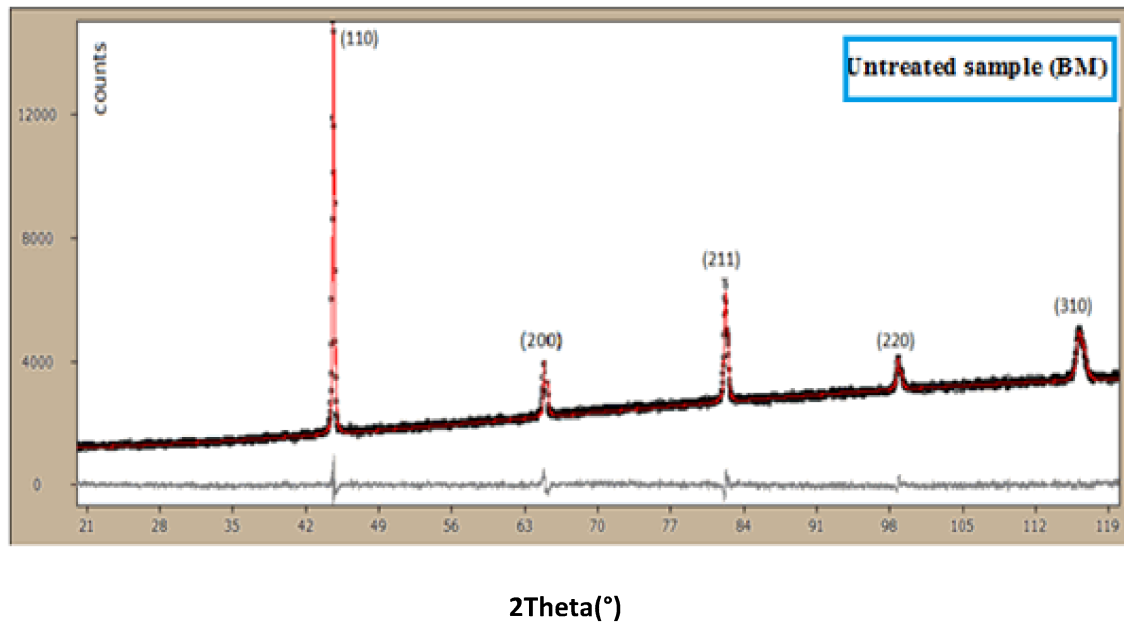


Figure VI.39 : (a) X-ray diffraction profile of the untreated sample (BM), (b) Fifth peak, (c) The mean domain size.

IV.5.1.2 Heat affected zone

The figure IV .40 presents the diffraction X-rays spectrum of the untreated heat affected zone (HAZ) and the Table VI.8 gives the results of PM2K calculus. The analysis proves that the coherent domains distribution of the diffraction is the : Lognormal, with mean value is equal to **810,4057nm**, and the standard deviation **Sd=81,04057nm**. The Wilkens parameter is the dislocation arrangement factor. Its value (**M=0,7649467**) is smaller than unity, than

there is a strong screening effect, a small value of $M(M < 1)$ indicate strong dipole character and strong screening indicates a faster decaying of the strain field [128].

Table VI.8 : Results of the PM2K calculus (sample 1 (HAZ)).	
Unit cell parameter [nm]	0,2871384
Burgers modulus(β)[nm]	0,2486692
Density of dislocation (ρ)x10 ¹⁴ [m ²]	6.501594
effective outer cut-off radius(Re)[nm]	30
Fraction of edge dislocation(f_e)	0,5
Domain size (D)[nm]	810,4057
Standard deviation(Sd)[nm]	81,04057
Wilkinsparameter(M)	0,7649467
WSS= 5429.99, Rwp=2.59495% GoF=1.35055	

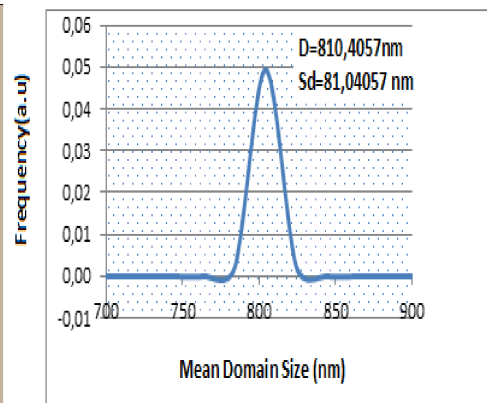
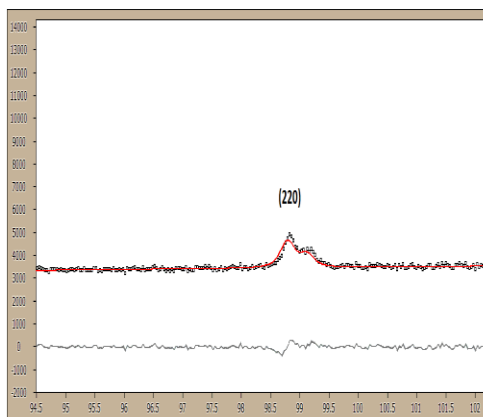
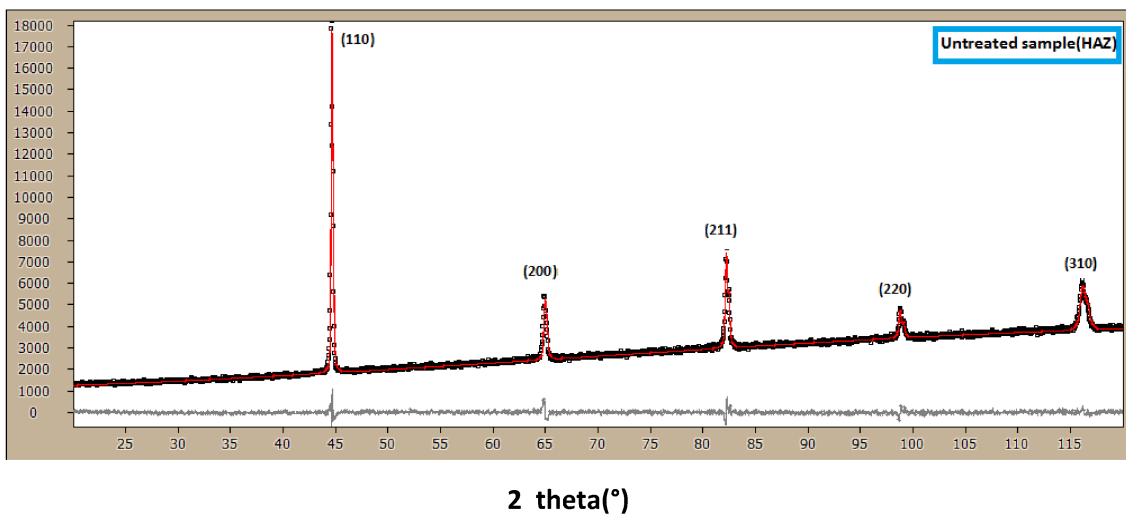
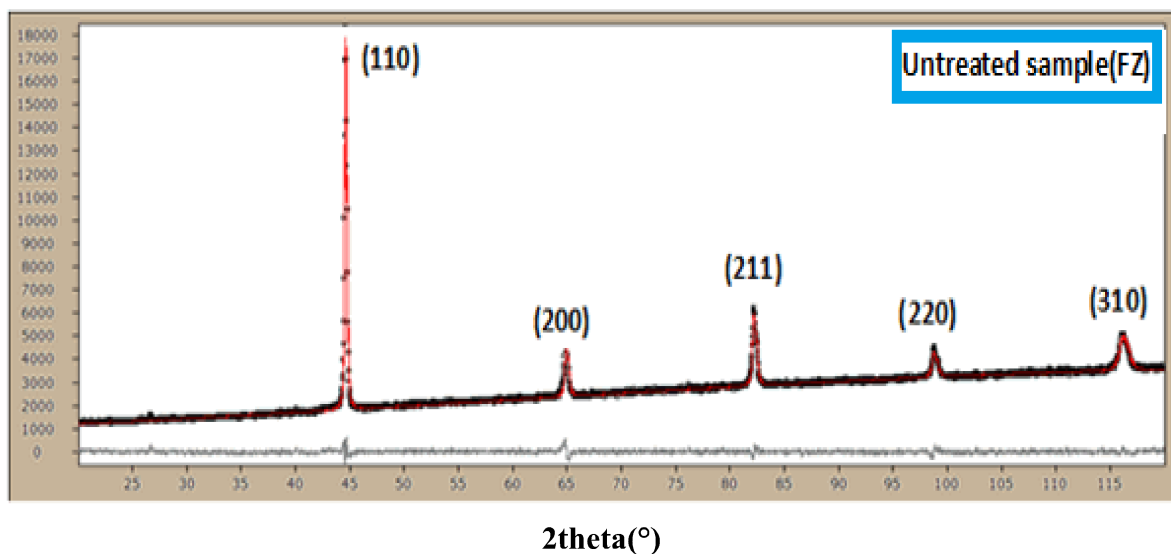


Figure VI.40: (a) X-ray diffraction profile of the untreated sample (HAZ), (b) Fourth peak, (c) The mean domain size.

IV.5.1.3 Fusion zone

The figure IV.41 presents the diffraction X-rays spectrum of the untreated heat affected zone (HAZ) and the Table VI.9 gives results of PM2K calculus. The analysis proves that the diffraction coherent domain distribution is the: Lognormal, with mean value is equal to $D=162,5463\text{nm}$, and the standard deviation $Sd=1.625504\text{nm}$. The Wilkens parameter is the dislocation arrangement factor, its value ($M=1.009818$) is near to the unity, this indicates that the arrangement of dislocation is quasi-homogeneous, where the dislocation stops to the aftermost or nearer dislocation. In This situation $Re \approx \rho^{-1/2}$ [121].

Tableau VI.9: Results of the PM2K calculus (sample 1 (FZ)).	
Unit cell parameter [nm]	0,287179
Burgers modulus(β) [nm]	0,2487043
Density of dislocations $\times 10^{14}[\text{m}^{-2}]$	10,18648
effective outer cut-off radius(Re) [nm]	31,63960
Fraction of edge dislocation(f_e)	0,0067276
Domain size(D) [nm]	162,5463
Standard deviation(Sd) [nm]	1.625504
Wilkinsparameter(M)	1.009818
WSS= 5133.63, Rwp=2.57792% GoF=1.31318	



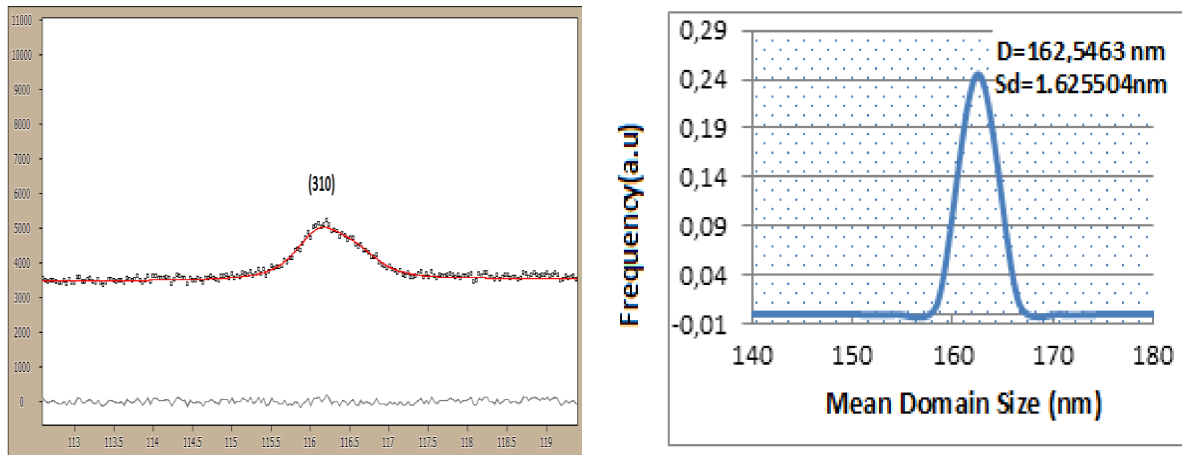


Figure VI.41: (a) X-ray diffraction profile of the untreated sample (FZ), fitting by PM2K, (b) Fifth peak, (c) The mean domain size

The figure IV.42 shows the graphic results of the WPPM (Whole Powder Pattern Modeling) in the base metal after heat treatment for 10 min at 200°C, 400°C and 600°C.

WPPM can provide the mean dislocation density (ρ) and the effective cut off radius (R_e) of the dislocation system; a further parameter was introduced to refine the relative fraction of edge (versus screw) dislocations. The domain size effect was modeled by a lognormal distribution (mean μ and variance σ) of spherical domains. All data were analyzed by the software PM2K [117]. The table IV.10 resumes the results of the calculus with this method.

The agreement between the experimental profiles (black points) and the modeled one (red continued line) is very clear. On the figures difference between the experimental and modeled profiles is marked by gray line. The shape of the gray line is plane with little reliefs, this indicates a good convergence. We observe the presence of the five first typical peaks of iron: (110), (200), (211), (220) and (310). These peaks were compatible the A.S.T.M folders. The intensities of the five peaks, decrease with the increase of the heat treatment temperature.

The values of the Wilkens parameter (M), the dimensionless parameter M is the factor for characterizing the dislocation arrangement. Before heat treatment and after heat treatment at 600°C, this factor is smaller than unity M ($M=0,8521$, $0,871789$ respectively), this indicates strong dipole character and strong screening indicates a faster decaying of the strain field [128, 132]. However this factor after heat treatment at 200°C and 400°C present values near the unity ($M=0,974594$ and $M=0,987871$ respectively), when ($M \approx 1$) indicates the arrangement of dislocation is quasi-homogeneous, where the dislocation stops to the aftermost or nearer dislocation. In This situation $R_e \approx \rho^{-1/2}$ [121]. In this case there is a strong

correlation between dislocation, strong screening of field strain (like in the dislocation walls or between the dipoles) [133].

The figure IV.43 shows the graphic results of the WPPM (Whole Powder Pattern Modeling) in the base metal after heat treatment for 30 min at 200°C, 400°C and 600°C.

The table IV.11 resumes the results of the calculus with this method.

The agreement between the experimental profiles (black points) and the modeled one (red continued line) is very clear on the figures, difference between the experimental and modeled profiles is marked by gray line. The shape of the gray line is plane with little reliefs, this indicates a good convergence. These constations are confirmed by the smaller values of WSS between (5120.72 and 7536.49) with the Gof (Goodness of fit) which is stranded between 1.0952 and 1.31174.

After heat treatment at 200°C there is an increase of the Wilkens parameter values (0,8521 1.171667). In this case there is a weak screening of dislocations field, which interpreted by slow decrease of strain fields, then there is random distribution and big quantity of dislocations ($\rho=11,6079$), this zone characterized by high energy. But after heat treatment at 400°C and 600°C there is a slight increase in the dislocation density, the Wilkens parameter values are around the unity ($M \approx 1$) indicates the arrangement of dislocation is quasi-homogeneous, where the dislocation stops to the aftermost or nearer dislocation. In this case there is a strong correlation between dislocation, strong screening of field strain (like in the dislocation walls or between the dipoles). This situation is characterized by low energy [121].

The figure IV.43 shows the graphic results of the WPPM (Whole Powder Pattern Modeling) in the base metal after heat treatment for 1H at 200°C, 400°C and 600°C.

The table IV.12 resumes the results of the calculus with this method.

The agreement between the experimental profiles (black points) and the modeled one (red continued line) is very clear on the figures, difference between the experimental and modeled profiles is marked by gray line. The shape of the gray line is plane with little reliefs, this indicates a good convergence. These constations are confirmed by the smaller values of WSS between (4293.62 and 5120.72) with the Gof (Goodness of fit) which is stranded between 1.20094 and 1.31174.

The intensities of the five peaks decrease with the increase of the heat treatment temperature.

The values of the Wilkens parameter (M), the dimensionless parameter M is the factor for characterizing the dislocation arrangement. Before heat treatment and after heat treatment at 600°C, this factor is smaller than unity ($M=0,852991$ and $0,890367$ respectively), this

indicates strong dipole character and strong screening indicates a faster decaying of the strain field [128, 132]. We can conclude that zone is characterized by total low energy. While this factor after heat treatment at 200°C and 400°C present values near the unity ($M=1.025483$ and 0.9815030 respectively), when ($M \approx 1$) indicates the arrangement of dislocation is quasi-homogeneous, where the dislocation stops to the aftermost or nearer dislocation. In this case there is a strong correlation between dislocation, strong screening of field strain (like in the dislocation walls or between the dipoles) [133] We can conclude that zone is characterized by low energy

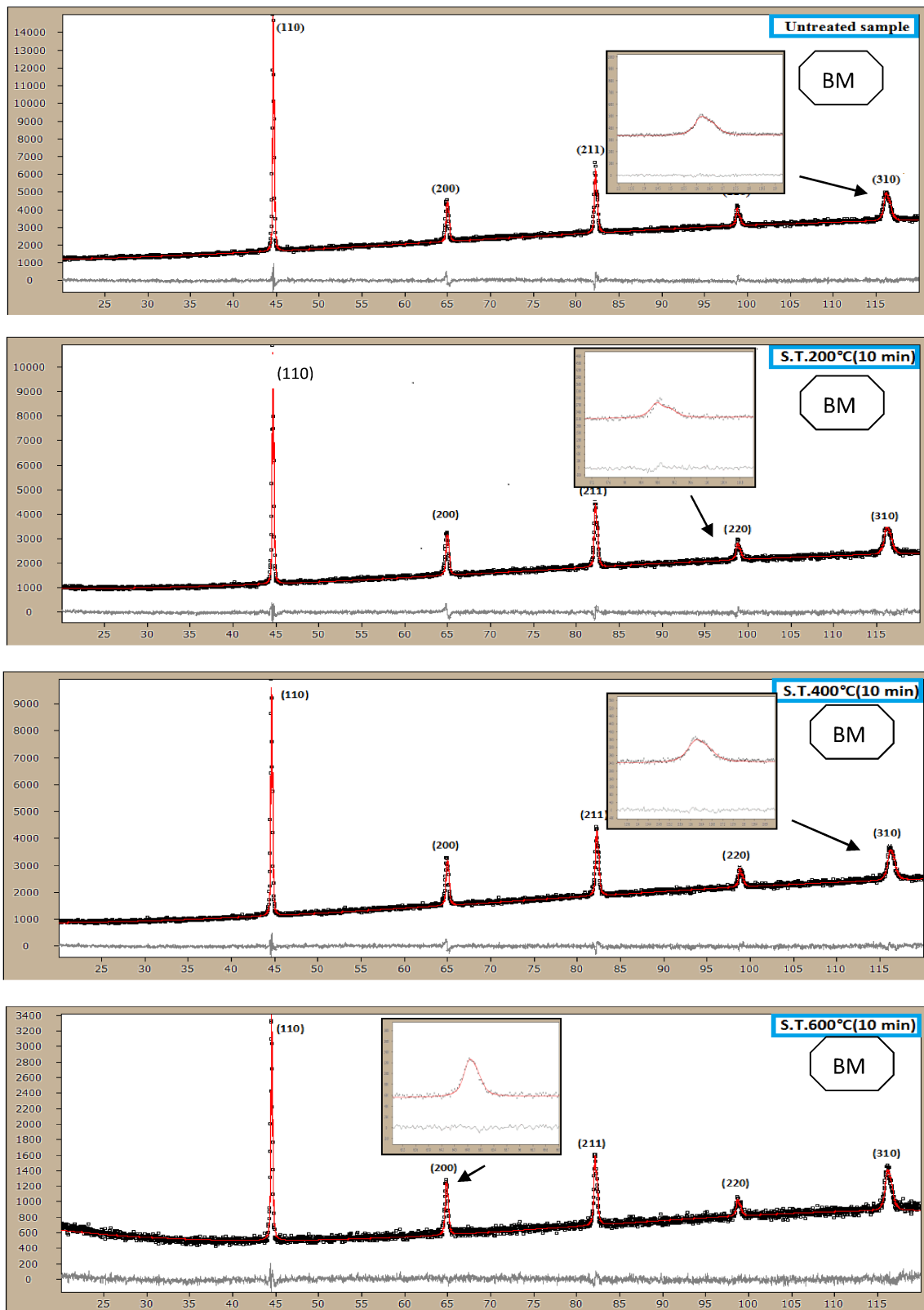


Figure VI.42: X-ray diffraction profiles of base metal before and after heat treatments for 10 min at 200°C, 400°C and 600°C respectively, fittings by PM2K.

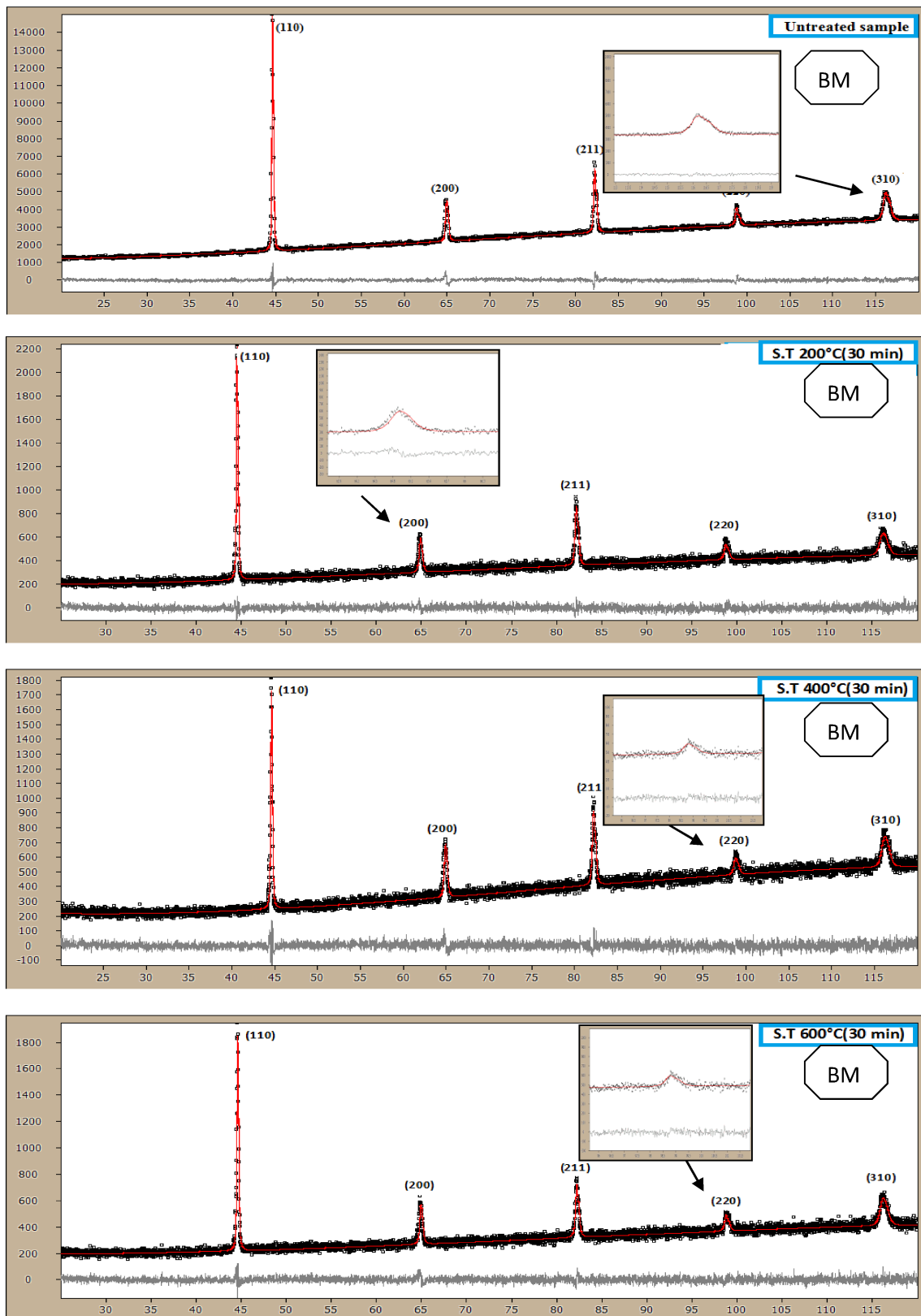


Figure VI.43: X-ray diffraction profiles of base metal before and after heat treatments for 30 min at 200°C, 400°C and 600°C respectively, fittings by PM2K.

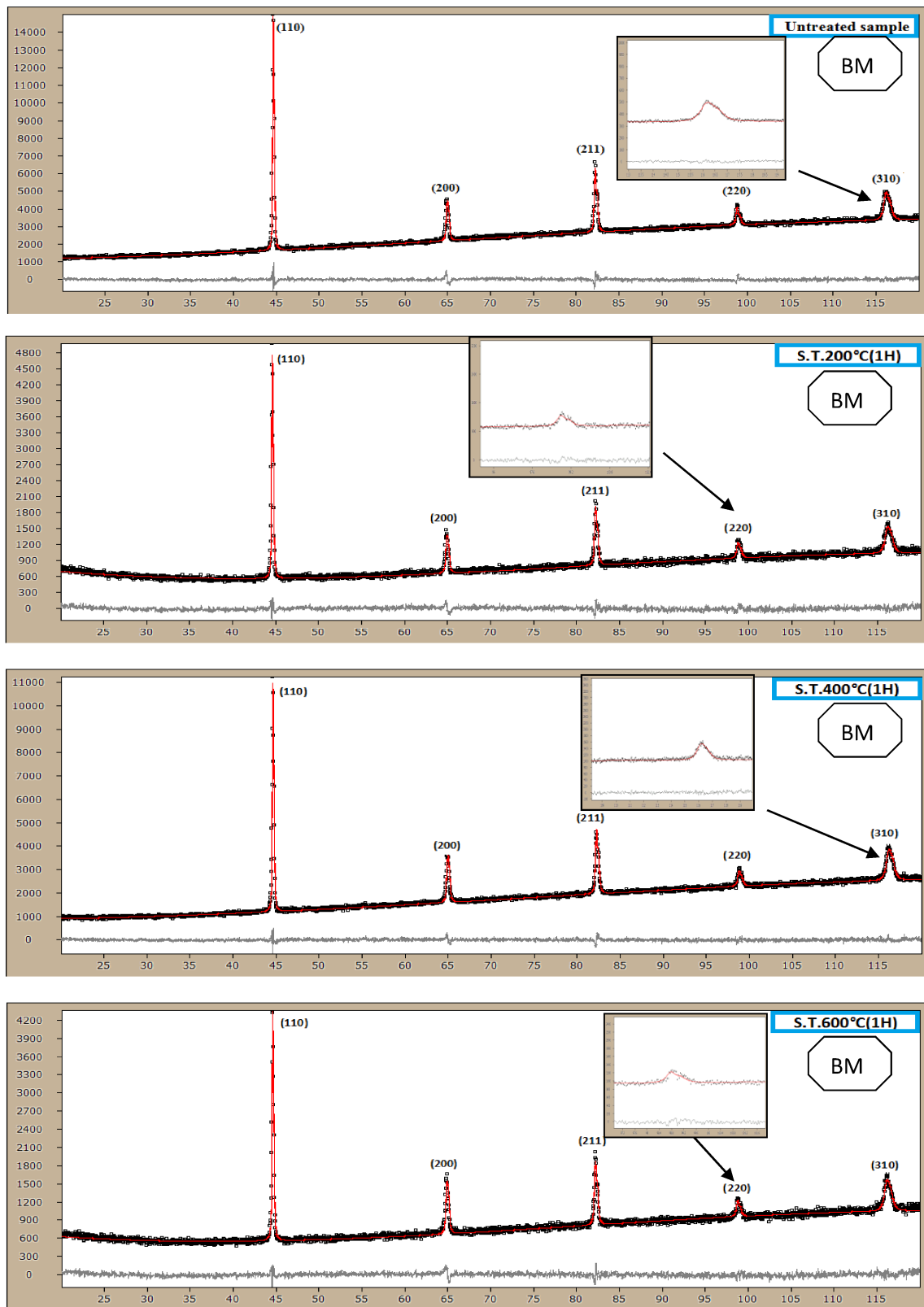


Figure VI.44: X-ray diffraction profiles of base metal before and after heat treatments for 1h at 200°C, 400°C and 600°C respectively, fittings by PM2K.

TableVI.10: Results of the PM2K calculus in the base metal before and after heat treatment for 10 min.

parameters		UN sample	200C	400C	600C
Unit cell parameter	[nm]	0,287113	0,287114	0,287084	0,2870148
Burgers vector modulus (b)	[nm]	0,248647	0,248648	0,248622	0,2485633
Density of dislocations(ρ)	$\times 10^{14}[\text{m}^{-2}]$	7.80774	9.918946	10,16470	7.746255
Effective outer cut-off radius (Re)[nm]		30,52714	30,94502	30,9851	31,32314
Domain size average(D_{ave})		710,1456	354,5189	423,5498	113,1483
Standard deviation(Sd)		7.585354	1.304960	4.235604	1.131511
Wilkens parameter(M)		0,8521	0,974594	0,987871	0,871789
Edge dislocation fraction(f_e)		0,299691	0,065188	0,149028	$1.82 \cdot 10^{-12}$
Lognormal mean (μ)	[nm]	6.565413	5.870085	6.048621	4.728649
Variance (σ)		0,010681	0,036797	0,01	0,01
WSS		5120.72	4851.17	4053.42	4347.8
Rwp		2.6599	3.08996	2.81979	4.60718
Rexp		2.02776	2.42058	2.41654	3.8136
Gof		1.31174	1.27654	1.16687	1.20809

TableVI.11: Results of the PM2K calculus in the base metal before and after heat treatment for 30 min.

Parameters		UN sample	200°C	400°C	600°C
Unit cell parameter	[nm]	0,287113	0,287062	0,2870772	0,287116
Burgers vector modulus (b)	[nm]	0,248647	0,248603	0,2486162	0,2486497
Density of dislocations(ρ)	$\times 10^{14}[\text{m}^{-2}]$	7.80774	11,6079	9,758948	8,9844
Effective outer cut-off radius (Re)[nm]		30,52714	34,38962	30	32,57935
Domain size average(D_{ave})	[nm]	710,1456	/	1.840235	187,5451
Standard deviation (Sd)		7.585354	/	1.844845	1.879619
Wilkens parameter(M)		0,8521	1.171667	0,9371795	0,9961124
Edge dislocation fraction(f_E)		0,299691	$4.3791 \cdot 10^{-47}$	0,5	0,1394931
Lognormal mean (μ)	[nm]	6.565413	1.006590	5.210063	5.233969
Variance (σ)		0,010681	0,1	0,1	0,01002197
WSS		5120.72	7207.57	7536.49	6800.95
Rwp		2.6599	6.09011	5.80209	6.21657
Rexp		2.02776	5.40112	5.16358	5.6762
Gof		1.31174	1.12756	1.12366	1.0952

Table VI.12: Results of the PM2K calculus in the base metal before and after heat treatment for 1h.

parameters		UN sample	200C	400C	600C
Unit cell parameter	[nm]	0,287115	0,2871020	0,2870529	0,287079
Burgers vector modulus (β)	[nm]	0,248647	0,2486376	0,2485951	0,248618
Density of dislocations (ρ) $\times 10^{14}$	[m ⁻²]	7.80774	9.552684	9.575792	9.21073
Effective outer cut-off radius(Re)	[nm]	30,52714	33,17920	31,71789	29,1623
Domain size average(Dave)		710,1456	320,1261	1035,777	206,305
Standard deviation(Sd)		7.585354	3.201341	1.238911	2.67574
Wilkens parameter(M)		0,852991	1.025483	0,9815030	0,890367
Edge dislocation fraction(f_e)		0,299691	1.3178.10 ⁻¹⁸	0,3115504	0,076996
Lognormal mean (μ)	[nm]	6.565413	5.768665	6.942836	5.32927
Variance (σ)		0,010681	0,01	1.196074	1.296931
WSS		5120.72	4697	4477.87	4293.62
Rwp		2.6599	4.46442	2.89312	4.27509
Rexp		2.02776	3.55421	2.35975	3.55978
Gof		1.31174	1.25609	1.22603	1.20094

The figure IV.45 shows the graphic results of the WPPM (Whole Powder Pattern Modeling) in the heat affected zone (HAZ) after heat treatment for 10 min at 200°C, 400°C and 600°C. The table IV.13 resumes the results of the calculus with this method.

The agreement between the experimental profiles (black points) and the modeled one (red continued line) is very clear. On the figures, the difference between the experimental and modeled profiles is marked by a gray line. The shape of the gray line is plane with little reliefs, this indicates a good convergence. These constations are confirmed by the smaller values of WSS between (4793.54 and 5429.9) with the Gof (Goodness of fit) which is stranded between 1.26893 and 1.35055.

The intensities of the five peaks decrease just after heat treatment temperature at 400°C. This can be interpreted by the beginning of recrystallization phenomenon.

After heat treatment at 400°C and 600°C we found a decrease in the density of dislocation ($\rho = 5.166125 \cdot 10^{14} \text{ m}^{-2}$ and $5.676957 \cdot 10^{14} \text{ m}^{-2}$ respectively) the values of Wilkens factor are small than unity before and after heat treatment, excepting for 600°C this parameter is superior than unity ($M = 1.230876$).

According to Abdelatif et al [117] such small values of M (< 1) can result from an increasing interaction among dislocations, as in dipoles or in domain walls and crystal grain

boundary regions, in such a way that the overall lattice distortion effect tends to saturate. In this case the material was in configuration characterized by total low energy [121].

The figure IV.46 shows the graphic results of the WPPM (Whole Powder Pattern Modeling) in the heat affected zone (HAZ) after heat treatment for 30 min at 200°C, 400°C and 600°C. The table IV.14 resumes the results of the calculus with this method.

The agreement between the experimental profiles (black points) and the modeled one (red continued line) is very clear. On the figures difference between experimental and modeled profiles is marked by gray line. The shape of the gray line is plane with little reliefs, this indicates a good convergence.

The density of dislocation before heat treatment ($\rho = 6,501594 \cdot 10^{14} \cdot \text{m}^{-2}$), we find a slight increase of ρ after 400°C and 600°C heat treatment, but there is remarkable increase after 200°C heat treatment. The values of the Wilkens parameter (M). The dimensionless parameter M is the factor for characterizing the dislocation arrangement. Before heat treatment this factor is smaller than unity M ($M = 0,7649467$) this indicates strong dipole character and strong screening indicates a faster decaying of the strain field [128, 132]. However this factor after heat treatment at 200°C and 600°C present values near the unity ($M = 0,9924736$ and $M = 1,030758$ respectively), when ($M \approx 1$) indicates the arrangement of dislocation is quasi-homogeneous, where the dislocation stops to the aftermost or nearer dislocation. In This situation $\mathbf{Re} \approx \rho^{-1/2}$ [fellah]. In this case there is a strong correlation between dislocation, strong screening of field strain (like in the dislocation walls or between the dipoles) [133]. While this factor after heat treatment at 400°C present value bigger than unity ($M = 1,158797$) According to Abdelatif et al [117] such small values of M (< 1) can result from an increasing interaction among dislocations, as in dipoles or in domain walls and crystal grain boundary regions, in such a way that the overall lattice distortion effect tends to saturate. In this case the material was in configuration characterized by total low energy [121]. According to Scardi et al [133] the high values of Wilkens parameter ($M \ll 1$) mean that there is a random distribution of dislocation.

The figure IV.47 shows the graphic results of the WPPM (Whole Powder Pattern Modeling) in the heat affected zone (HAZ) after heat treatment for 1h at 200°C, 400°C and 600°C. The table IV.15 resumes the results of the calculus with this method.

The agreement between the experimental profiles (black points) and the modeled one (red continued line) is very clear on the figures, difference between the experimental and modeled

profiles is marked by gray line. The shape of the gray line is plane with little reliefs, this indicates a good convergence. These constations are confirmed by the smaller values of WSS between (4382.4 and 5429.9) with the Gof (Goodness of fit) which is stranded between 1.21289 and 1.37594.

The intensities of the five peaks, decrease with the increase of the heat treatment temperature specially after 400°C and 600°C there is a remarkable decrease, this indicated that the presence of recrystallization phenomenon. There is also an augmentation in the dislocation density after all heat treatments. The values of the Wilkens parameter (M), The dimensionless parameter M is the factor for characterizing the dislocation arrangement. Before and after heat treatment at 400°C, this factor is smaller than unity M (M=0,7649467 and M= 0,8197933), this indicates strong dipole character and strong screening indicates a faster decaying of the strain field. In this case the material was in configuration characterized by total low energy. However this factor after heat treatment at 200°C and 600°C present values near the unity (M=0,9229247, M=0,9367769 respectively), when (M≈1) indicates the arrangement of dislocation is quasi-homogeneous, where the dislocation stops to the aftermost or nearer dislocation. In this case there is a strong correlation between dislocation, strong screening of field strain.

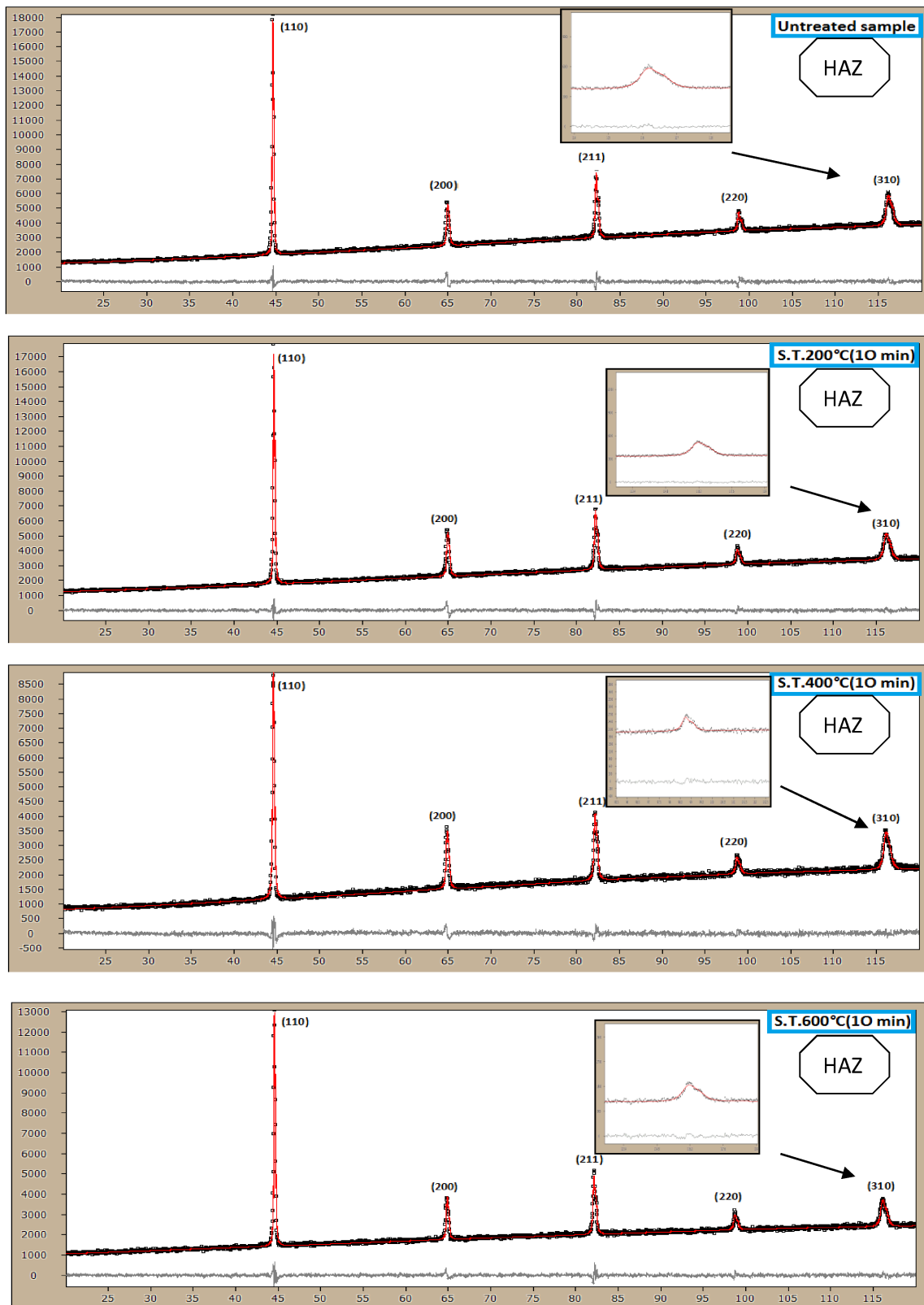


Figure VI.45: X-ray diffraction profiles of heat affected zone before and after heat treatments for 10 min at 200°C, 400°C and 600°C respectively, fittings by PM2K.

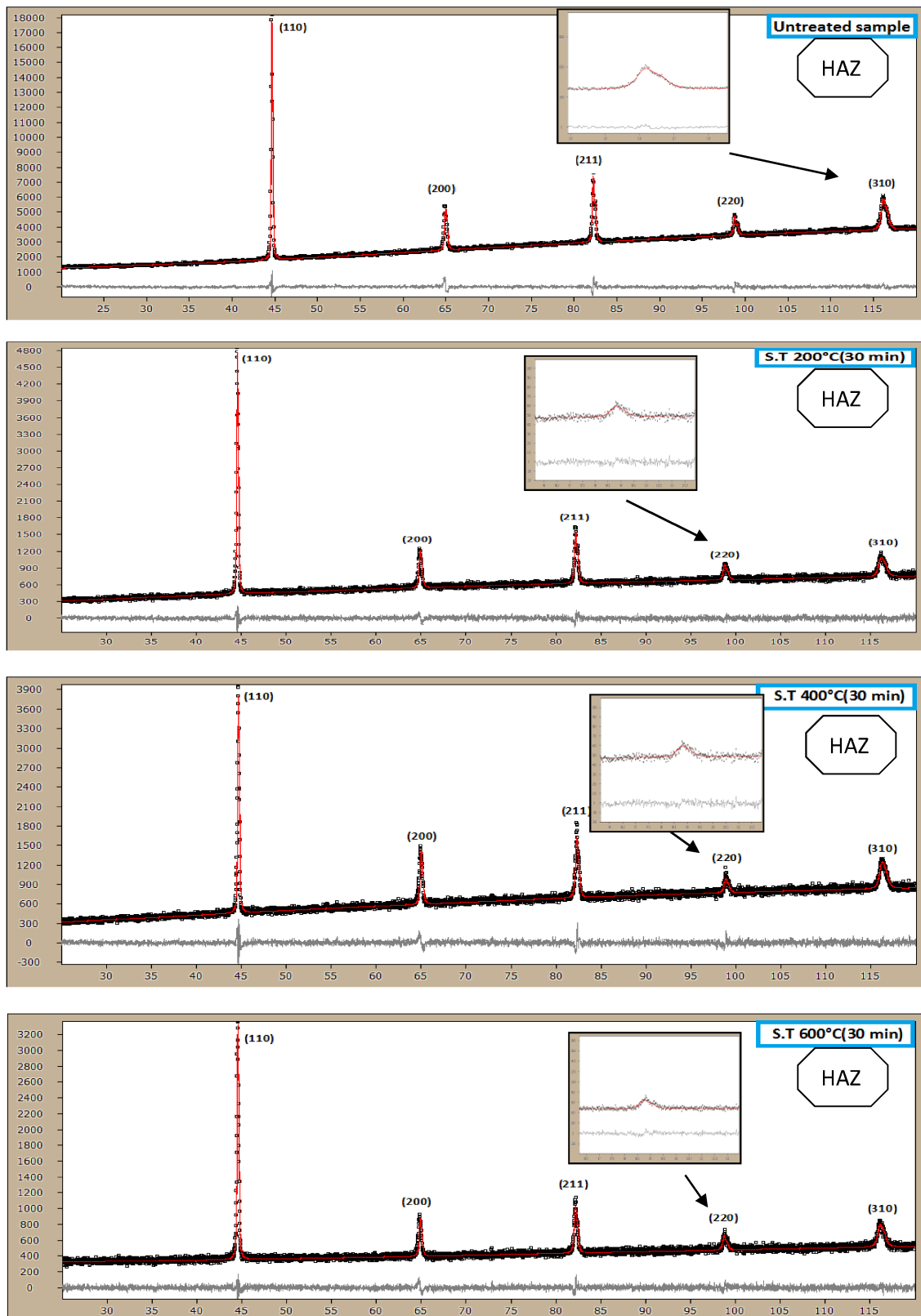


Figure VI.46: X-ray diffraction profiles of heat affected zone before and after heat treatments for 10 min at 200°C, 400°C and 600°C respectively, fittings by PM2K.

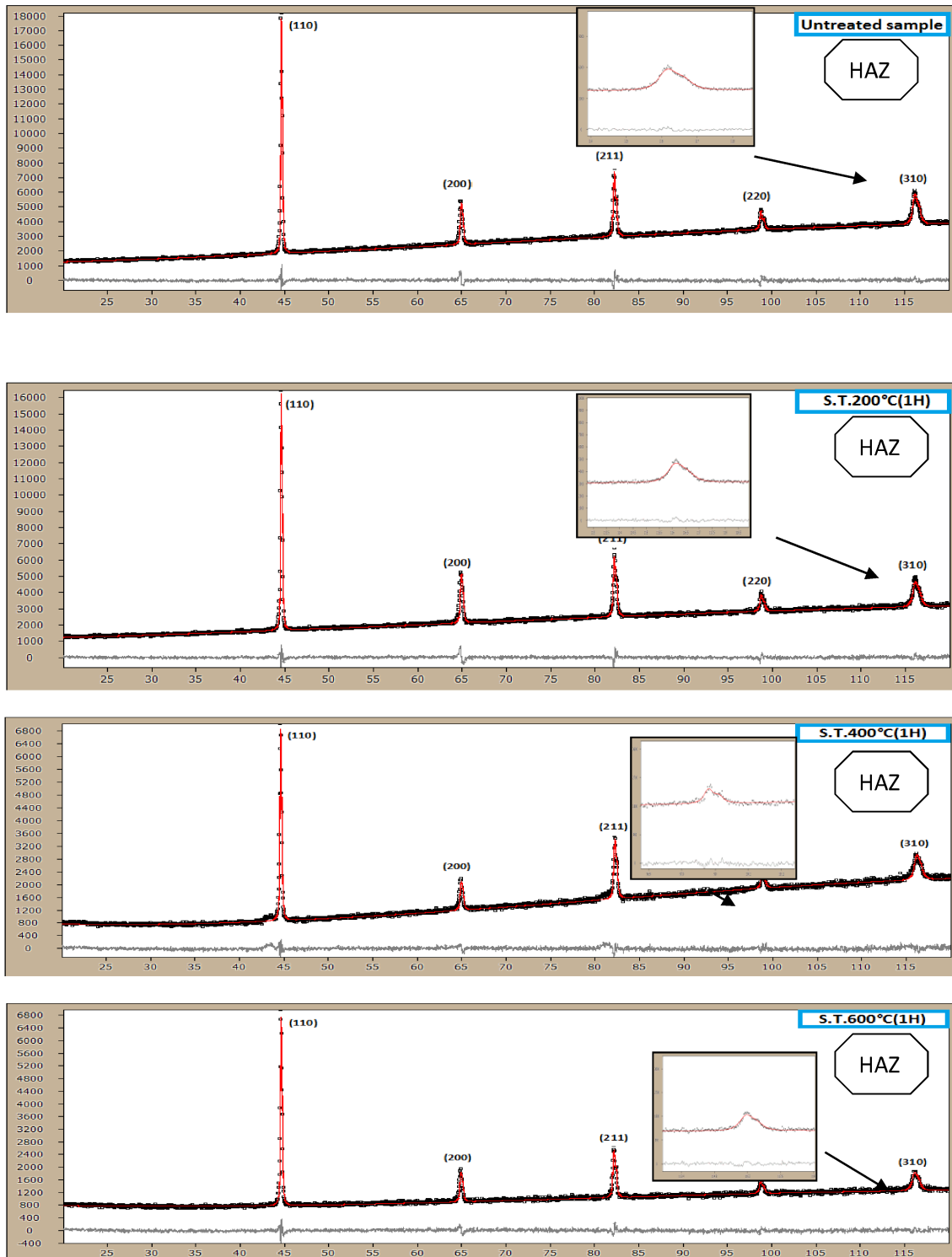


Figure VI.47: X-ray diffraction profiles of the heat affected zone before and after heat treatments for 30 min at 200°C, 400°C and 600°C respectively, fittings by PM2K.

TableVI.13 : Results of the PM2K calculus in the heat affected zone before and after heat treatment for 10 min.

Parameters		UN sample	200C	400C	600C
Unit cell parameter	[nm]	0,2871384	0,287147	0,287122	0,2871363
Burgers vector modulus (b)	[nm]	0,2486692	0,248677	0,248655	0,2486673
Density of dislocations (ρ)x10 ¹⁴	[m ⁻²]	6,501594	8,005329	5,166125	5,676957
Effective outer cut-off radius(Re)	[nm]	30	30,68783	29,3576	51,66025
Domain size average(Dave)	[nm]	808,3805	265,6629	70,01531	171,6204
Standard deviation(Sd)		81,04057	2,656696	0,700171	88,89095
Wilkens parameter(M)		0,7649467	0,868272	0,667272	1,230876
Edge dislocation fraction(f _E)		0,5	0,369253	1,7347.10 ⁻¹⁸	0,991255
Lognormal mean (μ)	[nm]	6,690033	5,582178	4,248664	5,026457
Variance (σ)		0,1	0,01	0,01	4,875000
WSS		5429,9	5390,93	5135,97	4793,54
Rwp		2,59495	2,68683	3,23713	2,91588
Rexp		1,92141	1,99663	2,46538	2,2979
Gof		1,35055	1,34568	1,31303	1,26893

TableVI.14 : Results of the PM2K calculus in the heat affected zone before and after heat treatment for 30 min.

Parameters		UN sample	200C	400C	600C
Unit cellparameter	[nm]	0,2871384	0,2870932	0,2870651	0,2871351
Burgers vector modulus (b)	[nm]	0,2486692	0,24863	0,2486057	0,2486661
Density of dislocations (ρ)x10 ¹⁴	[m ⁻²]	6,501594	9,401322	7,8273	7,212047
Effective outer cut-off radius(Re)[nm]		30	32,36864	40,58845	37,86786
Domain size average(Dave)		808,3805	1723,215	235,7098	183,689
Standard deviation(Sd)		81,04057	918,3708	124,4654	60,26885
Wilkens parameter(M)		0,7649467	0,9924736	1,158797	1,030758
Edge dislocation fraction(f _E)		0,5	0,4051887	0,9607629	0,7505229
Lognormal mean (μ)	[nm]	6,690033	7,326947	5,339628	5,162123
Variance (σ)		0,1	0,5	0,4846354	0,3197529
WSS		5429,9	7558,41	8168,86	7128,76
Rwp		2,59495	4,73665	4,71903	5,35317
Rexp		1,92141	4,10249	3,93155	4,77414
Gof		1,35055	1,15458	1,2003	1,12128

Table VI.15 : Results of the calculus PM2K in the heat affected zone before and after heat treatment for 1h.

Parameters	UN sample	200C	400C	600C
Unit cellparameter [nm]	0,2871384	0,2871980	0,2870943	0,2871605
Burgers vector modulus (b) [nm]	0,2486692	0,2487208	0,2486310	0,2486883
Density of dislocations (ρ) $\times 10^{14}[\text{m}^{-2}]$	6.501594	9.464332	8.476201	7.402515
Effective outer cut-off radius(R_e) [nm]	30	30	28,15812	33,54078
Domain size average(D_{ave})	808,3805	622,2587	150,6685	216,7146
Standard deviation(S_d)	81,04057	6.238176	1.506723	20,49809
Wilkens parameter(M)	0,7649467	0,9229247	0,8197933	0,9367769
Edge dislocation fraction(f_E)	0,5	0,5	4.4408910 ⁻¹⁶	0,04570348
Lognormal mean (μ) [nm]	6.690033	6.428356	5.015032	5.374128
Variance (σ)	0,1	0,1	0,01	0,09.437511
WSS	5429.9	5639.91	5005.12	4382.4
Rwp	2.59495	2.85484	3.45403	3.80825
Rexp	1.92141	2.07482	2.66384	3.13982
Gof	1.35055	1.37594	1.29664	1.21289

The figure IV.48 shows the graphic results of the WPPM (Whole Powder Pattern Modeling) in the fusion zone (FZ) after heat treatment for 10 min at 200°C, 400°C and 600°C. The table IV.16 resumes the results of the calculus with this method.

The agreement between the experimental profiles (black points) and the modeled one (red continued line) is very clear on the figures. The difference between the experimental and modeled profiles is marked by gray line. The shape of the gray line is plane with little reliefs, this indicates a good convergence. These constations are confirmed by the smaller values of WSS between (5133.63 and 6822.47) with the Gof (Goodness of fit) which is stranded between 1.09693 and 1.35146.

The intensities of the five peaks, decrease with the increase of the heat treatment temperature, Specially after 400°C and 600°C there is a remarkable decrease, this indicated that the presence of recrystallization phenomenon. There is a decrease of FWHM after heat treatments of some peaks, this can be explained by the diminution of internal stress which interpreted by the decrease of the density of dislocation.

There is decrease in the dislocation density after all heat treatments specially after 600°C when the value of ρ diminished from 10,18648 to 5.267170. The values of the Wilkens parameter (M), Before and after heat treatment present values near the unity ($M=1.009818$), when ($M \approx 1$) indicates the arrangement of dislocation is quasi-

homogeneous, where the dislocation stops to the aftermost or nearer dislocation. In this case there is a strong correlation between dislocation, strong screening of field strain [133]. However after heat treatment at 200°C, 400°C and 600°C, this factor is smaller than unity ($M=0,8582155$, $M=0,9085898$ and $M=0,853199$), this indicates strong dipole character and strong screening indicates a faster decaying of the strain field [128,132]. In this case the material was in configuration characterized by total low energy [121].

The figure IV.49 shows the graphic results of the WPPM (Whole Powder Pattern Modeling) in the fusion zone (FZ) after heat treatment for 30 min at 200°C, 400°C and 600°C. The table IV.17 resumes the results of the calculus with this method.

The agreement between the experimental profiles (black points) and the modeled one (red continued line) is very clear on the figures, difference between the experimental and modeled profiles is marked by gray line. The shape of the gray line is plane with little reliefs, this indicates a good convergence.

There is decrease in the dislocation density after all heat treatments excepting after 200°C there is an increase of the value of ρ ($\rho=23,5705.10^{14}.m^{-4}$), with very big Wilkens factor ($M=1.604181$) and the fraction of edge dislocation equal to the unity ($f_E=1$). According to Leoni et al [25] Extreme values of f_E (0 or 1) may suggest that the dislocation model is not correct (Different slip systems and/ or dislocation types) but might also indicate that the observed line broadening is incompatible with that produced by line defects. After heat treatment present values near the unity ($M=1.009818$), when ($M \approx 1$) indicates the arrangement of dislocation is quasi-homogeneous, where the dislocation stops to the aftermost or nearer dislocation. In this case there is a strong correlation between dislocation, strong screening of field strain.

The figure IV.50 shows the graphic results of the WPPM (Whole Powder Pattern Modeling) in the fusion zone (FZ) after heat treatment for 1h at 200°C, 400°C and 600°C. The table IV.18 resumes the results of the calculus with this method.

The agreement between the experimental profiles (black points) and the modeled one (red continued line) is very clear on the figures, difference between the experimental and modeled profiles is marked by gray line. The shape of the gray line is plane with little reliefs, this indicates a good convergence. These constations are confirmed by the smaller values of WSS between (4674.37 and 5548.07) with the Gof (Goodness of fit) which is stranded between 1.25264 and 1.36515.

The intensities of the five peaks, decrease with the increase of the heat treatment temperature, Specially after 400°C and 600°C there is a remarkable decrease, this indicated that the presence of recrystalization phenomenon. There is a decrease of FWHM after heat treatments of some peaks, this can be explained by the diminution of internal stress which interpreted by the decrease of the density of dislocation, there is decrease in the dislocation density after all heat treatments. After heat treatment at 200°C, 400°C and 600°C, the Wilkens factor (M) is smaller than unity ($M=0,8582155$, $M=0,9085898$ and $M=0,853199$), this indicates strong dipole character and strong screening indicates a faster decaying of the strain field [128,132]. In this case the material was in configuration characterized by total low energy [121].

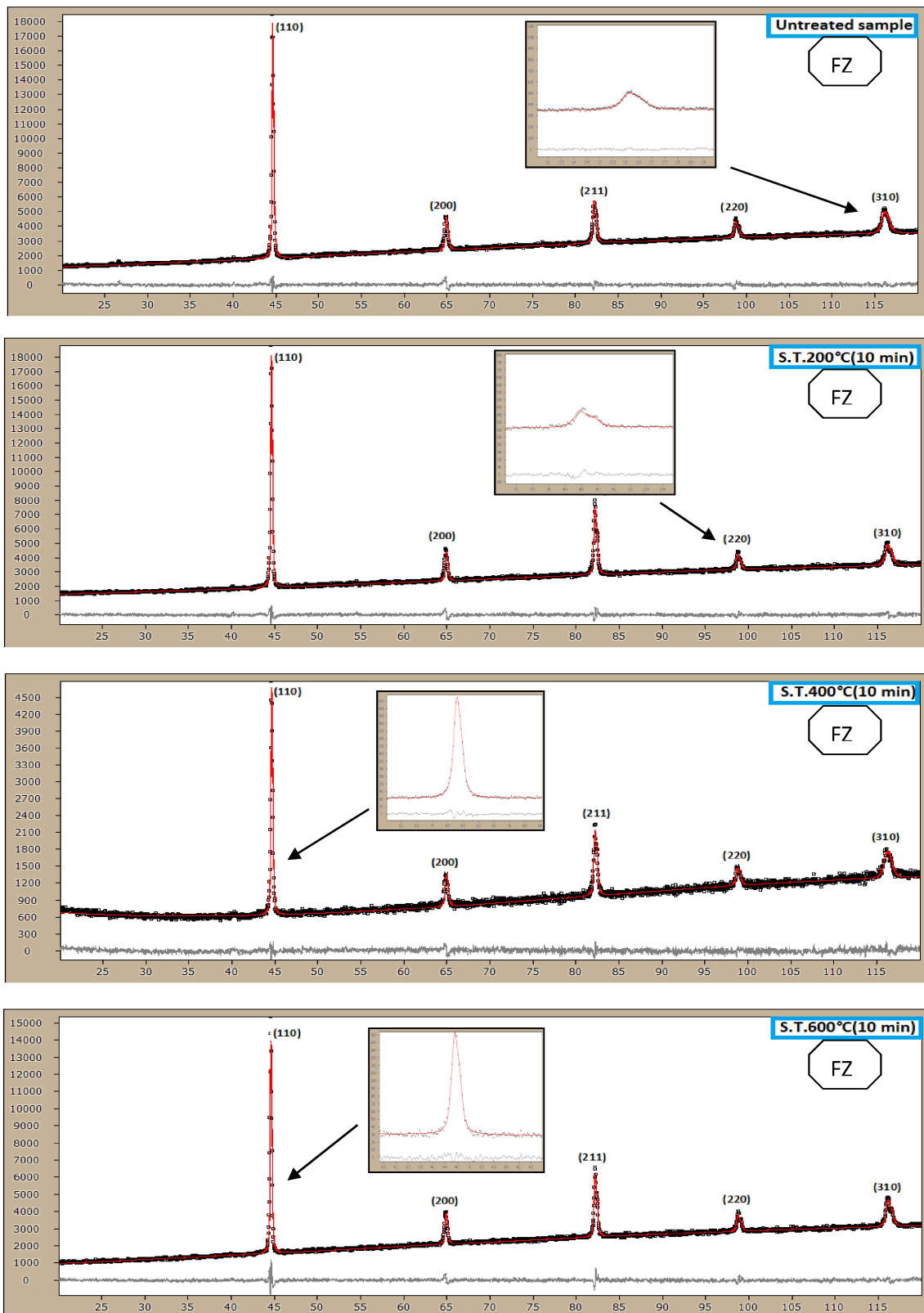


Figure VI.48: X-ray diffraction profiles of fusion zone before and after heat treatments for 10 min at 200°C, 400°C and 600°C respectively, fittings by PM2K.

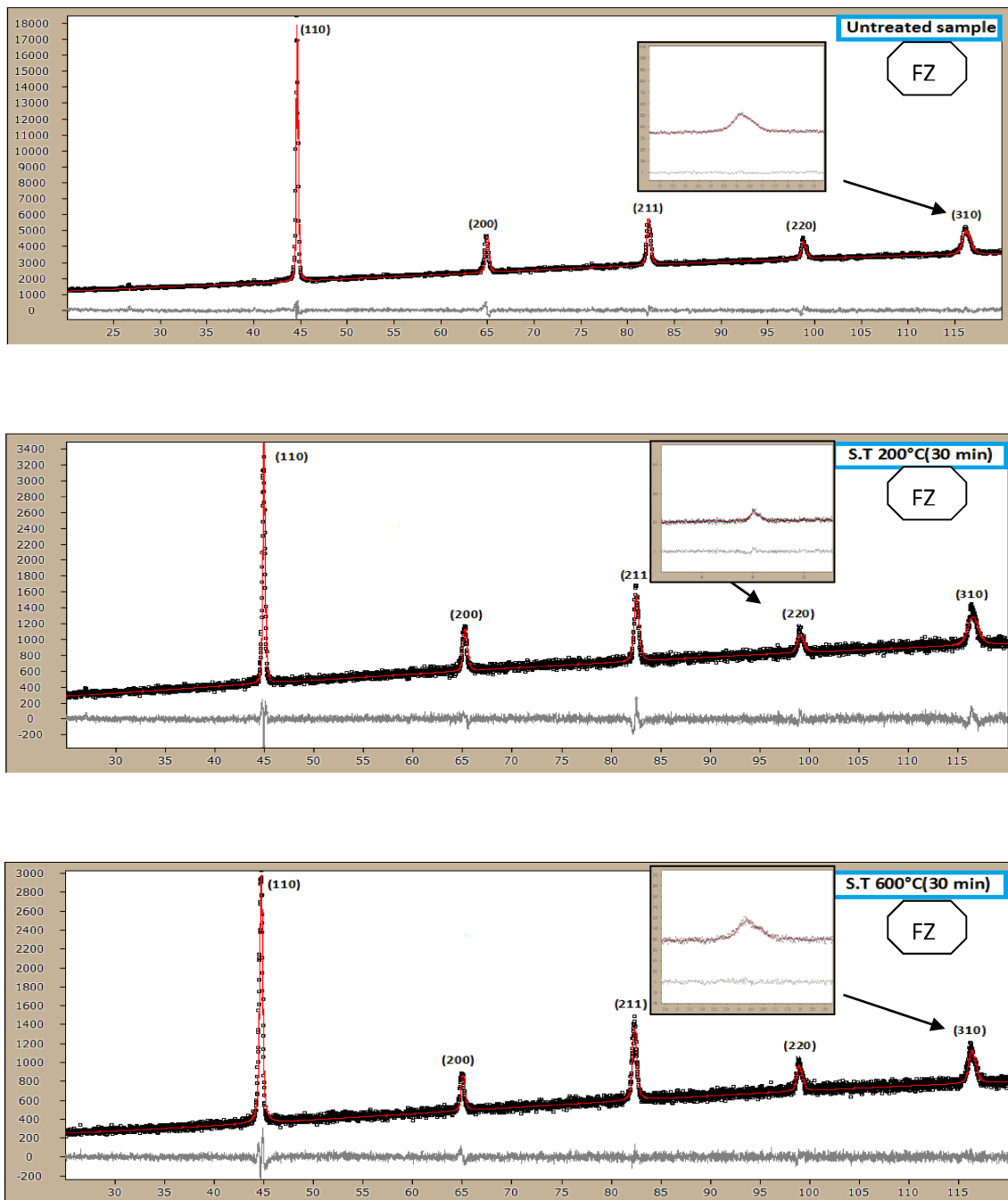


Figure VI.49: X-ray diffraction profiles of fusion zone before and after heat treatments for 30 min at 200°C and 600°C respectively, fittings by PM2K.

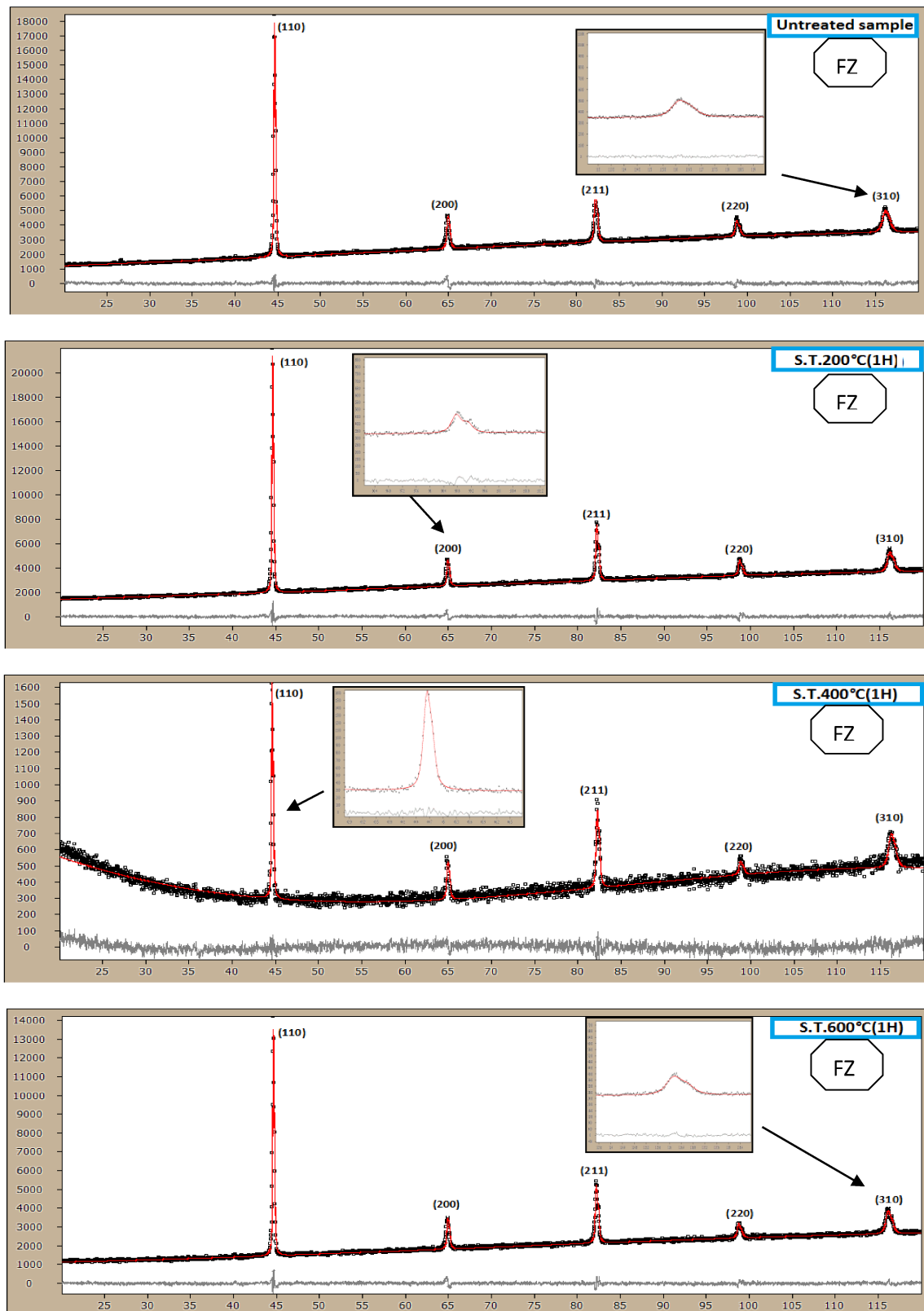


Figure VI.50: X-ray diffraction profiles of fusion zone before and after heat treatments for 1h at 200°C, 400°C and 600°C respectively, fittings by PM2K.

TableVI.16 : Results of the PM2K calculus in the fusion zone before and after heat treatment for 10 min.

Parameters	UN sample	200C	400°C	600C
Unit cell parameter [nm]	0,2871790	0,2871456	0,2871113	0,287134
Burgers vector modulus (b) [nm]	0,2487043	0,2486754	0,2486457	0,248665
Density of dislocations(ρ) $\times 10^{14}$ [m ⁻²]	10,18648	7.495153	9.172616	5.267170
Effective outer cut-off radius(Re)[nm]	31,63960	31,34773	30	37,17592
Domain size average(D _{ave})	162,5463	129,1493	175,3	108,9754
Standard deviation(Sd)	1.625504	1.291611	17,57393	2.245768
Wilkens parameter(M)	1.009818	0,8582155	0,9085898	0,853199
Edge dislocation fraction(f _E)	0,00672761	2.243.10 ⁻¹⁶	0,5	0,753344
Lognormal mean (μ) [nm]	5.090913	4.860919	5.1615	4.67033
Variance (σ)	0,01	0,0100007	0,16811	0,203941
WSS	5133.63	5221.76	6822.47	5437.32
Rwp	2.57792	2.58834	8.27741	2.83713
Rexp	1.96312	1.95435	7.545	2.09931
Gof	1.31318	1.3244	1.09693	1.35146

TableVI.17 : Results of the PM2K calculus in the fusion zone before and after heat treatment for 30 min

Parameters	UN sample	200C	400C	600C
Unit cellparameter [nm]	0,2871790	0,2870814	2.870422	0,2871044
Burgers vector modulus (b) [nm]	0,2487043	0,2486198	//////////	0,2486397
Density of dislocations(ρ) $\times 10^{14}$ [m ⁻²]	10,18648	23,5705	7.466191	//////////
Effective outer cut-off radius [nm]	31,63960	33,04220	33,86925	30
Domain size average(D _{ave})	162,5463	//////////	//////////	330,122
Standard deviation(Sd)	1.625504	//////////	//////////	3.010268
Wilkens parameter(M)	1.009818	1.604181	//////////	//////////
Edge dislocation fraction(f _E)	0,0067276	1	1.20371.10 ⁻³⁵	0,5
Lognormal mean (μ) [nm]	5.090913	4.157727	5.921799	3.492737
Variance (σ)	0,01	0,1	0,01	0,0909978
WSS	5133.63	8666.35	//////////	7729.11
Rwp	2.57792	4.75622	//////////	4.92373
Rexp	1.96312	3.84712	//////////	4.21717
Gof	1.31318	1.23631	//////////	1.16754

TableVI.18 : Results of the PM2K calculus in the fusion zone before and after heat treatment for 1h.

Parameters		UN sample	200C	400C	600C
Unit cell parameter	[nm]	0,287179	0,2871720	0,2870322	0,2871605
Burgers vector modulus (b)	[nm]	0,248704	0,2486982	0,2485772	0,2486882
Density of dislocations (ρ)	$\times 10^{14}[\text{m}^{-2}]$	10,18648	7.428689	9.221969	7.846794
Effective outer cut-off radius(R_e)	[nm]	31,63960	27,62903	30,84044	30,65996
Domain size average(D_{ave})	[nm]	162,5463	273,3689	154,0416	183,2156
Standard deviation(S_d)		1.625504	2.733757	1.540455	38,04479
Wilkens parameter(M)		1.009818	0,7530464	0,9365531	0,8640696
Edge dislocation fraction(f_E)		0,006728	0,5298764	$3.6576 \cdot 10^{-99}$	0,7160729
Lognormal mean (μ)	[nm]	5.090913	5.610772	5.037173	5.189556
Variance (σ)		0,01	0,0 1	0,01	0,2054628
WSS		5133.63	5548.07	4809.59	4674.37
Rwp		2.57792	2.60551	6.39827	2.79862
Rexp		1.96312	1.90858	5.03383	2.23418
Gof		1.31318	1.36515	1.27106	1.25264

IV.6 Study of the residual stress

The X-ray diffraction technique for stress measurement can rapidly and destructively measure applied and residual stress in small area on the surface of polycrystalline materials. This technique is based on the fact that the shift of the location of the diffraction line profile, called the peak position, is proportional to the stress value, thus peak position determination is of fundamental importance in X-ray diffraction stress analysis [134].

In arc welding operations residual stresses are introduced within the welded metal owing to the non-uniform temperature distribution and severe temperature gradients. These residual stresses may be responsible for brittle fracture, decreasing fatigue life as well as stress corrosion cracking [135]. Consequently, it is very important to understand and quantify the residual stresses.

Figures IV.51, IV.52 and IV.53 present both residual stresses distribution in the weld region of X70 pipeline steel at different states and the peak width evolution in weld region respectively.

Concerning the stress distributions, it is clear that all curves have the same shape but not the same magnitude because the the effect of heat treatments is obvious. The magnitude of

residual stresses decrease significantly with increasing a temperature. For example, figure IV.51 presents the stress distributions in the weld region of X70 pipeline steel. Compressive residual stresses in two directions were observed in weld seam, heat affected zone (HAZ) and base metal. The results indicate that in weld seam the value of stress is -195 in longitudinal direction and - 265 MPa in transversal direction. The maximum of compressive residual stresses are at 2 mm from weld seam (- 265 Mpa and 300 MPa). From 10 mm to weld seam the level of stress becomes low compressive in both directions (-100 MPa). For example, Ranjbarnodeh et al [136] have been found that when dissimilar metals are joined by fusion process such as TIG welding technique, mixing of the base metals and the filler metal results in the weld region to have different mechanical properties and this phenomenon on affects the distribution of residual stress after welding operation. Generally, the predominant cause of welded residual stresses is quenching, because according to Macherauch et al [137].

The principal sources of residual stresses after welding are: shrinkage, quenching or phase transformation. Shrinkage causes the appearance of tensile stresses, whereas quenching and phase transformation cause compressive stresses at the weld seam. On the other hand, Prabhat et al [138] considered that the distribution of residual stresses in a girth welded pipe is complex. Weld shrinkage in the circumferential direction induces both shearing and bending that result in stress components in the circumferential direction (hoop stress) and in the axial direction (meridian stress).

However, heat treatments induce a phenomenon of relaxation in the material, because the width peak diminishes with increasing temperature. For example, the heat treated specimen at 200°C, the width peak of diffraction varies from 1,34° to 1,97° which corresponds to high relaxation in all zones (Fig IV.52b). The same evolution has been observed in heat treated sample at 600°C (Fig. IV.53). In addition, the level of stresses became null after the heat treatment at 600°C. There is reasonable agreement between the stress distributions and width peak of diffraction in weld region.

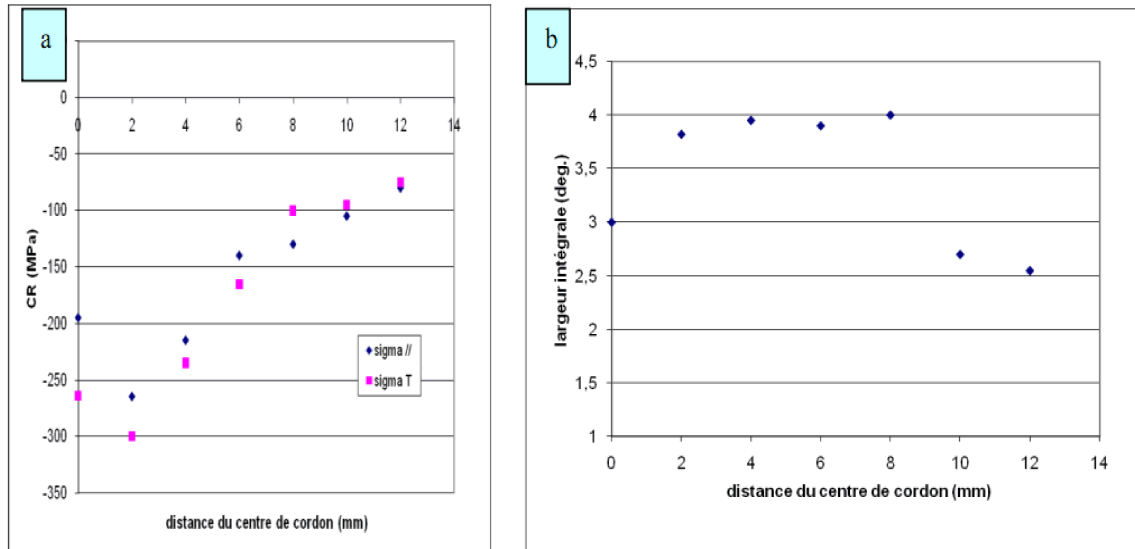


Figure IV.51: (a) Stress distributions and (b) width peak evolution in the weld region of X70 pipeline steel

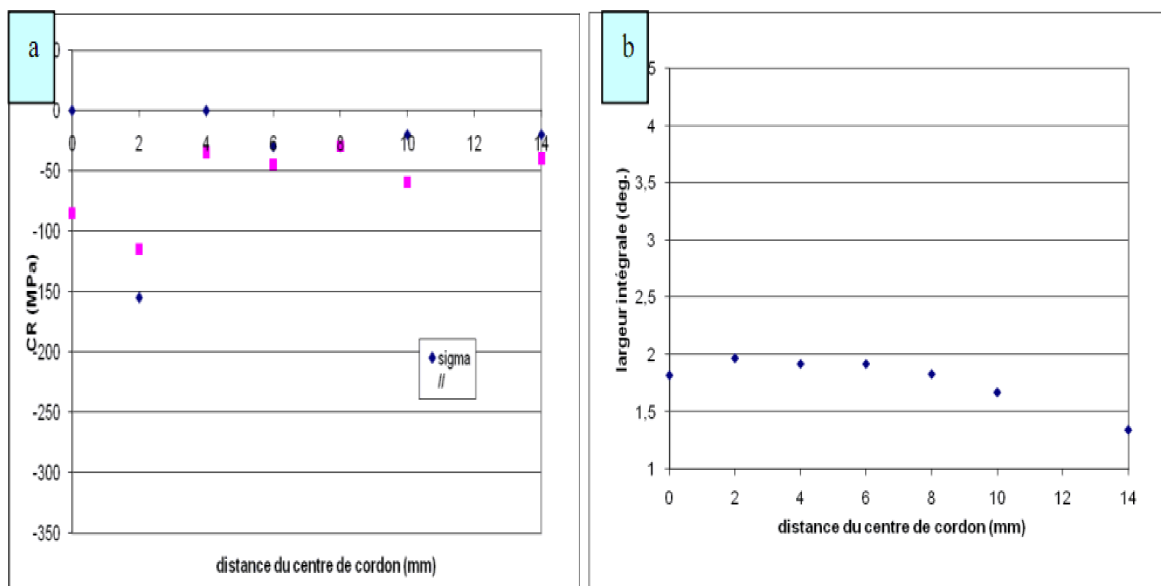


Figure IV.52: (a) Stress distributions and (b) width peak diffraction evolution in the weld region of X70 pipeline steel heat treated 1 h at 200°C.

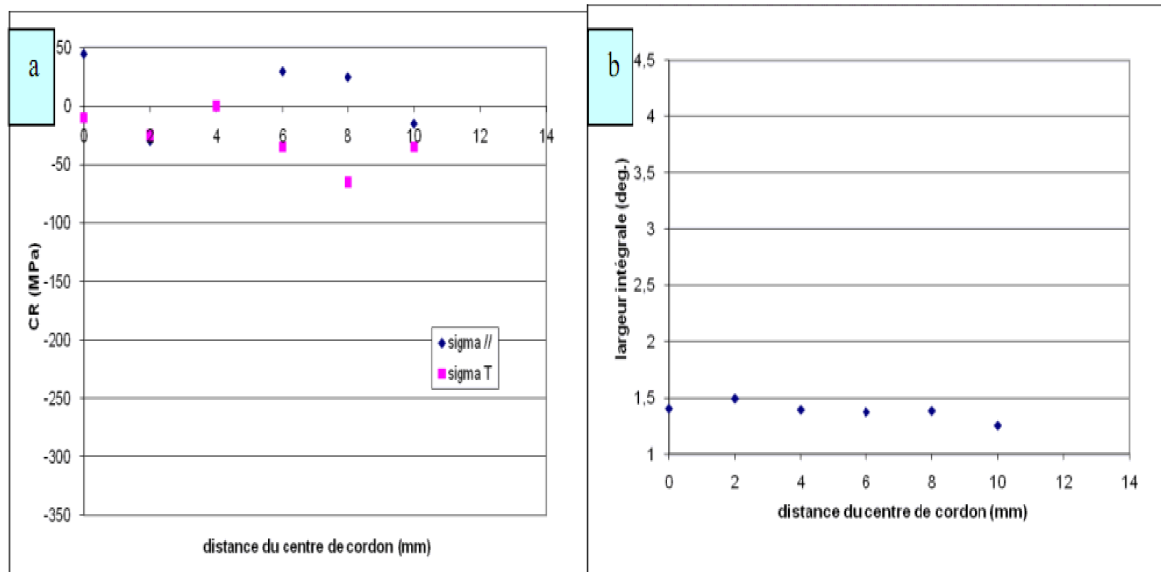


Figure IV. 53: Stress distributions and (b) width peak diffraction evolution in the weld region of X70 pipeline steel heat treat 1 h at 600°C.

IV.7 Hardness examination

It was reported that a hardness testing is the usual approach in delineating the properties of these various zones, but the information obtained is very limited [139]. For other researchers, a simple rapid way to obtain important information is by hardness testing [140].

Hardness graphs in the first pass and in the last pass of the tested specimens and the points at which those hardness measurements were taken are given to gather in the figures VI.54-59. The average values of hardness measurement before and after heat treatments in the first and last pass are resumed in the tables VI.19 and VI.20

The hardness graph in the first pass of the untreated sample, heat treated at 200°C, 400°C and 600°C for 10 min, 30 min and 1 h are given in the figure VI.54-56. From these figures it can be seen an increase in the hardness in weld zone; may be induced by residual stress on microstructure refinement due to the rapid solidification of the weld pool [141]. It was investigated it was observed the highest hardness was obtained in the fusion zone (FZ) of the main specimen (untreated sample), and the hardness values decreased towards the heat affected zone (HAZ).

There is a decrease in all hardness values due to the heat treatment after 10 min, 30 min specially at 200°C and 600°C, but for 1h the lowest values of hardness are corresponding to 200°C and 400°C heat treatment, similarly to the main specimen the smaller hardness values are occurred in the heat affected zone(HAZ). Gural et al [140] confirmed that the maximum hardness values are measured in the area of weld metal, where on the contrary lowest values are at the HAZ.

The hardness graph in the last pass of the untreated sample, heat treated at 200°C, 400°C and 600°C for 10 min,30 min and 1 h is given in the figures VI.57-59 is investigated it was observed the highest hardness was obtained in the fusion zone(FZ) of the main specimen(untreated sample), and the hardness values decreased towards the heat affected zone(HAZ).After heat treatment for 10 min and 1h we found the decrease in the hardness values in the fusion zone and in the heat affected zone, specially at 200°C and 600°C, however after 30 min at 200°C the hardness is increased in the FZ and HAZ, but there is a remarkable decrease after 30 min heat treatment at 600°C in the HAZ. According to Bordbar et al [142] this increase due to the refining in grain size.

❖ Discussion

In general, in the roots of weldments, the hardness distribution is lower than the upper surface of weldment, which is mainly due to tempering effects of filler pass [143].

The weld metal has the highest hardness before and after heat treatments. This increase can be attributed to the presence of lower transformation products such as Widmanstätten ferrite (WF)[19]. This increase due also by the presence of some ferrite morphologies like acicular ferrite [141]. In addition to microstructural transformation, plastic deformation due to residual stress increased the WM hardness. As result of plastic deformation the dislocation density increased throughout WM. The hardness of WM decreased during heat treatment due to the removing the residual stress, reduction of lattice defects generated during welding, grain growth and formation of considerable ferrite in the microstructure [142].

TableVI.19 :The average hardness values in the first pass

	Time	Fusion zone	Heat affected zone
U.Sample	0 min	202,22	192,17
S. T 200°C	10 min	175,075	170,9
	30 min	174,033	171
	1 h	180,83	169,25
S. T 400°C	10 min	196,95	196,3
	30 min	////////	////////
	1 h	198,55	170,35
S. T 600°C	10 min	178,3	162,65
	30 min	191	184
	1 h	178,26	180,6

TableVI.20 :The average hardness values in the last pass

	Time	Fusion zone	Heat affected zone
U.Sample	0 min	208,35	192
S. T 200°C	10 min	184,8	178,16
	30 min	215,23	203,25
	1 h	191,85	171,86
S. T 400°C	10 min	194,13	190,05
	30 min	202,56	187,875
	1 h	197,375	196,13
S. T 600°C	10 min	192,33	169,25
	30 min	205,46	183,03
	1 h	184,63	178,93

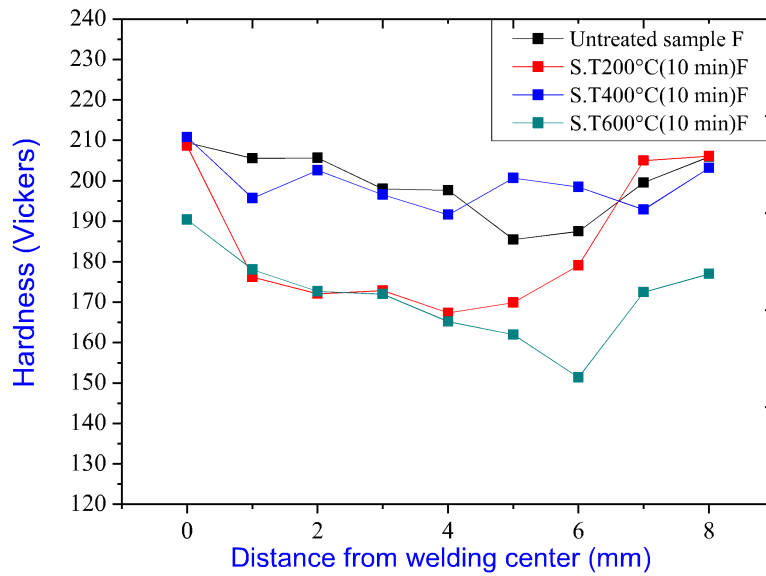


Figure VI.57: Hardness graphs in first pass of welding samples before and after heat treatments at 200°C, 400°C and 600°C for 10 min .

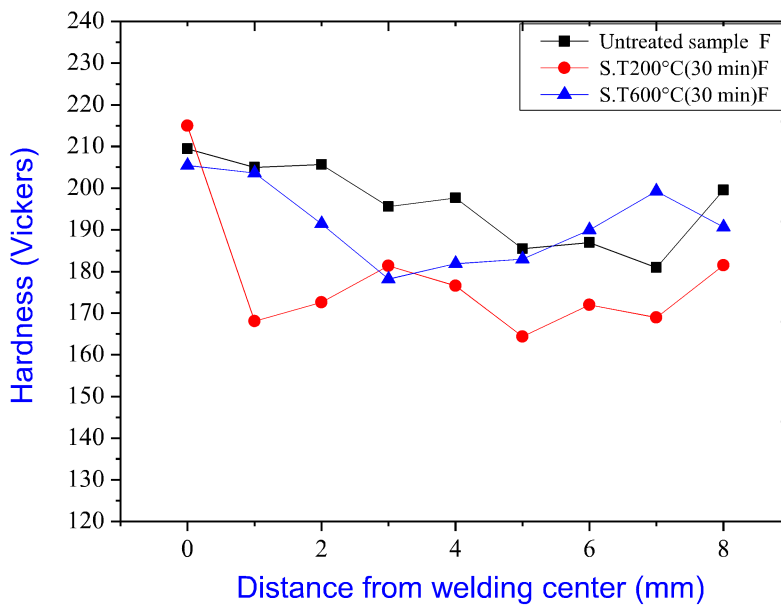


Figure VI.58: Hardness graphs in first pass of welding samples before and after heat treatments at 200°C, 400°C and 600°C for 30 min.

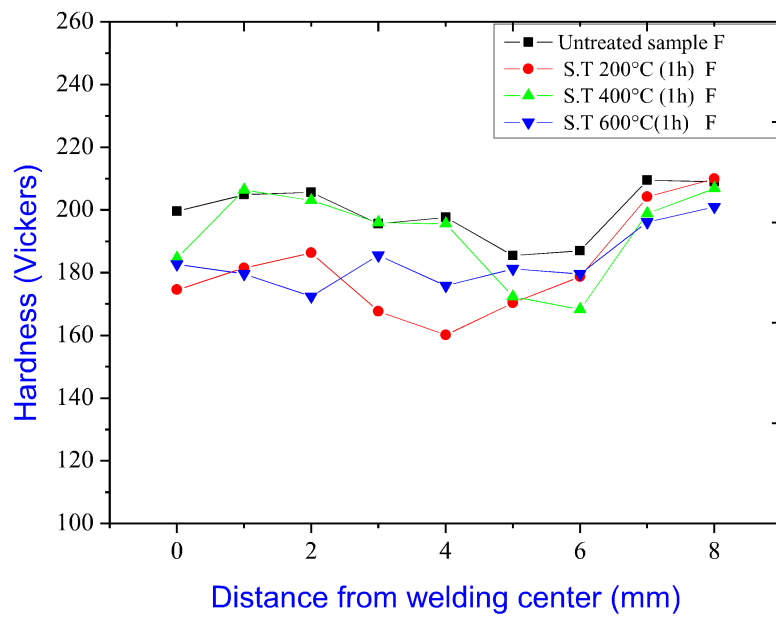


Figure VI.59: Hardness graphs in first pass of welding samples before and after heat treatments at 200°C, 400°C and 600°C for 1h.

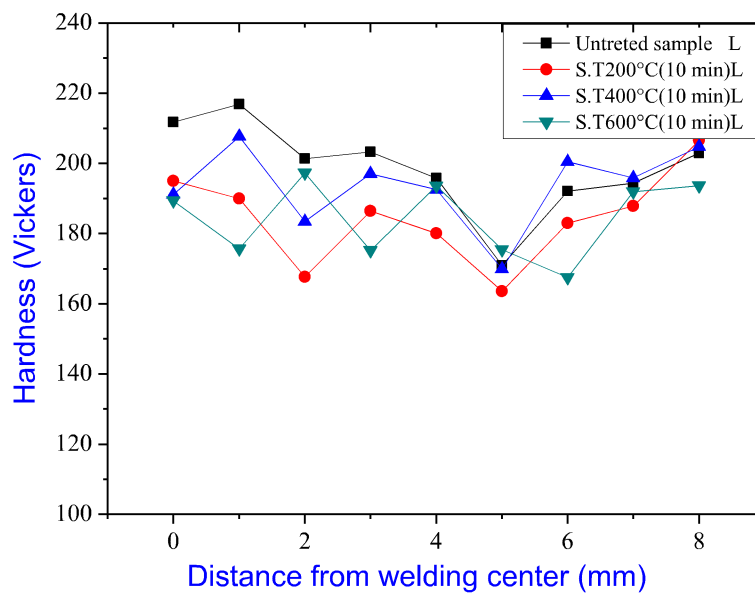


Figure VI.60: Hardness graphs in last pass of welding samples before and after heat treatments at 200°C, 400°C and 600°C for 10 min.

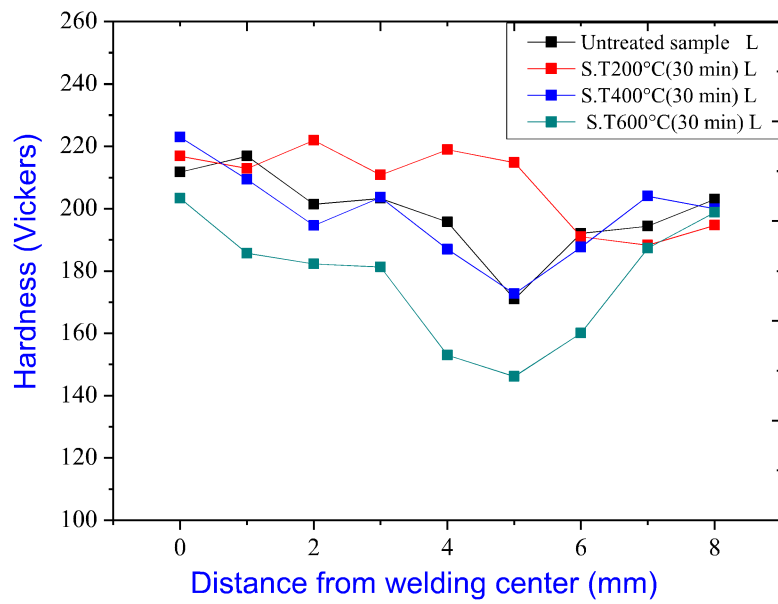


Figure VI.61: Hardness graphs in last pass of welding samples before and after heat treatments at 200°C, 400°C and 600°C for 30 min.

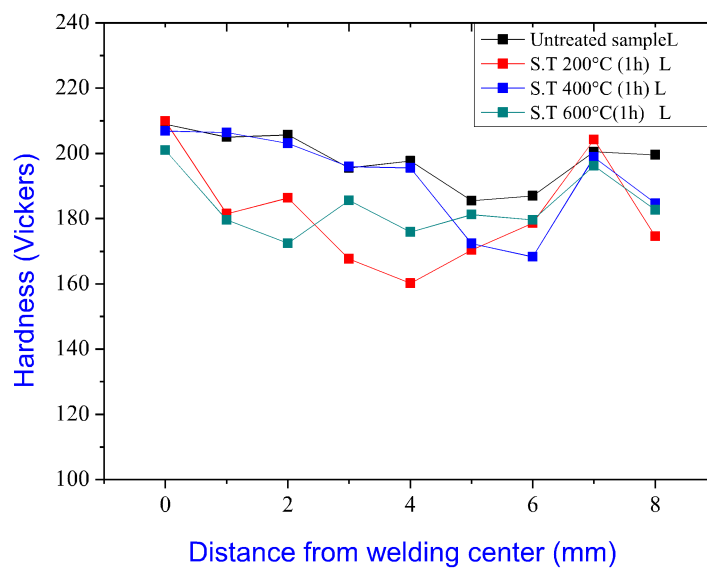


Figure VI.62: Hardness graphs in last pass of welding samples before and after heat treatments at 200°C, 400°C and 600°C for 1h.

GENERAL CONCLUSION

Conclusion

In this work we are used welded samples of microalloyed steel with low carbon content (0,064%), which are from X70 pipeline, fabricated by the COSIDER society for welding of pipelines.

Optical and scanning electron observation of the weld material has revealed the microstructures of different zones, i.e., weld seam, heat affected zone (HAZ) and base metal. Heat treatments were applied on welded specimens by isothermal annealing at 200, 400 and 600 °C during 10, 30 min and for 1 hour in order to study their effects on microstructures, phases, density of dislocations, hardness and residual stresses distribution in X70 pipeline steel.

The analysis of the microstructures obtained with isothermal treatments has shown, in the base metal the microstructure stays always ferrite and pearlite phases but with some changes in the grain size after some heat treatments.

Concerning the HAZ which was our main objective, we have obtained the following results :

- The HAZ can be divided into number of sub-regions. Each sub-region has its own distinct microstructure, sometimes we can identify them, but other times we can not.
- The heat affected zone presents equiaxed ferrite or fine ferrite grains in own sub-zones with different grain sizes after the heat treatments. After heat treatment for 10 min at 200°C and 400°C, microstructures of the HAZ and the FZ in the junction zone became more homogeneous. We obtained fine ferrite grains after 30 min heat treatment at 200°C and 600°C and the microstructures of the HAZ and FZ are more homogeneous. The most of heat treatments affect really the initial grain size. It is clear that these heat treatments induce a high mobility of grain boundaries

The fusion zone (FZ) shows many microstructures in every pass. The microstructures of the first pass are characterized by ferrite phase (F) with rare pearlite colonies (P) observed at some grain boundaries. The microstructure of the fusion zone in second pass was largely composed of fine and coarse ferrite grains (FG and CG), acicular ferrite (AF) with some grain boundaries of ferrite (GBF), however the third pass shows different ferrite morphologies such as, ferrite side plates (FS) and acicular ferrite (AF). We obtained also a new phenomenon at 600°C heat treatment for 1h in the FZ (First pass) which is the fragmentation of the lamellar cementite (In other terms the degradation of Lamellar pearlite to fragment of Fe_3C)

Conclusion

These results have obtained by restoration and recrystallization of the microstructure after the heat treatments.

XRD patterns of low carbon steel before and after heat treatment exhibit high-intensity peaks corresponding to the α -Fe phase. As can be seen, the diffraction from three crystalline planes is more intense than that of others; (1 1 0), (2 0 0) and (211).

After heat treatment for 10 min, the intensities of the five peaks decrease just after heat treatment temperature at 400°C. This can be interpreted by the beginning of recrystallization phenomenon.

Before heat treatment the density of dislocation in the HAZ was ($\rho = 6.501594$) but at 400°C and 600°C for 10 min, we found a decrease in the density of dislocation ($\rho = 5.166125 \cdot 10^{14} \text{ m}^{-2}$ and $5.676957 \cdot 10^{14} \text{ m}^{-2}$ respectively).

In the fusion zone there is decrease in the dislocation density after all heat treatments specially after 600°C for 10 min, because the value of ρ diminished from 10,18648 to 5.267170.

after heat treatment for 30 min at 200°C, 400°C and 600°C, there is decrease in the dislocation density after all heat treatments excepting after 200°C there is an increase of the value of ρ ($\rho = 23,5705 \cdot 10^{14} \cdot \text{m}^{-4}$), with very big Wilkens factor ($M = 1.604181$) and the fraction of edge dislocation equal to the unity ($f_E = 1$). Extreme values of f_E (0 or 1) may suggest that the dislocation model is not correct (Different slip systems and/ or dislocation types) but might also indicate that the observed line broadening is incompatible with that produced by line defects

After heat treatment at 600°C for 1 h, the Wilkens factor value is smaller than unity ($M = 1.673410^{-30}$) This value indicates the total absence of dislocations, in this case ($\rho = 3.111510^{-63} \cdot 10^{14} \cdot \text{m}^{-2}$).

When we observe the residual stresses distribution in the weld region of X70 pipeline steel at different states and the peak width evolution in weld region respectively.

Heat treatments induce a phenomenon of relaxation in the material, because the width peak diminishes with increasing temperature. In addition, the level of stresses became null after the heat treatment at 600°C. There is reasonable agreement between the stress distributions and width peak of diffraction in weld region.

Stress distribution is characterised by high compressive stresses in weld seam. However, the heat treatments cause relaxation phenomenon in weld region which is due to the recrystallization reaction caused by the heat treatments.

Conclusion

Our hardness results are in good agreement with literature. The maximum and minimum hardness values are measured in the fusion metal (FZ) and in the heat affected zone (HAZ) respectively. In general we obtained a decrease in all hardness values after the most heat treatments and the hardness values in all zones became more convergent. The variation in properties across the weld can be attributed to several factors, mainly to residual stresses just after welding. On the other hand, other factors can contribute to this hardening like grain size, phase composition, metallic inclusions.

PERSPECTIVE

It will be interesting if we will :

- Using other mechanical testing like tensile test.
- Using MET in order to observe the dislocations.
- Study of the residual stress by the neutron diffraction.

REFERENCES

References

- [1] J.T. Assis, V.Monin, J.R.Teodosio, T.Gurova, *Advances in X-ray Analysis*, Vol 45, (2002).
- [2] Z.Boumerzoug, E.Raouache, F.Delaunois, Thermal cycle simulation of welding process in low carbon steel, *Materials Science and Engineering sectionA*, Vol.530, pp.191–195, (2011)
- [3] E.Gharibshahiyan, A.H.Raouf, N.Parvin, M.Rahimian, The effect of microstructure on hardness and toughness of low carbon welded steel using inert gas welding, *Materials and Design*, Vo.l32, pp.2042–2048, (2011),
- [4] M.H.Avazkonandeh-Gharavol, M.Haddad-Sabzevar, A.Haerian, Effect of copper content on the microstructure and mechanical properties of multipass MMA, low alloy steel weld metal deposits, *Materials and Design*, Vol.30, pp.1902–1912 (2009).
- [5] Y.Shi, Z.Han, Effect of weld thermal cycle on microstructure and fracture toughness of simulated heat-affected zone for a 800MPa grade high strength low alloy steel, *Materials processing technology*, Vol.207, pp.30–39 (2008).
- [6] M.Ceretti, ‘‘ Apport de la diffraction des neutrons a l’analyse des contraintes internes’’, H abilitation for directed researchs ,speciality. chemical sciences, university of Paris-sud, centre of Orsay, (2004)
- [7] S. Wroński, ‘‘Etude des micro-contraintes dans les matériaux texturés hétérogènes par diffraction et modèles de comportement’’, Ph.D thesis, Ecole nationale et supérieur d’arts et métiers, Cracovie, (2007).
- [8] A. Giraud et X. Boy, ‘ Géopolitique du pétrole et du gaz’, Ed. Technip. (1987).
- [9] J.N.H. Tiratsoo, ‘Pipeline pigging technology’, second Edition. (1992).
- [10] *Welding Handbook*, 7th ed. Vol.4, American Welding Society, Miami, FL, (1982), p.9.
- [11] Z.Boumerzoug, C.Derfouf and T.Baudin, ‘‘Effect of welding on microstructure and mechanical properties of an industrial low carbon steel’’, *Journal of Engineering*, Vol.2, pp.502-506, (2010).
- [12] F.B.Pickering, ‘‘Structure-Property Relationships in Steels’’, *Materials Science and Technology*, WILEY-VCH Verlag GmbH & Co KGaA, 41-94.
- [13] A.S.Podder, ‘‘Tempering of a Mixture of Bainite and Retained Austenite’’, University of Cambridge, (2011).
- [14] R.Steiner, ‘‘ASM Handbook, Properties and Selection: Irons, Steels, and High-Performance Alloys’’, Vol. 1, 10th Edition of Metals Handbook, (1990).

References

- [15] C.A.Harper, ‘‘Handbook Of Materials For Product Design’’, Third Edition, New York, NY 10121-2298, (2001).
- [16] J.E.Bringas, ‘‘The metals, Black book, Ferrous metals’’, Edmonton, Alberta, Canada, (1997),
- [17] G.A.Antaki, ‘‘Piping and Pipeline Engineering : Design, Construction, Maintenance’’, Integrity, and Repair, Marcel Dekker, Inc., 270 Madison Avenue, New York, NY 10016, U.S.A, (2003)
- [18] G.Krauss, ‘‘Steels : Processing, Structure, and Performance’’, University Emeritus Professor Colorado School of Mines, (2005).
- [19] G.Aggen et al, ‘‘ASM Handbook, Properties and Selection: Irons, Steels, and High Performance Alloys’’, Vol. 1,
- [20] K.Tamaki, H.Kawakami and J.Suzuki, ‘‘Effects of carbon content and peritectic reaction on hot, cracking of high-carbon steel weld metal’’, Welding International, vol. 17 (1) pp.26–35.
- [21] ‘‘A guide to the solidification of steels’’, Jernkontoret, Stockholm, (1977) pp.156.
- [22] S.Kou,welding metallurgy, second edition, a John Wiley & Sons, Inc., publication, (2002)
- [23] D.Hull and D.J.Bacon, ‘‘Introduction to Dislocations’’, Fifth Edition, Department of Engineering, Materials Science and Engineering, University of Liverpool, UK, (2011).
- [24] W.G.Burgers, Crystal Growth In The Solid State (Recrystallization), Physica XV, no1-2, (1949).
- [25] M.Leoni, J.Martinez-Garcia and P.Scardi, ‘‘WPPM: advances in the modeling of dislocation line broadening’’, Materials Science Forum, Vol. 651, pp 173-186,(2010)
- [26] ‘‘Imperfections of the Crystal Structure’’, by Taylor & Francis Group, LLC, (2008)
- [27] G.E.Dieter, ‘‘Mechanical metallurgy’’,SI Metric edition, University of Maryland, pp739, (1988).
- [28] ‘‘Steel Tanks For Liquid Storage ‘’, Steel Plate Engineering,Vol. 1, Published By American Iron and Steel Institute, (1992).
- [29] H.W.Rayson, ‘‘Tool Steels’’, Formerly Principal Lecturer, Department of Metallurgy and Materials Engineering, Sheffield City Polytechnic, Sheffield, U.K.
- [30] J.Philibert, A.Vignes, Y. Bréchet et P. Comrade, ‘‘Métallurgie du minerai au matériau Masson’’, Paris ,(1998).

References

- [31] H.Berns, and W.Theisen, Translated by Gillian Scheibelein, "Ferrous Materials Steel and Cast Iron", Springer-Verlag Berlin Heidelberg, (2008).
- [32] H.Ohtani, "Processing - Conventional Heat Treatments", Iron and Steel Research Laboratories, Sumitomo Metal Industries, Ltd., Amagasaki, Japan
- [33] U.S Army, *Welding_Theory_and_Applications*, TC-9-2, 1993 Washington.
- [34] I. Hrivnak, A. Review of the Metallurgy of Heat Treatment of Welded Joints, *Int. J. Pres. Ves. And Piping*, Vol.20, pp.223-237, (1985).
- [35] J.D.Verhoeven, *Metallurgy of Steel for Bladesmiths & Others who Heat Treat and Forge Steel*, Iowa State University, March 2005.
- [36] R.Scott Funderburk, "Key Concepts in Welding Engineering :Post weld Heat Treatment, *Welding Innovation*" ,Vol. XV, No. 2, (1998).
- [37] H.Chandler, "Heat treater's : Practices and procedure for irons and steels", ASM International, (1995).
- [38] G.Krauss, *Microstructure and Transformations in Steel*, Materials Science and Technology, Wiley-Vch Verlag GmbH & Co KGaA.
- [39] D.O.Wilshynsky, D.K.Matlock, and G .Krauss, "Metallurgy of Vacuum Degassed Steel Products": Pradhan, R. (Ed.). Warrendale, PA: The Minerals, Metals, and Materials Society, (1990).
- [40] F. Mohammadi, F. F.Eliyan and A.Alfantazi, "Corrosion of simulated weld HAZ of API X-80 pipeline steel", *Corrosion Science*, Vol.63, pp.323–333, (2012).
- [41] H.K.D.H.Bhadeshia and L.E.Svensson, "Modelling the Evolution of Microstructure in Steel Weld Metal, *Mathematical, Modelling of Weld Phenomena*", eds H. Cerjak, K. E. Easterling, Institute of Materials, London, pp.109–182, (1993).
- [42] J.Moon, J.Lee and C.Lee, "Prediction for the austenite grain size in the presence of growing particles in the weld HAZ of Ti-microalloyed steel", *Materials Science and Engineering*, section A, Vol.459, pp.40–46, (2007).
- [43] A.I.Zakya, A.El-Morsyb, and T.El-Bitar, Effect of different cooling rates on thermomechanically processed high-strength rebar steel,*journal of materials processing technology*, Vol.209,pp. 1565–1569, (2009).
- [44] J.Speer, D.K. Matlock, B.C. De Cooman, and J.G. Schroth, "Carbon partitioning into austenite after martensite transformation", *Acta Materialia*, Vol. 51, pp 2611–2622, (2003).

References

- [45] R.M.Alé, J.M.A.Rebello and J.Charlier, ‘‘A metallographic technique for detecting martensite-austenite constituents in the weld heat-affected zone of a micro-alloyed steel’’, *Materials Characterization* , Vol.37, pp89-93, (1996).
- [46] H.K.D.H.Bhadeshia, ‘‘Lecture 10: Ferrous Alloys’’, Course A, Metals and Alloys, Part IB Materials Science and Metallurgy, pp.58-64 (2005).
- [47] B.C.Muddle, J.F. Nie, Formation of bainite as a diffusional–displacive phase transformation, *Scripta Materialia*, Vol. 47, pp.187–192, (2002).
- [48] D. Quidort, Y. Brechet, The role of carbon on the kinetics of bainite transformation in steels, *Scripta Materialia*, Vol.47, pp.151–156, (2002).
- [49] E.Pereloma, D.V.Edmonds, ‘‘Phase transformations in steels’’, Diffusionless transformations, Volume 2, high strength steels, modelling and advanced analytical techniques, Oxford Cambridge Philadelphia New Delhi, Woodhead Publishing Limited, (2012).
- [50] H.K.D.H.Bhadeshia and S.R.Honeycombe. ‘‘Steels : Microstructure and Properties’’, Third edition, Published by Elsevier Ltd,(2006).
- [51] D.N.Croft, ‘‘Heat treatment of welded steel’’, Published by Abington Publishing ,Woodhead Publishing Ltd, Cambridge CB1 6AH, England, , pp.111, (1996).
- [52] B.M.Patchett, ‘‘The metals, Blue book, Welding filler metals’’, Edmonton, Alberta, Canada, (1997),
- [53] S. Genculu, ‘‘Structural Steel Welding’’,PDH Course S150, (2007).
- [54] P.T.Houldcroft ,’’Welding of Steel’’, Formerly The Welding Institute, Abington, Cambridge, U.K.
- [55] S.Shen, I.N.A.Oguocha , S.Yannacopoulos, ‘‘Effect of heat input in weld bead geometry of submerged arc welded ASM A709 Grad 50 steel joint’’, *Materials Processing Technology*, Vol. 212, pp.286–294, (2012).
- [56] Kishor.P.Kolhe and C.K.Datta ‘‘Prediction of microstructure and mechanical properties of multipass SAW’’, *Materials processing technology* Vol.197, pp.241-249. (2008).
- [57] J. H. Poincare, la science et l'hypothese,
- [58] B.Amri, Effet d'hysteresis de la dilatation thermique sur les contraintes résiduelles dues au soudage, montreal, (2008)
- [59] M.Okayasu, Y.Ohkura, T.Sakamoto, S.Takeuchi, H.Ohfuji and T.Shiraishi, ‘‘Mechanical properties of SPCC low carbon steel joints prepared by metal inert gas welding’’, *Materials Science and Engineering, section A*, Vol.560, pp.643–652 (2013).

References

- [60] W.Zhang, J.W.Elmer and T.DebRoy, "Modeling and real time mapping of phases during GTA welding of 1005 steel", *Materials Science and Engineering, section A*, Vol.333, pp. 320–335, (2002).
- [61] G.E.Linnert, "Welding Metallurgy Carbon and Alloy Steels" Vol.I, *Fundamentals* GML Publications,USA, pp.923,(1994).
- [62] M.H.Avazkonandeh-Gharavol, M. Haddad-Sabzevar and , A. Haerian,"Effect of copper content on the microstructure and mechanical properties of multipass MMA, low alloy steel weld metal deposits, *Materials and Design*, vol.30, pp.1902–1912, (2009).
- [63] J.F.Lancaster, "Metallurgy of welding",Sixth Edition,Abington Publishing, (1999).
- [64] J.Ronda, Y.Estrin and G.J.Oliver, "Modelling of welding. A comparison of a thermo-mechano-metallurgical constitutive model with a therrno-viscoplastic material model", *Materials Processing Technology*, Vol.60, pp.629-636, (1996).
- [65] J.B.Ju , W.S.Kim J.i. Jang "Variations in DBTT and CTOD within weld heat-affected zone of API X65 pipeline steel" *material science and ingeneering,section A*, Vol.546, pp.258-262 (2012).
- [66] H.K.D.H.Bhadeshia, "Possible Effects of Stress on Steel Weld Microstructures" *Mathematical Modelling of Weld Phenomena*, eds H. Cerjak, H. Bhadeshia, Institute of Materials, London, pp. 71-118,(1995).
- [67] Y.Q.Zhang, W.M.Liu, H.Hou, "Effects of Nb on microstructure and continuous cooling transformation of coarse grain heat-affected zone in 610MPa class high-strength low-alloy structural steels", *Materials Science and Engineering, section A*, Vol.499 pp.182–186 (2009).
- [68] V.B.da.Trindade-Filho, A.S.Guimarães, J.da.C.Payão-Filho and R.P.da.R. Paranhos, "Normalizing Heat Treatment Effect on Low Alloy Steel Weld Metals", *Journal of the Brazilian Society of Mechanical Sciences and Engineering*, Vol. XXVI,pp. 62-65, (2004)
- [69] W.W.Bose-Filho, A.L.M.Carvalho, M. Strangwood, "Effects of alloying elements on the microstructure and inclusion formation in HSLA multipass welds", *Materials Characterization*, Vol.58, pp.29–39, (2007).
- [70] Y.Pei,"High Frequency Induction Welding Post-Welding Heat Treatment of Steel Pipes" Ph.D thesis in of Philosophy Department of Materials Science and Metallurgy, University of Cambridge,(2011).

References

- [71] K.M.Wu, Y.Inagawa, and M.Enomoto , ”Three-dimensiona morphology of ferrite formed in association with inclusions in low-carbon steel ”, *Materials Characterization*, Vol.52, pp.121–127,(2004).
- [72] B. Hutchinson, J.Hagstro”m, O.Karlsson, D.Lindell, M.Tornberg, F.Lindberg, and M.Thuvander, “Microstructures and hardness of as-quenched martensites (0.1–0.5%C)”, *Acta Materialia*, Vol.59, pp.5845–5858, (2011),.
- [73] C.C. Huang, Y.C. Pan, and T.H. Chuang, “Effects of Post-Weld Heat Treatmentson the Residual Stress and Mechanical Propertiesof Electron Beam Welded SAE 4130 Steel Plates” *Materials Engineering and Performance*, Vol. 6, pp 61-68, (1997).
- [74] J.H.You, “Interfacial Stress in a Carbon-to-Metal BondJoint under Thermal Shock Loading” *Journal of Materials Engineering and Performance*,Vol.7, pp.114-121, (1998).
- [75] D.H.Bae, C.H.Kim, S.Y.Cho, J.K.Hong and C.L.Tsai, “ Numerical Analysis of Welding Residual Stress Using Heat Source Models for the Multi-Pass Weldment”, *KSME International Journal*, Vol. 16, pp. 1054–1064, (2002).
- [76] V.Ji,“Course about the determination of the residual stress by the X-ray diffraction”,*Second school of the X-ray diffraction, University of Biskra ,(2010).*
- [77] C.David, B.Marton, M.Valeria and C.Adam, “Residual Stress Evolution during the Manufacturing Process of Bearing Rings” *Advanced Materials Research* Vol. 996, pp. 664-669, (2014).
- [78] G.Totten, M.Howes and T.Inoue, ”Handbook of the residual stress and deformation, ASM international, pp550,(2001).
- [79] B. Cherifa, ”Etude du Joint soudé d’un Alliage d’Aluminium”Ph.D thesis in mechanical engineering, University of Biskra, (2015).
- [80] O.Anderoglu, “Residual stress measurement using X-ray Diffraction”,*Master thesis in science,university of Texas, (2004).*
- [81] T. K. Hirsch, A. d. S. Rocha and R. M. Nunes, “Characterization of local residual stress inhomogeneities in combined wire drawing processes of AISI 1045 steel bars”, *Int J Adv Manuf Technol*, Vol.70, pp. 661–668, (2014)
- [82] S.J. Lewis , H. Alizadeh, C. Gill, A. Vega , H. Murakawa, W. El-Ahmar,D.J. Smith, C.E. Truman, and P. Gilles, “Modelling and measurement of residual stresses in autogenously welded “stainless steel plates: Part 1 – fabrication and modelling” *Pressure Vessels and Piping* Vol.86, pp.798–806, (2009)

References

- [83] J.A.Francis, H.J.Stone, S.Kundu, R.B.Rogge, H.K.D.H. Bhadeshia P.J.Withers and L.Karlsson, "The Effects of Filler Metal Transformation Temperature on Residual Stresses in a High Strength Steel Weld, Journal of Pressure Vessel Technology, Vol. 131, (2009),
- [84] H.Alipooramirabad, A.Paradowska, R.Ghomashchi, and A.Kotousov, M.Rei, "Quantification of residual stresses in multi-pass welds using neutron diffraction", Journal of Materials Processing Technology, Vol.226, pp.40–49, (2015).
- [85] J.Zapata, M.Toro and D.Lopez, "Residual stresses in friction stir dissimilar welding of Aluminum alloys" Journal of Materials Processing Technology, Vol 15, pp 1-26,(2015).
- [86] G.Murry, "Soudage et soudabilité métallurgique des métaux", Techniques de l'ingénieur, M715.
- [87] B.D.Cullity and S.R.Stock, "Elements of X-ray diffraction X-ray diffraction" Third Ed, addison-wesley publishing company", inc, (1956).
- [88] E.Lifshin and L.Robert, "X-ray characterization of materials" WILEY-VCH Verlag GmbH, D-69469 Weinheim (Federal Republic of Germany), (1999).
- [89] C.E.Derfouf "Effet de la soudure sur la structure de l'acier" Ph.D thesis in mechanical engineering, University of Biskra,(2011).
- [90] A.S.Maxwell, A.Turnbull, "Measurement of residual stress in engineering plastics using the hole-drilling technique, Polym". Test, Vol.22, pp.231-238 (2003).
- [91] S. Chowdhury, MT.Laugier, and J.Henry, "XRD stress analysis of CVD diamond coatings on SiC substrates", Int. J. Refract Met Hard Mater, vol.25, pp.39-45, (2007).
- [92] JG Kim, J. Yu, "Behavior of residual stress on CVD diamond films", Mater Sci. Eng, Section B, Vol.57, pp. 24-7, (1998).
- [93] Y. Kang, Y. Qui, Z. Lei, M. Hu, "An application of Raman spectroscopy on the measurement of residual stress in porous silicon", Opt Laser Eng, Vol.43, pp.847-55, (2005).
- [94] T.Sasaki, S.Takahashi, Y.Kanematsu, Y.Satoh, K. Iwafuchi, M. Ishida, and Y. Moriti, Wear, 265:1402-7, (2008).
- [95] D. Devos D, M. Duquennoy, E. Roméro, F. Jenot , D. Locheignies, M. Ouafthouh, and M. Ourak, "Ultrasonic evaluation of residual stresses in flat glass tempering by an original double interferometric detection". U Ultrason, Vol.44, pp.923-7, (2006).

References

- [96] D. O'Sullivan, M. Cotterell, S. Cassidy, DA Tanner, and I. Meszaros, "Magneto-acoustic emission for the characterisation of ferritic stainless steel microstructural state", *J. Magn Mater*, Vol.271, pp.381-9, (2004).
- [97] J.Epp and T.Hirsch, "Residual Stress State Characterization of Machined Components by X-ray Diffraction and Multi parameter Micromagnetic Methods", *journal of society for Experimental Mechanics*, Vol.50, pp.195–204, (2010).
- [98] P.C.Chung, Y.Ham, S. Kim, J. Lim, C. Lee, "Effects of post-weld heat treatment cycles on microstructure and mechanical properties of electric resistance welded pipe welds", *Materials and Design*, Vol.34, pp.685–690 (2012).
- [99] X.Lin, "Heat affected zone, structure and properties of welded copper bearing HSLA steel", Ph.D thesis in philosophy, Departement of materials and engineering, university of Wollongong, Australia, (1991).
- [100] T.Cool, "Design of weld steel deposit" Ph.D thesis in philosophy, university of cambridge, (1996).
- [101] P.C.Reed, "The characterization an modeling of multipass steel weld heat affected zone" Ph.D thesis in phylosophy, university of Cambridge, (1990).
- [102] B.Eghbali, and A.Abdollah-zadeh, "The influence of thermomechanical parameters in ferrite grain refinement in a low carbon Nb-microalloyed steel", *Scripta Materialia*, Vol.53, pp.41–45, (2005).
- [103] H.Qiu, R.Ito, K.Hiraoka, "Role of grain size on the strength and ductile–brittle transition temperature in the dual-sized ferrite region of the heat-affected zone of ultra-fine grained steel", *Materials Science and Engineering, sectionA*, Vol.435–436, pp.648–652, (2006).
- [104] M. Eroğlu, and M. Aksoy, Effect of initial grain size on microstructure and toughness of intercritical heat-affected zone of a low carbon steel, *Materials Science and Engineering, section A*, Vol.286, pp.289–297, (2000).
- [105] G.S.Barritte, "The microstructure of weld metals in low alloy steels" PHD thesis in philosophy, University of Cambridge, (1982).
- [106] S.Wei, and S.Lu, "Effects of multiple normalizing processes on the microstructure and mechanical properties of low carbon steel weld metal with and without Nb", *Materials and Design*, Vol.35, pp.43–54, (2012).
- [107] M.Lord, "Formation of weld microstructure, chapter II", Ph.D thesis in philosophy, university of Cambridge, (1999).

References

- [108] E.Keehan, "Effect of Microstructure on Mechanical Properties of High Strength Steel Weld Metals, Ph.D thesis in philosophy, Chalmers university of technology and Göteborg university, Göteborg, Sweden, (2004).
- [109] X.L.Wan, R.Wei, K.M.Wu, Effect of acicular ferrite formation on grain refinement in the coarse-grained region of heat-affected zone, *materials characterization*, Vol.61, pp.726 – 731, (2010).
- [110] Y.M.Kim, H.Lee, and N.J.Kim, "Transformation behavior and microstructural characteristics of acicular ferrite in linepipe steels", *Materials Science and Engineering, sectionA*, Vol.478, (2008), pp.361–370
- [111] Y.Jing-Hong, V.Olden, A.Alvaro, and O.Akselsen, "Hydrogen diffusion and hydrogen influenced critical stress intensity in an API X70 pipeline steel welded joint Experiments and FE simulations", *international journal of hydrogen energy*, Vol.xxx, pp.1-13, (2012).
- [112] S.S.Babu, "The mechanism of acicular ferrite in weld deposits", *Current Opinion in Solid State and Materials Science*, Vol.8, pp.267–278. (2004).
- [113] M. Fattahi, N. Nabhani, M. Hosseini, N. Arabian, and E. Rahimi, "Effect of Ti-containing inclusions on the nucleation of acicular ferrite and mechanical properties of multipass weld metals", *Micron*, Vol.45 ,pp.107–114, (2013).
- [114] A. Ali, "Widmanstaetten ferrite and Bainite in Ultra-high Strength Steels", Ph.D. thesis , University of Cambridge, (1991).
- [115] Y. Zhong F.Xiao , J.Zhang , Y.Shan , W.Wang, and K.Yang," In situ TEM study of the effect of M/A films at grain boundaries on crack propagation in an ultra-fine acicular ferrite pipeline steel", *Acta Materialia*, Vol.54 pp.435–443, (2006).
- [116] V. Uvarov, I. Popov," Metrological characterization of X-ray diffraction methods for determination of crystallite size in nano-scale materials", *Materials Characterization*, Vol.58, pp.883–891,(2007).
- [117] M. Abdellatif, M. Abele, M. Leoni and P. Scardi," Solid State Nuclear Magnetic Resonance and X-ray Diffraction Line Profile Analysis of heavily deformed fluorite, *journal of thin solid films*, Vol.530, p44-48. (2013).
- [118] G.Benchabane," Les mécanismes de recristallisation et de croissance des grains dans les métaux et alliages métalliques légers"Ph.D thesis in physics of materials, University of Biskra,(2009).

References

- [119] A. Chatterjee, A. Sarkar, N. Gayathri, P. Mukherjee and P. Barat "Effect of Heat Treatment on the Portevin-Le Chatelier Effect of Al-2.5%Mg Alloy", World Academy of Science, Engineering and Technology, Vol:4 2010-10-20.
- [120] M.DE and S Gupta," Lattice imperfection studies in polycrystalline materiald by X-ray diffraction line profile analysis"Praman,Vol.23, pp.721-744 (1984).
- [121] L.FELLAH," L' effet de trefilage et de recuit sur les fils electriques de cuivre",Ph.D thesis in mechanical engineering,university of Biskra,(2015).
- [122] B Jóni, V Gonda, B Verő and T Ungár," X-ray line profile analysis of equal channel angular pressing processed Cu" IOP Conf. Series: Materials Science and Engineering, Vol.63 (2014).
- [123] A.M.Hussein, Satish I. Rao, Michael D. Uchic, D.M. Dimiduk and Jaafar A. El-Awady "Microstructurally based cross-slip mechanisms and their effects on dislocation microstructure evolution in fcc crystals"journal of Acta Materialia, Vol.85, pp.180–190, (2015).
- [124] E.J.Mittermeijer and U. Welzel, "The state of the art of the diffraction analysis of crystallite size and lattice strain", Z.Kristallogr, Vol.223, pp.552-560 (2008).
- [125] H.P.Klug and L.E.Alexander, X-ray diffraction procedures :for polycrystalline and amorphous material, second Ed, by Hrold p. Klug, Leruy E. Alaxander, ISBN0-471-49369-4,Willey-VCh,Vol.1, pp.992,(1974).
- [126] P. Scardi and M. Leoni, "Whole powder pattern modelling" Acta Crystallographica Section A, Vol.58, pp 190–200 (2002).
- [127] J.Martinez-Garcia, M.Leoni and P.Scardi "A general approach for determining the diffraction contrast factor of straight-line dislocations", Acta Crystallographica Section A, Vol.65, pp109–119,(2009).
- [128] A.Borbely, J.Dragomir-cernatescu, G.Ribarek and T .UNgar, "Computer program ANIZC for the calculation of diffraction contrast factor of dislocation in elastically anisotropic cubic, hexagonal and trigonal crystal",Journal of applied crystallography, Vol.36, pp166-162, (2003).
- [129] B.E.Warren, "X-ray studies of deformed metals"progress in metal physics, Vol.8, pp147-202,(1959).
- [130] M.Wilkens, "The determination of density and distribution of dislocation on deformed single crystal from broadened X-ray diffraction profiles", Physica status solidi section A, Vol.2, pp 359-370, (1970).

References

- [131] S.N.Dey, P.Chatterjee and S.P. Sengupta, "Dislocation induced line broadening in cold worked Pb-Bi binary alloy system in α phase using X-ray powder profile analysis, *Acta materialia*, Vol.51, pp.4669-4677, (2003).
- [132] S.N.Dey, P.Chatterjee and S.P. Sengupta, "Microstructure investigation in plastically deformed and annealed copper using a microstructural model", *journal of physics, section D : Applied physics*, vol.38, pp.1444 (2005),.
- [133] P.Scardi, M. Ortolani and M. Leoni "WPPM: microstructural analysis beyond the Rietveld method, *journal of Materials Science Forum* Vol. 651, pp. 155-171, (2010).
- [134] M.Kurita, "A new X-ray method for measuring residual stress and diffraction line broadening and its automation
- [135] Z. Boumerzoug, K. Digheche and V. Ji "X-Ray Analysis of Residual Stress in Weld Region of X70 Pipeline Steel" *journal of Advanced Materials Research*, Vol. 936, pp 2011-2016, (2014).
- [136] E. Ranjbarnodeh, S.Serajzadeh, A.H. Kokabi, and A Fischer, "Effect of welding parameters on residual stresses in dissimilar joint of stainless steel to carbon steel", *J. Mater Sci*, Vol.46, pp.3225-3232, (2011).
- [137] Macherauch, E. Kloos, K.H , "Origin, Measurements and Evaluation of Residual Stresses", *Residual Stresses in Science and Technology*. DGM Inform., Verlag, pp.3-26, (1987).
- [138] K.S.Prabhat, I.Raisul, P.Chandan, and K.Mohd, *Analysis of Residual Stresses and Distortions in Girth-Welded Carbon Steel Pipe*, IJRTE, Vol.2, Issue-2, pp.192-199, (2013).
- [139] G.R.Stewart, A.M. Elwazri, and R Varano, N. Pokutyłowicz, S. Yue and J.J. Jonas, "Testing of Welded Pipeline Steel", *Materials Science and Engineering, section A*, Vol.420, pp.115-121,(2006.).
- [140] A.Güral, B.Bostan, and A.T. Özdemir, "Heat treatment in two phase region and its effect on microstructure and mechanical strength after welding of a low carbon steel,*Materials and Design* Vol.28, pp.897-903, (2007).
- [141] P. Sathiya, M.K.Mishra, and B.Shanmugarajan, "Effect of shielding gases on microstructure and mechanical properties of super austenitic stainless steel by hybrid welding" *Journal of Materials and Design*, Vol.33, pp.203–212, (2012).
- [142] S.Bordbar, M.Alizadeh and S.H.Hashemi "Effects of microstructure alteration on corrosion behavior of welded joint in API X70 pipeline steel" *journal of Materials and Design*, Vol.45, pp.597–604, (2013).

References

[143] P.Yayla , E.Kaluc, and K.Ural,‘’ Effects of welding processes on the mechanical properties of HY 80 steel weldments’’ journal of Materials and Design, Vol.28, pp.1898–1906, (2007).

ANNEXE

ANNEXE

How to use the PM2K softwar :

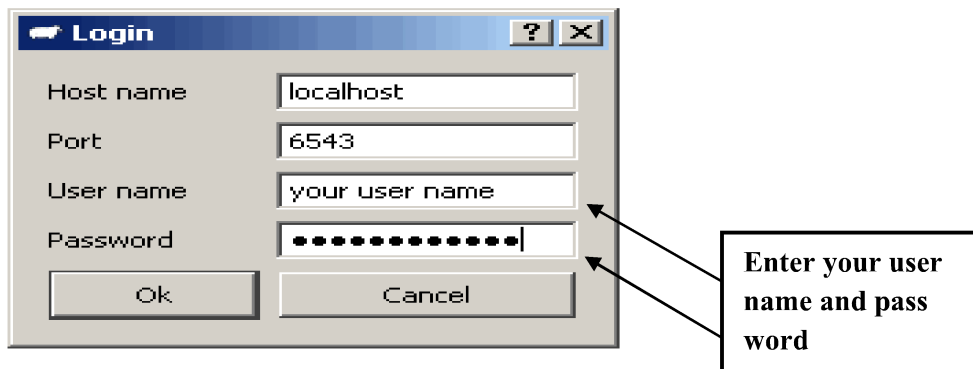
running an already prepared parameter file and dataset

This annexe, is specifically designed for first-time Users, to get immediately started and to learn some basics features of PM2K. The parameter file provided with this tutorial can also be used as a template for similar cases of study.

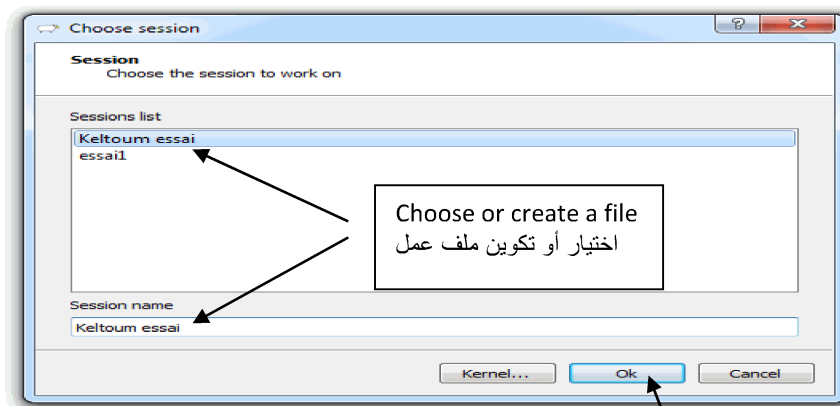
STEP 1 - getting started


Start kernel (NLSQ2.exe) and Graphical User Interface (GUI) ( PM2K2.exe).

Click on  Session and the following login window will appear:

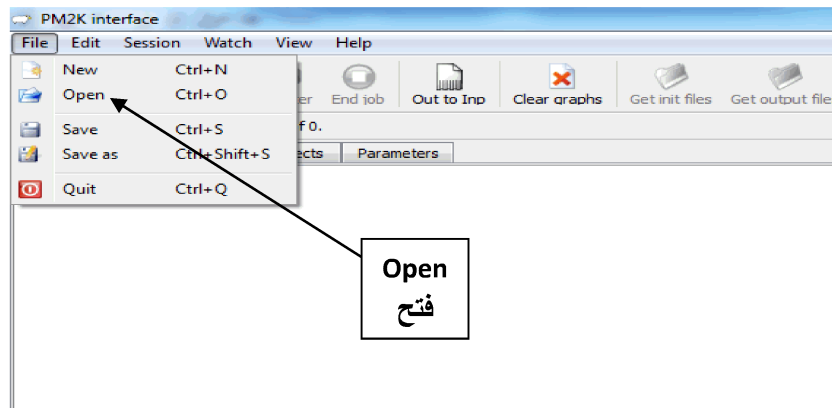


by entering your User name and Password the Session window is displayed:



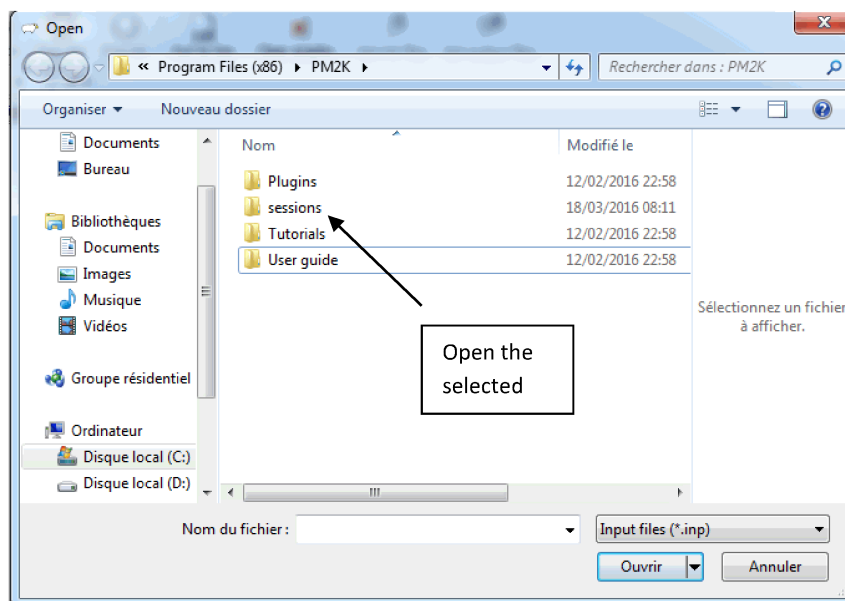
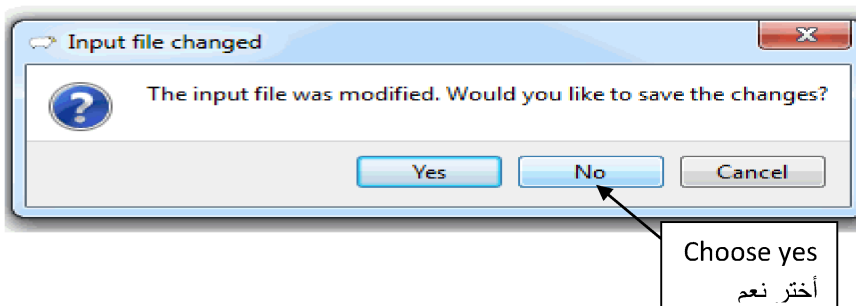
type a name for a new session or retrieve an existing one. If you enter a new name (e.g. Tutorial 1), then a new corresponding folder is created in the Session/UserName folder where PM2K was installed. Then the main window of the GUI appears again. Now select File/Open  .:

ANNEXE

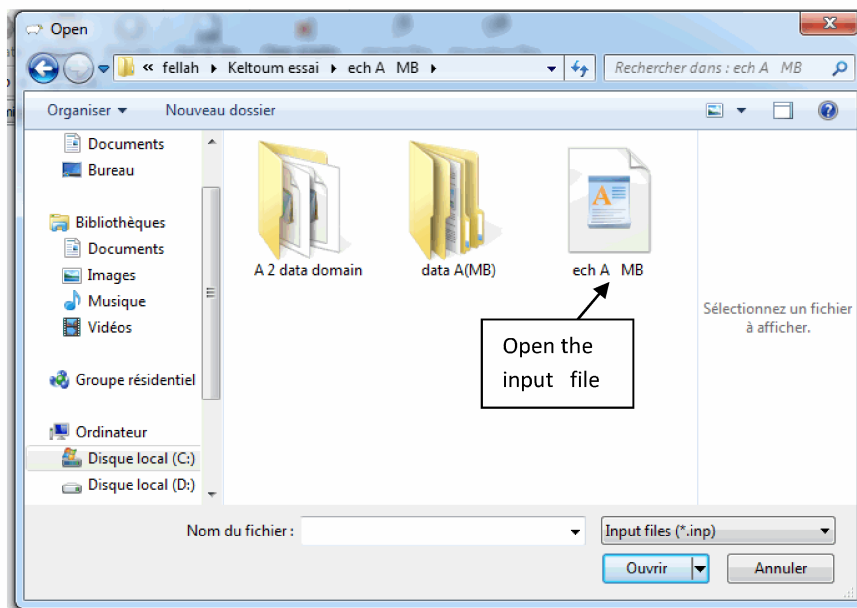
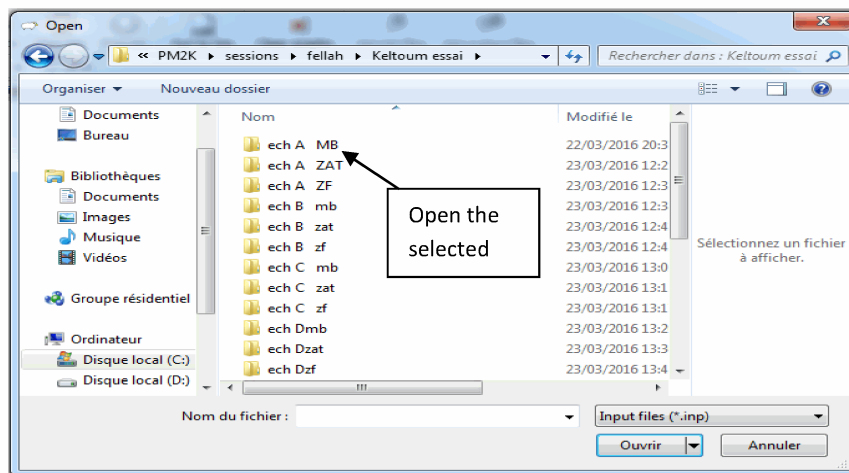
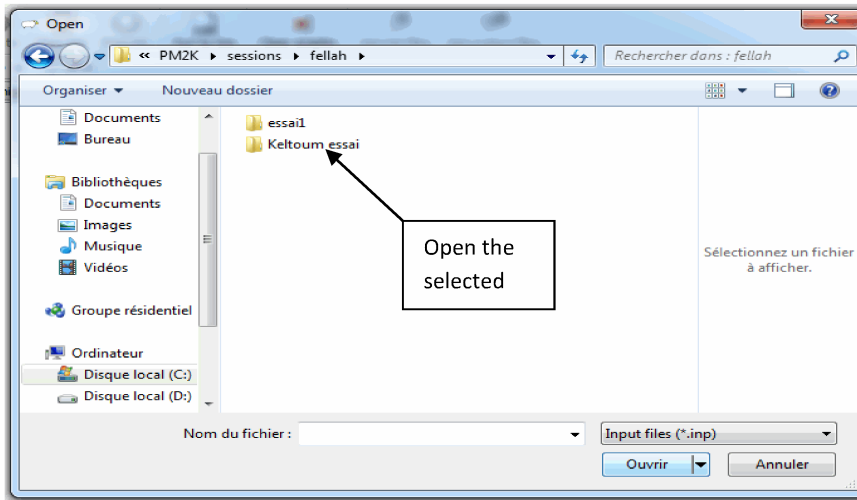


and load the demo file **Tutorial1.inp**. While doing so you are warned that any existing (already loaded) input file would be eliminated and substituted by the one you are just opening (mind this point in future use of PM2K!). Choose Yes, as you clearly have no input so far, and you actually want to load Tutorial1.inp. Select the proper path (where Tutorial files are stored in your PC) and load the file. Now the input file appears in the corresponding GUI window (see below in detail). Any text after double slashes (//) is a comment. Comments can also be inserted as `/* comment */`.

Empty lines are skipped.



ANNEXE



ANNEXE

Tutorial 1 - PARAMETERS INPUT FILE

```
// Analysis of ech A MB .xy sample - GETTING STARTED
// INSTRUMENTAL PROFILE - Coefficients of Caglioti equation and Lorentz fraction
par !W 1.122841e-002, !V -5.524408e-003, !U 8.197904e-003
par !a 3.408124e-001, !b 1.522058e-002, !c -1.080167e-004
par !wl1 1.54059800E-01 // Cu Ka1 wavelength in nm
par !wl2 1.54445650E-01 // Cu Ka2 wavelength in nm
loadData("ech A MB .xy", "xy", WPPM()) /* load data */
addWavelength(wl1, 1.0) // add Cu Ka1, with weight 1
addWavelength(wl2, 0.475) // add Cu Ka2, with weight 0.475
setMinX(20) /* set 2theta min value */
setMaxX(120) /* set 2theta max value */

// add bcc phase with unit cell parm. abc
par abc 2.873e-001 /*unit cell parameter in nm*/
addPhase(abc, abc, abc, 90, 90, 90, "bcc")
// multiply intensity by multiplicity
useMultiplicity()

// add profile components due to instrument, domain size and dislocations
convolveFourier(CagliotiUVWabc(U, V, W, a, b, c))
// domain shape and size distribution: lognormal mean (mu) and variance (sigma)
convolveFourier(SizeDistribution("sphere", "lognormal", !mu 4.0e+000 min 0.01, !sigma
1.0e-001 min 0.01 max 0.5))
par !Dave:=exp(mu+sigma^2/2); /* (arithmetic) mean size*/
par !sd:=sqrt(exp(2*mu+sigma^2)*(exp(sigma^2)-1)); /*standard deviation*/

// dislocations (Wilkens model)
// dislocation density and effective outer cut-off radius
par !rho 1.0e-002 /*x10^18 m^-2*/ min 0, !Re 3.0e+001 /* nm */ min 0
// edge dislocation fraction and burgers vector modulus for bcc metals
par !mixp 5.0e-001 min 0 max 1, burgers :=abc*sqrt(3.0)/2.0;
par !Wilk:=Re*sqrt(rho); /* Wilkens parameter */
```

ANNEXE

```
// include the contribution of faulting for an fcc structure
splitPeaks("fcc")
convolveFourier(FaultingWarren(@ 0.05e-000, @ 0.001e-000))

// average contrast factor parameters calculated for ALPHA Fe ONLY
Aedge = 2.65280E-01 // Ae,Be,As,Bs for alpha Fe (bcc)
Bedge = -3.55950E-01
Ascraw = 3.07288E-01
Bscrew = -8.19979E-01
convolveFourier(Wilkens(rho, Re, Aedge, Bedge, Ascraw, Bscrew, mixp, burgers))

// add peaks of bcc iron
addPeak( 1, 1, 0, I1 1.0e+002 min 0)
addPeak( 2, 0, 0, I2 5.0e+002 min 0)
addPeak( 2, 1, 1, I3 5.0e+001 min 0)
addPeak( 2, 2, 0, I4 5.0e+001 min 0)
addPeak( 3, 1, 0, I5 5.0e+001 min 0)
// LP factor for secondary graphite monochromator, Cu Ka radiation
// background: Chebyshev polynomial
add(Chebyshev(@ 0, @ 0, @ 0, @ 0))
//Specimen displacement for standard powder geometry, gonio radius in mm
shift(SpecimenDisplacement(240, !displ 0 /*specimen displacement in mm*/))
```

-Before starting, let's review what are we going to do - which data and models we are going to use. The dataset Tutorial1.raw is a powder pattern collected by a standard powder diffractometer (Bragg-Brentano geometry), using Cu K α radiation and a secondary monochromator (graphite bent crystal), set approximately to an angle of 26.57°. Data format is *.raw (see §3, Filetypes).

The instrumental function was obtained by using the NIST SRM 660a line profile standard (which is the object of study of Tutorial 3 and 4). Then U, V, W, a, b, c are kept constant (by adding "!" before the given parameter), as well as the wavelengths of the spectral components w11, w12, and their relative weight (in the addWavelength command). Deviations from

ANNEXE

the "theoretical" values 1 and 1/2, respectively for $K\alpha_1$ and $K\alpha_2$, may be due to several causes, in this case to the specific setting of the secondary monochromator.

The phase to be analysed is ferritic iron, which is body centred cubic. So the parameter abc is the unit cell parameter of iron. This is a ball milled powder, where crystalline domains are small and approximately equiaxed, so they can be assumed as spherical; a lognormal distribution of diameters proved to be appropriate in this case, to describe the so-called "size" broadening. An additional,

major effect contributing to the line profiles is the "strain" broadening due to dislocations produced by the grinding treatment. All in all, three factors contribute to the line profile in this specific case of study:

□ instrument (using Caglioti and Lorentz fraction parameterizations):

```
convolveFourier(CagliotiUVWabc(U, V, W, a, b, c))
```

□ size effects: lognormal distribution of spherical domains:

```
convolveFourier(SizeDistribution("sphere", "lognormal", !mu  
4.0e+000 min  
0.01, !sigma 1.0e-001 min 0.01 max 0.5))
```

□ edge/screw dislocations (in variable proportion):

```
convolveFourier(Wilkens(rho  
Re, Aedge, Bedge, Ascrow, Bscrew, mixp, burgers))
```

As already pointed out above, U, V, W, a, b, c are constant (since we already optimized their value using a line profile standard); our choice for "size" broadening model is a system of spheres with lognormally distributed diameters, so the lognormal mean (μ) and variance (σ) are to be refined; dislocations are in the primary slip system of ferritic iron, which is bcc, so we can use the Wilkens model, refining average dislocation density (ρ) and effective outer cut-off radius (R_e).

Primary slip is along $\langle 111 \rangle$ direction, so the Burgers vector is half the major diagonal of the cubic unit cell, written as `burgers := abc*sqrt(3.0)/2.0;`

(please note the dynamic link - `:=xxxxx;` - between Burgers vector modulus and unit cell parameter abc). Average contrast factor coefficients for the cubic case were calculated considering the elastic constants for iron, so A_{edge} , B_{edge} , A_{screw} , B_{screw} are constants,

ANNEXE

and the effective dislocation character (mixp, the fraction of edge vs screw dislocations) can be refined.

It is worth noting that in this input file, most quantities to be refined (mu, sigma, rho, Re, mixp) are initially kept constant (! symbol). This is part of the "refinement strategy" (see below).

In addition to the `convolveFourier` commands, the input file includes `addPeak` functions, to add the six peak profiles observed for bcc iron using $\text{CuK}\alpha$ radiation, corrections for the Lorentz - polarization factor (for a graphite bent crystal monochromator) and specimen displacement from the gonio axis. Gonio radius is set to 185 mm, whereas the displacement, at the beginning, is fixed to 0 mm. The background is modelled by a Chebyshev polynomial of 4th degree. Adding more coefficients (by simply adding: @ 0) correspondingly increases the degree (and flexibility) of the polynomial background.

Further instructions in the input file are:


```
par !Dave:=exp(mu+sigma^2/2);
```

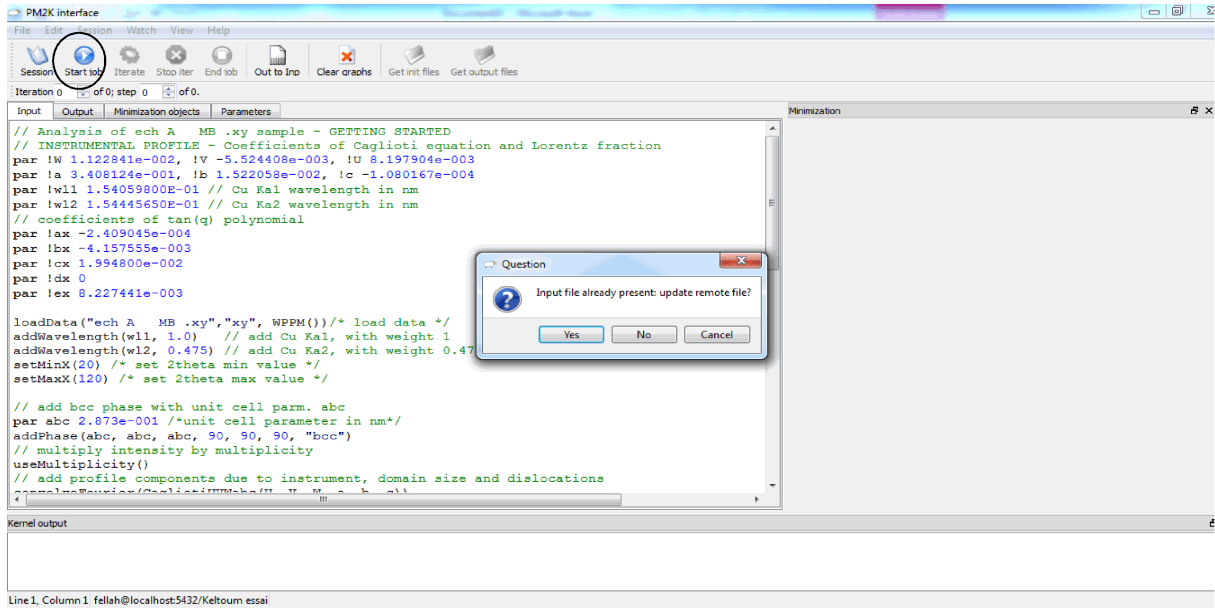
```
par !sd:=sqrt(exp(2*mu+sigma^2)*(exp(sigma^2)-1));
```

Dave and sd are additional parameters related to the size distribution, providing the arithmetic mean and standard deviation, respectively. They are not directly refined, but are calculated from the current values of mu and sigma, just as useful quantities to evaluate the result of the refinement.

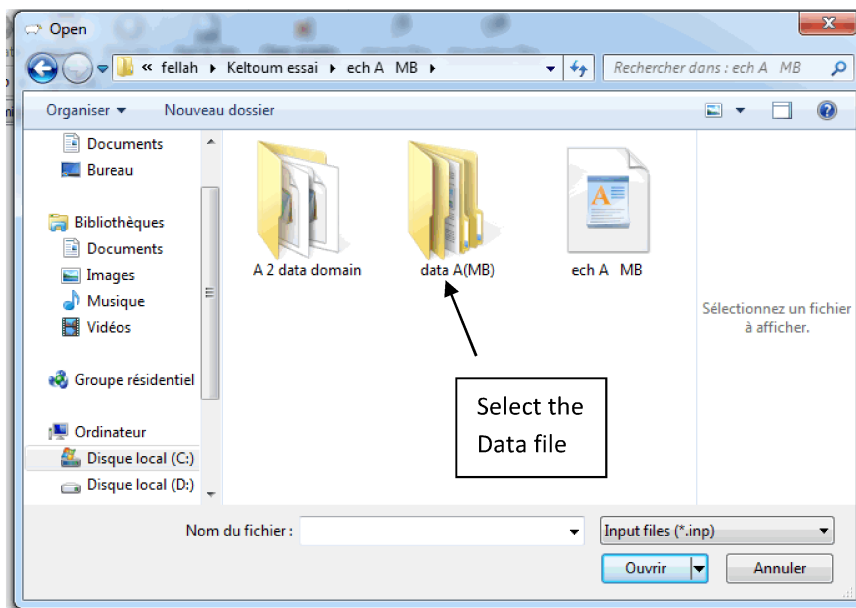
ANNEXE

STEP 2 - running the NLSQ refinement

To transfer the input data to the kernel you now need to click  Start job. You are then asked to provide the data file (Tutorial1.raw), as in the picture below (in this example files were stored in a folder named Tutorial).

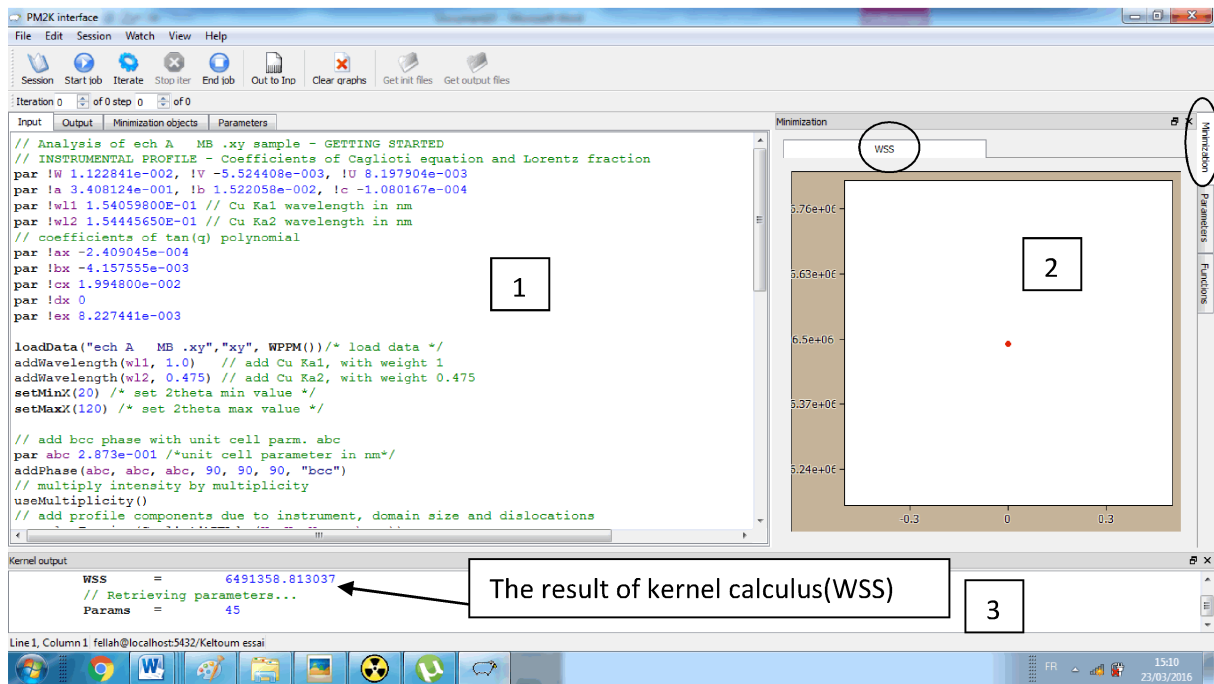


-You are invited for loading the Data file(data file= ech A MB_ xy),like in the following image



ANNEXE

By loading the data the following GUI main windows is returned:



1- Input file,

2- a window appears on the right with the starting value of the WSS (Weighted Sum of Squares), in this case 6491358,813037, which measures the discrepancy between the pattern simulated using the initial parameters (given by the Input file) and the experimental dataset.

3- At the bottom, the Kernel output gives further information on the refinement.

- In addition to that, new buttons are now active:



Iterate: to start the NLSQ, with your choice of number of iterations;



End Job: to quit the current job and create an Output File (in a window the tag of which is just aside Input File). It is worth noting that Output File gives refined parameters with their estimated standard deviations (esds). So far, you still have to run a refinement, so there are no esds yet.



Out to Inp: to transfer the output file to the input and overwrite the existing input window. You may wish to do so after running some iterations (see below), to continue refinement changing something in the input file (e.g., release some fixed parameter)



Clear graphics: to clear graphics in all windows.

ANNEXE

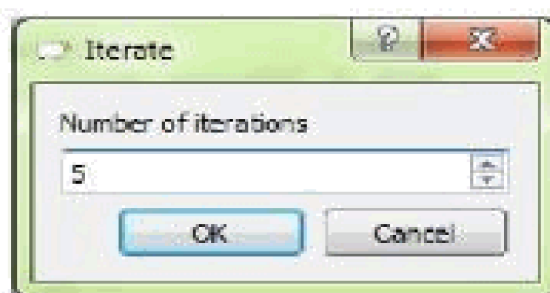
As part of the basic strategy in model refinement (see below), at the beginning not all parameters are refined simultaneously. It is more appropriate to first adjust to a reasonable match, **1** peak positions (i.e. unit cell parameters), **2** intensities and **3** background. Correspondingly (see the Input file window), the only free parameters are: abc, I1, I2, I3, I4, I5, I6 and the four nameless (@) background parameters.

To see the starting condition, click on the **Minimization Objects tag** to see the experimental data (black dots) and the calculated pattern (red line), as given by the current value of the parameters.

The difference (residual) is shown by a gray line.

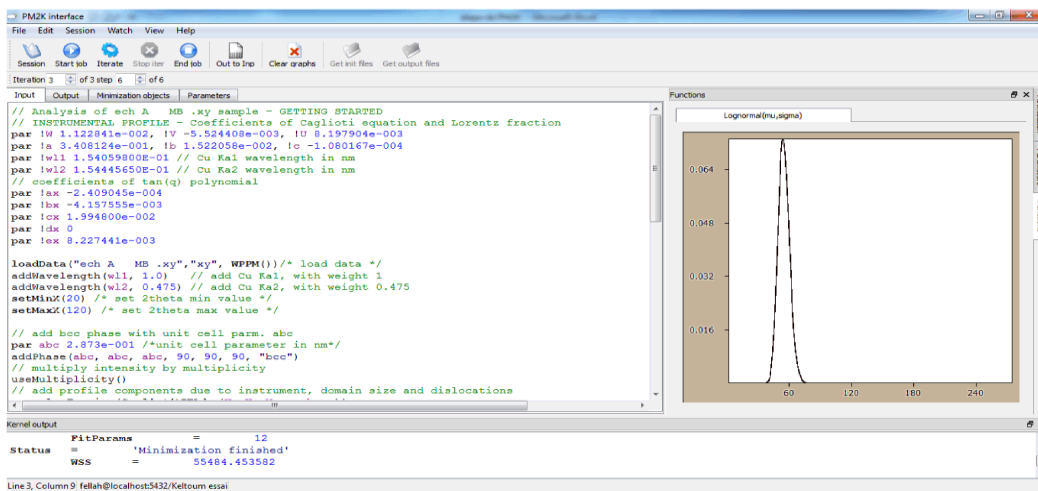
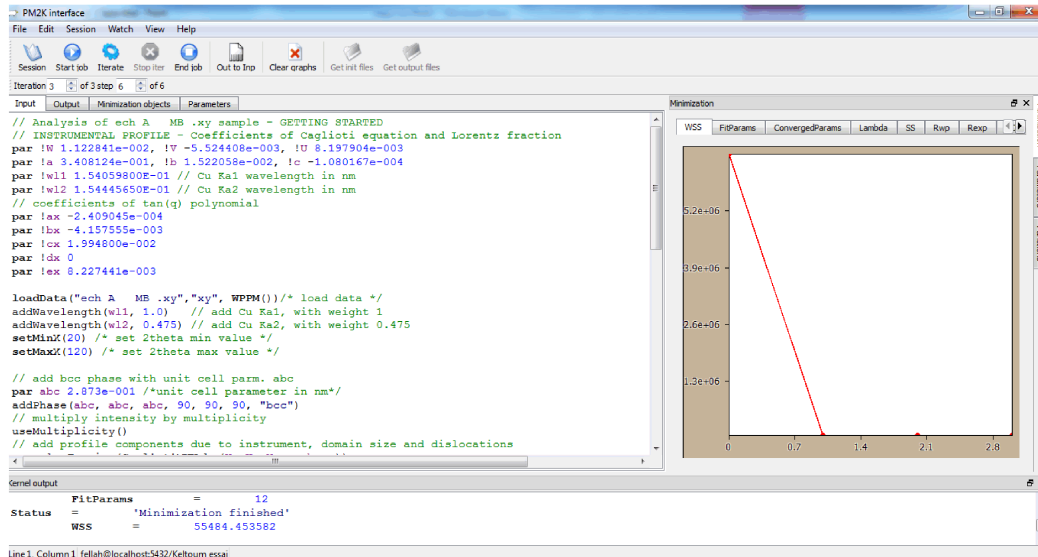
When working at other datasets and models, one might wish to manually adjust parameters to start from a condition reasonably close to the experimental data. To do so, then click

- End Job, then go to the Input file window, change parameters as needed, and then click
 - Start job again to see the new calculated pattern in the Parameters/Minimization Objects window. You may need to repeat the procedure several times before starting the refinement from a condition sufficiently close to the observed data.
 - It may be useful to keep the Parameters/Minimization Objects window open when running the refinement. To start the refinement, click on Iterate, then give 5 iterations.




You will then see the pattern changing, as the refinement of the active parameters proceeds. Even if you gave 10 iterations the refinement will stop after 4 iterations, reaching convergence for the active parameters. On the right, the WSS window shows the improvement in the match between model and data (value drops to 55484,453582). You can also see the number of parameters to convergence, by clicking on the ConvergedParams tag (right panel).


ANNEXE

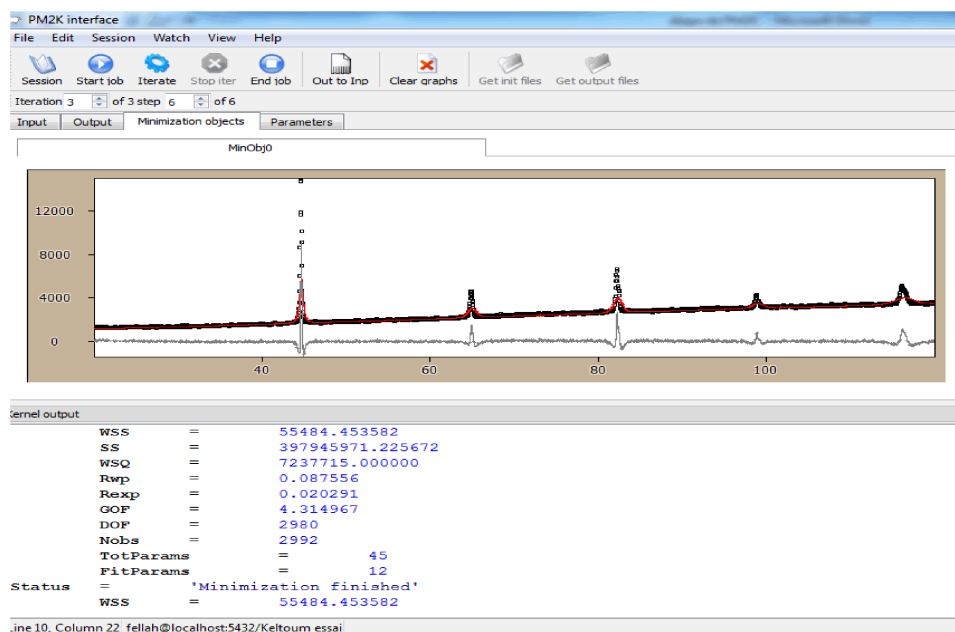



It is then possible to add other parameters to watch, like rho, Re, Wilk, Dave, sd. In addition to that, it is also convenient to watch the size distribution. This is done again through the Watch Menu, selecting the appropriate distribution (Lognormal in this Tutorial1), and entering the names used for lognormal mean and variance (as a default, in this Tutorial1, mu and sigma). Now, provided the Functions window is active (if not, activate it using the View Menu), the starting distribution appears :

We now wish to start again a refinement from this condition, adding more parameters to be refined. To this purpose we copy output to input,  Out to Inp. Now the Input file window has been updated to the new values of abc, I1, I2, I3, I4, I5, I6 and the four nameless (@) background parameters. Then we can remove the "!" from the other parameters we wish to refine: rho, Re, mixp, mu, sigma, displ.

ANNEXE

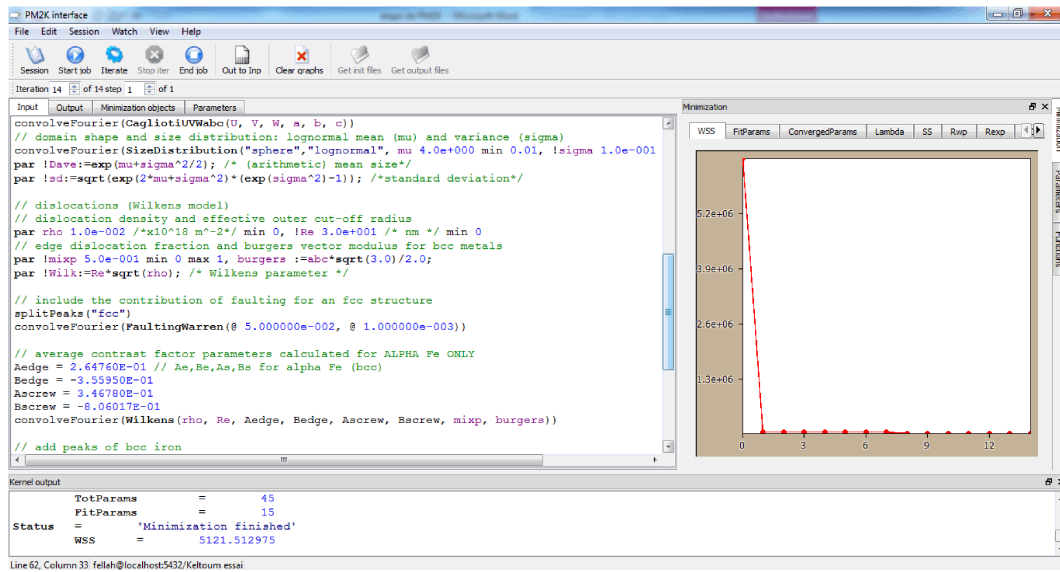
Important: this Tutorial1 is a simplified example, to go quickly through the main features of PM2K. In more general cases one would proceed by gradually releasing parameters (e.g., first rho, mu and displ, then, after some iterations, Re, mixp and sigma), which is usually a better strategy. If a larger window space to look at the input or output files is needed, a possible solution is to unlock graphics, by clicking on the  symbol. Graphics can be brought back by moving them manually on locked position (using the mouse with left button hold down) or by double clicking on them. Part of the windows can be temporarily hidden by deselecting the corresponding item in the View Menu. The following, e.g. might be obtained by undocking all extra windows (that can be positioned anywhere on Windows' desktop).



Now we can run the refinement on the newly modified Input file, with all necessary parameters released (so that they can be refined), by using Input file already present. Update remote file?).  Start job and confirming (Yes to the Question).

:

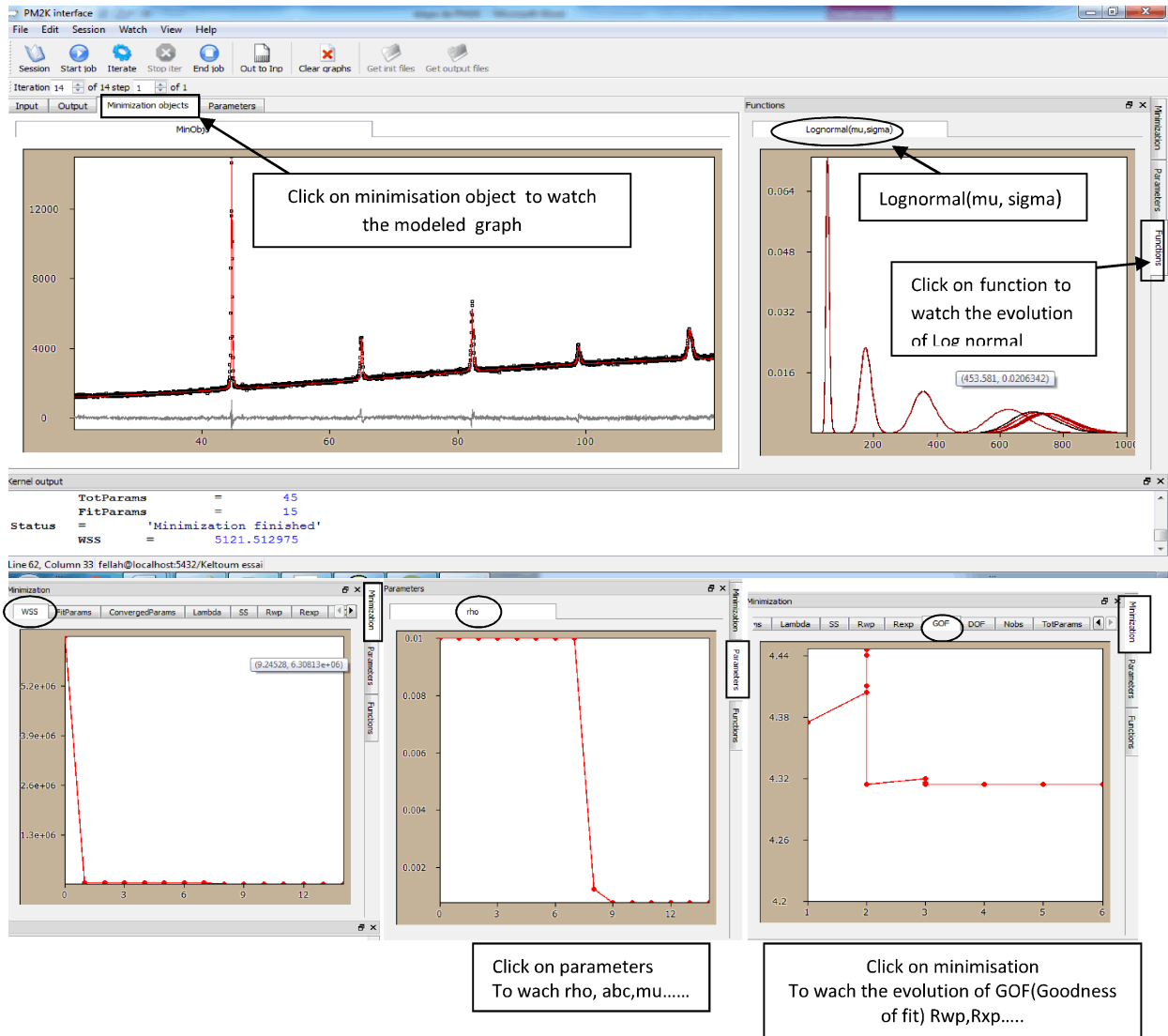
ANNEXE



We then enter 10 iterations (Iterate) and watch the action. You can freely change parameters to be watched, by clicking on the active tags in the Minimization and in the Parameters windows. You can also zoom in the windows to highlight some regions of interest. The right button offers a range of plotting options (such as the possibility of making a log plot or to freeze one or both axes during the refinement) The WSS now dropped to 5121,512975. If you click on Iteration (now showing " 25of 25"), you can review all the stages of the refinements, both in graphic form (model vs. experimental pattern in the Minimization Objects window) and in the Parameters window, to see values and esds of each refined parameter.

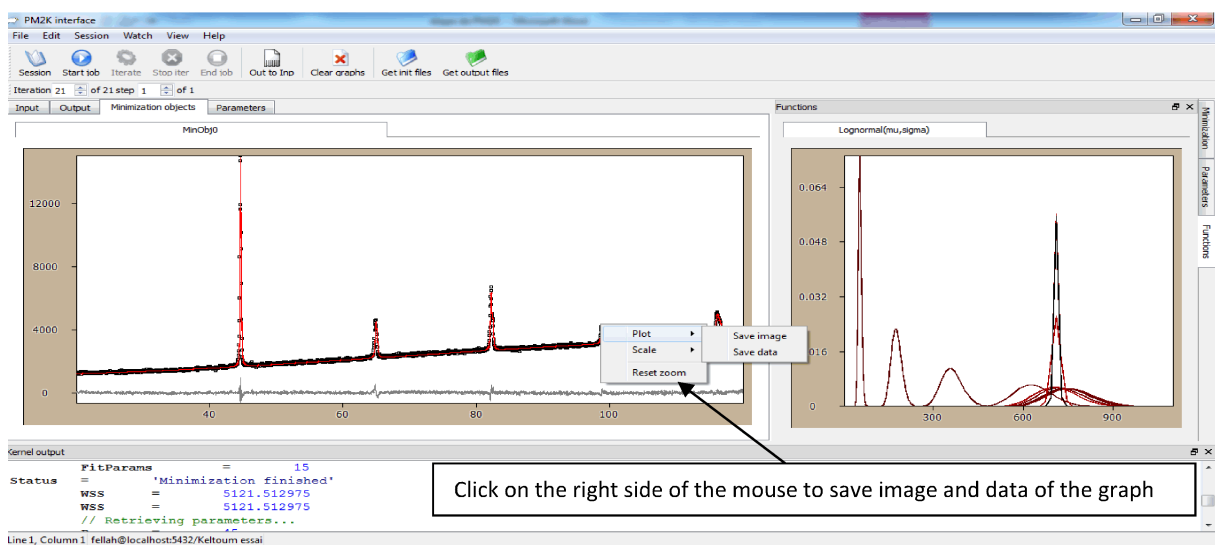
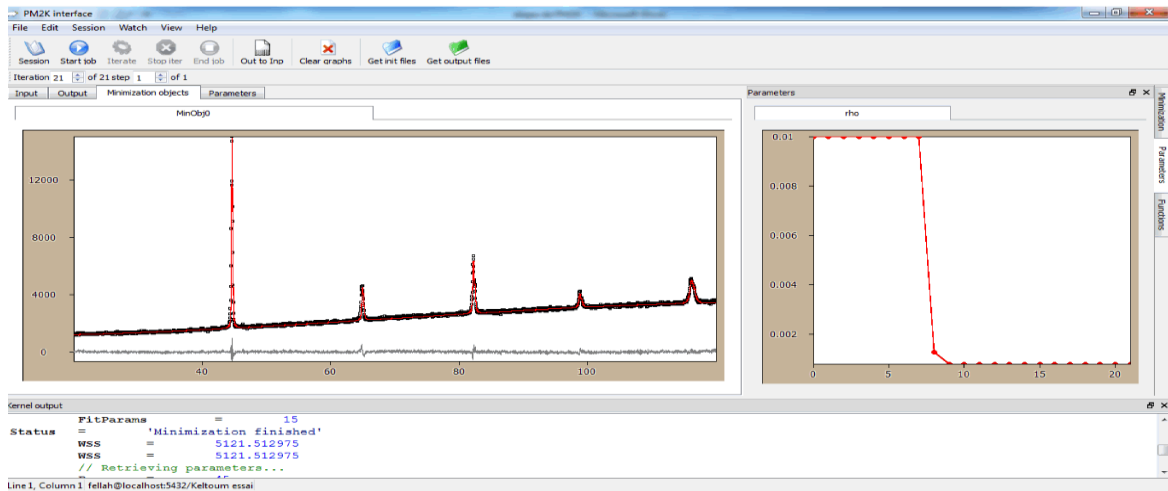
Before launching some iterations, we might wish to create some graphic windows to better follow the evolutions of parameters during the refinement. This is done through the Watch Menu, entering the name of a parameter to "Watch" during the refinement. Add the the density of dislocation ρ , unit cell parameter, abc, log normal for watch the mean domain size(D)... The plot of the behaviour of the parameter can be found under the Parameters tag (right panel)

ANNEXE



By checking the corresponding window, it can be seen that parameters that reached convergence are still a few, despite the good agreement between model and experimental data (the residual is quite flat and featureless). It may therefore be appropriate to run more iterations (Iterate) for a "final" result. The system reaches a good convergence at 27 iterations where it stops and where the WSS is stabilised at 5121,512975. Further iterations may reduce this value slightly more, but the result won't be affected (already within the error). Near convergence, parameter values do not change significantly anymore (e.g., see that abc, rho, Wilk reach a plateau), which is a good clue that parameters are now assuming their final value. The final status is shown below, where the "Watch" and Minimization windows have been docked.


ANNEXE

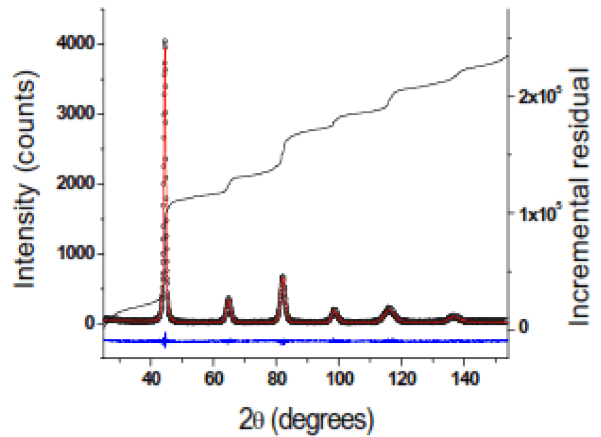
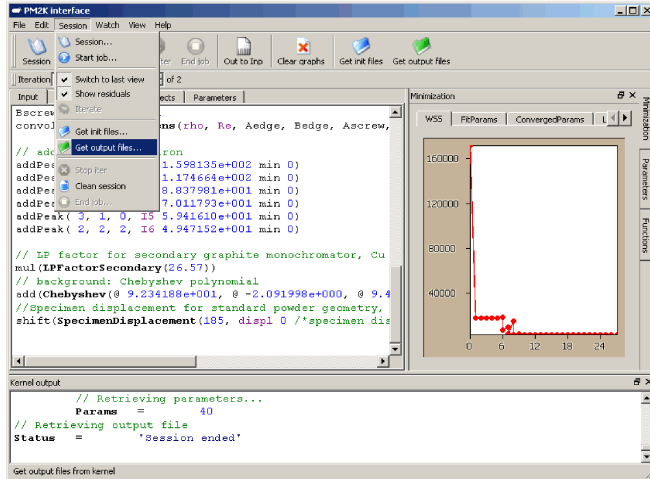


Also the size distribution is steady and the Functions window shows the "history", i.e., all attempts and stages of the NLSQ refinement. To complete this task, we now need to

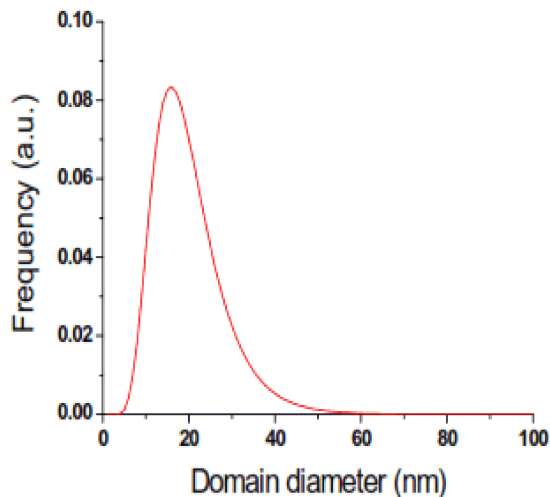
- End Job, so that an Output file is created with parameter values and esds.

ANNEXE

You can now save the output (e.g., Tutorial1.out), or you might copy Out to Inp, and then save as an input file (e.g. Tutorial1result.inp), but you can also save the graphic, for further editing. To do that, open the Session Menu and select  Get output files, then save the "out_Tutorial1.fit" file.



The *.fit file includes five columns: 2θ, exp. intensity (dots), model (calculated) intensity (red line), difference (residual, blue line below) and cumulative (integral) residual (black line, right axis). You may be willing to add the last column on a separate scale, as shown here, or just ignore it. All other parameters are in the Output file, where you read also the esds. In this file you find also the mu and sigma parameters, that you can quote as results and/or use to plot the refined size distribution, e.g., as shown below:



PM2K RESULTS (esd in parenthesis)	
Unit cell parameter (nm)	0.28730(2)
Burgers vector modulus	0.248811(4)
Dislocation density ($\times 10^{10} \text{ m}^{-2}$)	2.2(1)
Effective outer cut-off radius (nm)	14.3(14)
Edge dislocation fraction	0.68(3)
Mean domain diameter (nm)	20.0 (11)
Standard deviation (nm)	5.1(30)
Specimen displacement (mm)	0.028(6)
WSS=2752.13, Rwp=11.73%, GoF=1.036	

Esds are in units of the last significant digit. Esds for the mean size and standard deviation were obtained by error propagation from values and esds of μ and σ .

References

- [1] M. Leoni, T. Confente, and P. Scardi, "PM2K: a flexible program implementing Whole Powder Pattern Modelling," *Z. Kristallogr. Suppl.*, vol. Suppl.23, pp. 249-254, 2006.
- [2] P. Scardi, and M. Leoni, "Whole Powder Pattern Modelling: Theory and Applications," *Diffraction Analysis of the Microstructure of Materials*, Springer Series in Materials Science E. Mittemeijer and P. Scardi, eds., pp. 51-91: Springer Berlin Heidelberg, 2004.
- [3] P. Scardi, M. Leoni, and M. D'Incau, "Whole Powder Pattern Modelling of cubic metal powders deformed by high energy milling," *Zeitschrift fur Kristallographie*, vol. 222, no. 3, pp. 129-135, 2007.
- [4] M. D'Incau, M. Leoni, and P. Scardi, "High energy grinding of FeMo powders," *J. Mat. Research*, vol. 22, pp. 1744-1753, 2007.

Abstract

In this work we have used welded samples of microalloyed steel with low carbon content (0,064%), which are from X70 pipeline, fabricated by the COSIDER society (branch of OUMECH, BISKRA) for welding of pipelines. These samples are heat treated to obtain novel microstructures, to diminish the density of dislocations and to relax the residual stress after welding. X-ray diffraction method has been used to measure the density of dislocations and to analyze the residual stress distribution in weld region. The welding process has been realized by industrial arc welding. After heat treatments, residual stress relaxation phenomenon, diminution in the density of dislocations were observed in weld regions. Optical microscope, scanning electron microscope observations, and Vickers hardness measurements were also realized as complementary microstructure characterization techniques.

Key words : welding, microstructure, density of dislocations, residual stress, and X-ray diffraction.

Résumé

Dans ce travail nous avons utilisés des échantillons en acier microallié à faible pourcentage en carbone (0,064%) à partir d'une pipeline soudé de type X70 fabriqué par la société COSIDER (Filiale OUMACH, BISKRA) spécialisée dans le soudage des pipelines. Les échantillons sont traités thermiquement pour obtenir des nouvelles microstructures, pour diminuer la densité des dislocations et les contraintes résiduelles formées après le soudage. La méthode de la diffraction des rayons X a été utilisée pour mesurer la densité des dislocations et pour analyser la distribution des contraintes résiduelles dans la zone soudée. Le soudage a été réalisé à l'aide d'un arc électrique. Après traitements thermiques, le phénomène de la relaxation des contraintes résiduelles et la diminution de la densité des dislocations ont été observés dans la zone soudée. L'observation par le microscope optique et électronique avec des mesures de la micro dureté ont été réalisées aussi pour compléter la caractérisation microstructurale.

Mots clés : soudage, microstructure, densité des dislocations, contraintes résiduelles, et la diffraction des rayons X.

ملخص

في هذا العمل استعملنا عينات ملحمة من الفولاذ قليل الخلائط المعدنية و ذو نسبة قليلة من الكربون و هذه العينات مأخوذة من أنبوب ملح مصنوع من شركة كوسيدار (فرع اوماش ' بسكرة) لتلحيم الأنابيب . لقد عولجت هذه العينات حراريا و ذلك للحصول على بنيات جديدة, للتقليل من كثافة الإنخلاع' و أيضا لإرخاء الإجهادات المتبقية و الحاصلة بعد التلحيم. تستعمل تقنية الانعكاس بواسطة الأشعة السينية من أجل قياس كثافة الإنخلاع و تحليل توزع الإجهادات المتبقية في منطقة اللحام. ظاهرة إرخاء الاجهادات المتبقية و التقليل من كثافة الإنخلاع قد تم ملاحظتها بعد المعالجات الحرارية الناتجة من ترميم و إعادة بلورة البنية. بالإضافة إلى التقنية المستعملة سابقا تم استعمال تقنيات أخرى مثل الملاحظات بالمجهر الضوئي و الالكتروني و دراسة الصلادة و ذلك لتكملة دراسة البنية.

الكلمات المفتاحية: تلحيم, بنية, كثافة الإنخلاع, الإجهادات المتبقية و الانعكاس بواسطة الأشعة السينية